ISSN 1349-0087
SPring-8 Document D2011-004

SPring-8
Research Frontiers

2010

SPring-8

Research Frontiers

2010

CONTENTS
2010

Note: The principal publication(s) concerning each article is indicated with all author's names in italics in the list of references.

PREFACE

On March 11, 2011, Japan was struck by the Great East Japan Earthquake with an unprecedented 9.0 magnitude, which caused tremendous damage in the eastern part of Honshu, the main island of Japan. In this regard, I personally would like to extend my heartfelt thanks for the messages of concern and encouragement that we received from all over the world.

Fortunately, SPring-8, which is located far from the seismic epicenter, experienced no damage to its facilities and the staff were all found safe and well. The 2011A research period started in April, 2011, as usual, and at present SPring-8 users are conducting their experiments quite normally.

However, some of Japan's major synchrotron radiation facilities experienced significant damage, and their users are losing valuable research opportunities. Hence, we have decided to extend our help to these affected facilities by offering priority beamtime at SPring-8 to their users for implementing research proposals. We hope that cutting-edge research can be continued by utilizing this emergency program.

As for updates on SPring-8 research activities, 2009B and 2010A were marked yet again with fruitful research periods. Many outstanding scientific achievements have been reported in almost all fields of natural sciences and excellent articles have been published in major scientific journals by SPring-8 users, as you will read in SPring-8 Research Frontiers 2010.

As another update, the construction of the XFEL was successfully completed in March 2011. We have given the XFEL facility the nickname SACLA (SPring-8 Angstrom Compact Free Electron Laser). After tuning the system, "lasing" was achieved on June 7, 2011, at the world's highest energy level, and we expect programs for SACLA users to start by the end of March 2012. This will make the SPring-8 campus the No. 1 COE of photon sciences in the world in its truest sense.

Last but not least, I want to acknowledge the devoted effort of the editor in chief, Professor Seishi KIKUTA, who has painstakingly edited all the volumes of SPring-8 Research Frontiers from the very beginning and is now retiring following this publication. *We deeply appreciate your dedication, KIKUTA sensei, thank you very much!*

白川哲久

Tetsuhisa Shirakawa
President
SPring-8 / JASRI

EDITOR'S NOTE

SPring-8 Research Frontiers 2010 covers advances achieved during the last two consecutive research periods, the second half of 2009 (2009B) and the first half of 2010 (2010A). Remarkable scientific achievements at SPring-8 in various fields of basic and applied sciences including industrial applications are described, as well as the development of accelerators, beamlines and experimental apparatus, and the present status of the SPring-8 facility. The progress of the XFEL project at SPring-8 toward completion in FY2010 is also reported. In addition, activities using NewSUBARU, which forms an integral part of the research complex, are introduced.

The magnitude 9 earthquake that struck northeastern Japan recently has caused severe damage to many research institutes. Facing this situation, SPring-8 has decided to support the users of the affected facilities by offering beamtime. We expect that the users can maintain their activities owing to this support program.

The chief editor Professor Kikuta will retire after the publication of Research Frontiers 2010. He has edited thirteen volumes from the first Research Frontiers 1997/1998. Glancing over these volumes, it is clearly seen that recent research activities have reached a full mature phase and many cutting-edge studies appear one after another. Moreover, in the past three volumes, the profiles of some prominent group leaders have been introduced in the overview "A Place in the "X-ray" Sun."

In the contents, the title of "New Apparatus & Upgrades," which is contained in "Accelerators & Beamline," was changed to "New Apparatus, Upgrades & Methodology" in order to include papers concerning methodology, which cannot be classified in the other nine categories.

In the layout of Research Frontiers, photographs of flowers grown at the SPring-8 campus and the Harima Science Garden City have been inserted. Photographs taken by SPring-8 staff, Mr. T. Ozaki, Mr. M. Sugiura and Mr. M. Takata, are greatly appreciated.

Copies of SPring-8 Research Frontiers will be sent on request. The full text is also available on the SPring-8 website (http://www.spring8.or.jp/). For the list of publications produced by SPring-8 users and staff, please visit the publication database at http://www.spring8.or.jp/en/science/publication_database/.

We extend our appreciation to those who have recommended excellent research results suitable for publication in SPring-8 Research Frontiers. We would also like to express our sincere gratitude to the users and staff of SPring-8 for contributing their reports to this issue.

EDITORIAL BOARD

Scientific Frontiers

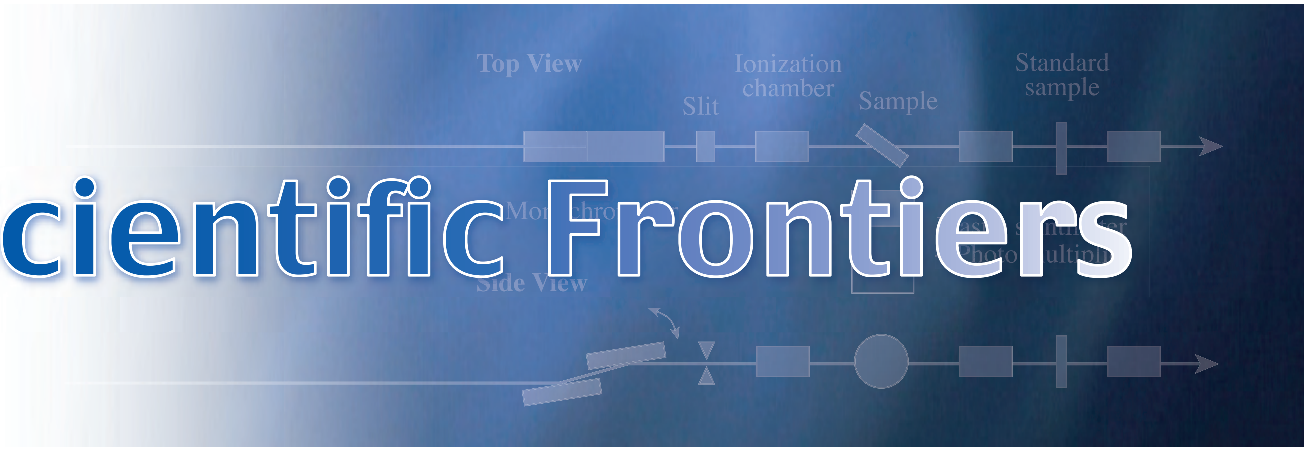

A Place in the "X-ray" Sun

At Vanguard of Science

Photon Science, now, contributes to improve the quality of life in our society by tackling the reduction of carbon dioxide problem, healthcare problem, energy problem, etc. Described here are three scientists in chemical science, materials science, medical science and technology who assume the problem-solving leaderships in photon science at SPring-8.

Wizard of Nano Coordination Space
Susumu KITAGAWA

"Structural Chemistry of Coordination Nanospace" is an exciting research field at SPring-8 developed by Professor Susumu Kitagawa of Kyoto University, who has been managing atoms and molecules and fabricating various porous materials since the early 1990s. His magic of self-organizing synthesis of porous crystalline compounds created a new concept, "*coordination space*", where the coordination bond plays an important role in the formation of spatial structures. The novel materials he synthesized are now well known as porous coordination polymers (PCPs) or metal-organic frameworks (MOFs). Because of the chemistry of coordination space, PCPs have advanced extensively, affording various functional architectures, which are constructed from a variety of molecular building blocks with different interactions between them. Professor Kitagawa is the first scientist in the world to have synthesized a novel PCP relevant to the gas storage of supercritical gases such as methane at ambient temperature, and to develop its functions not only for gas storage but also for separation and catalysis with higher capacity than conventional materials. Low molecular weight molecules, such as O_2, N_2, CO_2, CH_4, and alkanes (C_2 - C_3) are important gases for human life, since they are associated not only with energy sources, but also with global environmental issues.

In 2002, by MEM (Maximum Entropy Method)/ Rietveld structure determination via *in situ* synchrotron radiation powder diffraction experiment at BL02B2, Prof. Kitagawa discovered a one-dimensional (1D) regular assembly of adsorbed dioxygen molecules in *coordination space* that cannot be realized under normal conditions [1]. This finding opened the door for long-term research targets in chemistry and physics, i.e., low-dimensionality magnetism and photo-physical properties. The use of a uniform nanosized channel in a microporous compound, i.e., *coordination space*, became a promising approach to forming a 1D-specific assembly of molecules. His discovery of a 1D ladder structure of O_2 aligned to the host channel has provided better understanding of adsorption phenomena in a nanochannel and led to novel nanotechnologies. Molecular arrays for other gases,

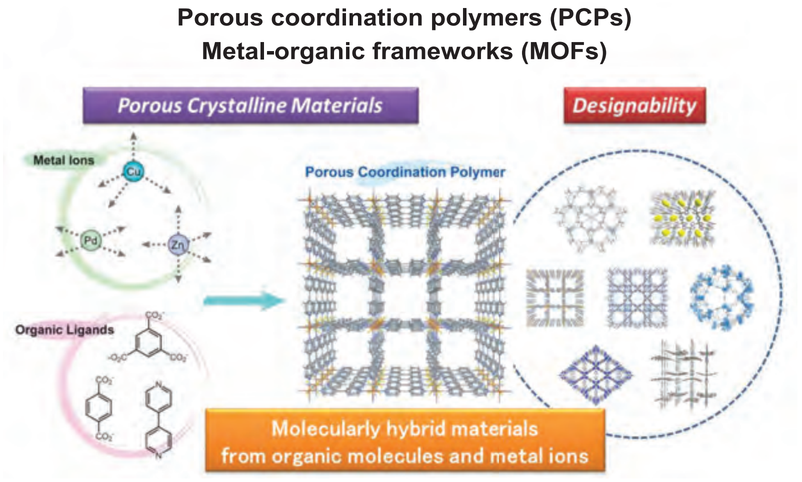

Coordination Space Synthesis

Susumu Kitagawa

namely, N_2, H_2, Ar, and CH_4 have also been determined, indicating that guest molecules are confined to forming crystalline-like regular ordered arrays in a linear fashion, in contrast to the situation in the gas and liquid states, even at temperatures above the boiling point.

For the latest global issues on energy and the environment, low molecular weight molecules, such as carbon dioxide (CO_2), methane (CH_4), acetylene (C_2H_2), and alkanes (C_2 - C_3) are gases important for human life. Acetylene is one of the key molecules used as a starting material for many chemical and electric materials. To obtain highly pure C_2H_2 for the preparation of these materials, the separation of C_2H_2 from a gas mixture containing carbon dioxide (CO_2) impurities without a large expenditure of energy is crucial. In addition, acetylene is well known to be a highly reactive molecule; therefore, it cannot be compressed above 0.2 MPa, otherwise, it will explode without oxygen, even at room temperature. With this background, more feasible and safe materials for C_2H_2 separation/storage are required. Professor Kitagawa attained extremely high levels of selective sorption of acetylene molecules onto the functionalized surface of porous coordination polymers, compared with a very similar molecule, carbon dioxide. This permits stable storage of acetylene at a density 200 times higher than the safe compression limit of free acetylene at room temperature [2].

Structural investigation using SPring-8 has performed crucial roles of his outstanding achievements described above. Every year, his paper regularly appears in our scientific highlights publications, "Research Frontiers". To date, many researchers have become involved in this new field. As a world leader in this field, Prof. Kitagawa is blazing a way to systemize the serendipity of porous material synthesis toward future gas storage/separation technology [3].

1) Formation of a One-Dimensional Array of Oxygen in a Microporous Metal-Organic Solid: *Science* 298 (2002) 2358.
2) Highly controlled acetylene accommodation in a metal-organic microporous material: *Nature* 436 (2005) 238.
3) Functional Porous Coordination Polymers: *Angew. Chem. Int. Ed.* (Review) 43 (2004) 2334.

Maverick Hunter in Advanced Materials Science
Hideo HOSONO

Professor Hideo Hosono of Tokyo Institute of Technology is a maverick hunter of novel functional materials by applying his quite unique approaches. The inventions of the electroconductive cement as an alternative transparent oxide semiconductor [1] to ITO (indium tin oxide) and of transparent amorphous oxide semiconductors facilitating the industrialization of high-performance thin-film transistors for driving next-generation flat-panel displays [2] as well as of iron pnictide superconductors [3] have been a result of his wild Element Strategy.

In particular, the discovery of an iron-based superconductor, $LaO_{1-x}F_xFeAs$, rekindled the second wave of superconductor fever in materials science. 43 K, the superconducting temperature (T_c) of this material under high pressure, is the highest T_c of non-copper-based materials ever reported. People can expect to hear of yet higher transition temperatures since this type of complexity of material offers considerable flexibility for chemical modification. Professor Hosono's discovery of iron-based high-T_c superconductors ended the monopoly of CuO_2 for high T_c over the past two decades.

Professor Hosono and his research group are now frequent users of SPring-8 and have all the time trying out new functional materials using various measurement techniques.

Hideo Hosono

Three functional materials created by Prof. Hosono

1) Light-induced conversion of an insulating refractory oxide into a persistent electronic conductor: *Nature* 419 (2002) 462.
2) Room-temperature fabrication of transparent flexible transistors using amorphous oxide semiconductors: *Nature* 432 (2004) 488.
3) Superconductivity at 43 K in an iron-based layered compound $LaO_{1-x}F_xFeAs$: *Nature* 453 (2008) 376.

Pioneer in Catching Breath via Biomedical Imaging
Rob LEWIS

Rob Lewis

Professor Rob Lewis of Monash University, Australia is a world-leading key scientist in the medical applications of synchrotrons. His research achievements based on high-resolution medical imaging at SPring-8 have assisted in the development of new diagnostic and therapeutic techniques. He and his research colleagues particularly physiologist, Professor Stuart Hooper (Monash University) have been conducting long-term program utilization at SPring-8

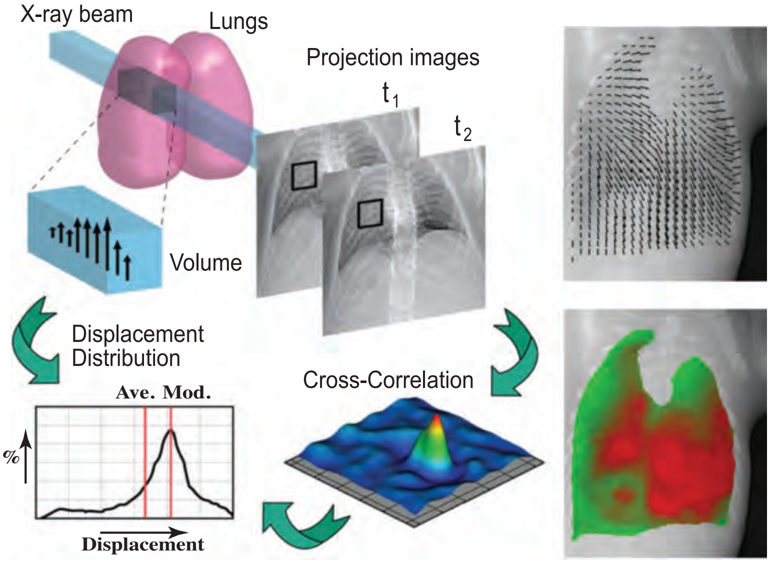

Catching Lung Motion by PIV

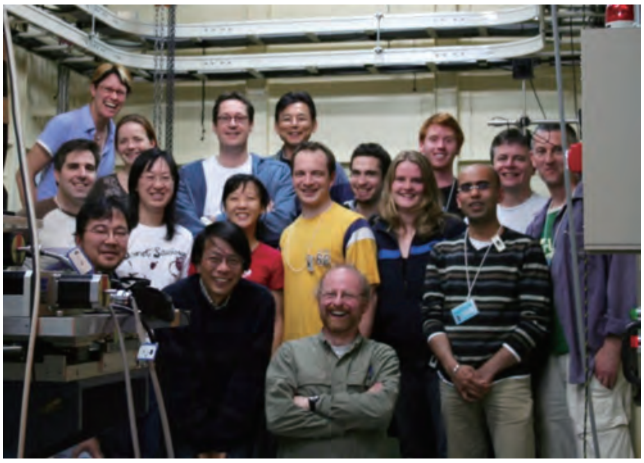

Rob & his team

to develop phase contrast imaging techniques using live rabbits and mice. Their strikingly clear images and movies visualizing lung aeration in newborn rabbits have provided new insights into the mechanism of lung liquid clearance at birth and how lungs can be injured during mechanical ventilation. The results of their work have been used to assist in training new clinical medical staff who are called upon to resuscitate very premature infants, immediately after birth. In the research program, the team recognized that the lungs can be clearly visualized throughout the full breath cycle, allowing lung motion to be studied at a level of detail sufficient to see small airways and even the alveoli. Such imaging quality has never been achieved and has only been possible using the outstanding phase contrast capabilities of the wide beam at BL20B2.

Professor Lewis said, "Most medical problems are problems of function. Static images, even in 3D, tell us little about function. Breathing is a dynamic process and so we had to develop methods to record movies so that we could see what was happening. To do that, we had to pull together a large multidisciplinary team that includes physicists, physiologists, engineers and medical doctors. Without all of them, it would have been impossible".

The first step was to develop methods of extracting reliable information about the volume of air in the lungs from phase contrast movies. The team then studied how different types of ventilation and gestational age affect the degree and uniformity of air distribution in the lung.

The second step was to try to use these techniques to study lung diseases such as asthma, fibrosis, and emphysema, as well as their treatments. A major step forward came by combining an engineering technique, i.e., Particle Image Velocimetry (PIV) used to study fluid motion, with synchrotron imaging. The groundbreaking methodology of quantitatively analyzing the motion of the lungs was developed by Dr. Andreas Fouras (Monash University). The team has succeeded in detecting the speed and direction of lung (particle) motion from the phase contrast movies obtained at SPring-8, and is now embarking on the application of their technical achievements to examine how normal lung motion is altered by diseases and subsequent pharmacological treatments, starting with asthma.

by Masaki Takata

LIFE SCIENCE:


"Fuji"- *Wisteria*

A fine X-ray beam penetrates the crystals of biological macromolecules and exposes their structural secrets, and bright synchrotron radiation contributes to expand the range of the analysis. However, many protein crystals, particularly tiny and/or ill-diffracting crystals, remain to be analyzed. Therefore, SPring-8 structural biology beamlines are continuously being developed for such tough samples. As a result of the incorporation of accumulated developmental knowledge and leading-edge technologies, the RIKEN microbeam beamline for structural biology (BL32XU) was established in 2010 under a national research project entitled Targeted Protein Research Program, which aims at advancing research and technologies as the next phase of structural genomics research. This beamline provides the world's finest and brightest X-ray beam with a size range of 1 μm^2 - 10 μm^2 with a flux density of 10^{10} photons/sec/μm^2. This beam is considered to affect any quantitative and qualitative changes in structural studies. The operation of the beamline has already been started and is open for people who are part and not part of the project. Thus, results obtained from the beamline would be actively reported in the near future.

This year, many outstanding results have been reported, particularly in the research field of nucleic acid-protein interactions. Yamashita *et al*. determined the structure of microRNA and the exportin complex. microRNA, a family of non-coding RNAs, is a key component in gene silencing by RNA interference. This molecule is produced in nuclei and exported to the cytosol by a large protein machinery. Kurumizaka *et al*. determined the unstable structure of the histone variant H3T. Histone is the key protein for DNA packaging and dynamically regulates chromatin by modifying itself. This protein might affect chromatin reorganization during sperm production. Ito *et al*. determined the structure of the glutamine transamidosome complex containing tRNA(Gln), Glu-tRNA

STRUCTURAL BIOLOGY

synthase and amidotransferase. The result indicates that error-free consecutive reactions are maintained by a dynamical structure of the multienzyme complex. Yanagisawa *et al*. performed structural and functional analyses of an aminoacyl-tRNA synthetase paralog, GenX, an enzyme that works with a tRNA mimicry protein, EF-P, similarly to aminoacyl-tRNA synthase and tRNA, and that shows a good example of convergent evolution.

Definitely, there are many remarkable reports in other fields, and four topics were selected. Inaba *et al*. determined the structure of human Ero1α, a flavoenzyme responsible for protein disulfide generation. The structural relationship among its four regulatory cysteines and FAD with the enzymatic function is clearly depicted. Takeda *et al*. revealed the mechanism of the regulation of the actin capping protein CP by the structures of two types of protein complex. CP functions to stop actin polymerization and affects cell motility. One of the inhibitors unexpectedly initiates the twisting motion of the heterodimeric CP structure, leading to depolymerization. Okumura *et al*. employed macromolecular crystallography and a chemical biology approach, providing a clue that the nuclear protein Pirin regulates melanoma cell migration. A small Pirin-binding compound was identified by chemical array screening and its binding structure was determined by synchrotron. This combinatory approach may be spread for investigating unknown protein functions. Nojiri *et al*. determined the crystal structure of copper-dependent nitrite reductase and the cytochrome *c* complex, which is essential to biological nitrite reduction in the global nitrogen cycle. The hydrophobic electron-transfer path is discovered at the docking interface of two proteins. Higuchi *et al*. showed the structure of oligomeric cytochrome *c* and the mechanism of its domain swapping polymerization by the combination of crystal analysis with X-ray solution scattering. Protein denaturants possibly form insoluble amyloid fibers and the mechanism of the protein polymerization is also interesting from the point of view in neurodegeneration.

Takashi Kumasaka

Crystal structure of the pre-microRNA nuclear export machinery

Mature microRNAs (miRNAs), which form a class of recently discovered non-coding RNAs, are present in a wide range of eukaryotes, fungi, plants, and animals [1]. miRNAs play important roles in the regulation of biological processes, including genetic development, cell proliferation, cell differentiation, apoptosis, transposon silencing, and antiviral defense [2]. miRNA biogenesis [3] begins in the nucleus, where capped and polyadenylated pri-miRNAs, several kilobases in length, are transcribed. The pri-miRNAs are processed by the nuclear RNase III enzyme Drosha to generate ~65 nt pre-miRNAs that form stem-loop structures containing 2-nt 3' overhangs. The pre-miRNAs are translocated from the nucleus to the cytoplasm through a nuclear pore complex by exportin-5 (Exp-5) in a RanGTP dependent manner. In the cytoplasm, the premiRNAs are further processed by the cytoplasmic RNase III enzyme Dicer, which excises a ~22-bp RNA duplex. One strand of the duplex binds to its target mRNA with imperfect complementarity, usually within the target's 3'-untranslated region, assisted by the RNA-induced silencing complex.

Exp-5 facilitates miRNA biogenesis by not only acting as the nuclear export factor for pre-miRNAs but also protecting pre-miRNAs from digestion by nucleases. The loss of Exp-5 results in the loss of cytoplasmic miRNA expression without the nuclear accumulation of pre-miRNAs. Pre-miRNA binding to Exp-5 requires GTP-bound forms of the small nuclear GTPase Ran cofactor (RanGTP). The Exp-5:RanGTP:pre-miRNA heteroternary complex formed in the nucleus is exported to the cytoplasm. We have determined the X-ray crystal structure of the Exp-5:RanGTP:pre-miRNA ternary complex at a 2.9 Å resolution [4]. Structural analysis was carried out using beamline **BL44XU**.

The crystal structure of the Exp-5:RanGTP:pre-miRNA complex, which contains full-length human Exp-5, canine RanGTP, and the human pre-miRNA-30a stem domain including the 2-nt 3' overhang, is shown in Fig. 1. The structure of Exp-5 contains 20 HEAT repeats, each comprising two antiparallel α-helices. The pre-miRNA-30a adopts a typical A-form RNA helical structure, 60 Å in length and 20 Å in diameter. The Exp-5:RanGTP:pre-miRNA complex is ellipsoidal with dimensions of $65 \times 80 \times 110$ Å^3. The Exp-5:RanGTP complex forms a baseball-mitt-like structure in which the pre-miRNA is caught (Fig. 2). A tunnel-like structure at the bottom of the mitt connects the inner space of the mitt with the outer space (Fig. 2). The double-stranded stem domain of the pre-miRNA is packed into the mitt and the 2-nt 3' overhang is located in the tunnel (Figs. 3 and 4).

The 2-nt 3' overhang structure is a characteristic feature of pre-miRNA. The protruding unpaired 2-nt 3' end is inserted deep into the tunnel constructed from the loop and the inner helix of HEAT12, the loop and the N-terminal end of the inner helix of HEAT13, the N-terminal region of the inner helix of HEAT14, the C-terminal half loop, and the N-terminal region of the inner helix of HEAT15. The tunnel is 15 Å in length, and its shortest diameter is 10 Å. The inner surface of the tunnel is positively charged (Figs. 2

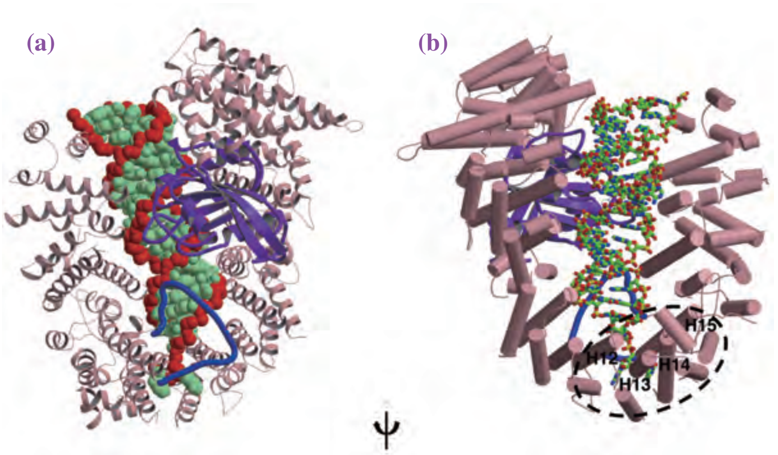

Fig. 1. Structure of the Exp-5:RanGTP:pre-miRNA-30a complex. **(a)** The structure shows human pre-miRNA-30a (red and green) bound to Exp-5 (pink) with RanGTP (purple). The long loop of HEAT15 is shown as a blue wire. In front of this view, the pre-miRNA is shielded by the long loop of Exp-5 and RanGTP. **(b)** The pre-miRNA molecule is viewed from the front open side. Exp-5 covers most of the stem moiety, and the 2-nt 3' overhang structure (circled black) has many interactions with HEAT12–15, each of which is given a letter "H" with a corresponding number.

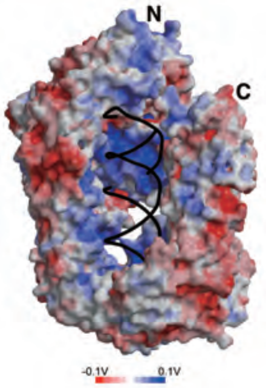

Fig. 2. Electrostatic surface potentials of Exp-5:RanGTP. The potentials are represented in a color gradient from red to blue for the vertex with potentials from –0.1 to 0.1 V. The black backbone represents the stem moiety of the pre-miRNA.

and 4(b)) and probably stabilizes the negatively charged 2-nt 3' overhang structure. The 2-nt 3' overhang structure in the tunnel is stabilized by a number of hydrogen bonds and salt bridges with amino acid residues of Exp-5, as shown in Fig. 4. Because all interactions involve atoms of the sugar-phosphate backbone, 2-nt 3' overhang recognition by Exp-5 is independent of the RNA sequence.

Although Exp-5 is an acidic protein with pI=5.6, it has localized positive charges from basic residues on the inner surface of the mitt that interact with a negatively charged double-stranded RNA (Fig. 2). The interacting residues of Exp-5 are distributed broadly on the inner helices of HEAT6-19 and a loop of HEAT15 to recognize the outer phosphodiester group of the pre-miRNA stem (Fig. 3). Thus, the stem of the pre-microRNA, 45 Å in length, is roughly recognized through a broad range of positively charged inner surface residues of the Exp-5:RanGTP mitt.

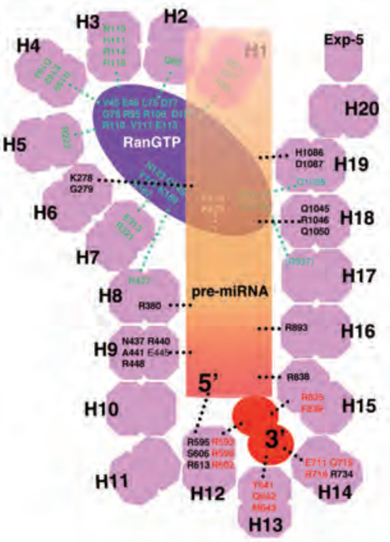

Fig. 3. Intermolecular interactions in the Exp-5:RanGTP:pre-miRNA-30a complex are shown schematically. The pre-miRNA is shown in red and light brown, where red regions interact with more basic residues of Exp-5 than light brown regions. A pink double octagon represents each HEAT repeat. Exp-5 residues shown in red are involved in the recognition of the 2-nt 3' end of the pre-miRNA, and black residues indicate interactions with the double-stranded stem of the pre-miRNA. Green residues indicate interactions between Exp-5 and RanGTP.

Since both 3' and 5' ends of the pre-miRNA are completely shielded in the tunnel, the pre-miRNA is protected from digestion by exonucleases. Exp-5:RanGTP surrounds the pre-miRNA on four sides, protecting it from ribonuclease digestion during export from the nucleus to the cytoplasm. Thus, Exp-5:RanGTP may act as both a nuclear export carrier and a molecular stabilizer of pre-miRNAs.

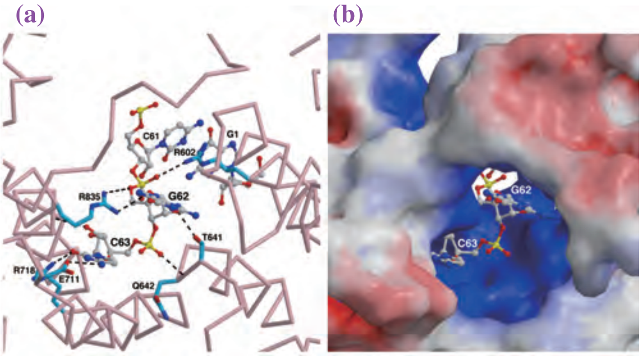

Fig. 4. Structure of the 2-nt 3' overhang of the pre-miRNA in the tunnel viewed from outside of the Exp-5 molecule. **(a)** Hydrogen bonds or salt bridges in the tunnel are represented by broken lines. Exp-5 is shown in pink for Cα, in deep blue for N, in red for O, and in sky blue for C of the side chain. RNA is shown in deep blue for N, in red for O, in yellow for P, and in gray for C. **(b)** Electrostatic potential is represented as in Fig. 2.

Eiki Yamashita[a], Chimari Okada-Jiko[b] and
Tomitake Tsukihara[a,c,*]

[a] Institute for Protein Research, Osaka University
[b] Career Path Promotion Unit for Young Life Scientists, Kyoto University
[c] Department of Life Science, University of Hyogo

*E-mail: tsuki@protein.osaka-u.ac.jp

References

[1] R.C. Lee *et al.*: Cell **75** (1993) 843.
[2] V. Ambros: Nature **431** (2004) 350.
[3] V.N. Kim *et al.*: Nat. Rev. Mol. Cell Biol. **10** (2009) 126.
[4] *C. Okada, E. Yamashita, S.J. Lee, S. Shibata, J. Katahira, A. Nakagawa, Y Yoneda, T. Tsukihara: Science* ***326*** *(2009) 1275.*

Crystal structure of the human nucleosome containing a testis-specific histone variant, H3T

Genomic DNA is compacted into the nucleus in the form of chromatin, which possesses the fundamental repeating structure called the nucleosome. In the nucleosome, a 146 base-pair DNA is wrapped 1.7 times around the histone octamer, which contains two each of the core histones H2A, H2B, H3, and H4. These core histones are composed of flexible N- and/or C-terminal tails and the histone-fold domain. The histone-fold domain provides interaction surfaces between the histones H2A and H2B (H2A/H2B), and between the histones H3 and H4 (H3/H4).

Nonallelic isoforms of histones have been identified in higher eukaryotes. For the histone H3, seven variants, i.e., H3.1, H3.2, H3.3, H3T, H3.X, H3.Y, and CENP-A, have been reported, and their common and specific functions have been discussed. H3.1 and H3.2 are expressed at the S phase of the cell cycle, and incorporated into chromatin in a replication-dependent manner. By contrast, H3.3 is constitutively expressed, and is incorporated into transcriptionally active chromatin regions and telomeres in a replication-independent manner. CENP-A is a centromere-specific H3 variant. The histones H3.X and H3.Y are novel histone variants that may be involved in the regulation of cellular responses to outside stimuli. The histone H3T was found as the testis-specific H3 variant in mammals. It may play an important role in the chromatin reorganization required for spermatogenesis.

We previously reported that H3T can be assembled into nucleosomes with H2A, H2B, and H4 (H3T nucleosome) [1]. The H3T nucleosome is not assembled by the conventional histone chaperone Nap1 [1,2]. On the other hand, Nap2 efficiently promotes the assembly of the H3T nucleosome [1,2]. These findings suggest that the H3T nucleosome has a specific structural feature and is assembled into chromatin by a specific chaperone-mediated pathway in the testis. H3T was also found in the comprehensive proteome analyses of nuclear extracts from HeLa cells. However, the nucleosomes containing H3T probably comprise an extremely small proportion of bulk chromatin in somatic cells. Therefore, H3T may have a limited function in somatic cells that is currently unknown.

To study the structure and function of the H3T nucleosome, we first prepared the human histones H2A, H2B, H3T, and H4, as bacterially expressed recombinant proteins [3]. The H3T nucleosome containing H2A, H2B, H3T, H4 and 146-base-pair DNA was reconstituted by the salt dialysis method and purified using the Prepcell apparatus. Our biochemical and cell biological experiments revealed that the H3T nucleosome is extremely unstable as compared with the H3.1 nucleosome, *in vitro* and *in vivo* [3]. To study the structural basis of the instability of the H3T nucleosome, the H3T nucleosome was crystallized and its crystal structure was determined at a 2.7 Å resolution (Fig. 1) [3]. We also crystallized the nucleosome containing the conventional histone H3.1, instead of H3T, and the crystal structure of the H3.1 nucleosome was determined at a 2.5 Å resolution (Fig. 1). The H3T nucleosome and H3.1 nucleosome crystals belonged

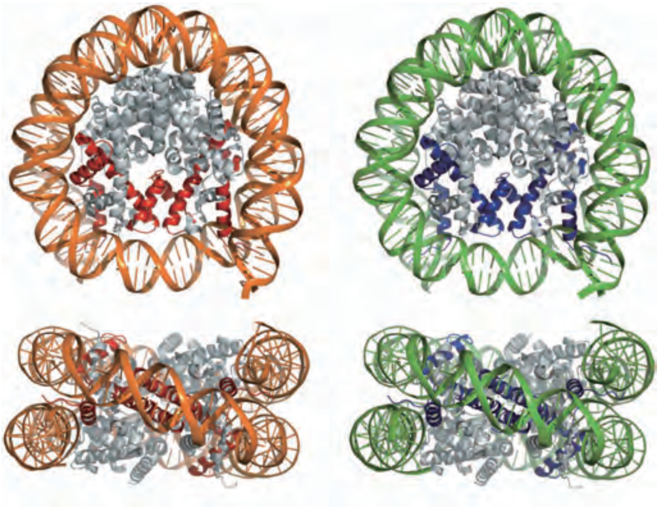

Fig. 1. Crystal structures of the H3T and H3.1 nucleosomes.

to the orthorhombic space group $P2_12_12_1$, with similar unit cell constants (a=105.5 Å, b=109.5 Å, c=181.1 Å for the H3T nucleosome, and a=105.8 Å, b=109.5 Å, c=180.9 Å for the H3.1 nucleosome). In both crystals, one nucleosome was present in the asymmetric unit. Diffraction data were obtained using beamline **BL41XU**. The structures of the H3T and H3.1 nucleosomes were determined by the molecular replacement method, using the previously solved human nucleosome structure (PDB ID: 2CV5) as a search model [4].

The overall structure of the H3T nucleosome was essentially similar to that of the H3.1 nucleosome (Fig. 1). However, careful structural comparison between H3T and H3.1 nucleosomes revealed significant differences between H3T and H3.1 near both ends of the central $\alpha2$ helix (Fig. 2). At these distorted sites, the van der Waals radii of the Met71 and Val111 residues come in close contact with that of the Val89 and Asp123 residues, respectively. The Met71 and Val111 residues are H3T-specific residues (in H3.1, Val71 and Ala111). Our mutational analysis revealed that the Met71 and Val111 residues contributed to the instability of the H3T nucleosome [3].

In the present study, we found that the H3T nucleosome structurally and biochemically differs from the conventional H3.1 nucleosome. H3T is highly expressed in the testis, and is anticipated to have a specific function in chromatin reorganization during sperminogenesis, in which drastic chromatin reorganization occurs by histone replacement with histone variants and protamines. The unstable nature of the H3T nucleosome may promote this global transition of the chromosome architecture during meiotic and/or postmeiotic events. It has been reported that about 4% of the sperm haploid genome is retained in nucleosomes [5]. The H3T nucleosomes may also be a constituent of sperm chromatin. Interestingly, sperm nucleosomes are significantly enriched around developmentally important genes, such as imprinted gene clusters, microRNA clusters, and *HOX* gene clusters, suggesting that these sperm nucleosomes have a specific epigenetic function. The specific biochemical and structural properties of the H3T nucleosome found in the present study may play an important epigenetic role in sperm chromatin.

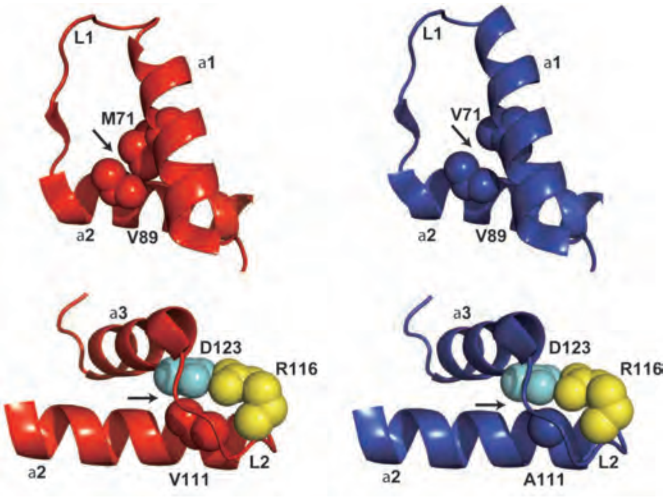

H3T-nucleosome **H3.1-nucleosome**

Fig. 2. Close-up views of the H3T region structurally different from H3.1. Arrows indicate the locations of H3T and H3.1 that are structurally different from each other.

Hiroaki Tachiwana, Wataru Kagawa and
Hitoshi Kurumizaka*

Laboratory of Structural Biology, Waseda University

*E-mail: kurumizaka@waseda.jp

References

[1] H. Tachiwana *et al.*: Nucleic Acids Res. **36** (2008) 2208.
[2] *H. Tachiwana, W. Kagawa, A. Osakabe, K. Kawaguchi, T. Shiga, Y. Hayashi-Takanaka, H. Kimura and H. Kurumizaka: Proc. Natl. Acad. Sci. USA* ***107*** *(2010) 10454.*
[3] A. Osakabe *et al.*: J. Biol. Chem. **285** (2010) 11913.
[4] Y. Tsunaka *et al.*: Nucleic Acids Res. **33** (2005) 3424.
[5] S.S. Hammoud *et al.*: Nature **460** (2009) 473.

Crystal structure of glutamine transamidosome reveals how two enzymes bound to one tRNA assume alternative conformations for consecutive reactions

Transfer RNA (tRNA) is the adaptor molecule between a codon in messenger RNA and the corresponding amino acid used in protein synthesis. Generally, each amino acid is attached to its cognate tRNA by its specific aminoacyl-tRNA synthetase, and the aminoacyl-tRNAs thus produced are transferred to the protein production machine, the ribosome. Therefore, faithful aminoacyl-tRNA formation is the prerequisite for accurate translation. However, most bacteria and all archaea lack glutaminyl-tRNA synthetase, the aminoacyl-tRNA synthetase specific to glutamine. Instead, such organisms use a two-step pathway to produce Gln-tRNA^{Gln}, as follows. The first step is the glutamylation of tRNA^{Gln} by a non-discriminating GluRS, which is also responsible for the formation of Glu-tRNA^{Glu}. The second step is the amidation of Glu-tRNA^{Gln} by a Glu-tRNA^{Gln} amidotransferase. The bacterial Glu-tRNA^{Gln} amidotransferase is the heterotrimeric GatCAB, consisting of GatA, GatB and GatC. However, the mechanism by which GluRS and GatCAB cooperate with each other in Gln-tRNA^{Gln} synthesis has not been elucidated.

To clarify the cooperation mechanism of GluRS and GatCAB, we first used a gel mobility shift assay to investigate whether bacterial GluRS, tRNA$^{Gln}_{CUG}$ and GatCAB form the ternary complex. We successfully identified the formation of the GluRS–tRNA^{Gln}–GatCAB ternary complex, also known as the bacterial 'glutamine transamidosome'. Next, to determine the mechanism at an atomic level, we solved the crystal structures of the GluRS–tRNA$^{Gln}_{CUG}$ binary complex and the glutamine transamidosome from *T. maritima* at 2.9-Å and 3.35-Å resolutions, respectively (Figs. 1(a) and 1(b)) [1]. The X-ray diffraction data were recorded at beamline **BL41XU**. The most notable characteristics of the elucidated structures are present in the glutamine transamidosome. tRNA$^{Gln}_{CUG}$ is recognized by both GluRS and GatCAB simultaneously. The coordinates of GluRS and tRNA$^{Gln}_{CUG}$ in the glutamine transamidosome are almost the same as those in the GluRS–tRNA$^{Gln}_{CUG}$ binary complex, except for the GatCAB-interacting region in tRNA$^{Gln}_{CUG}$, as detailed below.

GatCAB uses the tail body, which consists of the helical and tail domains located at the carboxy (C)-terminal region of the subunit GatB, to recognize the outer corner of tRNA$^{Gln}_{CUG}$. The GatCAB catalytic body, which consists of GatA, GatC and the amino (N)-terminal cradle domain of GatB, acts as one globule, and is located close to, but not in contact with, the acceptor arm of tRNA$^{Gln}_{CUG}$. In the present structure, GatCAB does not recognize the U1–A72 pair in the acceptor arm, although the recognition is indispensable for the amidation by GatCAB. Instead, the acceptor arm is in the catalytic site in GluRS, and the minor groove side of the acceptor stem is tightly recognized by the Rossmann-fold domain of GluRS. Furthermore, the 2′-hydroxyl group of A76 at the CCA end is located next to the co-crystallized L-glutamyl-sulfamoyl adenosine (Glu-SA), a non-hydrolyzable analogue of glutamyl-AMP. Thus, the glutamine transamidosome in the crystal represents the glutamylation state of tRNA^{Gln}. The GluRS molecule is in the productive form, whereas the GatCAB molecule is in the non-productive form.

The structures of C16 and U20 in the D-loop of tRNA$^{Gln}_{CUG}$ change upon the interaction with the tail body of GatCAB, as revealed by the superposition

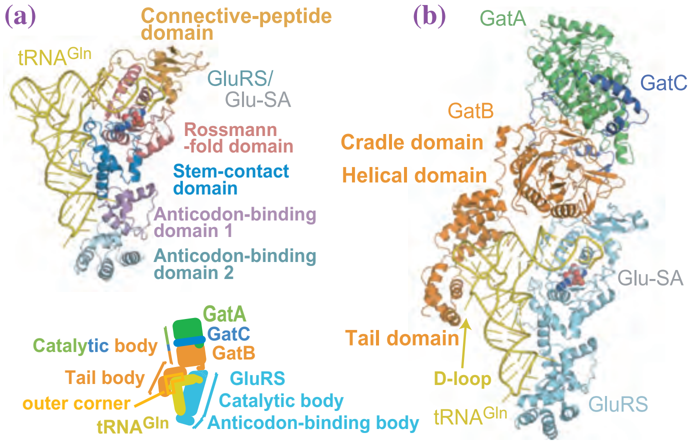

Fig. 1. Crystal structures of the GluRS–tRNA^{Gln} binary complex and the glutamine transamidosome. **(a)** Structure of the GluRS–tRNA^{Gln} binary complex from *T. maritima*. The overall structure is represented by a ribbon model, and the GluRS-bound Glu-SA is shown as a CPK model. The domain structure of GluRS is also indicated. **(b)** Structure of the glutamine transamidosome from *T. maritima*. The overall structure is represented by a ribbon model, and the GluRS-bound Glu-SA and the GatB-bound zinc ion are shown by CPK models. The names of the elements of GluRS and GatCAB are indicated on the left side.

of the structures of tRNA$^{Gln}_{CUG}$ in the glutamine transamidosome and the GluRS–tRNA^{Gln} binary complex. Since the structural features of C16 and U20 in the D loop are specific to tRNA^{Gln}, the tail domain of GatCAB interacts mainly with the tRNA^{Gln}-specific structure. To validate this tRNA^{Gln}-selection mechanism by GatCAB, we constructed tRNA$^{Glu}_{CUC}$ variants that resemble tRNA^{Gln}, and tested their ability to form Gln-tRNA^{Glu} with GluRS and GatCAB. Interestingly, the variant with both the U1–A72 pair substitution and the C20a deletion was able to form Gln-tRNA^{Glu} to some extent, and the addition of the C20U substitution augmented the ability. These results clearly showed that the tertiary structure of the D loop and the first U1–A72 pair in tRNA^{Gln} are the two major identity elements for the amidation by GatCAB.

The superposition of several GatCAB structures revealed that GatB possesses two flexible hinges at the domain boundaries. One is between the cradle and helical domains of GatB, or between the catalytic and tail bodies of GatCAB. The other is between the GatB helical and tail domains, within the tail body of GatCAB. As for GluRS, one hinge was identified between the anticodon-binding domains 1 and 2, when the structures in the transamidosome and the tRNA-free form were superimposed according to the C-terminal anticodon-binding domain 2. Consequently, GluRS can be divided into two bodies: the N-terminal catalytic body and the C-terminal anticodon-binding body [2].

These hinges in both GluRS and GatCAB may provide the flexibility required for the cooperative movements of the catalytic bodies in the functional glutamine transamidosome, as follows. First, when tRNA^{Gln}, GluRS and GatCAB cooperatively form the transamidosome, the anticodon-binding body of GluRS binds to the tRNA^{Gln} anticodon, whereas the tail body of GatCAB binds to the outer corner of tRNA^{Gln}. When the GluRS catalytic body assumes the productive form to interact with the acceptor arm of tRNA^{Gln}, the GatCAB catalytic body in the non-productive form is located near the catalytic body of GluRS. The present transamidosome structure represents this 'glutamylation state' (step Ia in Fig. 2).

After the synthesis of Glu-tRNA^{Gln} (step Ib in Fig. 2), the GluRS catalytic body is likely to leave the acceptor arm immediately, by a pivoting movement using the hinge, while the anticodon-binding body remains bound to the anticodon. As a result, the folded-back 3'-end moiety of Glu-tRNA^{Gln} can leave the catalytic site of GluRS. This state is characterized by GluRS and GatCAB in the non-productive states (step II in Fig. 2). In this state, the space between the two enzymes allows the single-stranded 3'-end moiety of Glu-tRNA^{Gln} to assume the normal, extended conformation, and it is thereby redirected towards the catalytic site of GatB (step III in Fig. 2).

In the next step, the pivoting transition of GatCAB from the non-productive form to the productive form probably brings the catalytic body closer to the acceptor arm of Glu-tRNA^{Gln}. The base-paired stem slightly bends by induced fitting, for the recognition of the determinant base pair U1–A72 by GatB. Thus, the 3'-end moiety of Glu-tRNA^{Gln} reaches the amidation catalytic site of GatCAB (step IVa in Fig. 2). In this 'amidation state', Glu-tRNA^{Gln} is converted to Gln-tRNA^{Gln} (step IVb in Fig. 2).

The 'alternative-conformation' mechanism of the glutamine transamidosome, shown in Fig. 2, clearly explains how GluRS and GatCAB are able to bind to the acceptor arm of tRNA^{Gln} in turn without steric hindrance, and how the misacylated intermediate Glu-tRNA^{Gln} can be immediately corrected to Gln-tRNA^{Gln} by GatCAB, with a low risk of releasing the misacylated product. The novel mechanism revealed in this study may serve as the structural basis for future studies on the expansion of the genetic code, in which glutamine and asparagine were incorporated at a later stage in the evolution of life.

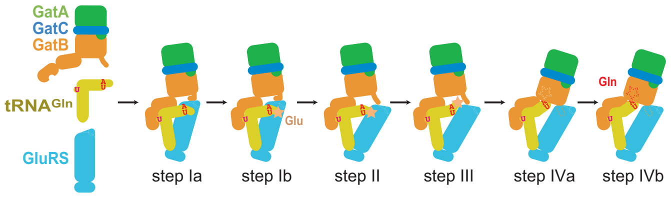

Fig. 2. Model for the pathway of Gln-tRNA^{Gln} formation. Proposed model for the pathway of Gln-tRNA^{Gln} formation by GluRS and GatCAB. The steps in the pathway are indicated under the schematic models.

Takuhiro Ito[a,b,c] and Shigeyuki Yokoyama[a,b,c,*]

[a] Lab. of Structural Biology, The University of Tokyo
[b] Dept. of Biophys. and Biochem., The University of Tokyo
[c] RIKEN Systems and Structural Biology Center (Yokohama)

*E-mail: yokoyama@biochem.s.u-tokyo.ac.jp

References

[1] *T. Ito and S. Yokoyama: Nature* ***467*** *(2010) 612.*
[2] *T. Ito, N. Kiyasu, R. Matsunaga, S. Takahashi and S. Yokoyama: Acta Crystallogr. D Biol. Crystallogr.* ***66*** *(2010) 813.*

Structure and function of a protein mimicking transfer RNA revealed from the structure of translation elongation factor P complexed with an aminoacyl–tRNA synthetase paralog, GenX

For accurate protein synthesis, the 20 canonical amino acids must be joined properly according to the genetic code. Aminoacyl–tRNA synthetases (aaRSs), enzymes that ligate a specific amino acid to its cognate tRNA, are essential components of protein synthesis. Besides the classical aaRS proteins, aaRS-related proteins lacking tRNA aminoacylation activity exist in various species, and several of these aaRS paralogs participate in amino acid biosynthesis, cofactor biosynthesis, and tRNA modification. Among the aaRS paralogs, GenX (PoxA, YjeA) is homologous to the C-terminal catalytic domain of lysyl–tRNA synthetase (LysRS). The absence of the tRNA anticodon-binding domain suggests that GenX by itself does not act as a classical aaRS. To obtain clues about the function of GenX, we determined the crystal structure of *E. coli* GenX in complex with a LysRS inhibitor [1]. A superposition of the GenX structure on that of LysRS revealed that the active site residues are highly conserved with those of LysRS (Fig. 1). In GenX, the active site pocket is slightly wider than that in LysRS, and it has sufficient space to accommodate tRNA. However, GenX did not aminoacylate *E. coli* tRNAs with lysine [1].

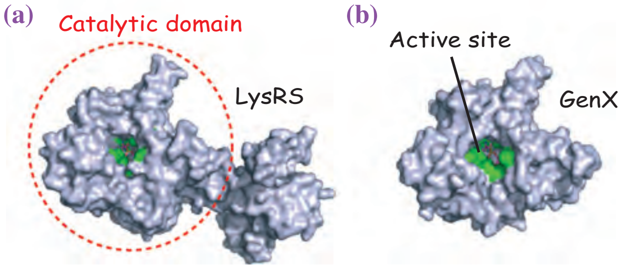

Fig. 1. Comparison of the structures of LysRS and GenX. LysRS **(a)** and GenX **(b)** are represented as surface models. The GenX residues that are conserved with those of LysRS are colored green. The structure of the catalytic domain of LysRS is similar to that of GenX.

We searched for a "tRNA-like" molecule in *Escherichia coli*, and noticed that translation elongation factor P (EF-P) assumes an L-shaped structure, which mimics that of tRNA [2]. EF-P reportedly binds to the ribosome, and stimulates the ribosomal peptidyl transferase activity [3]. A comparative genomic analysis predicted that GenX is functionally relevant to EF-P and the YjeK protein, encoded next to EF-P in the *E. coli* genome. Thus, we investigated whether EF-P is the GenX substrate, and whether EF-P is a binding partner of GenX. We successfully crystallized GenX complexed with EF-P, and determined the crystal structure of the GenX•EF-P complex at 2.5 Å resolution [1], using diffraction data collected at beamline **BL41XU**. The GenX•EF-P complex forms a GenX$_2$•EF-P$_2$ heterotetramer (Fig. 2(a)). The GenX•EF-P interactions are mediated mainly by the active site loops wrapping around the EF-P domain 1. The structure resembles that of the aspartyl–tRNA synthetase (AspRS)•tRNA^{Asp} complex, because a conserved lysine residue (Lys34) in the exposed loop of EF-P appears to be located at the 3′-adenosine of the tRNA. The GenX•EF-P complex is an aaRS•tRNA mimic, and Lys34 appears to react with the lysine moiety. We examined whether GenX ligates lysine to EF-P, and found that GenX ligates Lys34 of EF-P with lysine [1]. This is a novel example of a post-translational protein modification, and GenX is the first aaRS paralog that has been shown to modify a protein side chain with an amino acid. Our crystallographic and biochemical analyses suggest that the lysyl modification of EF-P by GenX mimics the aminoacylation of tRNA by an aaRS ("aaRS•tRNA mimicry") (Fig. 2(b)).

In bacteria, EF-P is post-translationally modified with lysine. In eukaryotes, a conserved lysine residue (Lys50) of translation initiation factor 5A (eIF5A), a distant ortholog of EF-P, undergoes a unique post-translational hypusine modification (Fig. 3) [4]. Hypusine is introduced in a two-step reaction catalyzed by deoxyhypusine synthase (DHS) and deoxyhypusine

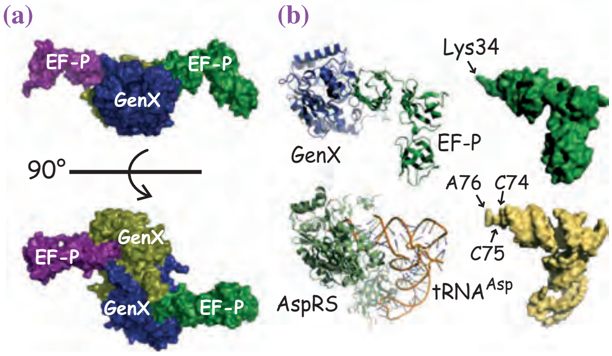

Fig. 2. **(a)** Structure of the GenX•EF-P complex. The GenX dimer (gold and blue) complexed with EF-Ps (violet and green) is represented as a surface model. The lower panel represents a view after a 90° rotation about the horizontal axis from the upper panel. **(b)** Structural comparison between the EF-P•GenX complex and the tRNA•aaRS complex. The complex of aspartic acid tRNA and aspartyl–tRNA synthetase (tRNA^{Asp}•AspRS) is shown, as an example of a tRNA•aaRS complex. The structures of the EF-P•GenX complex (upper left) and the tRNA•aaRS complex (lower left) are very similar. The Lys34 residue of EF-P corresponds to the CCA terminus (A76) where an amino acid binds to tRNA.

hydroxylase (DOHH). The conserved lysine residues at the tip of eIF5A and EF-P are both modified, and the modified residues (hypusine in eIF5A and lysyl–lysine in EF-P) are structurally similar. However, the modification enzymes (DHS and DOHH in eIF5A and GenX in EF-P) are phylogenetically unrelated to each other.

During the last decade, tRNA-protein mimicry has been proposed for several translation factors possessing structural features resembling those of tRNA. A recent crystallographic analysis revealed that EF-P binds to a new functional site between the peptidyl (P)- and exit (E)-sites of the ribosome. EF-P stabilizes the P-site-binding of fMet–tRNA^{fMet}, and thereby promotes the entry of the aminoacyl-tRNA into its binding site (A-site) [5]. Actually, the shape of the putative aminoacyl–EF-P resembles that of an aminoacyl–tRNA. The *Thermus thermophilus* EF-P Arg32 residue (corresponding to the modified Lys34 in *E. coli* EF-P), at the tip of the ribosome-bound EF-P, points toward the P site (50S ribosome). In the hypothetical structure of lysyl–Lys34, obtained by substitution of the Arg residue, the lysyl–lysine side chain might be able to reach the peptidyl transferase center (Fig. 4). Therefore, it would be interesting to determine how the putative aminoacyl–EF-P functions in the peptidyl transferase active site.

Our *in vivo* analyses revealed that YjeK (lysine 2,3-aminomutase paralog) enhanced the EF-P lysylation by GenX [1], and might convert (S)-α-lysyl–EF-P to (R)-β-lysyl–EF-P (Fig. 3(b)). Furthermore, *in vivo* analyses revealed that the EF-P modification by GenX and YjeK is essential for cell survival [1]. These results indicated that lysyl–EF-P is a functional form *in vivo*, and the lysyl modification at Lys34 in EF-P is important *in vivo*. Further details about the post-translational EF-P modification still remain unclear (e.g., what is the target gene of lysyl–EF-P?; what is the physiological role of the lysyl–EF-P *in vivo*?). Next, we will attempt to elucidate the answers to these questions.

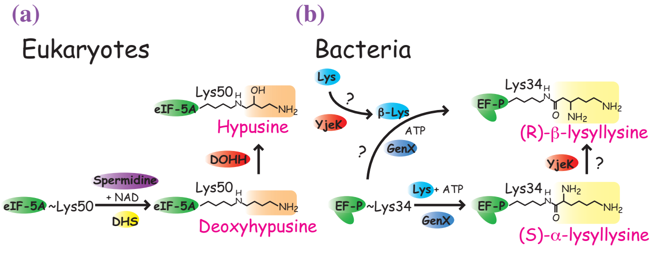

Fig. 3. Post-translational modifications of eIF5A and EF-P. **(a)** Deoxyhypusine modification of eukaryotic eIF5A, and the following hydroxylation of deoxyhypusine-modified eIF5A. **(b)** Lysyl modification of bacterial EF-P. GenX produces (S)-α-lysyl–EF-P from (S)-α-lysine (Lys), ATP, and EF-P, and then YjeK may catalyze the isomerization of (S)-α-lysyl–EF-P to (R)-β-lysyl–EF-P *in vivo*. β-Lys represents (R)-β-lysine.

In the present study, we crystallized the complex of EF-P and GenX and determined its structure, which is very similar to that of the tRNA-aaRS complex. Based on this finding, we elucidated that EF-P accepts the amino acid lysine from GenX, in a reaction similar to that of a tRNA. This is the first discovery of the striking similarities in both the structure and reaction between a nucleic acid and a protein, although they are completely different molecules. This phenomenon seems to be analogous to convergent evolution, in which different living organisms acquire similar shapes and living behaviors through evolution. GenX exists only in bacteria, such as *E. coli* and *Salmonella*, and not in eukaryotic organisms, such as humans. Therefore, GenX is a promising target for developing new antimicrobial agents for pathogenic bacteria and antimicrobial-agent-resistant bacteria, without adverse side effects.

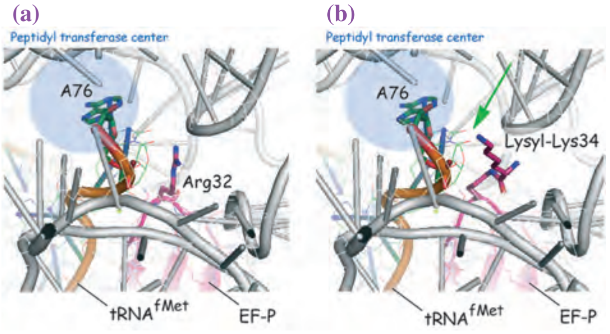

Fig. 4. Lysyl–Lys34 of EF-P docked with the EF-P–bound ribosome. **(a)** The Arg32 residue (corresponding to the modified Lys34 in *E. coli* EF-P), at the tip of the ribosome-bound *T. thermophilus* EF-P, points toward the P-site of the 50S ribosome. **(b)** In the hypothetical structure, obtained by substituting the Arg residue with lysyl–Lys34, the lysyl–lysine side chain could potentially reach the peptidyl transferase center (a green arrow).

Tatsuo Yanagisawa[a], Tomomi Sumida[a] and Shigeyuki Yokoyama[a,b,*]

[a] RIKEN Systems and Structural Biology Center
[b] Department of Biophysics and Biochemistry, The University of Tokyo

*E-mail: yokoyama@biochem.s.u-tokyo.ac.jp

References

[1] *T. Yanagisawa., T. Sumida, R. Ishii, C. Takemoto and S. Yokoyama: Nat. Struct. Mol. Biol.* **17** (2010) 1136.
[2] K. Hanawa-Suetsugu *et al.*: Proc. Natl. Acad. Sci. USA **101** (2004) 9595.
[3] M.C. Ganoza *et al.*: Microbiol. Mol. Biol. Rev. **66** (2002) 460.
[4] M.H. Park: J. Biochem. **139** (2006) 161.
[5] G. Blaha *et al.*: Science **325** (2009) 966.

Crystal structure of Ero1α, a flavoenzyme responsible for protein disulfide generation in human cells

Many secretory and membrane proteins form disulfide bonds in the endoplasmic reticulum (ER), under the assistance of numerous thiol-disulfide oxidoreductases. The major players in this oxidative reaction are protein disulfide isomerase (PDI) and Ero1, both highly conserved from yeast to mammals. Ero1 generates disulfide bonds *de novo* in conjunction with a flavin adenine dinucleotide (FAD) cofactor and transfers them to PDI. Importantly, since the generation of each disulfide bond by Ero1 is accompanied by the production of one molecule of hydrogen peroxide (H_2O_2), a potential reactive oxygen species (ROS) source, Ero1 activity must be strictly regulated in living cells. Recent studies have suggested that human Ero1, called Ero1α, has four regulatory cysteines (Cys94, Cys99, Cys104, and Cys131) and modulates its own oxidative activity through disulfide rearrangement among these cysteines: an active form contains the Cys94-Cys99 disulfide while an inactive form possesses the Cys94-Cys131 and possibly Cys99-Cys104 disulfides [1,2]. A similar feedback regulation mechanism is likely to operate in yeast Ero1p [3].

In this work, we determined the crystal structures of active and inactive forms of human Ero1α at 2.35 and 3.07 Å resolutions, respectively, using beamline **BL44XU** [4]. The entire human Ero1α chain was found to have a single globular fold highly rich in α-helices, in which five intramolecular disulfide bonds were identified (Cys35-48, Cys37-46, Cys85-Cys391, Cys208-Cys241, and Cys394-Cys397) (Fig. 1). The catalytic core region of human Ero1α constitutes the four-helix bundle scaffold with an interior electron-accepting cofactor, which is a hallmark of disulfide bond-generating enzymes widely distributed from bacteria to eukaryotes [5]. The detailed structure of the FAD-proximal site revealed that a protein disulfide bond is generated *de novo* by the cooperation of the Cys394-Cys397 pair and bound FAD (Fig. 2). We thus propose that a charge transfer (CT) complex and a C(4a) covalent adduct between flavin and a thiolate anion of Cys397 are transiently formed as obligatory steps for disulfide bond generation (Fig. 2).

Notably, all of the regulatory cysteines were contained in the highly flexible loop lacking electron density (called a 'regulatory loop'), and therefore their locations could not be specified in active Ero1α (Fig. 3(a), left). It is conceivable that the intrinsically flexible nature of this loop is essential for electron shuttling from PDI to the FAD-proximal site of Ero1α. In sharp contrast, inactive Ero1α exhibited significant electron density derived from the Cys94-Cys131 disulfide and its neighboring segment (Fig. 3(a), right). This was most likely due to the increased constraint caused by the disulfide linkage between Cys94 and Cys131, which could be the primary reason for the impaired intramolecular electron shuttle in Ero1α. In agreement with this notion, the insertion of a three- or six-glycine repeat into the site immediately after Cys131 significantly restored the PDI oxidation activity of inactive Ero1α, probably because of the increase in the mobility of the regulatory loop. Thus, human Ero1α modulates its oxidative activity by properly positioning regulatory cysteines within an intrinsically flexible loop, and by finely tuning the electron shuttle ability of the loop through disulfide rearrangements (Fig. 3(b)).

Another central issue concerning the Ero1α-PDI oxidative system is how Ero1α specifically and effectively oxidizes PDI among the nearly twenty ER-resident PDI family member proteins. Although PDI and ERp57 assume a similar overall fold and three-dimensional arrangement of four thioredoxin-like domains, the latter was reported to be a poor and presumably nonphysiologic substrate of Ero1α.

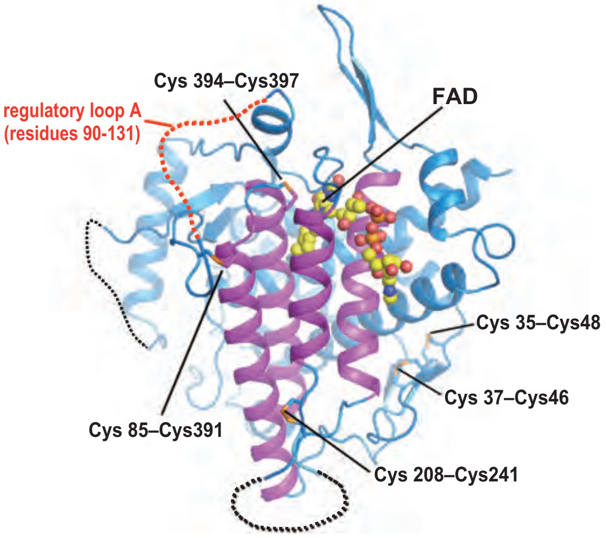

Fig. 1. Overall structure of human Ero1α. The crystal structure of the active form of human Ero1α is represented by a ribbon diagram. Loop segments that could not be modeled owing to the lack of electron density are shown by dotted lines. The regulatory loop including Cys94, Cys99, Cys104, and Cys131 is illustrated by a red dotted line. Structural and active-site disulfides characterized in this study are represented by sticks. The four-helix bundle constituting the catalytic core region of Ero1α is shown in magenta. The FAD molecule is represented by balls, in which carbon, nitrogen, oxygen, and phosphorus atoms are shown in yellow, blue, red, and orange, respectively.

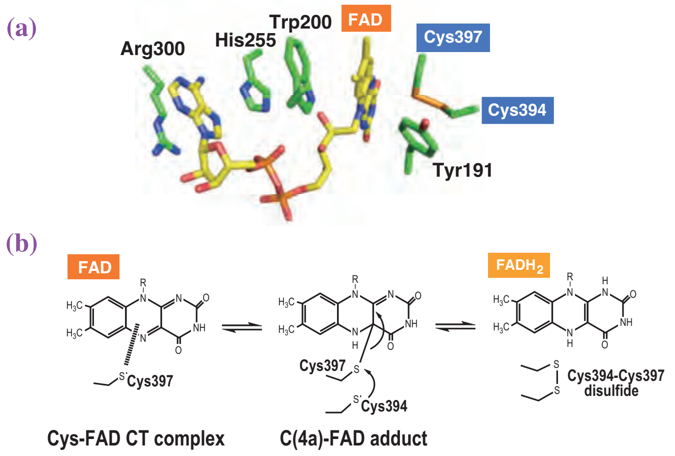

Fig. 2. FAD-binding mode of human Ero1α. **(a)** Structure of the FAD-binding site in human Ero1 α. Residues involved in aromatic ring stacking and van der Waals contact with the FAD moiety are numbered and shown in stick representation. **(b)** Proposed chemical scheme of *de novo* disulfide bond generation by the cooperation of the Cys394-Cys397 pair of human Ero1α and FAD.

Taking into account that the b'-domain of PDI uniquely contains a hydrophobic pocket, we constructed two chimeric proteins in which the b'-domain was mutually replaced between PDI and ERp57. Interestingly, the ERp57-based chimera possessing the PDI b'-domain in place of the ERp57 b'-domain was oxidized by Ero1α as effectively as wild-type PDI. Conversely, the PDI-based chimera that had the ERp57 b'-domain substituted for the PDI b'-domain exhibited an extremely slow oxidation by Ero1α. The surface plasmon resonance measurements also demonstrated that the replacement of the b'-domain between PDI and ERp57 strongly affected the affinity for Ero1α of these two enzymes. Taken together, we conclude that the PDI b'-domain is a key functional element that determines the affinity and reactivity between PDI and Ero1α. The present findings elucidate the molecular basis of regulated and specific PDI oxidations by Ero1α.

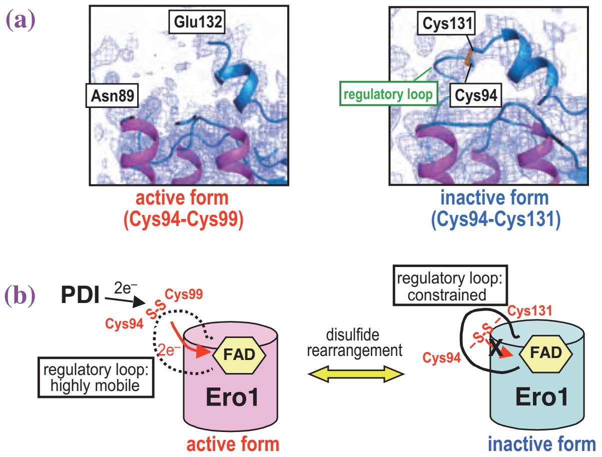

Fig. 3. Structural basis of Ero1α regulation. **(a)** Local conformational changes upon disulfide rearrangement within the regulatory loop. The Cys94-Cys131 disulfide formed in inactive Ero1α is shown in stick representation. The electron density map is shown at the 1.0 contour level. Note that electron density is completely invisible for the regulatory loop (residues 90-131) in the active form, but not in the inactive form. **(b)** Proposed model of Ero1α regulation through the internal disulfide rearrangement within the regulatory loop. The difference in combination pattern between the regulatory cysteines finely tunes the electron shuttle ability of the loop.

Kenji Inaba

Medical Institute of Bioregulation, Kyushu University

E-mail: inaba-k@bioreg.kyushu-u.ac.jp

References

[1] C. Appenzeller-Herzog *et al.*: EMBO J. **27** (2008) 2977.
[2] K.M. Baker *et al.*: EMBO J. **27** (2008) 2988.
[3] C.S. Sevier *et al.*: Cell **129** (2007) 333.
[4] *K. Inaba, S. Masui, H. Iida, S. Vavassori, R. Sitia and M. Suzuki: EMBO J.* ***29*** *(2010) 3330.*
[5] K. Inaba: Genes Cells **15** (2010) 935.

Structural basis for actin capping protein regulation by two different inhibitors

Actin-based cell motility is fundamental to various biological events such as neuronal development and immune response. Actin shows a highly dynamic behavior: monomeric actin reversibly assembles into a filamentous structure of actin filaments. Actin filaments have polarity and, in cells, their polymerization reaction occurs exclusively at the barbed end. When cells migrate, actin filaments concertedly elongate by pointing their barbed end toward the plasma membrane, which provides the driving force for the migration. Thus, the regulation of the barbed end is important for precisely controlled cell movement. The actin capping protein (CP) plays a key role in this process, since it binds tightly to the barbed end thereby stopping the elongation of the "capped" actin filaments [1]. CP is a heterodimeric protein composed of the α- and β-subunits and its crystal structure revealed that both subunits exhibit remarkably similar 3D architectures despite the lack of apparent similarity in their amino acid sequences (Fig. 1 and [2]). The α-tentacle is the major barbed end binding site in CP, located at the C-terminal region of the α-subunit (shown in red in Fig. 1). When CP caps the actin filament, it wedges between the two barbed end actin subunits with its α-tentacle region [3].

In motile cells, changes in the CP concentration lead to the formation of different actin cytoskeleton structures that cause alterations in cell shape and motility, indicating that the local concentration of CP and its affinity to the barbed end are key determinants for cellular actin assembly. Accordingly, cells exploit several proteins that can modulate the capping activity of CP. At present, V-1 and CARMIL are the only proteins that have been known to bind directly to CP and suppress its capping activity. V-1, also known as myotrophin, is a small ankyrin repeat protein implicated in a variety of cellular events such as muscle development and insulin secretion. CARMIL is a large, multi-domain protein and its down-regulation in amoeba and mammalian cells results in impaired cell motility. Previous studies demonstrated that the two inhibitory proteins affect the capping activity of CP in distinct manners. V-1 completely inhibits CP from interacting with the barbed end, whereas CARMIL acts on CP that has already capped the filament and facilitates its dissociation from the barbed end (uncapping activity). However, the molecular mechanisms underlying these differences are poorly understood. To address this important issue, we solved the crystal structures of CP in complex with V-1 or CARMIL. X-ray diffraction data were collected at **BL26B1** beamline and the structures of the crystals were determined at 1.7-2.2 Å resolutions.

Our results revealed that V-1 physically prevents CP from filament capping. V-1 directly interacts with the α-tentacle, the main actin binding site of CP, and therefore effectively sequesters CP from the barbed end (Fig. 2(a)). In contrast to V-1, CARMIL binds CP on an opposite surface to its actin binding site (Fig. 2(b)), indicating that CARMIL does not compete with the barbed end for the binding surface on CP. This finding is consistent with the ability of CARMIL to uncap the filament, since CARMIL can bind CP even when it caps the filament. However, this raises a fundamental question as to why the binding of CARMIL leads to an attenuated capping activity.

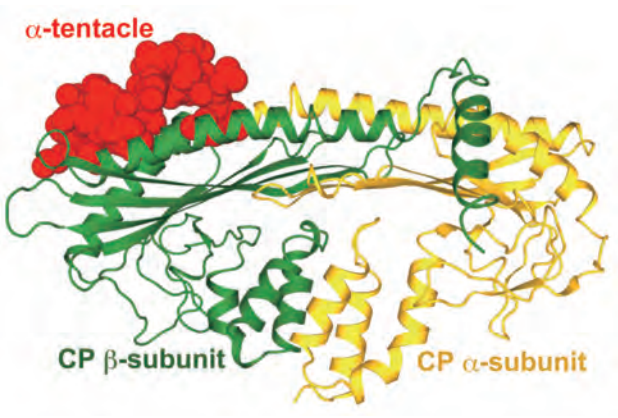

Fig. 1. Crystal structure of CP. The α- and β-subunits are shown in yellow and green, respectively. The main actin binding site, i.e., the α-tentacle, located at the C-terminal end of the α-subunit, is shown in red.

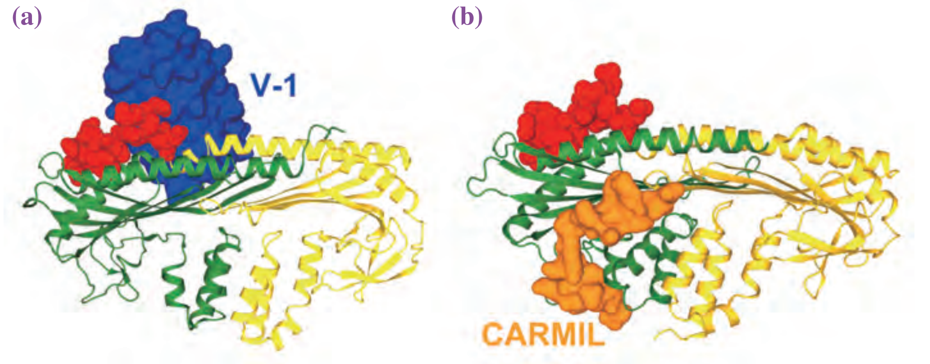

Fig. 2. Crystal structures of the CP/V-1 **(a)** and CP/CARMIL **(b)** complex structures. V-1 and CARMIL are shown in blue and orange, respectively. V-1 directly binds to the α-tentacle, demonstrating that V-1 physically prevents CP from barbed end capping. In contrast, CARMIL acts as an allosteric inhibitor for CP, since it does not physically obstruct actin binding.

Another important finding from our study provides a key to answer this question. A detailed comparison of several CP structures revealed that CP has two stable domains, CP-L and CP-S, which are continuously twisting relative to each other (Figs. 3(a) and 3(b)). This is a completely unexpected result, since CP had been considered as a rigid heterodimeric molecule. CARMIL simultaneously interacts with the two domains (Fig. 3(c)). We therefore concluded that CARMIL attenuates the binding of CP to actin filaments by suppressing the twisting motion required for tight barbed end capping.

Our results suggest that CP is not a constitutively active inhibitor of actin filament elongation; rather, its capping activity is fine-tuned for the highly orchestrated assembly of the cellular actin machinery and the conformational flexibility of CP provides the structural basis for the regulation.

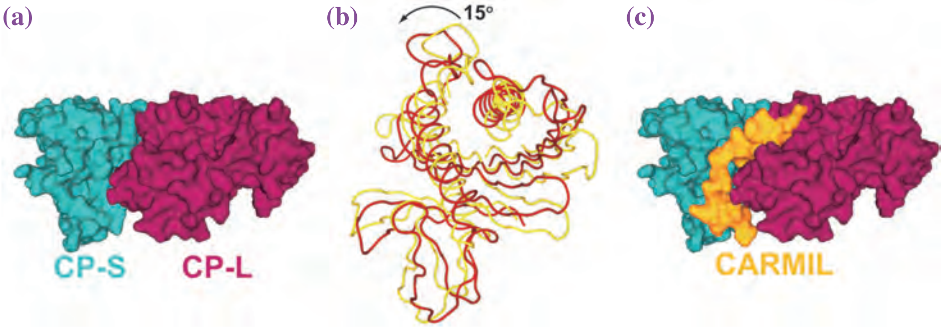

Fig. 3. Conformational flexibility of CP. **(a)** Two CP domains, CP-L and CP-S, are shown in purple and cyan, respectively. **(b)** Two different CP structures are superposed over the CP-L domain. CP-S domain structures, viewed from the left-hand side in (a), are shown in different colors and CP-L domain was removed for clarity. The CP-S domain rotates relative to the CP-L domain by about 15 degrees. **(c)** CARMIL (orange) binds to CP across the two domains, thereby restricting the twisting movement between them.

Shuichi Takeda[a,*], Yuichiro Maéda[a] and
Yasushi Nitanai[b]

[a] Structural Biology Research Center,
Nagoya University
[b] SPring-8 / RIKEN

*E-mail: takeda.shuichi@f.mbox.nagoya-u.ac.jp

References

[1] J.A. Cooper and D. Sept: Int. Rev. Cell Mol. Biol. **267** (2008) 183.
[2] A. Yamashita *et al.*: EMBO J. **22** (2003) 1529.
[3] A. Narita *et al.*: EMBO J. **25** (2006) 5626.
[4] *S. Takeda, S. Minakata, R. Koike, I. Kawahata, A. Narita, M. Kitazawa, M. Ota, T. Yamakuni, Y. Maéda, Y. Nitanai: PLoS Biol.* ***8*** *(2010) e1000416.*

Regulation of melanoma cell migration by pirin is revealed by a small molecule inhibitor

The discovery of small molecules that bind to a specific target and disrupt the function of proteins is an important step in chemical biology, especially for poorly characterized proteins. Chemical array methods enable us to isolate new ligands that bind to target proteins. Although proteins have large surface areas, many of the small-molecule ligands that have been identified in chemical array screens bind to functionally important sites in these proteins, thereby inhibiting their functions. Furthermore, many of these ligands presumably block protein-protein interactions, thereby affecting phenotypic and genetic changes in cells.

Human pirin is a nuclear protein widely expressed in punctate subnuclear structures in human tissues, but its function remains obscure. Pirin interacts with the nuclear factor I (NFI) [1] and Bcl-3 [2]. Pirin protein members are highly conserved between mammals, plants, fungi, and prokaryotic organisms and are considered to belong to the cupin superfamily. The cupin family is functionally diverse from every other protein family and comprises enzymatic and nonenzymatic members. Although the exact function of pirin is unknown, pirin orthologs have been reported to participate in many biological processes. There is evidence that the expression of human pirin is associated with the potential for cancer malignancies. The putative regulation of cancer cells by pirin is based on evidence that pirin binds to Bcl3, which is a proto-oncogene in chronic B-cell lymphocytic leukemia. Bcl3 interacts with the nuclear factor (NF)κB by binding to p50 and p52, and an increased Bcl3 expression level can enhance cell survival, proliferation, and tumor malignancy in many tumor cell lines.

A small molecule that binds specifically to pirin or proteins that interact with pirin would be a useful tool for determining the function of pirin, but no such molecule has been reported yet. To obtain pirin ligands, we performed a chemical array screen of mammalian cell lysates that overexpressed DsRed-fused proteins of interest. To obtain pirin binders, we screened more than 20,000 small molecules from a chemical library at the RIKEN Natural Products Depository (NPDepo) [3] using chemical arrays. From the screen, we isolated a small-molecule compound, which we named triphenyl compound A (TPh A; Fig. 2); it showed a positive binding signal on an array glass slide (Fig. 1). To confirm the specific binding signal from TPh A on the array slide and to study its structure-affinity relationship, we also spotted one structurally related compound onto the same slide (TPh B; Fig. 2). After the glass slide was incubated with cell lysates that expressed DsRed-fused pirin, an area that was spotted with TPh A generated a significant signal. By contrast, we found no significant signal in the area onto which TPh B was immobilized, relative to the background level.

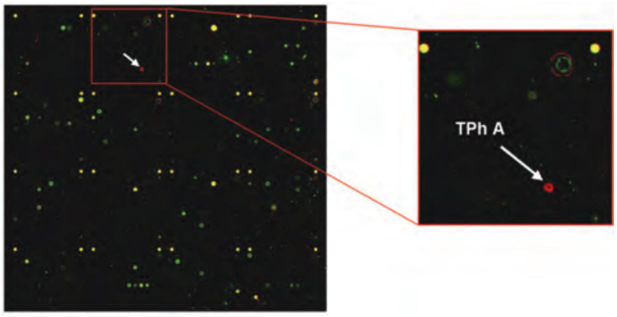

Fig. 1. The slide was treated with HEK293T cell lysates that overexpressed DsRed or DsRed-fused pirin. A fluorescent image is shown by merged display analysis of a glass slide. The positive signal of the area spotted with TPh A is indicated by white arrows.

To determine how TPh A binds to pirin, we solved the crystal structure of pirin complexed with TPh A at a 2.35-Å resolution using diffraction data collected at beamline **BL26B2**. Pirin is composed of two structurally similar β-barrel domains that are arranged

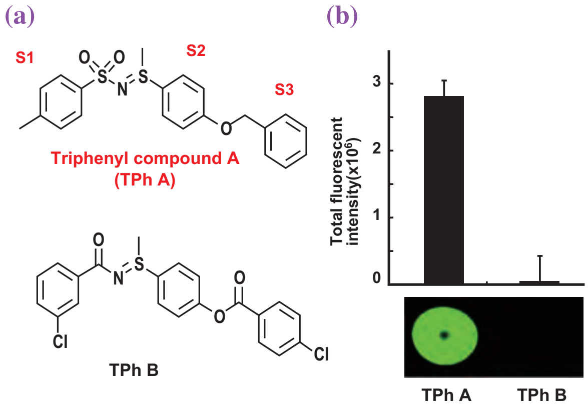

Fig. 2. **(a)** The structures of TPhs A and B are shown. TPh A has three phenyl groups (S1-S3) and a sulfilimine moiety. **(b)** TPhs A and B (10 mM) were immobilized onto a glass slide. The slide was incubated with HEK293T cell lysates that overexpressed DsRed-fused pirin. A fluorescent image is shown, and the total fluorescent intensity was corrected for background intensity. The error bars denote the s.d. of three replicates.

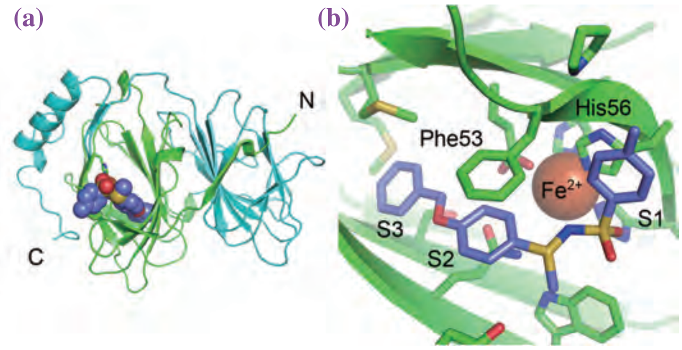

Fig. 3. **(a)** Overall view of crystal structure of pirin in complex with TPh A. Pirin is showed in green and cyan for the N- and C-terminal regions, respectively. The N- and C-terminal domains are cross-linked, with a single iron ion (brown) in the N-terminal domain. TPh A is shown as a CPK model. **(b)** TPh A molecule and the surrounding residues of pirin. The phenyl groups at the S1 and S2 positions of TPh A are stabilized by stacking interactions with His56 and Phe53, respectively.

face to face, with Fe^{2+} bound in the cavity of the N-terminal domain [4]. Our crystallography data revealed that TPh A binds in the cavity, where the metal binding site is found (Fig. 3(a)). The overall structure of the complex with TPh A resembled the structure without TPh A. The phenyl group in the S2 position of TPh A lay in the middle of the cavity, and this moiety interacted with Phe53 and the S1 ring interacted with the imidazole ring of His56 by a stacking effect (Fig. 3(b)). The metal-binding site, in which the Fe^{2+} was fixed by His56 and three coordinated sidechains, was exposed to two water molecules, one of which formed a hydrogen bond with the nitrogen atom in the *N*-(*p*-tolylsulfonyl)sulfilimine moiety of TPh A.

To gain insight into the effect of TPh A on cells, we measured the expression of pirin in several human cell lines. We found that pirin was highly expressed in the melanoma cell line WM266-4 (human malignant melanoma cells). In a screen of phenotypic changes in cells that were treated with TPh A, TPh A was found to have an effect on wound healing in WM266-4 cells, that is, the inhibition of cell migration was dose-dependent (Fig. 4). To determine whether knockdown of pirin affects melanoma cell migration, we treated cells with small inhibitory RNAs. The knockdown of pirin suppressed melanoma cell migration, as measured by wound-healing assay, but caused no change in cell proliferation.

We have identified an inhibitor of pirin, TPh A, and determined the role of pirin in melanoma cell migration. Furthermore, our crystallography data on the pirin-TPh A complex have revealed a small molecule-binding pocket in pirin, providing a new avenue through which we can gain a more thorough understanding of its structure and interactions with Bcl3 [5].

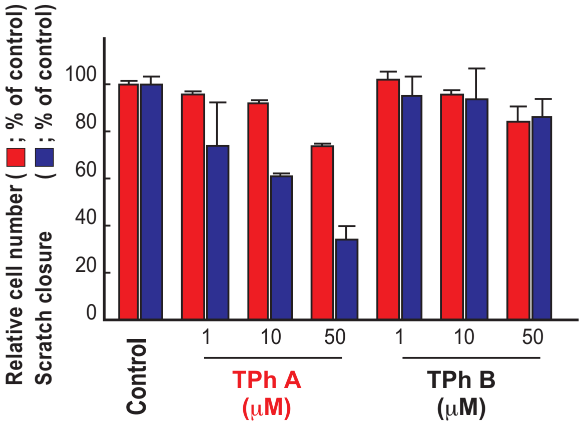

Fig. 4. Percentage of wound repair after 18 h in the absence or presence of various concentrations of TPh A or B (blue and red bars indicate cell proliferation and scratch closure, respectively). The relative cell number was calculated after 48 h (blue bars).

Hideo Okumura*,†, Isao Miyazaki and Hiroyuki Osada

RIKEN Advanced Science Institute (Wako)

*E-mail: okumurah@spring8.or.jp

† Present address: SPring-8/JASRI

References

[1] W.M. Wendler *et al.*: J. Biol. Chem. **272** (1997) 8482.
[2] R. Dechend *et al.*: Oncogene **18** (1999) 3316.
[3] H. Osada: Biosci. Biotechnol. Biochem. **74** (2010) 1135.
[4] H. Pang *et al.*: J. Biol. Chem. **279** (2004) 1491.
[5] I. Miyazaki, S. Simizu, H. Okumura, S. Takagi and H. Osada: Nat. Chem. Biol. ***6*** *(2010) 667.*

Atomic description of inter-protein electron transfer reaction for biological nitrite reduction in the global nitrogen cycle

Protein electron transfer (ET) reactions play a critical role in biologically vital processes in living cells, most notably respiration and photosynthesis. The reactions occur between protein-bound prosthetic groups separated by long distances, often greater than 10 Å and display high efficiency and specificity. In addition to a dependence on factors inherent to the long-range ET processes, numerous studies have revealed that inter-molecular ET reactions requiring a balance of specific binding and fast dissociation are highly sensitive to protein association modes and their protein-protein interfaces. Hence, the conformational changes of the amino acid residues and the behavior of solvent molecules at the interface formed by redox-partner proteins have the potential to regulate inter-protein ET [1].

Recent earth science and geochemical studies have pointed out that the massive acceleration of the global nitrogen cycle as a result of the production and industrial use of artificial nitrogen fertilizers worldwide has led to a host of environmental problems, ranging from eutrophication of terrestrial and aquatic systems to global acidification. Denitrification is one of the biological processes contributing to the maintenance of the nitrogen balance on the earth. Dissimilatory copper-containing nitrite reductase (CuNIR) is a key enzyme in denitrification, catalyzing one-electron reduction of nitrite (NO_2^-) to nitrogen monoxide (NO). The reaction is specifically regulated by the efficient inter-protein ET reaction with a redox-partner protein. CuNIRs fold a trimeric structure with two distinct Cu sites per a *ca*. 37-kDa monomer unit. The type 1 Cu site (T1Cu) buried within each monomer relays an electron from the redox-partner protein to the catalytic type 2 Cu site (T2Cu), where NO_2^- is reduced to NO. Despite much effort by several groups, a crystal structure of the protein–protein complex between CuNIR and its redox-partner protein has not yet been determined. Here we have determined the binary complex of CuNIR with its redox partner cytochrome *c* (Cyt *c*) at 1.7 Å resolution by X-ray three-dimensional crystallographic analysis [2]. The data sets were collected at beamline **BL44XU**.

A model of the binary CuNIR:Cyt *c* complex, which consists of one Cyt *c* and one CuNIR molecule within an asymmetric unit, contains 8,242 protein atoms, one heme *c* group, six copper atoms, and 1,073 solvent molecules (Fig. 1). Only one Cyt *c* molecule is bound to one subunit (Sub-I) of trimeric CuNIR. The high-resolution crystal structure allows an accurate description of the complex interface between Sub-I and Cyt *c*. At the center of the interface, the Cyt *c* docking site near the T1Cu site of Sub-I and the heme *c* group are in close contact at a 3.5-Å distance between the Cε atom of Met87 in Sub-I and the edge CBC methyl carbon of the thioether-bonded substituent on heme *c*. At least 10 amino acid residues of CuNIR are associated with 11 amino acid residues and the heme *c* group of Cyt *c* at the interface. Interestingly, there is no salt bridge at the interface, and only three direct hydrogen bonds were observed. It was suggested that direct salt bridge and hydrogen bonds between the docking proteins are unfavorable for a transient ET complex because of energetically disadvantageous desolvation.

The building blocks of the interface between CuNIR and Cyt *c* are shown in Fig. 2. The interacting residues of CuNIR are localized both at the hydrophobic patch near the T1Cu site and at the "tower loop" region extending toward the T1Cu site in the CuNIR molecule. These primarily non-polar and neutral residues in both molecules indicate that hydrophobic and van der Waals interactions strongly contribute to complex formation. Contact between both hydrophobic patches brings the redox centers of heme *c* and T1Cu within 10.5 Å, which are close enough to allow for rapid

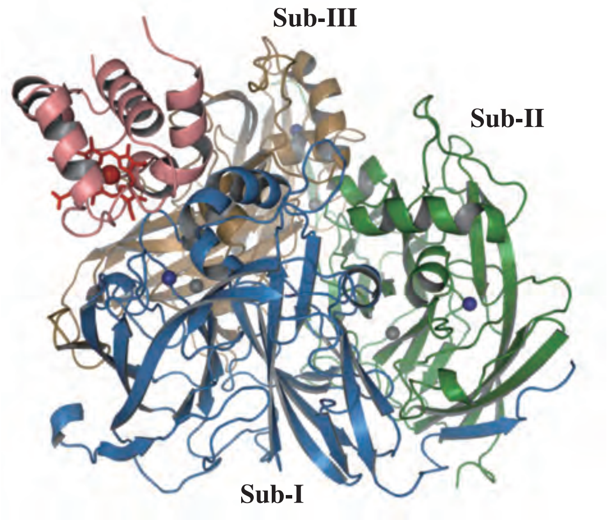

Fig. 1. Overall structure of the interprotein ET complex of CuNIR with Cyt *c*. The Cyt *c* molecule is represented as a pink-colored ribbon, and the Cyt *c*-docked subunit (Sub-I) of CuNIR is shown in sky blue, the undocked subunit (Sub-II) in green, and the other one (Sub-III) in sand color. The heme group (red), T1Cu (dark blue), and T2Cu (gray) are depicted as balls and sticks.

ET [3]. Furthermore, 25 water molecules are located at the docking interface. Eight waters bridging the two proteins through hydrogen bonds stabilize the partner proteins, and the remaining waters also provide stabilization through hydrogen bonds and van der Waals contacts to either Sub-I or Cyt *c* (Fig. 2). All of the water molecules form a characteristic semi-circle around the hydrophobic patch, and the non-polar core interface is sealed off from the aqueous environment.

PATHWAY [4,5] analysis of the CuNIR:Cyt *c* complex was performed to determine the most efficient predicted ET pathway from heme *c* to T1Cu. The predicted pathway through the entry/exit port inside the hydrophobic patches of the interfaces is exhibited in Fig. 3. An electron that leaves iron via the exposed CBC methyl group in the CuNIR:Cyt *c* complex is directly transferred to the Cδ atom of Pro88 of CuNIR by a through-space jump and then shifts from Pro88 to T1Cu through the His89 ligand. The ET pathway represents the most favorable route between the redox centers in the core of the hydrophobic interface.

Recognition and interaction between the protein surfaces, as observed in the transient donor-acceptor (Cyt *c*-CuNIR) complex structure occur through sufficient specificity of polar and non-polar interactions, providing a minimal site at the core of the protein–protein interface that ensures the geometry suited for ET reaction. It is particularly important for a deeper understanding of biological ET processes to explore how interface constructions for efficient ET reaction vary with protein–protein shape complementarity, surface charge and polarity, and dynamic fluctuations of the proteins and the organized water molecules at the interface.

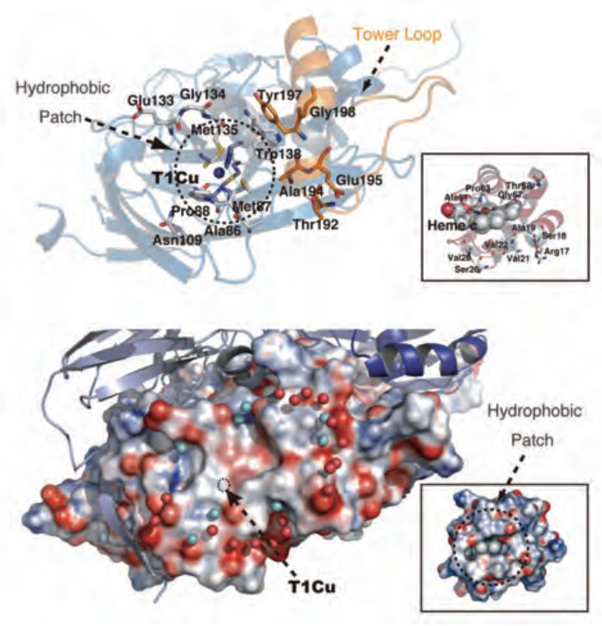

Fig. 2. Docking interface of the CuNIR:Cyt *c* complex. **(a)** The building block of the interface. The amino acid residues at the protein interface and the T1Cu ligands are represented as sticks. The T1Cu ligands are colored in blue, the residues involved in the hydrophobic patch in gray, and the residues of the "tower loop" in orange. Inset: the residues around the heme group in Cyt *c*. The heme group is shown as spheres. **(b)** Electrostatic potentials of contact protein surfaces. Twenty-five water molecules at the interface are represented as spheres. Eight water molecules bridging between the partner proteins through hydrogen bonds are colored in cyan and the other waters binding to Sub-I or Cyt *c* in red.

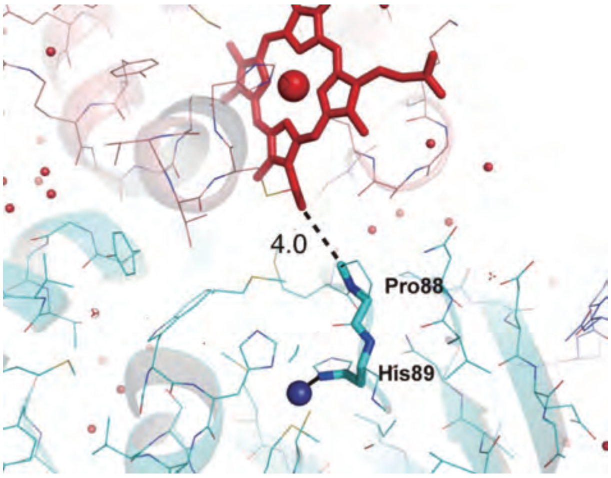

Fig. 3. Theoretically dominant ET pathway between heme *c* and T1Cu. Interprotein ET pathway in the CuNIR:Cyt *c* complex. The best pathway is shown as a broken-line (through-space process) and sticks (through-bond process). The distance of through-space jump between the CBC methyl group and the Cδ atom of Pro88 is given in angstrom. The heme group (red), the T1Cu atom (dark blue), and waters (red) are depicted as balls and sticks.

Masaki Nojiri

Department of Chemistry, Osaka University

E-mail: nojiri@ch.wani.oaka-u.ac.jp

References

[1] C.C. Page *et al.*: Curr. Opin. Chem. Biol. **7** (2003) 551.
[2] *M. Nojiri, H. Koteishi, T. Nakagami, K. Kobayashi, T. Inoue, K. Yamaguchi and S. Suzuki: Nature* ***462*** *(2009) 117.*
[3] R.A. Marcus *et al.*: Biochim. Biophys. Acta **811** (1985) 265.
[4] C.C. Page *et al.*: Nature **402** (1999) 47.
[5] J.N. Onuchic *et al.*: Annu. Rev. Biophys. Biomol. Struct. **21** (1992) 349.

Structures of dimeric and trimeric cytochrome *c* and its polymerization mechanism

Cytochrome *c* (cyt *c*) is a well-known globular heme protein. It receives electrons from the cytochrome bc_1 complex and provides them to cytochrome *c* oxidase in the respiratory chain in mitochondria. It also plays a key role in apoptosis, where it is released to the cytosol when permeabilization of the mitochondrial outer membrane occurs. Cyt *c* contains three long α-helices, and the heme of cyt *c* forms covalent bonds with two cysteine residues through their sulfur atoms and is coordinated in native form by His18 and Met80. Met80 dissociation from heme iron induces peroxidase activity and leads to cardiolipin oxidation, which in turn leads to the release of proapoptotic factors.

Protein polymerization has gained interest owing to its relationship with neurodegeneration. The crystal structure of a stable dimer of serpin, a family of proteins that forms large stable multimers leading to intracellular accretion and disease, revealed a domain-swapped structure of two long antiparallel β-strands inserting into the center of the neighboring monomer [1]. Domain swapping is a phenomenon where the secondary or tertiary structural unit of a protein molecule is replaced by the corresponding unit of another molecule of the same protein [2]. It has also been shown that β_2-microglobin can oligomerize and form amyloid fibils via runaway domain swapping [3]. It has been known for nearly half a century that cyt *c* forms polymers, but the polymerization mechanism remains unknown [4]. Recently, we have solved the X-ray crystal structures of dimeric and trimeric cyt *c* (Figs. 1(d) and 1(f), respectively) [5]. Diffraction experiments were carried out at **BL26B2** beamline. From the dimeric and trimeric structures and the physicochemical properties of the oligmers of cyt *c*, we found that it forms polymers by successive domain swapping (runaway domain swapping), where the C-terminal helix is displaced from its original position in the monomer and Met-heme coordination is perturbed significantly (Fig. 2) [5].

Ferric horse cyt *c* oligomers were prepared by the treatment of monomeric ferric horse cyt *c* with ethanol. Both dimeric and trimeric cyt *c* exhibit domain-swapped structures, where the C-terminal regions beyond Thr78 of the dimer and Lys79 of the trimer are relocated from their original position observed in the monomer owing to Met80 dissociation from the heme (Fig. 2). The relocated C-terminal region includes one α-helix, and the vacant area produced is occupied by the corresponding region of another cyt *c* molecule (Figs. 1(a), 1(d), and 1(f)). Polyethylene glycol (PEG) molecules, added for crystallization, were identified in the crystal structures. Diethylene glycol lies at the interface between two protomers in dimeric cyt *c*, whereas it interacts with the hinge loop (Thr79–Ala83) in trimeric cyt *c*. These interactions contribute to the stabilization of the dimer and trimer structures, resulting in closed-ended mutual swapping and cyclic structures, respectively. Tetraethylene glycol interacts with Lys55 and sits at the interface between the oligomers in the crystal structures of both dimeric and trimeric cyt *c*. This interaction reduces the positive

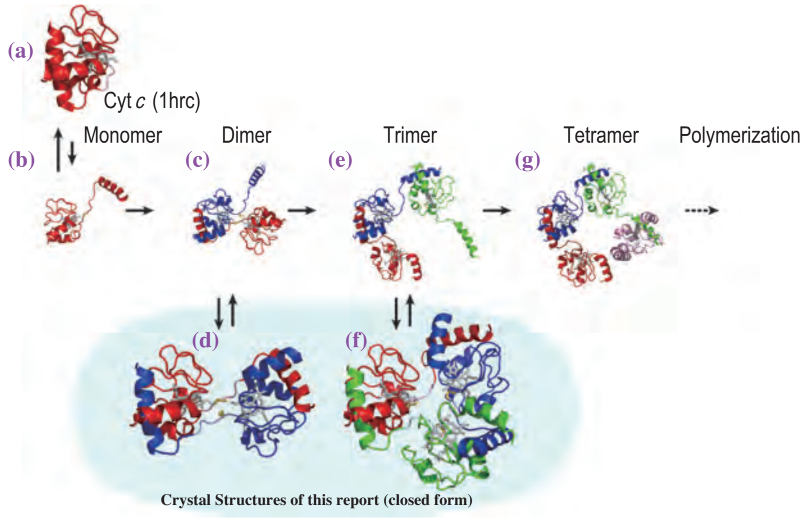

Fig. 1. Structures of monomeric and oligomeric cyt *c*. Crystal structures of monomeric (**a**, 1 hrc), dimeric (**d**) and trimeric (**f**) cyt *c* from horse heart. Model structures of monomeric (**b**), dimeric (**c**), trimeric (**e**), and tetrameric (**g**) cyt *c* in solution. The cyclic forms of dimeric and trimeric cyt *c* were produced owing to interaction with PEG and $(NH_4)_2HPO_4$ molecules, which were added as crystallization precipitants. Oligomeric cyt *c* is formed by the displacement of the C-terminal helix of one monomer from its original position and the vacant area produced is occupied by the corresponding helix of another molecule. Each protomer is shown in red, blue, and green.

charge of the protein surface and the repulsion between the oligomers in the crystals. However, the linker loop is not long enough to cause domain swapping without steric hindrance, consequently, perturbation in the protein structure around the heme is induced. The heme–heme distance is shorter in the dimer (18.4 Å) than in the trimer (19.8–20.0 Å). As a result, the Thr78 residual position moves toward the solvent in the dimer, whereas it remains the same as that in the monomer in the trimer. However, the solution structures of dimeric, trimeric, and tetrameric cyt *c* were linear on the basis of small-angle X-ray scattering measurement (Figs. 1(b), 1(c), 1(e) and 1(g)), where the trimeric linear structure shifted toward the cyclic structure with the addition of PEG and $(NH_4)_2HPO_4$ (Fig. 1(f)).

Met80 was dissociated from the heme in cyt *c* oligomers allowing the C-terminal α-helix to swap (Fig. 2). For dimeric, trimeric, and tetrameric cyt *c*, the ΔH of the oligomer dissociation to monomers was estimated to be about -20 kcal/mol per protomer unit, where Met-heme coordination appears to contribute largely to ΔH. This suggests that Met–heme coordination stabilizes the interaction of the C-terminal helical region with the N-terminal region, resulting in a native monomeric structure (Fig. 1(a)). In fact, residues 83-86 are reported to be among the highest disordered regions in the solution structure of horse ferric cyt *c* according to NMR investigation. The side chain of Met80 is exposed to the solvent and Phe82 occupies the Met80 position in the dimer (Figs. 2(a) and 2(b)), while the side chains of Met80 and Phe82 in the trimer move but remain in the vicinity of their corresponding positions in the monomer (Figs. 2(a) and 2(c)). The dissociation of Met80 from heme iron allows a water molecule or a hydroxide ion to bind in its place. According to the absorption spectra of the dimer and trimer and the previous reports on Met-depleted cyt *c*, a hydroxide ion appears to be coordinated to the heme in the crystal (pH 8.5). The peroxidase activity of cyt *c* is thought to play an important role in apoptosis, where it depends on the perturbation of the Met-heme coordination. In fact, the peroxidase activity of dimeric cyt *c* was higher than that of monomeric cyt *c*.

Although the dimer and trimer have different heme pocket environments their optical absorption spectra were similar, which can be due to coordination of the hydroxide ion in both oligomers. The absorption and CD spectra of high-order oligomers (~40mer) were similar to those of dimeric and trimeric cyt *c* but different from those of monomeric cyt *c*. The present results suggest that cyt *c* polymerization occurs by the successive domain swapping of the C-terminal helix. We believe that the present new structural and thermodynamic work on cyt *c* polymerization provides a new and important concept, which may lead to a common mechanism of protein polymerization.

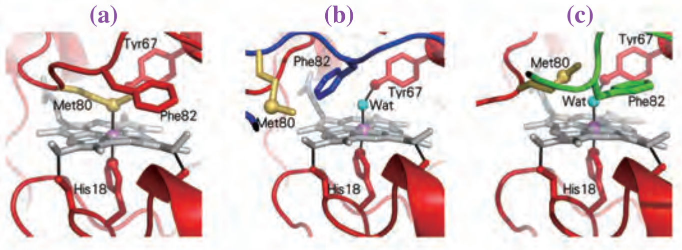

Fig. 2. Enlarged view around the heme pocket of monomeric, dimeric and trimeric cyt *c*. Heme is supported by two thioether bonds with two cysteine residues and Fe is coordinated by His18 and Met80 in the native monomeric form **(a)**. Met80 is shifted away from the heme and Phe82 occupies the Met80 position in the dimer **(b)**, whereas the side chains of Met80 and Phe82 in the trimer move but remain in the vicinity of their corresponding positions in the monomer **(c)**. In the dimer and trimer, additional species (probably a hydroxide ion) are coordinated to Fe at the Met80 ligand position in the monomer. The heme and side chain atoms of His18, Tyr67, Met80, and Phe82 are depicted as stick models. Fe of heme (pink), Nε2 of His18, Oη of Tyr67, Sδ of Mat80 and O of the water molecule (cyan) are shown as spheres. Each protomer is shown in red, blue and green except for the heme (gray) and the side chain of Met80 (yellow).

Shun Hirota[a,*] and Yoshiki Higuchi[b]

[a] Graduate School of Materials Science,
Nara Institute of Science and Technology
[b] Department of Life Science, University of Hyogo

*E-mail: hirota@ms.naist.jp

References

[1] M. Yamasaki *et al.*: Nature **455** (2008) 1255.
[2] M.P. Schlunegger *et al.*: Adv. Protein Chem. **50** (1997) 61.
[3] C. Liu *et al.*: Nat. Struct. Mol. Biol. **18** (2011) 49.
[4] E. Margoliash and J. Lustgarten: J. Biol. Chem. **237** (1962) 3397.
[5] *S. Hirota, Y. Hattori, S. Nagao, M. Taketa, H. Komori, H. Kamikubo, Z. Wang, I. Takahashi, S. Negi, Y. Sugiura, M. Kataoka and Y. Higuchi: Proc. Natl. Acad. Sci. USA* ***107*** *(2010) 12854.*

LIFE SCIENCE:

"Shyakunage"- *Rhododendron*

Remarkably diverse types of research are included in the Life Science II section for this year. Some are directly related to medical problems and others are on the basic analysis of biomedical specimens including methodologies.

The report most closely related to clinical medicine is that by Schwenke *et al*. who studied the mechanism of pulmonary arterial hypertension (a disease that increases the blood pressure of pulmonary artery) by angiography. They develop rat models of the disease by two methods: by prolonged exposure to a low oxygen concentration and by drug (monocrotaline) use. Both models had fewer branches of blood vessels than normal rats. By high-resolution synchrotron angiography, they found that the 100-200 μm blood vessels of the former model are more sensitive to a sympathetic stimulus than those of the latter model. The results suggest the presence of different types of pulmonary hypertension in humans.

The work on the mouse lung by Hooper *et al*. used a technique called particle image velocimetry (PIV) in combination with propagation-based phase-contrast imaging, which enhances the contrast of the lung much better than conventional projection imaging. PIV reveals a motion in each part of the lung during respiration. In this study, abnormal movements were observed in a mouse with bleomycin-induced pulmonary fibrosis, which induces the formation of excess fibrous tissues in the lung. Thus, PIV has potential as a novel method for disease detection.

The study by Ochala *et al*. is quite medically related but not based on imaging; it uses small-angle X-ray diffraction analysis. Human muscle samples were collected by biopsy from patients who suffer from genetic diseases of the skeletal muscle. These diseases are caused by the mutation of a protein (tropomyosin) that regulates muscle contraction. X-ray diffraction analysis can tell how the protein undergoes a conformational change during contraction. The results show that the mutated molecule does not change its conformation sufficiently to cause complete contraction. The approach used in this study shows that X-ray diffraction can be utilized for better understanding of the inherited muscle diseases at the molecular level.

MEDICAL BIOLOGY

Kanzaki *et al*. also used small-angle X-ray scattering to study the molecular change of a protein classified as a chaperonin that assists the folding of other proteins. Since proper folding of proteins is essential for the normal function of cells, the dysfunction of this class of proteins is related to a variety of diseases such as Alzheimer's and Parkinson's. The chaperonin studied here was from a thermophilic bacterium that has the highest activity at high temperatures. Three mutant proteins were prepared to study their activities at low temperatures. Although all the mutants retained intact folding capability at 60ºC, unlike the wild-type protein, two of the mutants kept the high conformational change ability even at 40ºC, which correlated with their higher folding ability. The difference seems to originate from the locations of the mutations in the protein, showing that these amino acids are crucial to the conformational stability of the protein.

The study by Matsuyama and Yamauchi is performed at the cellular level; they carried out high-resolution mapping of elements in NIH/3T3 cells using Kirkpatrick-Baez mirrors. The probe size can be as small as 29 nm × 48 nm, but is adjustable so that a larger area can be quickly scanned to find the most interesting regions. All elements between Na (Z=11) and Pb (Z=82) were studied and interesting results were obtained: elements like S and Cu are relatively evenly distributed in a cell, and P, Ca and Fe are much more concentrated in the nucleus. The non-uniform distribution of the elements suggests the different roles of these elements in a cell.

The imaging of soft biomedical samples such as brain, breast and abdominal organs is challenging, and synchrotron radiation has been used to overcome this difficulty. Yashiro and Momose developed a new imaging technique for low-contrast objects suitable for biological imaging. The technique uses a combination of two optical devices, a zone plate and a grating which is a unique idea. Although this technique is still in the early stage of development, it has a potential to be employed as a clinical imaging modality.

Both clinical and basic studies are required for future advancement in medicine. Although the methods used in these reports are not directly applicable to the diagnosis of human diseases, they will contribute to a better understanding of these diseases that are indispensable to conquer them.

Naoto Yagi

Pulmonary blood flow distribution is impaired in two distinctly different forms of pulmonary hypertension

Pulmonary arterial hypertension (PAH) is a common adverse complication associated with several cardiopulmonary pathologies, and has a bleak long-term prognosis. The underlying mechanisms governing the pathogenesis of PAH remain poorly understood, which is partly due to the varying etiologies for PAH, such as that caused by monocrotaline (MCT) and chronic hypoxia (CH) [2,5]. Indeed, the literature seems to suggest that both the cellular signal pathways that are involved in the pathogenesis of these forms of PAH, and the resultant morphological changes in the pulmonary vasculature, may differ between CH and MCT [1,2,5]. Whether these cellular and morphological differences between MCT and CH ultimately culminate in differing patterns of pulmonary blood flow distribution is not currently known. Yet, it is these changes in blood flow distribution, regardless of etiology, which are responsible for the adverse increase in pulmonary arterial pressure (PAP). In this study, we aimed to assess the changes in pulmonary blood flow distribution following MCT-induced PAH, and compare it with CH-induced PAH. We utilized SR microangiography, which has enhanced sensitivity to contrast material and superior visualization of pulmonary vessels compared to more conventional angiography methods. The results from this study will help to ascertain whether the nature of change in pulmonary blood flow distribution in two distinctly different models of PAH is etiology-dependant.

All experiments were performed at beamline **BL28B2**. We used control rats and rats with PAH, which was induced by either (i) injecting monocrotaline (60 mg/kg, sc.) three weeks prior to experimentation or, (ii) exposing rats to chronic hypoxia (10% O_2) for 4 weeks [3]. On the day of experimentation, rats were anesthetized and surgically prepared for pulmonary microangiography as previously described [4]. Angiogram images of the pulmonary microcirculation were recorded during air-breathing (baseline) and following the 4 min of acute hypoxia (8% O_2); before and after sympathetic beta-adrenoreceptor blockade (propranolol, 2 mg/kg i.v.).

Using SR, we could clearly visualize pulmonary vessels, ranging from the main axial artery (~1200 μm) to the 4th generation of branching (> 80 μm), in the left lung of control rats as well as rats with PAH, induced with either MCT or CH (Fig. 1). Importantly we observed that rats with PAH, regardless of etiology, had significantly fewer perfused vessel branches of the 4th generation compared to normal-rats (Fig. 2). This reduction in parallel blood flow in the hypertensive lung is the leading causal factor for the increase in pulmonary vascular resistance and, consequently, pulmonary arterial pressure.

Interestingly, the magnitude of acute hypoxic pulmonary vasoconstriction (HPV) was not modified by either form of PAH. Beta-adrenoreceptor blockade (propranolol) accentuated the magnitude of HPV in

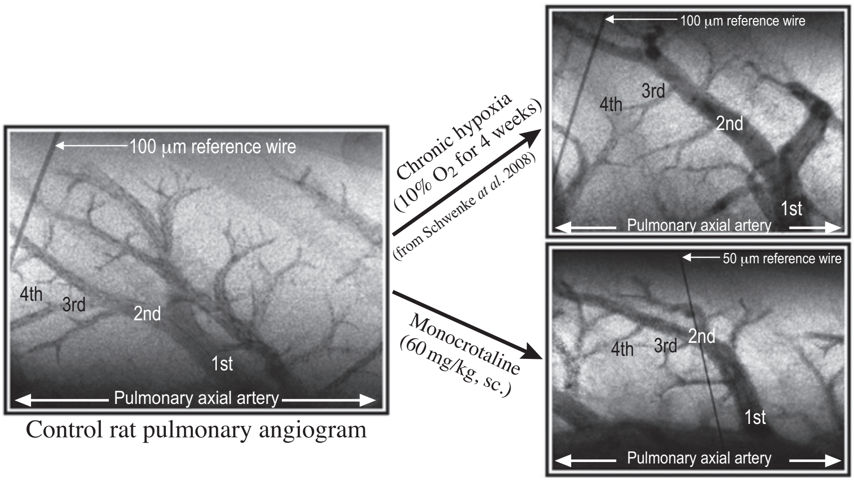

Control rat pulmonary angiogram

Hypertensive rat pulmonary angiogram

Fig. 1. Typical microangiogram images showing the first 4 branching generations of small pulmonary arteries in control rats (n = 7) and rats with PAH, induced with either chronic hypoxia (n = 5; TOP) or monocrotaline (n = 7; BOTTOM).

both control-rats and PAH-rats, particularly in the 300-500 μm sized vessels. However, in only those PAH-rats that were exposed to CH, did beta-blockade also accentuate the HPV in 100-200 μm vessels (Fig. 3).

In summary, we have utilized the resource of SR microangiography to show that the adverse changes in pulmonary blood flow distribution in the hypertensive lung are comparable between MCT and CH models. We also demonstrated that the acute HPV was not altered in both forms of PAH, although sympathetic modulation of pulmonary vasoreactivity becomes critically important in the CH-model, but not the MCT-model. Both models of PAH represent specific types of PAH typically observed in humans and, therefore, such differences between the two PAH models should be considered in future studies, especially those studies investigating potential therapeutic interventions for a specific form of PAH.

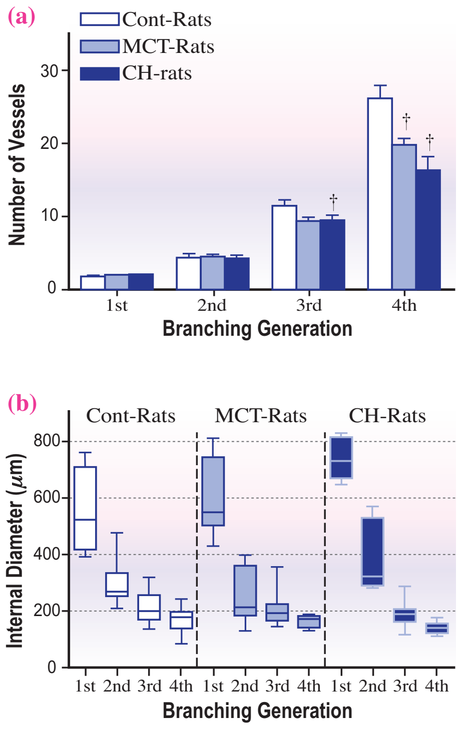

Fig. 2. **(a)** The distribution of blood flow through the pulmonary circulation was impaired in PAH, evident by a decrease in the number of perfused vessel, particularly those of the 3rd and 4th generation, in PAH rats compared to control rats († $P < 0.05$). There was no significant difference between MCT-rats (n = 7) and CH-rats (n = 5). **(b)** The range in vessel size for each branching generation did not change following the development of PAH.

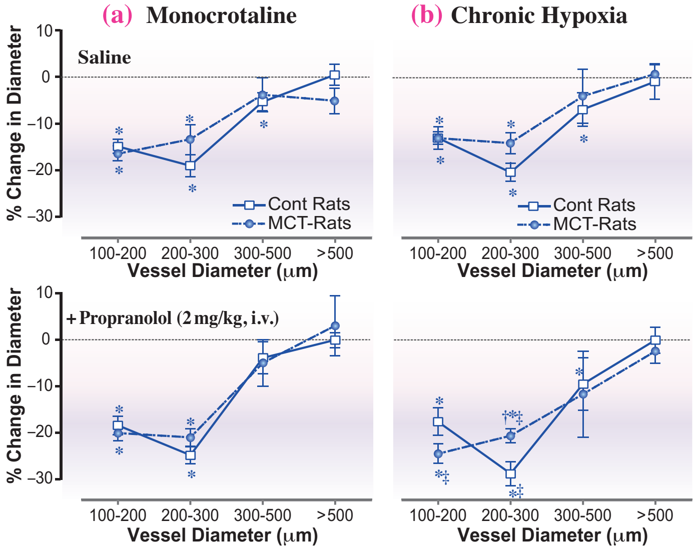

Fig. 3. The magnitude of vasoconstriction (% decrease in vessel diameter) during acute hypoxia in control-rats and rats with PAH induced either by (i) CH for 4 weeks, or (ii) a single injection of monocrotaline. Sympathetic β-adrenergic blockade was achieved using propranolol (2 mg/kg, i.v.). * Significant response to acute hypoxia ($P < 0.05$). † Significant difference between control-rats and CH-rats ($P < 0.05$). ‡ Significant effect by propranolol administration ($P < 0.05$).

Daryl O. Schwenke [a,*], Keiji Umetani [b] and
Mikiyasu Shirai [c]

[a] Department of Physiology, University of Otago,
New Zealand
[b] SPring-8 / JASRI
[c] Department of Cardiac Physiology, National Cerebral
and Cardiovascular Research Institute, Japan

*E-mail: daryl.schwenke@stonebow.otago.ac.nz

References

[1] J.T. Crossno Jr. *et al*.: Am. J. Physiol. Lung Cell Mol. Physiol. **292** (2007) L885.
[2] W. Raoul *et al*.: Respiration Research **8** (2007) 8.
[3] *D.O. Schwenke, J.T. Pearson, K. Kangawa, K. Umetani and M. Shirai: J. Appl. Physiol.* ***104*** *(2008) 88.*
[4] D.O. Schwenke *et al*.: J. Appl. Physiology **102** (2007) 787.
[5] R.J. van Suylen *et al*.: Am. J. Respir. Crit. Care Med. **157** (1998) 1423.

Imaging lung motion to detect lung disease

Lung diseases restrict the airflow into or out of the lungs during breathing due to increases in airway resistance or to changes in the mechanical properties of lung tissue. For example, pulmonary fibrosis increases the stiffness of tissue surrounding the distal airways, asthma increases airway resistance and emphysema reduces lung tissue recoil thereby increasing its compliance. Although these diseases vary markedly in both cause and consequence, by altering the movement of air into and out of the diseased regions they must also alter lung motion within those regions [1,2].

Little is known about the dynamics of lung motion during breathing, particularly how different regions move in relation to other regions during both inspiration and expiration. For instance, it is unknown whether the lung expands and deflates uniformly, whether specific regions lead or trail other regions due to differences in local compliances or due to their proximity to the diaphragm or chest wall. Similarly, it is unknown how these diseases affect regional lung motion and whether motion in healthy regions is altered to compensate for diseased regions. Although regional information is best provided by imaging the lung *in vivo*, until recently it has not been possible to image the lung with sufficiently high spatial and temporal resolution.

Previous techniques used to measure lung motion have relied on the inhalation of contrast agents or other techniques that utilize invasive procedures [3]. More recently, MRI and X-ray CT techniques have been developed to assist in radiotherapy treatment planning or the development of lung biomechanical models. However, these approaches are limited, particularly by the need to image the lung while it is stationary to minimize blurring. Thus, interpolation is required to deduce lung motion between two steady state positions within a breath and assumes that lung motion between these positions follows a linear or defined path.

Although standard X-ray imaging has the capacity to identify diseased regions of the lung, substantial changes in lung tissue characteristics are required to provide sufficient contrast (e.g. changes in X-ray absorption) between diseased and healthy regions. Thus, for diseases like asthma, which affect airway caliber and resistance, standard imaging techniques offer little benefit in identifying diseased airways. To improve the detection, assessment and management of most lung diseases, there is a need to develop techniques that provide accurate measures of regional lung function.

In this study, we demonstrated that the combination of Particle Image Velocimetry (PIV) and Phase Contrast X-ray Imaging (PCXI) can produce quantitative measures of regional lung motion which can be used to differentiate between normal and abnormal lung tissue. PIV utilizes a cross-correlation analysis to track the movement of lung tissue between consecutive frames allowing the reconstruction of velocity fields that define speed and direction of regional lung motion throughout a breath (Fig. 1). Reconstruction of the velocity fields throughout a breath demonstrates that motion is very heterogeneous across the lung and that the speed and direction of motion within a region is highly position dependent. To control for the regional differences in motion across the lung, regional maps of expansion (Fig. 2) and average time of expansion can be generated, revealing regions with abnormal movement caused by disease. Experimental induction of non-uniform lung disease, specifically pulmonary fibrosis in mice, caused abnormal motion in both diseased and healthy regions within the same lung. In particular, we discovered that

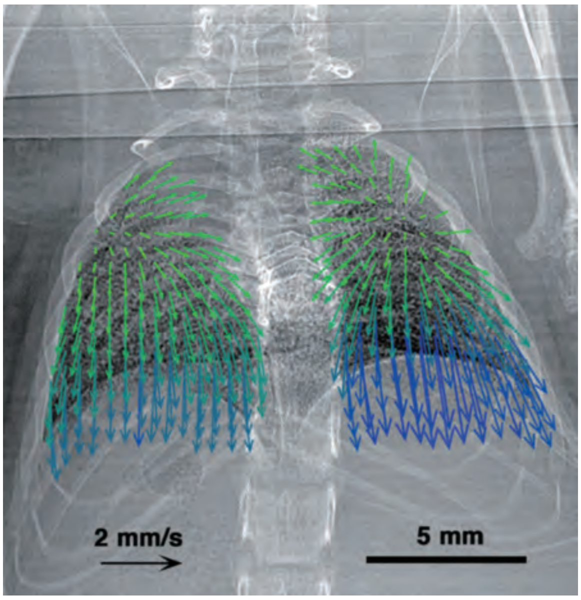

Fig. 1. *In vivo* detection of lung tissue motion. Instantaneous velocity of a healthy mouse lung, ~14 ms after start of inspiration, shown as a vector field. Vectors are reduced in number (293 of 2640 displayed) for clarity. Vectors are colored according to magnitude (from lowest; green, to highest; blue) of velocity.

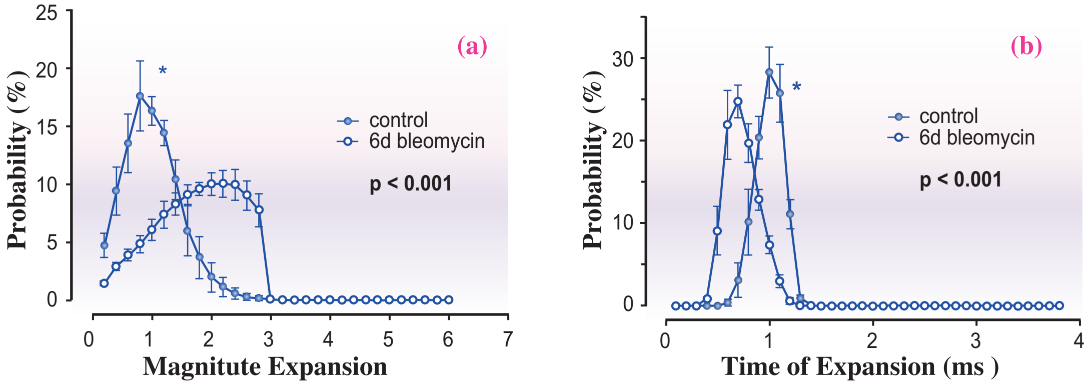

Fig. 2. Velocimetry measures of lung pathology after bleomycin exposure. **(a)** Frequency distribution of the magnitude of expansion (normalized to the average of controls) is compared for treated groups (n=4) with controls (n=3). Data are normalized by the average of the controls. Treated mice have 76% greater expansion on average and 47% of treated lungs expand at over 2× the control average compared with less than 4% for control lungs. Frequency distributions of the average time of expansion **(b)** in control and treated mice. Asterisks indicate significant differences between control and treated animals ($p<0.001$).

motion in healthy regions increased to compensate for slower moving diseased regions (Fig 3). We conclude that X-ray velocimetry can quantify regional lung motion and detect lung disease by identifying regions with abnormal movement. Furthermore, this technology is more sensitive and quantitative for disease detection than other conventional measures such as global lung function and histological changes.

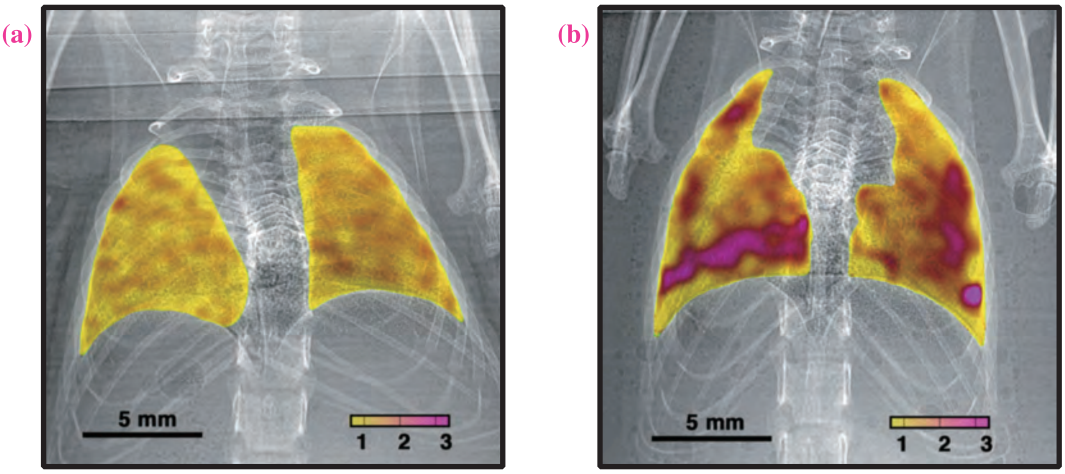

Fig. 3. Regional expansion within the lung. Color maps of regional lung expansion determined using PIV for typical: **(a)** control and; **(b)** bleomycin-treated mice. Data are normalized by the average regional expansion across the control group and color maps were generated using the same color-scale (see legend). The mice treated with bleomycin **(b)** have dramatic regional alterations in the pattern of lung expansion.

Stuart B. Hooper [a,*], Andreas Fouras [b] and
Robert A. Lewis [c]

[a] The Ritchie Centre, Monash Institute for
Medical Research, Monash University, Australia
[b] Division of Biological Engineering,
Monash University, Australia
[c] Monash Centre for Synchrotron Science,
MonashUniversity, Australia

*E-mail: stuart.hooper@monash.edu

References

[1] R. Blundell *et al.*: J. Pathol. **202** (2004) 141.
[2] J.C. Hogg: Lancet **364** (2004) 709.
[3] S.P. Albert *et al.*: J. Appl. Physiol. **106** (2009) 757.

Revealing the molecular mechanisms of muscle weakness in an inherited myopathy

Inherited myopathies are a newly discovered class of muscle diseases normally present at birth. They are diverse but often characterized by weakness in facial, masticatory, limb and respiratory muscles [1]. This class of diseases is due to mutations in different genes encoding proteins involved in muscle contraction [1]. Among the related genes, there are *TPM2* and *TPM3*. They encode tropomyosin which is a 284-residue coiled-coil protein composed of two α-helical chains, forming a rod-shaped coiled-coil dimer. This protein binds head-to-tail along the length of actin filaments and plays a key role in force generation [2]. In fact, when Ca^{2+} binds to the troponin complex, tropomyosin moves toward the inner domain of actin filaments, exposing sites on actin that allow weak binding of myosin cross-bridges (displacement from the B-state to C-state, both being considered as off-states). Weak-to-strong transition induces a further tropomyosin movement (to the M-state, known as on-state), exposing more sites on actin filaments, permitting additional binding of myosin cross-bridges and, ultimately, leading to force generation (Fig. 1) [2].

Recently, a novel mutation in *TPM2* has been discovered and has been associated with an inherited myopathy, limb muscle weakness and distal arthrogryposis (joint contractures) [3]. This gene mutation changes just one DNA nucleotide and results in the substitution of just one amino acid in tropomyosin (Arg133Trp). This raises the question of the molecular mechanisms by which such minor change induces limb muscle weakness. To answer this question, limb muscle biopsies from individuals carrying the Arg133Trp mutation and from healthy controls were taken (using protocols approved a local ethics committee). Single muscle fibers were subsequently isolated, mounted in a special chamber and low-angle X-rays were applied at beamline **BL45XU**. Tropomyosin (far off-meridional part of the second actin layer line at 1/19 nm^{-1}) and actin (sixth and seventh actin layer line at 1/5.9 and 1/5.1 nm^{-1}, respectively) intensity changes were monitored during contraction (Fig. 2) under two conditions: first, when no overlap between actin and myosin filaments

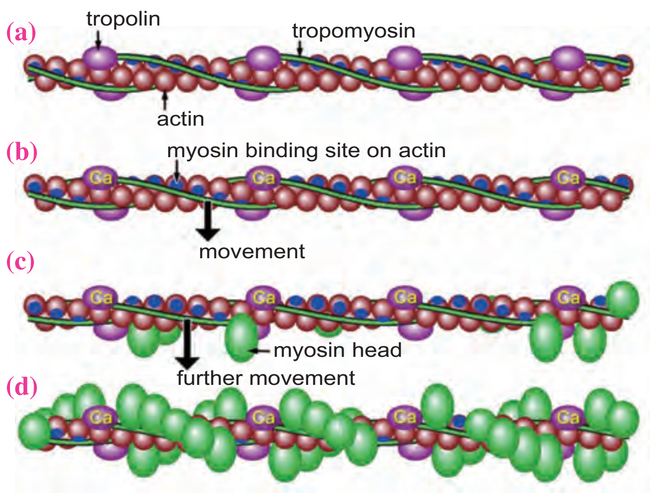

Fig. 1. Tropomyosin B-state: because tropomyosin completely covers the binding sites on actin, myosin cross-bridges cannot be formed **(a)**. Tropomyosin C-state: when Ca^{2+} binds to troponin, this allows the movement of tropomyosin **(b)**; binding sites on actin are then exposed and permit the formation of weak myosin cross-bridges **(c)**. Tropomyosin M-state: weak-to-strong myosin cross-bridge transition induces a further tropomyosin movement, exposing more binding sites on actin, permitting additional binding of myosin cross-bridges and force production **(d)**.

exists; second, when actin and myosin filaments fully overlap [4].

During contraction, when no overlap exists between actin and myosin filaments, the intensity change of the second actin layer line (1/19 nm^{-1}) was weaker in muscle fibers from individuals carrying the Arg133Trp mutation when compared with controls. This directly proves that the mutation partially hinders tropomyosin movement from the B-state to C-state over the surface of actin. In addition, when actin and myosin filaments fully overlap, intensity changes of the second, sixth (1/5.9 nm^{-1}) and seventh (1/5.1 nm^{-1}) actin layer lines were even more attenuated in cells from persons expressing the Arg133Trp mutation when compared with controls. This demonstrates that the tropomyosin displacement between the C-state and M-state is also disturbed and this phenomenon inhibits activation-induced actin conformational changes. One obvious reason for such dysfunction is that the Arg133Trp mutation, located in a highly conserved tropomyosin region, modifies the structure of the protein and the affinity for other surrounding molecules, provoking a local unusual stability and flexibility and altering the normal equilibrium positions (B-, C- and M-states). Hence, fewer myosin binding sites can be exposed on actin filaments and fewer myosin cross-bridges can exist, ultimately leading to a large deficit in force generation and muscle weakness [4].

There is an increasing awareness in the scientific community concerning the importance and need of a detailed understanding of muscle weakness in inherited myopathies. However, to date, basic and clinical research has primarily focused on characterizing the causative genes, ignoring the molecular mechanisms underlying frailty. The above use of low-angle X-rays appears as a powerful methodological tool and, therefore, opens up a new field of investigation in order to design future therapeutic interventions in inherited myopathies.

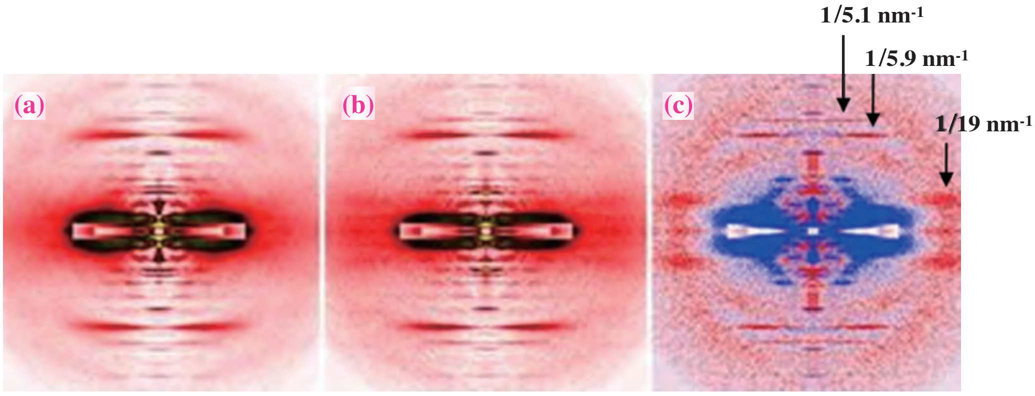

Fig. 2. X-ray diffraction patterns of human control fibers where actin and myosin filaments fully overlap. These patterns were recorded at the BL45XU beamline during relaxation **(a)** and contraction **(b)**. Differences in intensity profiles between relaxation and contraction also appear **(c)**. Tropomyosin (far off-meridional part of the second actin layer line at 1/19 nm^{-1}) and actin (sixth and seventh actin layer line at 1/5.9 and 1/5.1 nm^{-1}, respectively) are shown with arrows.

Julien Ochala[a,*], Hiroyuki Iwamoto[b] and Naoto Yagi[b]

[a] Department of Neuroscience, Uppsala University, Sweden
[b] SPring-8 / JASRI

*E-mail: julien.ochala@neuro.uu.se

References

[1] C.A. Sewry *et al*.: Curr. Opin. Neurol. **21** (2008) 569.
[2] W. Lehman *et al*.: Adv. Exp. Med. Biol. **644** (2008) 95.
[3] H. Tajsharghi *et al*.: Neurology **68** (2007) 772.
[4] *J. Ochala, H. Iwamoto, L. Larsson and N. Yagi: Proc. Natl. Acad. Sci. USA* ***107*** *(2010) 9807.*

Adaptation of a hyperthermophilic group II chaperonins to relatively moderate temperatures

Chaperonins constitute one of the principal molecular chaperone families. They are ubiquitous and take indispensable roles in protein folding in cells. They form large cylindrical complexes composed of two stacked rings of 7-9 subunits of about 60 kDa. Each ring has a large central cavity for the productive folding of a non-native protein in an ATP-dependent manner. On the basis of their protein sequence and structural features, chaperonins are divided into two groups: I and II [1]. Group I chaperonins including GroEL of *Escherichia coli* are found in bacteria and endosymbiotic organelles. On the other hand, group II chaperonins are found in archaea and the eukaryotic cytosol. The most important difference between them is the requirement of a co-chaperonin, GroES. GroES acts as a detachable lid for group I chaperonins by forming a heptameric ring-shaped structure. In contrast, group II chaperonins have a built-in lid called the helical protrusion, which is composed of an extension of the apical domain (Fig. 1) [2]. The helical protrusion plays the equivalent role of GroES, sealing off the central cavity of the chaperonin complex. We have been studying the reaction mechanism of group II chaperonins using that from a hyperthermophilic archaeon, *Thermococcus* sp. strain KS-1 (*T.* KS-1) [3]. Although *T.* KS-1 chaperonin provided advantages for our study in terms of its high stability and activity, its high thermophilicity caused difficulty in using various analytical methods. To resolve this problem, we tried to adapt *T.* KS-1 chaperonin to moderate temperatures by mutations [4]. A comparison of the amino acid sequences between 26 thermophilic and 17 mesophilic chaperonins showed that three amino acid replacements (187th, 323rd, and 523rd residues of the *T.* KS-1 α subunit) are likely to be responsible for the difference between their optimal temperatures. Among thermophilic chaperonins, E187, K323, and A523 were strongly conserved. On the other hand, among mesophilic chaperonins, the residues are substituted for D, R, and K. The locations of these amino acid residues are displayed in the closed conformation of *T.* KS-1 chaperonin (Fig. 1). E187 is located in the β-sheet of the intermediate domain and K323 in an α-helix in the bottom of the apical domain. These amino acids are located in the hinge region between the intermediate and apical domains. In contrast, A523 is located at a β-sheet of the resolvable C-terminal region in the crystal structure, which constitutes the bottom of the cavity. We introduced amino acid replacements in three amino acid residues of *T.* KS-1 chaperonin and examined whether they adapted to cold temperature.

To examine the folding activities of the mutants, protein folding assay was carried out at 60°C, 50°C, and 40°C using citrate synthase from *Thermoplasma acidophilum* (TCS) (Fig. 2). The refolding activity of all the single mutants at 60°C was lower than that of the wild type. On the other hand, only K323R exhibited improved folding activity at lower temperatures such as 50°C and 40°C. E187D did not exhibit significant improvement in folding activity at 50°C. The activities of A523K at 50°C and 40°C were lower than those of the wild type.

Group II chaperonins take the open conformation in the absence of ATP, and they change to the closed conformation after ATP binding and hydrolysis. The

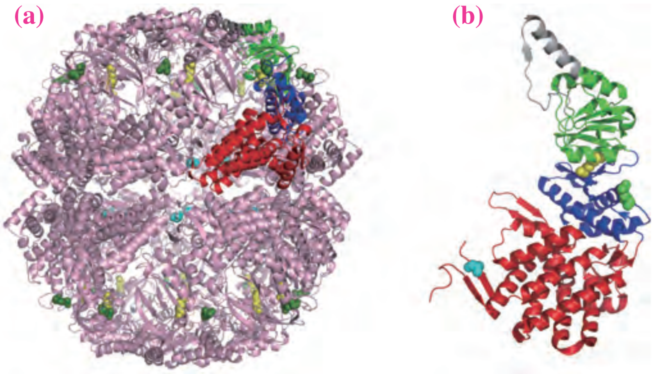

Fig. 1. Location of amino acids mutated for cold adaptation. Crystal structures of *T.* KS-1 α chaperonin oligomer **(a)** and α subunit **(b)** in the closed conformation. The equatorial, intermediate, and apical domains are shown in red, blue, and green, respectively. The helical protrusion, which is located at the tip of the apical domain, is shown in silver. The mutated residues for cold adaptation, i.e., E187, K323, and A523, are shown as Corey-Pauling-Koltun (CPK) style in green, yellow, and cyan, respectively. In **(a)**, only one subunit is shown in the above colors, and the mutated residues within a chaperonin oligomer are shown as CPK style in colors corresponding to E187, K323, and A523.

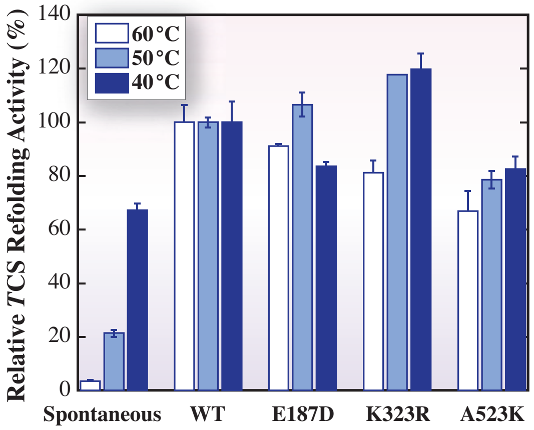

Fig. 2. *Thermoplasma* citrate synthase refolding activities of mutant chaperonins. Refolding activities for *Thermoplasma* citrate synthase (*TSC*) of chaperonin variants were determined at 60°C, 50°C, and 40°C. The activities of *TCS* refolded by wild-type chaperonin (WT) at 60°C, 50°C, and 40°C were taken as 100% (0.30, 0.27, 0.22 mU, respectively). Error bars indicate standard deviation (n = 5).

ATP-dependent conformational change ability of mutant chaperonins was examined by small angle X-ray scattering (SAXS) experiments at 60°C and 40°C (Table 1). All mutants exhibited ATP-dependent differences in the scattering curves at both temperatures. At 40°C, the ATP-dependent differences in the scattering curves of K323R were clearly larger than those of the wild type and other mutant chaperonins. SAXS gives the size of the molecule using two structural parameters, the radius of gyration (R_g) and the maximum particle distance (D_{max}). R_g indicates the mean particle size, and D_{max} is the maximum particle distance or the maximal intramolecular distance. At 60°C, ATP-dependent changes in D_{max} and R_g (ΔR_g) were observed in all chaperonins. There was no significant difference in ΔR_g among the chaperonins. The ATP-dependent ΔR_g parameters for the wild type, E187D, K323R, and A523K were -7.4 Å, -6.7 Å, -6.5 Å, and -7.4 Å, respectively. At 40°C, the ATP-dependent ΔR_g parameters for the wild type, E187D, K323R, and A523K were -3.8 Å, -5.3 Å, -6.6 Å, and -4.5 Å, respectively. These results showed that the ATP-dependent conformational change abilities of the wild type and A523K reduced at 40°C, correlating with their weak folding activities at that temperature. In contrast, K323R possessed the same ATP-dependent conformational change ability at 40°C and 60°C. The difference between the ΔR_g values of E187D at 60°C and 40°C seemed to be small. The mutation sites of E187D and K323R are located in the hinge region between the intermediate and apical domains. Considering that the conformational change is induced from the equatorial domain to the apical domain, SAXS experiments suggested that the amino acid substitutions in the hinge region, such as K323R, are important for the conformational change at relatively moderate temperatures. Since K323 may secure helix 12 in the closed conformation by interacting with D198, the replacement of Lys with Arg is likely to induce a higher mobility of the built-in lid, resulting in higher activities at relatively low temperatures.

Although the cold adaptation of the mutants was not sufficient for practical application, the results gave important information on the protein folding mechanism of group II chaperonins.

The experiments were performed at beamline **BL40B2**.

Table 1: Structural parameters of wild-type and single mutant chaperonins determined by small angle X-ray scattering experiments at 60ºC and 40ºC

Chaperonin	Nucleotide	60 ºC			40 ºC		
		R_g (Å)	ΔR_g (Å)	D_{max} (Å)	R_g (Å)	ΔR_g (Å)	D_{max} (Å)
Wild type	Free	75.4	—	191	76.6	—	198
	+ATP	68.1	−7.3	170	72.8	−3.8	192
	+ADP	76.0	0.6	196	75.2	−1.4	195
E187D	Free	74.6	—	195	74.5	—	194
	+ATP	67.9	−6.7	169	69.2	−5.3	182
	+ADP	73.9	−0.7	195	73.6	−0.9	196
K323R	Free	74.3	—	191	74.4	—	195
	+ATP	67.8	−6.5	170	67.8	−6.6	169
	+ADP	73.5	−0.8	189	74.7	0.3	195
A523K	Free	75.7	—	194	75.7	—	197
	+ATP	68.3	−7.4	171	71.2	−4.5	180
	+ADP	74.9	−0.8	193	75.4	−0.3	188

Error values of delta-radius of gyration (ΔR_g) and maximum particle distance (D_{max}) were estimated to be about ±1.0 Å, and ±5%, respectively.

Taro Kanzaki[a], Toshihiko Oka[b,*], and Masafumi Yohda[a]

[a] Department of Biotechnology and Life Science,
Tokyo University of Agriculture and Technology
[b] Department of Physics, Faculty of Science,
Shizuoka University

*E-mail: stoka@ipc.shizuoka.ac.jp

References

[1] F. U. Hartl and M. Hayer-Hartl: Nat. Struct. Mol. Biol. **16** (2009) 574.
[2] Y. Shomura *et al.*: J. Mol. Biol. **335** (2004) 1265.
[3] T. Kanzaki *et al.*: J. Biol. Chem. **283** (2008) 34773.
[4] *T. Kanzaki, S. Ushioku, A. Nakagawa, T. Oka, K. Takahashi, T. Nakamura, K. Kuwajima, A. Yamagishi and M. Yohda: Protein Eng. Des. Sel.* ***23*** *(2010) 393.*

Trace element mapping of a single cell using a hard X-ray nanobeam focused by a Kirkpatrick-Baez mirror system

The elucidation of cellular functions is rapidly progressing owing to techniques that identify and handle genes and proteins. New observation techniques will lead to breakthroughs, as the use of novel microscopes historically paves the way for new discoveries. Here, we describe a new microscope that enables the observation of intracellular elemental distributions with high resolution and high sensitivity [1].

We have developed a scanning X-ray fluorescence microscope (SXFM), which consists of both X-ray fluorescence analysis and X-ray focusing [2]. SXFM is one of the most suitable tools for visualizing elemental distributions in biological samples owing to its capability to obtain multi-element distributions with submicron resolution and sub-femtogram sensitivity and the ready acquisition of images without complex sample preparations such as sectioning and coating. We demonstrated our SXFM performance for biological applications by obtaining intracellular elemental distributions at the single-cell level.

Figure 1 shows the layout of our microscope. Kirkpatrick-Baez (KB) mirrors [3] consisting of two elliptical mirrors aligned at right angles to each other are placed approximately 100 m downstream of the undulator. The working distance is fixed at 100 mm in order to set up various components near samples in the near future. The depth of focus is 50-200 μm depending on the selected beam size, making it unnecessary to consider the thickness of thin samples such as cells. A noticeable feature of our focusing system is that the beam size is controllable within a wide range, from 29×48 nm (diffraction limit) to ~2000×~2000 nm (at 15 keV), which is achieved by adjusting a slit (TC1 slit) installed just downstream of the DCM; that is, we can select the optimum beam size for the scan area (Fig. 2). An energy dispersive detector (SDD) is employed to detect X-ray fluorescence. A linear-encoder-based feedback X-Y stage with a positioning resolution of 1 nm is used to obtain a high-resolution raster scan of the sample. The sample and scanner are inclined 60° to the incident X-ray beam to enable the SDD to be set up near the sample. Details of the performance such as the optimum spatial resolution and beam stability have been described in our previous study [2].

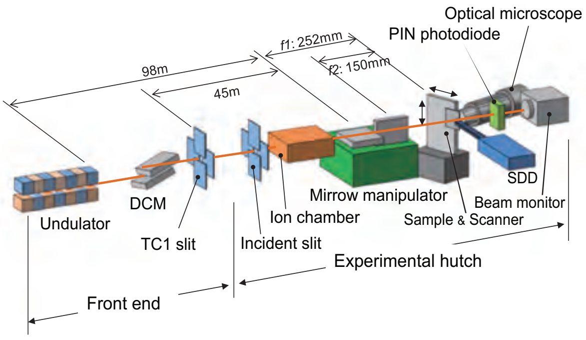

Fig. 1. Layout of the SXFM system.

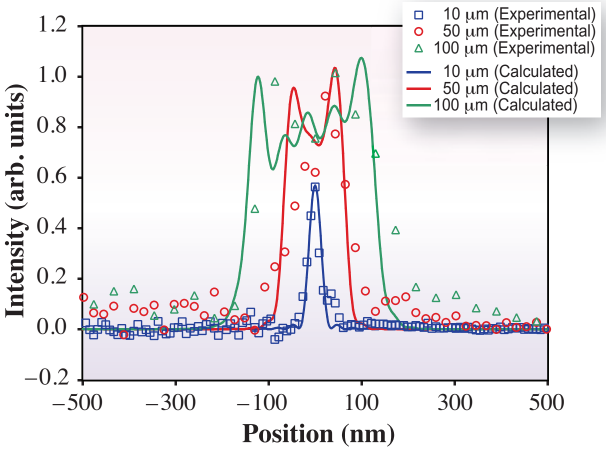

Fig. 2. Profiles of typical X-ray beams used in the study (direction: horizontal focusing, X-ray energy: 15 keV). The lines indicate the profiles measured by a wire scanning method and calculated ones. The values shown in the graph indicate the sizes of the virtual X-ray source formed by the TC1 slit. The narrowest beam has a full width at half maximum of 30 nm with a slit size of 10 μm.

X-ray fluorescence spectrum data detected by the SDD are sent to two multichannel analyzers (MCAs) for pulse height analysis and then downloaded to a personal computer. All X-ray fluorescence spectra detected for every pixel are recorded and processed using software to integrate the counts in each region of interest (ROI), as well as to visualize elemental distributions according to the ROI. Recording a large number of raw spectra for every pixel enables background correction, noise reduction, and peak separation to be performed after the observations are completed.

NIH/3T3 cells, which were plated on a polymer film of 4 μm thickness, were observed at the second experimental hutch (EH2) at beamline **BL29XUL**. An X-ray energy of 15 keV was selected for detecting of elements from Na (Z=11) to Pb (Z=82). In this experiment, the temperature of the whole SXFM system was maintained within ±0.1°C to ensure the stability of beam position and size. Elemental distribution maps obtained by SXFM at the single-cell level are shown in Fig. 3. The Au distribution image and the fluorescence image obtained using visible light correspond to the mitochondrial distribution, as a result of the use of antibodies with fluorescence dye and colloidal gold. Compared with other elements, Zn and Cu are particularly colocalized with the Au distribution, except at the nucleus, while P, Ca, and Fe are highly concentrated at the nucleus. Zn and Cu seem to be mainly included in the mitochondria and nucleus.

To acquire higher-resolution images of the mitochondria, the beam was sharpened by closing the TC1 slit. Figure 4 shows high-resolution elemental distribution maps. As can be seen from the distribution maps, the signal intensities of Zn were partially colocalized with those of Au (indicated by arrow). The signal intensities of Ca, P, and Zn, which appear granular, likely correspond to other organelles that could not be identified in the experiments.

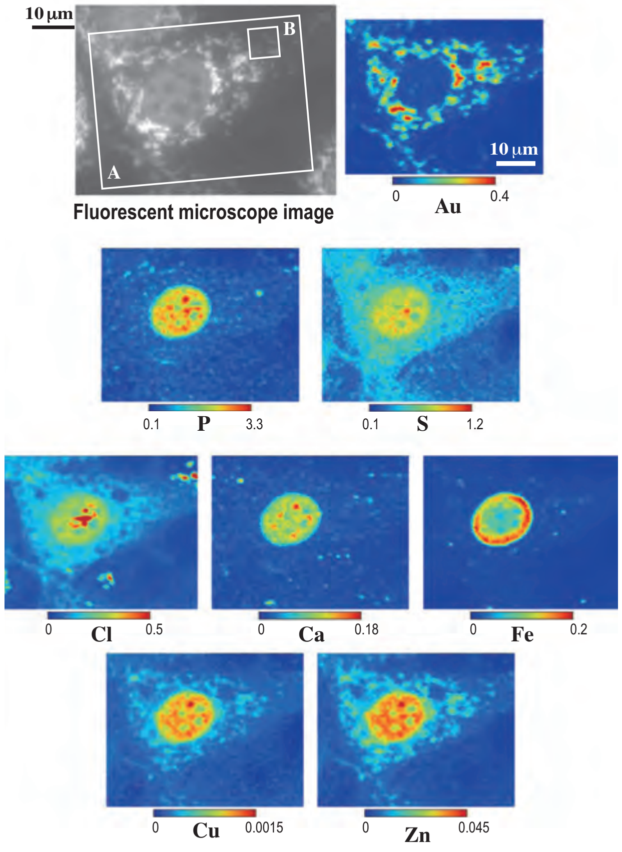

Fig. 3. Fluorescent microscope image obtained using a visible light microscope and elemental distribution maps at a single cell level in area A. The fluorescent microscope image and the Au distribution map show the existence of ATP synthase β localized in mitochondria. Color bars indicate the elemental contents (fg) of an irradiation area.

Recently, we have improved the SXFM to enable observation at cryogenic temperatures [4] of specimens with user-friendliness. The improvements allow us to accelerate the study of the biological and medical applications of SXFM. We believe that the accurate visualization of intracellular elemental distributions will help to clarify cellular functions and to overcome diseases. SXFMs are thus likely to be an important tool for such investigations in the near future.

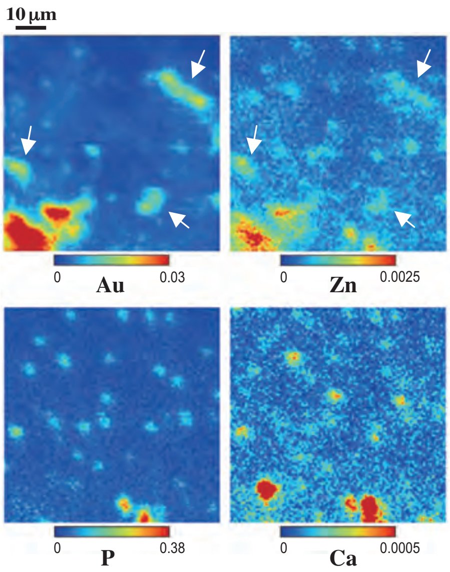

Fig. 4. High-resolution elemental distribution maps in area B in Fig. 3. The elliptical object indicated by arrows in the Au distribution map shows a single mitochondrion and the dense region at the lower left represents piles of mitochondria. Color bars indicate the elemental contents (fg) of an irradiation area.

Satoshi Matsuyama[a,b,*] and Kazuto Yamauchi[a,b]

[a] Department of Precision Science and Technology, Osaka University
[b] Research Center for Ultra-Precision Science and Technology, Osaka University

*E-mail: matsuyama@prec.eng.osaka-u.ac.jp

References

[1] *S. Matsuyama, M. Shimura, H. Mimura, M. Fujii, H. Yumoto, Y. Sano, M. Yabashi, Y. Nishino, K. Tamasaku, T. Ishikawa and K. Yamauchi: X-Ray Spectrometry* ***38*** *(2009) 89.*
[2] S. Matsuyama *et al.*: Rev. Sci. Instrum. **77** (2006) 103102.
[3] H. Mimura *et al.*: Jpn. J. Appl. Phys. **44** (2005) L539.
[4] S. Matsuyama *et al.*: X-Ray Spectrometry **39** (2010) 260.

Hard X-ray phase-difference microscopy using self-imaging phenomenon of a transmission phase grating

Nondestructive and quantitative nanometer-scale visualization of internal structures of materials consisting of light elements will bring about significant progress in biological and material sciences. For an imaging technique, not only its spatial resolution but also its sensitivity is a key factor that determines its performance. In conventional hard X-ray imaging, the difference in absorption among materials has been used for contrast formation; however, the sensitivity of this method is low especially for materials consisting of light elements. In the early 1990s, several imaging techniques measuring the phase shift of X-rays were proposed. The so-called ‘X-ray phase imaging’ has attracted considerable attention owing to its sensitivity to light elements, being three orders of magnitude higher than that of absorption contrast imaging (e.g., [1,2]). Zernike phase-contrast microscopy has been applied to hard X-rays and is now widely used; however it remains nonquantitative for strong-phase objects.

We have proposed a novel X-ray phase imaging microscope consisting of an objective lens and a single transmission grating [3,4]. The microscope can provide a phase image with no high spatial coherence and is quantitative even for strong-phase objects, which is difficult to be covered by Zernike phase-contrast imaging technique. The method uses self-imaging as in X-ray Talbot interferometry [5]; the self-image is largely magnified by placing a grating just behind the back focal plane and resolved using an image detector. This allows us to obtain twin phase images with opposite signs separated by a specific distance. Furthermore, the twin images can be processed to generate a phase image through simple algorithms. The spatial resolution of our microscope was not degraded by the presence of the grating, and the sensitivity to light elements was about two orders of magnitude higher than that of the absorption contrast microscope that was obtained by simply removing the grating. Our proposed method is attractive for easily appending a quantitative phase-sensitive mode to normal X-ray imaging microscopes, and has potentially broad applications in biology and material sciences.

The experimental setup is shown in Fig. 1. The experiments were performed at beamline **BL20XU**. The X-ray beam from an undulator was monochromatized using a Si 111 double-crystal monochromator. The experimental station was located 245 m downstream from the source, the width of which in the horizontal direction (the x-direction in Fig. 1) was 0.4 mm. A commercially available 0.7-μm-thick tantalum Fresnel zone plate (NTT-AT, outermost zone width: 86.6 nm, diameter: 416 μm) fabricated on a 2-μm-thick SiC membrane was used as an objective lens. The X-ray energy was fixed at 9 keV, and the focal length *f* of the Fresnel zone plate (FZP) was 261 mm. To maximize the magnification, we put the detector as far away as possible within the experimental space (6461 mm downstream of the FZP), and put the sample on the object plane (272 mm upstream of the FZP), resulting in a magnification of 23.7. An X-ray camera consisting of a phosphor screen (10-μm P43, Gd_2O_2S:Tb + fine powders), a relay lens, and a cooled charge-coupled device (CCD) camera (Hamamatsu Photonics C4742-98-24A, 1344 × 1024 pixels) was used as the detector. The effective pixel size of the detector was 4.34 μm, which corresponds to 183 nm on the object plane.

A 4.3-μm-pitch gold Ronchi grating (Howa Sangyo Co., Ltd.) was used. Its thickness was set at 0.92 μm as it works as a $\pi/2$ phase grating at 9 keV. It was placed 67.8 mm downstream of the back focal plane of the objective lens, which corresponds to a Talbot order *p* of 1/2.

Figure 2(a) shows a phase-difference image of polystyrene (PS) spheres. We used a 43-step fringe scan with an exposure time of 2 sec each. In this case, the twin images, each of which is a phase image, are separated. The standard deviation of the noise in the background area (the area with no sample) was $2\pi \times 0.003$ rad. Figure 2(b) shows an absorption image of the same area but obtained without the grating. The exposure time was the same as that used to obtain the image in Fig. 2(a). The gray scale of Fig. 2(b) is adjusted such that its background

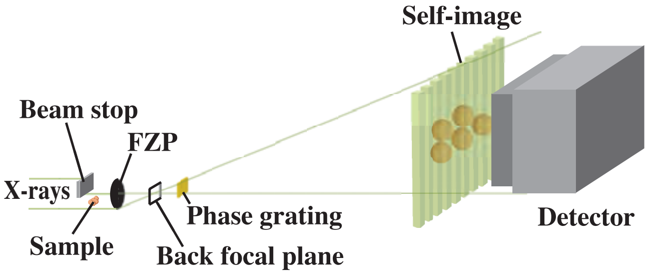

Fig. 1. Setup of phase-difference X-ray microscopy with a transmission phase grating (side view). [3]

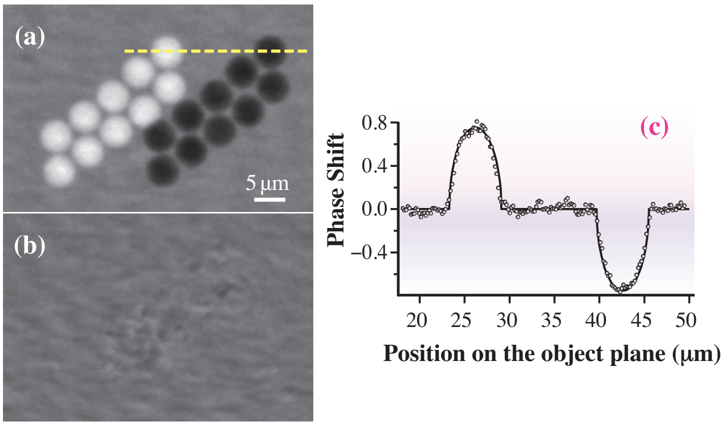

Fig. 2. **(a)** Enlarged phase-difference image of the PS spheres (gray scale, -0.3π - 0.3π). **(b)** Absorption image of the same area as **(a)** obtained by simply removing the grating. **(c)** Section profile along the dashed line in **(a)**. [4]

area is displayed in the same contrast as that of Fig. 2(a). No contrast due to the PS spheres can be seen in the absorption image, indicating that our imaging method has a much higher sensitivity than the conventional imaging microscopy based on the absorption of X-rays. The filled circles in Fig. 2(c) show the section profile along the dashed line in Fig. 2(a), and the solid line in Fig. 2(c) is the phase shift calculated for a PS sphere with a diameter of 5.8 µm. The good agreement of the experimental data with the calculated data shows that the phase shift by the sample is quantitatively retrieved.

The reconstruction of a phase image from a differential phase image was also successfully performed. Figure 3(a) shows the differential phase image of a 1-µm-thick tantalum Siemens star chart and Fig. 3(b) shows its phase image retrieved from Fig. 3(a). The reconstruction was performed in an adaptive deconvolution process based on a Bayesian framework, where the statistical distribution of noise was taken into account. Thus, our method can be used for the phase imaging of a sample larger than the separation distance.

The spatial resolution in the horizontal direction was estimated to be 450 nm from the edge of the Siemens star pattern. The resolution was almost the same as that of the absorption-contrast image obtained simply by removing the grating. The degradation in the spatial resolution due to the grating was thus avoided.

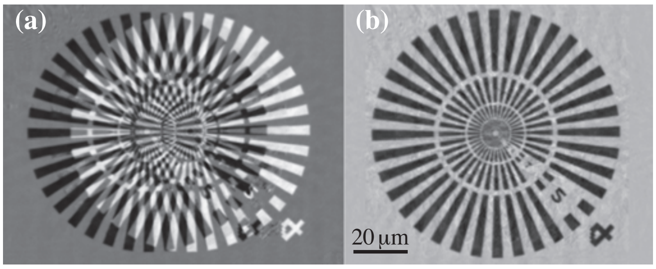

Fig. 3. **(a)** Differential phase image of a 1-µm-thick tantalum Siemens star chart and **(b)** its phase image retrieved from **(a)**. [4]

Wataru Yashiro* and Atsushi Momose

Department of Advanced Materials Science,
The University of Tokyo

*E-mail: yashiro@mml.k.u-tokyo.ac.jp

References

[1] R. Fitzgerald: Phys. Today **53** (2000) 23.
[2] A. Momose: Jpn. J. Appl. Phys. **44** (2005) 6355.
[3] *W. Yashiro, Y. Takeda, A. Takeuchi, Y. Suzuki and A. Momose: Phys. Rev. Lett.* ***103*** *(2009) 180801.*
[4] *W. Yashiro , S. Harasse, A. Takeuchi, Y. Suzuki and A. Momose: Phys. Rev. A* ***82*** *(2010) 043822.*
[5] For example, A. Momose *et al.*, "X-ray Phase Imaging with Talbot Interferometry", in Biomed. Math.: Promising Directions in Imaging, Therapy Plan. & Inverse Problems, ed. by Y. Censor, M. Jiang and G. Wang (Medical Physics Publishing, Madison, WI, USA, 2009), Ch. 14 (p.281).

MATERIALS SCIENCE:

STRUCTURE

An increasing variety of materials has come to Materials Science in SPring-8. This year, two structural studies have been selected for superconducting materials. One is the phase transition research of the well-known fulleride superconductor, Cs_3C_{60}, providing tactics to design the atomic arrangement of a superconductive fulleride. The other is the research about the morphological dependence of superconductivity of a novel promising material, $FeSe_{1-x}$ thin films. Recent years have been marked by the expanding morphological approaches to create characteristic functional properties. The research on the morphotropic phase boundary in ferromagnets by Sen Yang and the study of nano-oriented crystals of iPP with ultrahigh performance crystallized by extreme melt elongation by Kiyoka Okada are major and quite important achievements for the new trend of materials science in SPring-8.

The recent increase in photoinduced reaction research should also be noted. This year, three studies are selected: "Symmetry switch of cobalt ferrocyanide framework by alkaline cation exchange" by Yutaka Moritomo, "Photoindued guest trapping and conversion by photoresponsive nanoporous crystal" by Ryotaro Matsuda and "How do phase-change materials crystallize so fast?" by Noboru Yamada. This is closely related to the improvement of the experimental performance of beamlines for the laser pump and probe diffraction experiment. In addition, the 3D imaging researches using high brilliance, high parallel beam and/or coherence of light source are also increasing.

The materials science in SPring-8 is now undergoing a great change from structural characterization toward sophisticated strategies building advanced material design.

Masaki Takata

Face-centered-cubic structured Cs_3C_{60}: the Holy Grail of fulleride superconductivity

The structural and electronic properties of C_{60}-based solids have been exhaustively explored in the last 20 years. They have been long recognized as archetypal examples of molecular superconductors with superconducting transition temperatures (T_c) as high as 33 K. The superconducting T_c of the face-centered cubic (fcc) A_3C_{60} (A = alkali metal) fullerides has been shown to increase monotonically with the inter C_{60} separation, which is in turn controlled by the sizes of the A^+ cation intercalants. However, following these seminal discoveries many years ago, the established fulleride chemistry had chronically failed to deliver new materials. Very recent work in our laboratories based on new synthetic ideas and coupled with detailed structural and electronic property measurements has removed this bottleneck. We specifically targeted high-symmetry (i.e. retaining t_{1u} orbital degeneracy in the solid) fullerides with varying C_{60} orientations and packings (*i.e.* tuning geometrical frustration in order to enhance molecular superconductivity). This approach culminated in the discovery of pressure-induced bulk superconductivity at 38 K in bcc-structured A15 Cs_3C_{60}, the highest T_c known for any molecular material. This was the first example of a superconducting C_{60}^{3-} fulleride with non-fcc sphere packing – this single non-fcc material has a higher T_c than all the fcc A_3C_{60} fullerides studied over the past 20 years [1]. Our subsequent work showed that the electronic ground state in competition with superconductivity, and found at ambient pressure, not only contains magnetic moments localised on the C_{60}^{3-} anions but is antiferromagnetically ordered with a Néel temperature, T_N = 46 K – this is the hallmark of strong electron correlations [2]. The antiferromagnetic Mott-Hubbard insulator-superconductor (AFMI-SC) transition maintains the threefold degeneracy of the active t_{1u} orbitals in both competing electronic states, and is thus a purely electronic transition to a superconducting state with a dependence of the transition temperature on pressure-induced changes of anion packing density that is not explicable by conventional BCS theory.

In our most recent work, we have now isolated the fcc polymorph of Cs_3C_{60} (Fig. 1) to show how the spatial arrangement of the electronically active units controls the competing superconducting and magnetic electronic ground states. We found that unlike all the other fcc A_3C_{60} solids, the most expanded fcc-structured fulleride, Cs_3C_{60} is not a superconductor but a magnetic insulator at ambient pressure, and becomes superconducting under pressure [3]. The antiferromagnetic ordering occurs at an order of magnitude lower temperature in the fcc polymorph (T_N = 2.2 K) than in the bcc-based packing (T_N = 46 K). The prime reason for the suppression of the well-defined transition to magnetic order in contrast to the bcc-based A15 material is the geometrical frustration of the fcc lattice. The isotropic molecular structure and weak spin-orbit coupling in the C_{60}^{3-} anion should make the fcc Cs_3C_{60} phase a good example of the nearest neighbor Heisenberg fcc lattice, where the ground state is infinitely degenerate, preventing long-range antiferromagnetic order. As magnetic anisotropies are very small in fullerides, the observed gradual crossover to a highly disordered frozen state over a broad temperature range followed by the onset of magnetic long-range order but of an extremely disordered nature at a much lower temperature can be assigned to the suppression of the frustration globally via the next-nearest neighbor exchange interactions, coupled with the presence of merohedral (orientational) disorder, which locally removes the frustration. The qualitative contrast with the sharp transition to magnetic long-range order on the non-frustrated bipartite bcc lattice is very clear.

Magnetization measurements under pressure reveal that fcc Cs_3C_{60} becomes superconducting upon the application of moderate applied pressures. Superconductivity is initially observed with a rapidly increasing T_c, which rises to a maximum of 35 K (lower than the 38 K T_c found for the A15 polymorph) at ~0.7 GPa before decreasing upon further pressurization. The resulting variation of T_c with P shows a rather broad maximum. Synchrotron X-ray powder diffraction

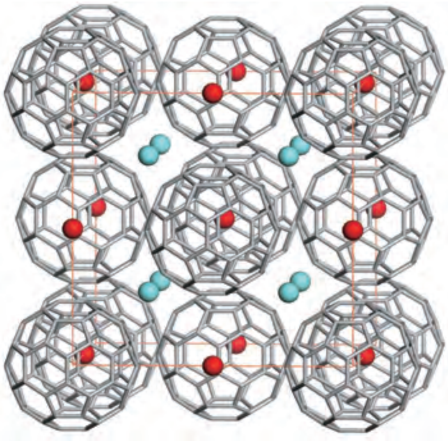

Fig. 1. Face-centered cubic structure of Cs_3C_{60}. Two orientations related by 90° rotation about [100] occur in a disordered manner (merohedral disorder) - only one of these orientations is shown for clarity.

measurements (beamline **BL10XU**) at the pressures used in the magnetization measurements and at temperatures below the observed T_c show that the fcc structure is preserved at all relevant T and P. The low temperature, high pressure diffraction results allow the superconducting T_c to be related to the C_{60} packing density measured by V. After peaking at 35 K for $V = 759.6$ Å^3/$C_{60}{}^{3-}$, the $T_c(V)$ dependence at the highest pressures (lowest volumes) correlates well with that observed for the less expanded fcc A_3C_{60} superconductors at ambient pressure (Fig. 2(a)).

The different sphere packings in the fcc and A15 bcc-based Cs_3C_{60} polymorphs produce distinct dome-like $T_c(V)$ relationships (Fig. 2(a)). Within each polymorph, the packing density V represents the ratio of U to the bare bandwidth W, which controls the metal-insulator transition, as expansion reduces W. At the same V the bcc-based polymorph has a higher T_c, consistent with band structure calculations [4]. The bandwidths W in the less dense A15 phase are also higher, allowing the metallic state to remain stable to larger V than is possible in the fcc phase – the details of the intermolecular overlaps in the two sphere packings allow this combination of larger W and higher $N(E_F)$ in the bcc packing, which, in combination with orientationally ordered anions and considerably reduced static positional disorder on the Cs positions, give a higher T_c. As W_c is controlled by the lattice packing, we can use this parameter to scale T_c in the two polymorphs by replacing V – which represents U/W within each polymorph but does not allow direct comparison between sphere packings – with $(U/W)/(U/W)_c = (W_c/W)$. Both Cs_3C_{60} polymorphs have the same dependence of T_c on this reduced variable, showing that T_c is controlled by proximity to the metal-insulator transition independent of the sphere packing adopted.

Normalization to the maximum T_c in each family permits the mapping of all the bcc and fcc $C_{60}{}^{3-}$ superconductors onto a single packing-independent dome-shaped universal curve (Fig. 2(b)), suggesting that it is the separation from the competing localized electron ground state that determines T_c in fullerides, with the absolute values observed depending on the details of the molecular overlap within the two different sphere packings. Electron correlations are also important in high-T_c superconductors like the cuprates, where the packing of the electronically active ions is essentially identical (two-dimensional square) in all known superconducting families. Cs_3C_{60} is unique as the same electronically active unit can be packed in two distinct lattice motifs to reveal that T_c scales in a lattice-independent manner with proximity to the correlation-driven metal-insulator transition.

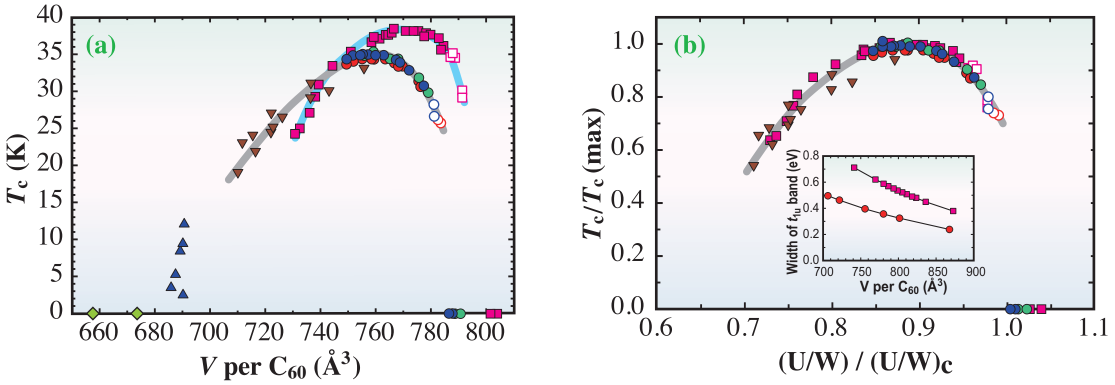

Fig. 2. **(a)** T_c as a function of volume occupied per fulleride anion, V, at low temperature in the two sphere packings of A_3C_{60} superconductors. The red/green/blue circles and pink squares correspond to the bulk $T_c(V)$ behavior observed in fcc- and A15-structured Cs_3C_{60}, respectively. Open symbols represent data at pressures where trace superconductivity is observed and where in the A15 phase superconductivity coexists with antiferromagnetism. The yellow rhombi, dark blue triangles and brown inverted triangles correspond to the ambient pressure T_c of fcc $C_{60}{}^{3-}$ anion packings with Li_2CsC_{60}, $Pa\bar{3}$ symmetry, and $Fm\bar{3}m$ symmetry, respectively. **(b)** Normalized superconducting transition temperature, T_c/T_c(max), as a function of the ratio (U/W) divided by the critical value $(U/W)_c$ required to produce localization in the A_3C_{60} fulleride structures with fcc- and bcc-sphere packings. Inset, dependence of the t_{1u} conduction bandwidth on volume occupied per fulleride anion, V, for fcc-sphere (red circles) and bcc-sphere (pink squares) packings, as determined by electronic structure calculations.

Kosmas Prassides[a,*] and Matthew J. Rosseinsky[b]

[a] Department of Chemistry, Durham University, UK
[b] Department of Chemistry, University of Liverpool, UK

* E-mail: K.Prassides@durham.ac.uk

References

[1] A.Y. Ganin *et al.*: Nature Mater. **7** (2008) 367.
[2] Y. Takabayashi *et al.*: Science **323** (2009) 1585.
[3] *A.Y. Ganin, Y. Takabayashi, P. Jeglič, D. Arčon, A. Potočnik, P.J. Baker, Y. Ohishi, M.T. McDonald, M.D. Tzirakis, A. McLennan, G.R. Darling, M. Takata, M.J. Rosseinsky and K. Prassides: Nature* ***466*** *(2010) 221.*
[4] G.R. Darling *et al.*: Phys. Rev. Lett. **101** (2008) 136404.

Crystal orientation and thickness dependence of the superconducting transition temperature of tetragonal $FeSe_{1-x}$ thin films

Superconductivity was discovered in tetragonal $FeSe_{1-x}$, which has the simplest Fe planar structure, with a transition temperature $T_C \sim 8$ K [1]. It was noted that a low temperature structural distortion was observed in $FeSe_{1-x}$ superconductors [1] without accompanying a magnetic ordering, which is quite different from the Fe-pnictide superconductors. Wu *et al*. have reported the suppression of the superconductivity in Cu-substituted $Fe_{1-y}Cu_ySe_{1-x}$ samples, which have no low temperature structural distortion [2]. Cava *et al*. have also reported that a low temperature structural distortion is observed in the superconducting $Fe_{1+\delta}Se$ (δ~0.01) samples, but not in the non-superconducting $Fe_{1+\delta}Se$ (δ~0.03) samples [3]. This correlation suggested that the low temperature structural distortion might be essential for the occurrence of superconductivity. In this work [4], we further confirmed the importance of the low temperature distortion to the occurrence of superconductivity in $FeSe_{1-x}$ thin films, which exhibit strong orientation and film thickness dependence.

The superconducting tetragonal $FeSe_{1-x}$ thin films on (001) MgO substrates were grown using a pulsed laser deposition (PLD) technique. In this report, the films were grown at substrate temperatures of 320°C (referred to as LT-FeSe films) and 500°C (HT-FeSe films). The detailed structure analysis at low temperature was performed using 4-circle X-ray diffractometer with incident beam (12.4 keV) at beamlines BL13A in NSRRC and **BL12B2** in SPring-8.

Figure 1(a) shows the X-ray diffraction patterns of the LT-FeSe and HT-FeSe films. The thicknesses of both films are estimated to be ~140 nm. We observed in the LT-FeSe sample only (001) peaks of the tetragonal phase $FeSe_{1-x}$, suggesting a strong *c*-axis preferred orientation. However, the HT-FeSe film shows the (101) peaks to be dominant. It was surprising to find, as shown in Fig. 1(b), that the LT-FeSe film exhibits only a slightly resistive drop at 2 K without a complete superconducting transition. On the contrary, a clear superconducting transition takes place in the HT-FeSe films.

To understand this puzzling phenomenon on superconductivity suppression in the LT-FeSe thin film, a series of LT- and HT-FeSe films with different thicknesses were prepared. For the LT-FeSe films, as the film is made thicker, the onset T_C of film recovers more closely to the bulk result. On the other hand, the HT-FeSe film does not exhibit significant film thickness dependence. The superconducting transition temperatures for HT-FeSe films are close to the bulk sample value.

The detailed lattice constants of films determined from high resolution X-ray diffraction show that both the LT- and HT-FeSe samples have lattice constants close to the values of bulk, a=3.78 Å and c=5.54 Å at room temperature. Thus, the lattice mismatch is unlikely to be the cause for the strong thickness dependence of superconductivity in LT-FeSe films.

To better understand our observations, we carried out detailed low temperature structure characterizations

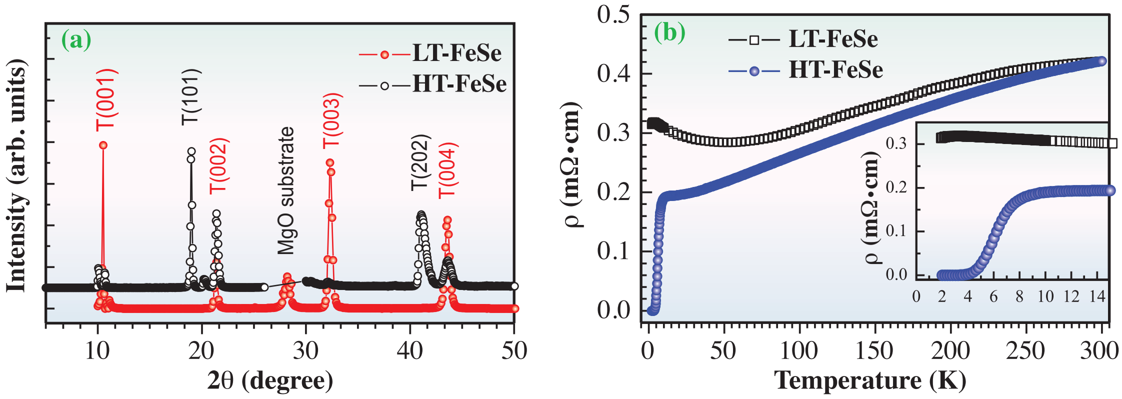

Fig. 1. **(a)** X-ray diffraction pattern of LT- and HT-$FeSe_{1-x}$ films. **(b)** ρ-T curves of LT- and HT-$FeSe_{1-x}$ films. Superconducting transition is observed only for HT-FeSe. The inset is a close-up of the ρ-T below 15 K.

at SPring-8, and the results are shown in Fig. 2. Figure 2(a) is the (220) peaks at different temperatures of the HT-FeSe film (thickness ~400 nm). The results clearly show the splitting of (220) peak confirming the presence of a structural distortion. On the other hand, the non-superconducting LT-FeSe film (~140 nm) showed no structural distortion at low temperature, as shown in Fig. 2(b). However, the distortion re-appears in thicker LT-FeSe film as evidenced by the gradual broadening of the (221) diffraction peak, and the maximum value is decreasing as the temperature decreases, as shown in Fig. 2(c). These observations clearly confirmed that the low temperature structural distortion is not affected in HT-FeSe films, but is suppressed in relatively thin LT-FeSe films. Our results further confirm the importance of the low temperature structural distortion to the origin of superconductivity in the FeSe system. Although the actual mechanism has yet to be identified, our results may provide an important clue to understand the origin of superconductivity in FeSe.

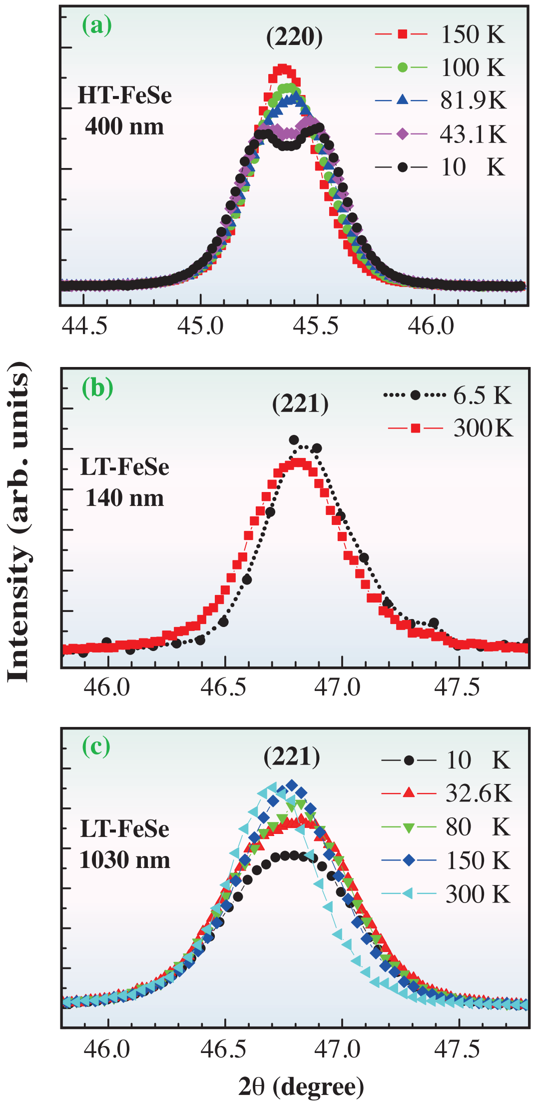

Fig. 2. **(a)** Low temperature X-ray diffraction (220) peaks of HT-FeSe film. The splitting of the Bragg peak indicates that structural distortion occurs at around 82 K. X-ray diffraction patterns of LT-FeSe films of **(b)** 140 and **(c)** 1030 nm thicknesses. The (221) Bragg peak does not change with temperature for the 140-nm-thick film, but broadens at low temperature for the 1030-nm-thick.

M. J. Wang[a] , T.W. Huang[b] and M. K. Wu[b,c,*]

[a] Institute of Astronomy and Astrophysics,
Academia Sinica, Taiwan
[b] Institute of Physics, Academia Sinica, Taiwan
[c] Department of Physics, National Tsing Hua University,
Taiwan

*E-mail: mkwu@phys.sinica.edu.tw

References

[1] F.-C. Hsu *et al.*: Proc. Natl. Acad. Sci. USA **105** (2008) 14262.
[2] M.K. Wu *et al.*: Physica C (Amsterdam) **469** (2009) 340.
[3] T.M. McQueen *et al.*: Phys. Rev. Lett. **103** (2009) 057002.
[4] [4] *M.J. Wang, J.Y. Luo, T.W. Huang, H.H. Chang, T.K. Chen, F.C. Hsu, C.T. Wu, P.M. Wu, A.M. Chang and M.K. Wu: Phys. Rev. Lett.* ***103*** *(2009) 117002.*

Morphotropic phase boundary in ferromagnets - a way leading to large magnetostriction

The morphotropic phase boundary (MPB), a phase boundary separating two ferroelectric phases of different crystallographic symmetries in the composition-temperature phase diagram, is crucial in ferroelectric materials, because MPB can lead to a great enhancement of piezoelectricity, the most useful property of this large class of functional materials. The current workhorse of piezoelectric materials, i.e., PZT ($PbZrO_3$-$PbTiO_3$) and PMN-PT ($PbMg_{1/3}Nb_{2/3}O_3$-$PbTiO_3$), is designed to have a composition close to the MPB to achieve a maximum piezoelectric effect. Figure 1(a) shows a typical ferroelectric MPB in PZT, which separates a ferroelectric rhombohedral (R) phase on the $PbZrO_3$ side and a ferroelectric tetragonal (T) phase on the $PbTiO_3$ side. The R and T ferroelectric phases share a common cubic paraelectric phase at high temperatures. Theoretical and experimental studies have shown that, at the MPB composition, $\boldsymbol{P_s}$ can be easily rotated under a small external field, thereby causing a high piezoelectric effect.

Ferromagnetic systems are physically parallel to ferroelectric ones; the former involve an ordering of magnetic moment and the latter involve an ordering of polarization below a critical temperature (Curie temperature) T_c. In both systems, the order parameter is coupled to the lattice, respectively leading to the magnetoelastic and piezoelectric effects. From the physical parallelism between ferromagnetism and ferroelectricity, it is tempting to ask an interesting question: Can a similar MPB situation exist in ferromagnetic systems? If yes, can such magnetic MPB yield large magnetostriction (magnetic-field-induced distortion, an effect analogous to the piezoelectricity in ferroelectrics)? Following the definition of MPB in ferroelectrics, a magnetic MPB should be a phase boundary separating two different ferromagnetic states with different crystallographic symmetries.

So far, the major obstacle to the existence of MPB in ferromagnets has been the general observation (by conventional X-ray diffractometry (XRD)) that a difference in $\boldsymbol{M_s}$ direction does not result in a difference in crystal symmetry, differently from the ferroelectric case. Therefore, for ferromagnetic systems, the condition for MPB seems not satisfied. However, with the great enhancement in the structure resolution using synchrotron XRD (**BL15XU**), recent studies have proved that different ferromagnetic states indeed correspond to different crystal symmetries

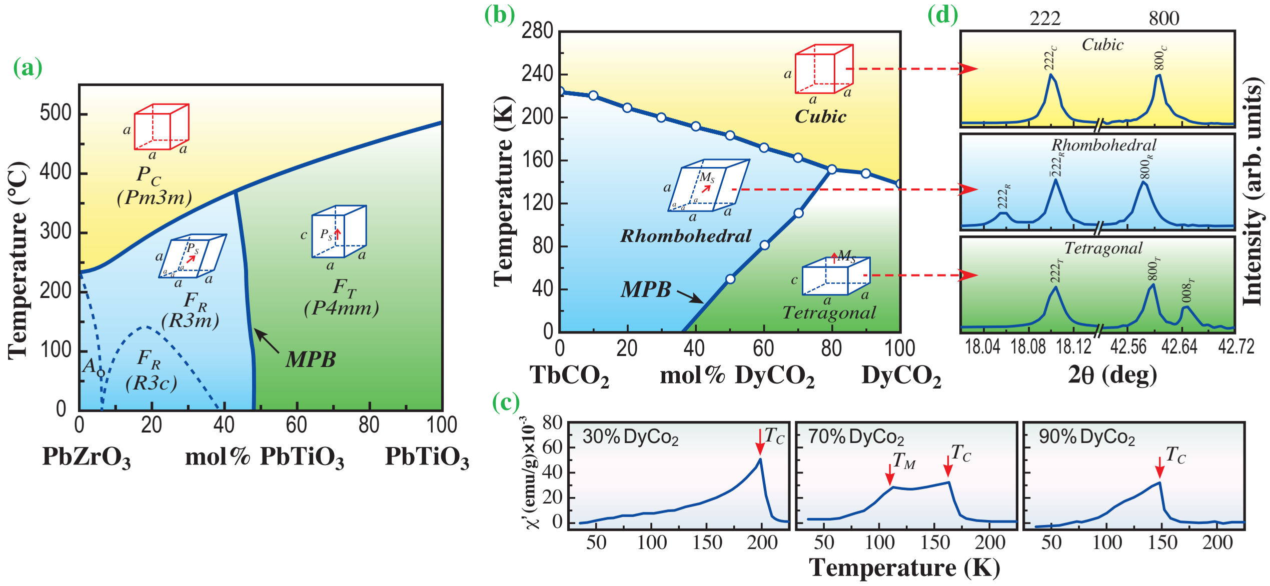

Fig. 1. **(a)** Phase diagram of PZT. **(b)** Phase diagram of $TbCo_2$-$DyCo_2$. **(c)** Temperature dependence of ac susceptibility χ'. T_c and T_M denote the para-ferro and ferro-ferro transition temperatures, respectively. **(d)** Synchrotron XRD profiles of cubic paramagnetic, rhombohedral ferromagnetic and tetragonal ferromagnetic phases.

[1,2], the same as in the ferroelectric case; however, the lattice distortion due to a difference in crystal symmetry is usually too small to be detected by conventional XRD analysis.

Now, we have a good reason to expect the existence of a magnetic MPB and therefore we propose to detect a magnetic MPB in a pseudo binary ferromagnetic system $TbCo_2$-$DyCo_2$, using of BL15XU beamline. The results are shown in detail in Fig. 1, Fig. 2, and Fig. 3. The MPB composition demonstrates a 3-6 times larger "figure of merit" of magnetostrictive response than the off-MPB compositions (Fig. 3). The finding of MPB in ferromagnets may help to discover novel high-performance magnetostrictive and even magnetoelectric materials [3].

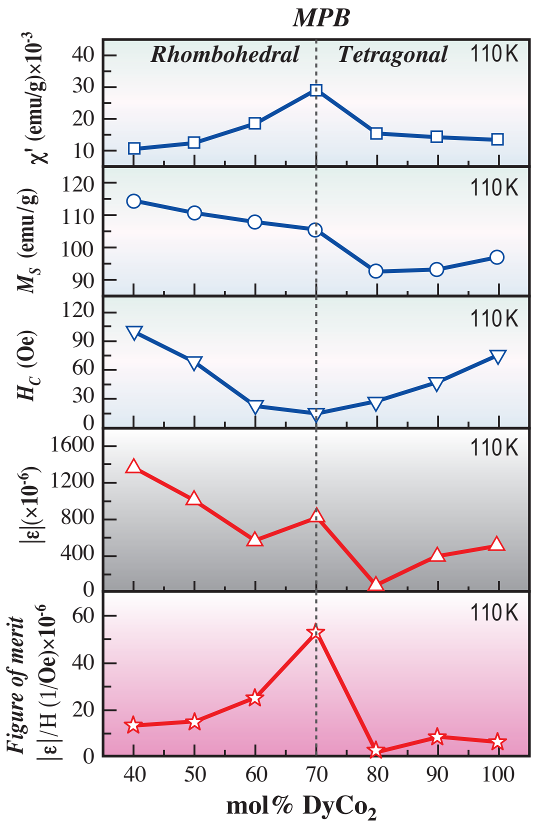

Fig. 2. **(a)** XRD profiles of rhombohedral phase at 150 K (above MPB), a mixture of rhombohedral and tetragonal phase at 110 K (at MPB), and tetragonal phase at 90 K (below MPB). The red and blue peaks underneath the experimental peaks are Lorentzian rhombohedral and tetragonal peaks respectively, giving the best fit to the experimental profiles. **(b)** Temperature dependence of lattice parameters (a_R and α_R stand for the lattice parameters of the R-phase with M_s||[111], and a_T and c_T for that of the T-phase with M_s||[001]); the MPB corresponds to a 2-phase mixture of rhombohedral and tetragonal phases. The error bars are determined by the fitting error in Fig. 2(a).

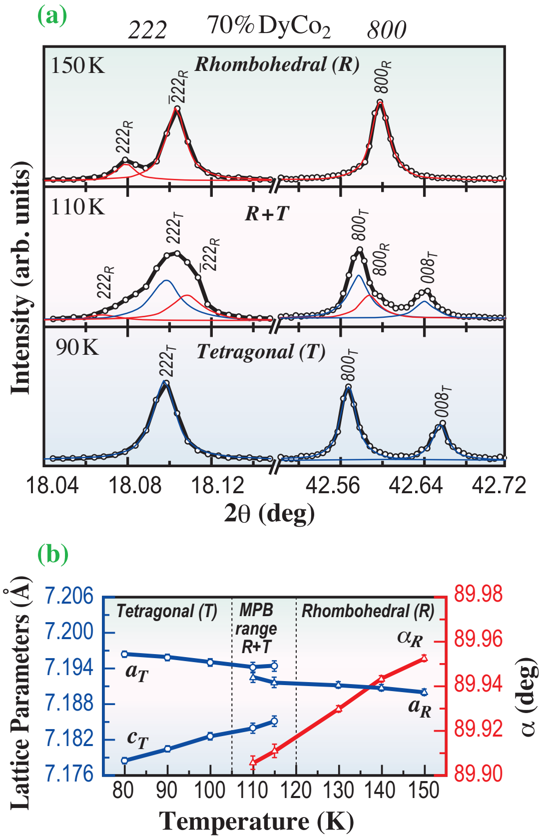

Fig. 3. Composition dependences of Ac susceptibility χ', saturation magnetization M_s, coercivity H_c, magnetostriction ε (absolute value) at 10 kOe field, and figure of merit ε/H_c, in relation to MPB composition at 110 K.

Sen Yang[a,†,*] and Xiaobing Ren[b]

[a] NIMS Beamline Station SPring-8,
National Institute for Materials Science
[b] Ferroic Physics Group, National Institute for
Materials Science (NIMS)

Email: yang.sen@mail.xjtu.edu.cn

[†] Present address: Department of Materials Physics, Xi'an Jiaotong University, China

References

[1] S. Yang and X. Ren: Phys. Rev. B **77** (2008) 014407.
[2] S. Yang, X. Ren and X. Song, Phys. Rev. B **78** (2008) 174427.
[3] *S. Yang, H. Bao, C. Zhou, Y. Wang, X. Ren, Y. Matsushita, Y. Katsuya, M. Tanaka, K. Kobayashi, X. Song and J. Gao: Phys. Rev. Lett.* ***104*** *(2010) 197201.*

Symmetry switch of cobalt ferrocyanide framework by alkali cation exchange

Nanoporous coordination polymers are attracting increasing interest from materials scientists, because they can be utilized in various devices, for example, Li ion batteries, electrochromic devices, hydrogen storage devices, molecular sensors and molecular filters. Among nanoporous materials, Prussian blue analogues, represented as $A_xM[\mathrm{Fe(CN)_6}]_y z\mathrm{H_2O}$ (where A and M are an alkali metal and a transition metal, respectively), form a nanoporous three-dimensional (3D) framework (- M - NC - Fe - CN - M -). In Fig. 1, we schematically show the framework structure, together with the guest alkali cation A^+. A significant feature of the compounds is the controllability of the guest concentration (x) by an electrochemical method [1] or by adjusting external voltage on all solid devices [2,3]. Imanishi *et al.* reported lithium intercalation into the host framework as well as the charge-discharge behavior in a series of cyano-bridged transition metal compounds with M = V, Mn, Co, Ni and Cu. The average discharge potential for the V compound is about 3.6 V, corresponding to the reduction of the V^{3+} ion, while those for the Mn, Co, Ni and Cu compounds are around 3.3 V, corresponding to the reduction of the $\mathrm{Fe^{3+}(CN)_6}$ unit. The charge capacity of the Cu compound reaches 140 $\mathrm{mAhg^{-1}}$, which is comparable to that of the actually used material, $\mathrm{LiCoO_2}$ (capacity, 140 $\mathrm{mAhg^{-1}}$). Thus, the compounds are quite promising as positive electrode materials. In order to extract better electrode performance from the compounds, an exhaustive structural investigation is needed to clarify the interaction between the guest cations and the host framework.

Now, let us discuss the interrelation between the ionic size of A^+ and the interval (~0.5 nm) of the framework (see Fig. 1). The ionic radius r of A^+ increases with atomic number: r = 0.092 nm for $\mathrm{Li^+}$, r = 0.182 nm for $\mathrm{Na^+}$, r = 0.151 nm for $\mathrm{K^+}$, r = 0.161 nm for $\mathrm{Rb^+}$, and r = 0.174 nm for $\mathrm{Cs^+}$. Here, we emphasize that the transition metal ions are bridged by CN groups, and hence the 'frame' is rather thick. Recently, Moritomo *et al.* [4] have investigated the cation channel in the cobalt ferrocyanide framework. They confirmed that the $\mathrm{Na^+}$ ions go through the square window of the framework, while the larger ions, i.e., the $\mathrm{K^+}$ and $\mathrm{Rb^+}$ ions, take a detour channel along the vacancies. The cation dependent behavior is well reproduced by the cation potential, which is calculated by *ab initio* total energy calculation with use of a WIEN2k program. The cation dependence of the channel suggests that the nanopores of the host framework are rather large for the $\mathrm{Na^+}$ and $\mathrm{Li^+}$ ions, but fit well for the $\mathrm{K^+}$, $\mathrm{Rb^+}$ and $\mathrm{Cs^+}$ ions.

We investigated the crystallographic symmetry of the cobalt ferrocyanide framework while changing A^+. The cobalt ferrocyanide with larger cations, i.e., A^+ = $\mathrm{K^+}$, $\mathrm{Rb^+}$, and $\mathrm{Cs^+}$ belongs to the face-centered cubic lattice ($Fm\bar{3}m$; Z=4), while the cobalt ferrocyanide with smaller $\mathrm{Na^+}$ ions belongs to the rhombohedral lattice ($R\bar{3}m$; Z=2). We suspect that the displacement of the $\mathrm{Na^+}$ ion is the origin for the rhombohedral distortion. In the nanopore, the $\mathrm{Na^+}$ ion is surrounded by our $[\mathrm{Fe(CN)_6}]^{4-}$ ions and four $\mathrm{Co^{2+}}$ ions, and hence, feels an asymmetric (T_d symmetry) electrostatic potential. Then, the local potential minimum is not at the central position of the cube, but at the tetrahedral sites toward the four $\mathrm{Fe(CN)_6]^{4-}}$ ions. Then, a cooperative displacement of the $\mathrm{Na^+}$ ion can cause the rhombohedral distortion.

We further found that a simple dipping

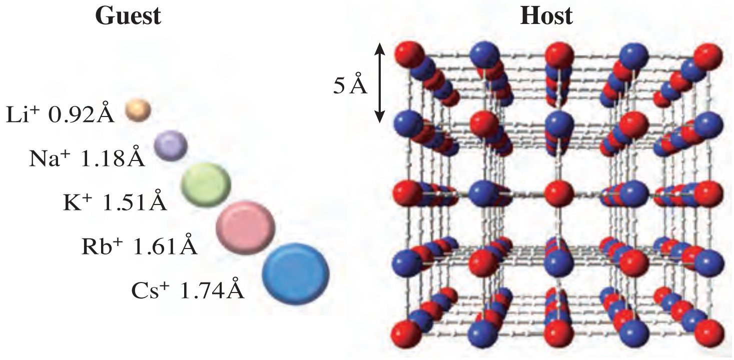

Fig. 1. Schematic pictures of the guest alkali cations and host framework for Prussian blue compounds.

procedure can exchange the guest alkali cation between K^+ and Na^+, and switch the symmetry of the framework between cubic and rhombohedral ones [5]. Figure 2 shows the X-ray powder diffraction patterns for $K_{1.88}Co[Fe(CN)_6]_{0.97}\cdot 3.8H_2O$ **(1)**, $Na_{1.52}K_{0.04}Co[Fe(CN)_6]_{0.89}\cdot 3.9H_2O$ **(2)** and $Na_{0.04}K_{1.48}Co[Fe(CN)_6]_{0.88}\cdot 2.6H_2O$ **(3)**, obtained at **BL02B2** beamline. **2** was obtained by dipping **1** in 1 mol dm^{-3} of NaCl solution, and **3** was obtained by dipping **2** in 1 mol dm^{-3} KCl solution. The wavelength of the X-ray was 0.50243 Å, which was calibrated by the lattice constant of standard CeO_2 powder. We performed Rietveld analysis to determine the lattice symmetry and lattice constant. **1** shows a face-centered-cubic structure with a lattice constant a = 10.057(7) Å. In contrast, the diffraction pattern of **2** was different from that of **1**. We could index the pattern with a rhombohedral structure: a = 10.340(2) Å and α = 91.32°. Again, **3** shows a face-centered-cubic structure with a lattice constant a = 10.082(3) Å. The elemental analysis by ICP-AES spectrometry after respective dipping procedures revealed nearly complete cation exchange at least for 8 cycles (Fig. 3).

We investigated the valence states of **1** and **2** using infrared (IR) spectra and the magnetic susceptibility. The CN stretching peaks of $[Fe^{II}(CN)_6]$ were observed at 2079.9 cm^{-1} in **1** and at 2086.6 cm^{-1} in **2**. The products of the magnetic susceptibility (χ_M) and temperature (T) plots are observed at 300 K and are almost equal to the expected spin-only values of 3.0, i.e., 3.06 (**1**) and 3.02 cm^3 K mol^{-1} (**2**). These data indicate that the valence states are the same, i.e., $Co^{II}{}_{hs}$-$Fe^{II}{}_{ls}$. Thus, the symmetry switch observed in the present system has a purely structural origin. We further investigated the diffuse reflectance spectra. The cation exchange alters the position of the absorption band from 520 nm (**1**) to 610 nm (**2**). The rather sharp 610 nm band in **2** can be ascribed to the *d-d* transition of $Co^{II}{}_{hs}$. The rhombohedral distortion of the framework can dipole-activate such a *d-d* transition.

In summary, we found a reversible symmetry switch of the cobalt ferrocyanide framework by alkali cation exchange. The symmetry change switches the optical properties of the compound. We suspect that the displacement of the Na^+ ion is the origin of rhombohedral distortion. The Li^+ substitution effect on structural properties is the key to the comprehensive understanding of the guest-host interaction of the Prussian blue analogues.

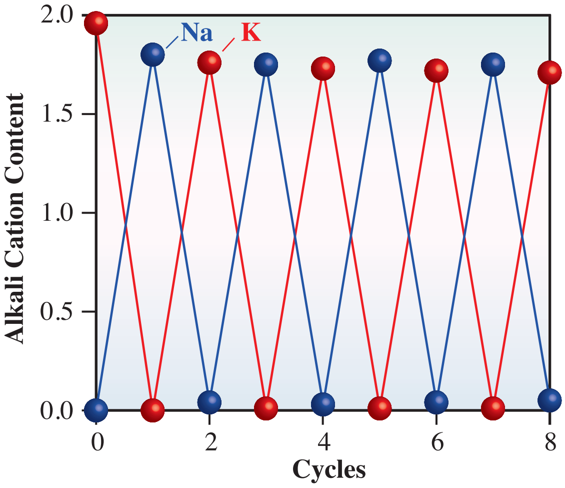

Fig. 3. Reversible alkali cation exchanges. The Na and K contents determined by ICP-AES are plotted after respective cation exchanges.

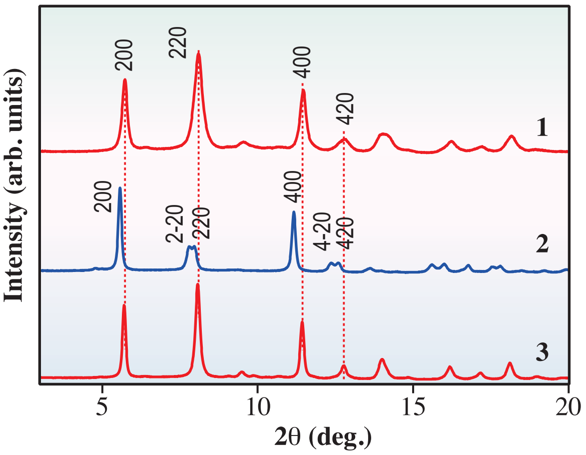

Fig. 2. X-ray powder diffraction patterns for 1 (upper), 2 (middle), and 3 (bottom) measured at BL02B2 beamline. X-ray wavelength was 0.50243 Å.

Yutaka Moritomo* and Tomoyuki Matsuda

Graduated School of Pure and Applied Science,
University of Tsukuba

*E-mail: moritomo@sakura.cc.tsukuba.ac.jp

References

[1] N. Imanishi *et al.*: J. Power Source **81-82** (1999) 530.
[2] Y. Moritomo and T. Shibata: Appl. Phys. Lett. **94** (2009) 043502.
[3] T. Shibata and Y. Moritomo: Appl. Phys. Ex. **2** (2009) 105502.
[4] Y. Moritomo *et al.*: Appl. Phys. Ex. **2** (2009) 085001.
[5] *T. Matsuda, J.E. Kim and Y. Moritomo: J. Am. Chem. Soc.* ***132*** *(2010) 12206.*

Photoindued guest trapping and conversion by photoresponsive nanoporous crystal

Nanoporous compounds are ubiquitous and indispensable in daily life as adsorbents and catalysts. The discovery of a new porous compound having unique properties based on intrinsic nanosized space and surface functionalities is scientifically and technologically important. Surface activity on nanopores is essential for porous properties [1,2]. However, functional species that can be introduced are limited to those that are sufficiently inert so as not to spoil the porous structures. This has prevented access to highly reactive functionalities such as electronically open-shell atoms, which play a pivotal role in many important chemical transformations but often elude isolation and characterization. Furthermore, if it is possible to activate a nanopore surface by external stimuli where and when desired, on-demand gas storage/trapping systems can be realized. Here, we show a new strategy to achieve a crystalline porous material with a pore surface regularly decorated with highly reactive "bare" nitrenes that are photonically generated from stable "dormant" precursors at will. The bare triplet nitrenes are accessible to and react with adsorbed oxygen molecules, which show not only the activation of the pore surface, but also a high probability of chemical trapping and conversion of guest molecules by light stimulation on demand (Fig. 1) [3]. To achieve the on-demand activation of porous compounds, highly designable host porous frameworks are prerequisite. In this point of view, we adopted porous coordination polymers (PCPs) or metal–organic frameworks (MOFs) [4] as a new platform to create a pore surface having highly reactive species because of their designability based on various functional metal and/or organic sites.

We prepared a linker-type building block having an azide module, 5-azidoisophthalic acid (H_2N_3-ipa), because azide modules can be converted to nitrenes, which are reactive open-shell atoms, by photoirradiation. Then, we synthesized single crystals of a new PCP composed of H_2N_3-ipa ligands, Zn ions and 4,4'-bipyridine (bpy) $[Zn_2(N_3\text{-ipa})_2(bpy)_2(DMF)_{1.5}]_n$ (CID-N_3). CID-N_3 was constructed from interdigitated 2-D layers. A winding 1-D channel with a cross-section of 5 × 6 $Å^2$ runs through the layers, with aryl azides exposed on the channel surface. We studied the sorption properties of dried CID-N_3 which was obtained by heating single crystals of CID-N_3 at 120°C in vacuum for 6 h. The dried CID-N_3 was found to be non-porous for N_2, O_2 and CO at 77 K because of the slow diffusion of gaseous molecules into the micropore. In contrast, at higher temperatures, the adsorption isotherms of O_2 at 120 K displayed a steep rise in the low-relative-pressure region, indicative of typical physisorption by a microporous compound.

We performed the photoirradiation of CID-N_3 and dried CID-N_3 and tried to observe triplet nitrene species in the frameworks by *in situ* measurements through IR, ESR, and single-crystal X-ray diffraction. The results of the IR and ESR measurements of CID-N_3 and dried CID-N_3 show characteristic signals of triplet nitrene, which ensure the formation of triplet nitrene in CID-N_3 and dried CID-N_3 by photoirradiation. Further clear evidence of the photochemical generation of nitrene species was obtained from crystallographic experiments with he synchrotron X-ray at beamline **BL02B1**. We photoirradiated a single crystal of CID-N_3 for 40 min in vacuum at 77 K and observed a clear change in its diffraction image, which was attributed to a crystal transformation in a space group in a part of the single crystal from *P*2/*n* to *C*2/*m*. The conversion of azide

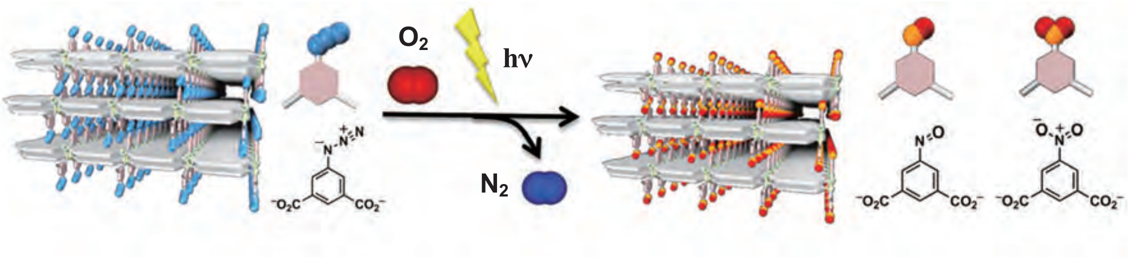

Fig. 1. Schematic representation of concept shown in this work. A new PCP composed of N_3-ipa (left panel) is converted to NO_2-ipa- or NO-ipa based PCPs (right panel) by photoirradiation in O_2 atmosphere. N_2 is released during the conversion process.

moieties was estimated to be 31% in the transformed structure from structural analysis. The above-mentioned direct observation indicated that the triplet nitrene anchored on the pore surface was well isolated and sufficiently stable kinetically.

On the basis of the photochemical generation of the highly reactive nitrenes on the pore surface, we sought to demonstrate the usefulness of our porous crystalline material for the on-demand photoactivation of the pore surface. We found that 1) the chemical transformation of adsorbed guest molecules by photoirradiation and 2) the photoinduced adsorption of guest molecules are possible.

We carried out the photoirradiation of dried CID-N_3 in an O_2 atmosphere (80 kPa) at 120 K for 10 h. We confirmed that the photochemical products from dried CID-N_3 were nitro-(NO_2-ipa) and nitroso-(NO-ipa) isophthalic acids by ^{1}H-NMR. It is worth noting that triplet nitrene is well known to react with oxygen to give a nitro compound, but few reports on the formation of a nitroso compound by the reaction of nitrene and oxygen have been published. These results clearly show that the porous structure is essential so that the photonically generated nitrene can specifically react with oxygen to give NO_2-ipa and NO-ipa in the solid state. We demonstrated that the *in situ* photoirradiation of dried CID-N_3 remarkably impacts on its sorption property (Fig. 2). As previously mentioned, the original dried CID-N_3 shows an almost non-porous behavior for O_2 at 77 K. However, by *in situ* photoirradiation, the adsorbed amount of O_2 significantly increases in the low-pressure region. An adsorption isotherm of O_2 for the completely converted dried CID-N_3 is obtained considering the photochemical conversion (15%) estimated from the ^{1}H-NMR spectrum of the photoirradiated sample. According to the isotherm, the photochemically activated dried CID-N_3 can adsorb 29 times as much O_2 at 0.2 kPa compared with the original dried CID-N_3, indicating that photoirradiation achieves a significant enhancement in the adsorption ability of CID-N_3.

Our photoactivation method can be utilized for a wide range of photoreactive species incorporated in PCPs and can be a general strategy to produce PCPs with reactive open-shell atom (ROSA) sites such as radicals and carbenes, which cannot be realized under conventional synthetic conditions. Furthermore, regularly aligned electron deficient species in nanospace are of potential use in selective adsorption for nucleophilic molecules and various topologically controlled chemical reactions. These results will open up a new dimension of porous compounds as platforms for various surface conversions and selective guest trapping.

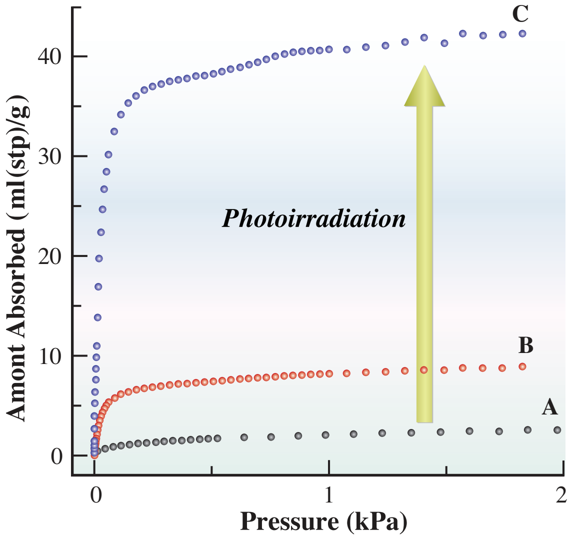

Fig. 2. *In situ* photoactivation of CID-N_3 with adsorption of oxygen. Adsorption isotherms of O_2 at 77 K on dried CID-N_3 without **(A)** and under **(B)** photoirradiation, and completely activated CID-N_3 **(C)**. The photochemical conversion (15%) after the adsorption measurement (isotherm **b**) was estimated from the ^{1}H-NMR spectrum of the photoactivated sample. The isotherm for completely activated CID-N_3 **(C)** was obtained from the isotherms (**A** and **B**) considering the photochemical conversion (15%).

Ryotaro Matsuda[a,b,c,*], Hiroshi Sato[a,b] and
Susumu Kitagawa[a,b,c]

[a] Exploratory Research for Advanced Technology (ERATO), Japan Science and Technology Agency (JST)
[b] Institute for Integrated Cell-Material Sciences, Kyoto University
[c] SPring-8 / RIKEN

*E-mail: ryotaro.matsuda@kip.jst.go.jp

References

[1] R. Matsuda *et al.*: Nature **436** (2005) 238.
[2] S. Shimomura *et al.*: Nat. Chem. **2** (2010) 633.
[3] *H. Sato, R. Matsuda, K. Sugimoto, M. Takata, S. Kitagawa: Nat. Mater.* ***9*** *(2010) 661.*
[4] S. Kitagawa *et al.*: Coord. Chem. Rev. **251** (2007) 2490.

How do phase-change materials crystallize so fast?

In phase-change (PC) materials, a laser-induced rapid transformation to the crystalline phase can occur within tens of nanoseconds, and their amorphous phases are stable at room temperature (RT) for several decades. Until today, two classes of materials, namely, GeTe–Sb_2Te_3 pseudobinary compounds (group 1 in Fig. 1(a)) and Sb–Te binary compounds with small amounts of In, Ag and/or Ge (group 2 in Fig. 1(a)) have been practically completed and used extensively in rewritable high-density optical disks such as DVDs and Blu-ray Discs^{TM}. Furthermore, non-volatile electric solid-state memory called PC-RAM (random access memory) has also been launched in the market in recent years [1]. However, the accurate PC mechanism has remained the subject of speculations despite their brilliant commercial successes. For example, it is well-known that crystallization processes are strikingly different between the two groups of materials, as shown in Fig. 1(b). Nevertheless, the origin of the difference has not been systematically explained at the atomistic level, yet. Since crystallization is the rate-limiting process in all PC devices, an atomistic understanding of the difference is essentially important for obtaining next-generation PC alloys.

Such a delay in understanding the mechanism is caused by the lack of structure information of amorphous materials. To solve the situation, our research group has constructed an “X-ray pinpoint structural measurement system” at SPring-8 that enabled us to perform real-time and high-quality observation of nanoscaled structure change from the amorphous phase to the crystalline phase [2]. Using the system, we found that the crystallization processes were very different on the nanosecond order at the atomistic level between GST and AIST, and succeeded in finding NaCl-like fragments as nuclei in amorphous $Ge_2Sb_2Te_5$ [3]. Furthermore, we proposed an effective method of analyzing the structure of amorphous materials. We combined density functional (DF)-molecular dynamics (MD) and reverse Monte Carlo (RMC) simulations for amorphous GST (a-GST) and successfully reproduced using the obtained simulation the experimental data of X-ray diffraction (XRD) and hard X-ray photoelectron spectroscopy (HXPS) [4].

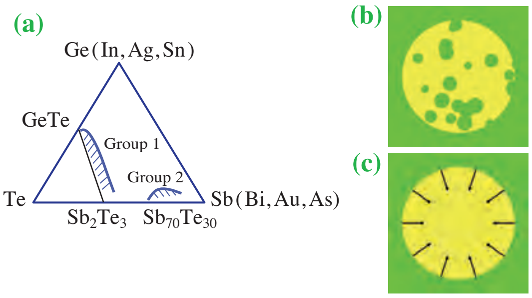

Fig. 1. Phase diagram of typical PC materials and crystallization patterns. **(a)** The most commonly used materials for optical recording are groups 1 and 2. **(b)** Nucleation-dominated recrystallization (as in GST). **(c)** Growth-dominated recrystallization (AIST).

In the present study, we applied several techniques (XRD experiment, HXPS and extended X-ray absorption fine structure (EXAFS) combined with DF-MD simulations) to determine the amorphous and crystalline structures of the AIST alloy $Ag_{3.5}In_{3.8}Sb_{75.0}Te_{17.7}$ (AIST). Consequently, we found distinct differences between the structures of GST (group 1) and AIST (group 2), which have wider implications. The experiments were carried out at beamlines **BL04B2**, **BL14B2**, and **BL47XU**.

Figure 2 shows the XRD data for AIST (Fig. 2(a)) together with that for GST (Fig. 2(b)), and their atomistic configurations obtained by DF-RMC simulation. These results show that the calculated structure finely agrees with experimental results including XRD data and HXPS measurements of the electronic structure (not shown here). The structural difference between a-AIST and a-GST is clearly visible in Figs. 2(c) and 2(d) [5]. Amorphous AIST has a highly random network structure whose ring statistics range widely, whereas a-GST has many small rings with ‘AB alternation’ (A=Ge or Sb; B=Te) that act as nuclei in the (nucleation-driven) crystallization process involving large fraction of cavities.

Then, a rough image of a-AIST is obtained. The next step is analyzing the detailed local structure. It is natural that an understanding of the rapid crystallization mechanism will be gained by comparing the bonding and atomic distributions in a-AIST and c-AIST. The principal information obtained through this study is as follows: (i) Crystalline AIST (c-AIST) has short (2.93 Å) and long (3.30 Å) bonds, while a-AIST has the shortest bond of 2.86 Å with a shoulder at 3.5 Å. (ii) The bond angle distribution in a-AIST is very similar to that in c-AIST; the maximum bond angle for short bonds (<3.1 Å) of a-AIST is 95 degrees as in c-AIST as though the distribution range of a-AIST is wider than that of c-AIST. (iii) The chemical coordination numbers N_{bond} of Ag , Sb and Te in a-AIST are almost the same as those in c-AIST; for instance, the N_{bond} values for Sb are 3.1 in a-AIST and 3.2 in c-AIST. (iv) The profiles of the bond order (the number of chemical bonds between two atoms) are very similar in both phases for each kind of bond and

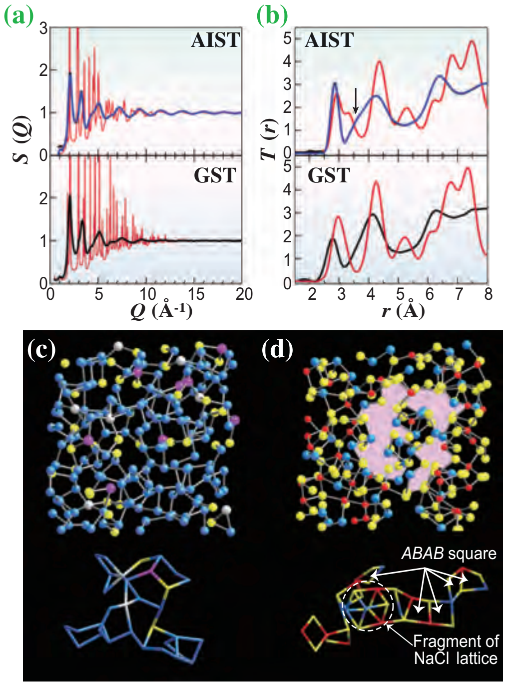

Fig. 2. HXRD data for AIST and GST, and atomic configurations of a-AIST and a-GST. **(a, b)** Structure factors *S(Q)* and total correlation functions *T(r)* of AIST and GST (Ref. 4). Red line, experimental data of crystalline phase; black line, experimental data of amorphous phase; blue line, DF-RMC model of a-AIST. The DF-RMC and experimental results are practically indistinguishable. **(c)** Section of 640-atom DF-MD model of a-AIST (24 Å_24Å_12 Å). Ag, silver; In, magenta; Sb, blue; Te, yellow. **(d)** Section of 460-atom DF-MD model of a-GST (24 Å_24Å_12 Å). Ge, red; Sb, blue; Te, yellow; large cavity, pink.

the value is less than unity everywhere, showing that both phases are not perfectly covalent. (v) The main peak of the bond-order profile in c-AIST is located at 0.67 and that in a-AIST is located at 0.75, suggesting that a-AIST is more covalent than c-AIST.

With this information, we reached an understanding of the local environment around Sb atoms (main component) and drew a picture of the rapid crystallization process of a-AIST.

As shown in Fig. 3, both a-AIST (upper left in Fig. 3) and c-AIST (upper right in Fig. 3) resemble a distorted 3+3 octahedron. The bonds in a-AIST are slightly shorter (stronger) than those in c-AIST, with enhanced insulating or semiconducting features; however, c-AIST has a Jahn-Teller distorted octahedral structure (nearly simple cubic) and more metallic features. When the bond electrons in a-AIST are excited by laser light or electric stimulation, the center atom with three short (red) and three long (dashed) bonds slightly moves and eventually changes its position to the center of the octahedron with a bond interchange between short (strong) and long (weak) bonds. The resultant resonant bonding produced between periodic short and long bonds leads to a crystalline A7 network. This is just the beginning of the rapid PC in group 2, including AIST. Each vector in the lower figures defines the direction of the corresponding distorted octahedron. In the recording marks of a-AIST, the direction of the vector is random (lower left in Fig. 3), and laser irradiation or electric heating can lead to a sequence of small atomic shifts that align the vectors along the c-axes of crystalline (A7, hexagonal) cells in the rim; therefore, the entire amorphous mark assume the A7 structure (lower right in Fig. 3). This is the origin of the 'growth-dominated' crystallization in group 2. In contrast, there are many fragments of the NaCl lattice in a-GST as previously reported, and crystallization starts simultaneously from many such nuclei in the amorphous mark ('nucleation-dominated' crystallization).

It cannot be denied that our model has some speculations. We hope to clarify more details of its mechanism through our future works and to create novel PC materials suitable for the ultrahigh-density storage media in the near future.

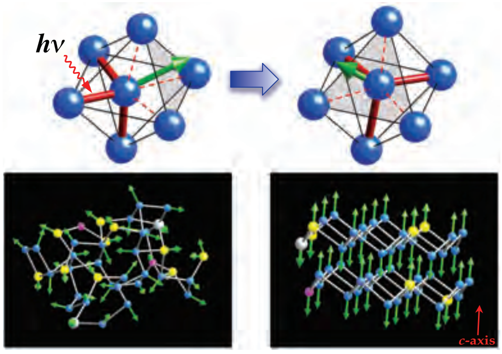

Fig. 3. PC mechanism of a-AIST.

Noboru Yamada[a,d,*], Toshiyuki Matsunaga[b,d] and Masaki Takata[c,d]

[a] Digital Network Technology Development Center, Panasonic Corporation
[b] Materials Science and Analysis Technology Center, Panasonic Corporation
[c] SPring-8 / RIKEN·JASRI
[d] CREST

* E-mail: yamada.noboru@jp.panasopnic.com

References

[1] M. Wuttig and N. Yamada: Nature Mater. **6** (207) 824.
[2] S. Kohara *et al.*: Appl. Phys. Lett. **89** (2006) 201910.
[3] Y. Fukuyama *et al.*: Appl. Phys. Exp. **1** (2008) 045001.
[4] J. Akola *et al.*: Phys. Rev. B **80** (2009) 020201.
[5] *T. Matsunaga, J. Akola, S. Kohara, T. Honma, K. Kobayashi, E. Ikenaga, R.O. Jones, N. Yamada, M. Takata and R. Kojima: Nature Mater.* ***10*** *(2011)129.*

Formation of nano-oriented crystals of iPP with ultrahigh performance crystallized by extreme melt elongation

String- or chain-like molecules can form complex structures; they perform multiple functions and can carry information. As we can see with most natural materials such as DNA and proteins, many sophisticated materials have developed over several billion years. However, in the case of polymers, it is impossible to obtain ideal crystals with ultimate performance of function, because “entanglements” of molecular chains suppress structure formation and the expression of function. For example, polymer chains are conventionally ordered from isotropic melts during “crystallization.” However, this ordering is difficult, since it is not easy for entangled chains to slide along their chain axes and disentangle into an ordered parallel arrangement. Therefore, amorphous areas remain in the solid. As conventional polymer solids are composed of amorphous and crystal parts, their crystallinity is much less than unity [1]. Such polymer solids show poor performance, as the amorphous portion takes the structure of a frozen melt.

Crystallization is a well-known ordering process from the melt or a gas. The structures and physical properties depend on crystallization conditions. If we could control the entanglements of polymer chains by crystallization, we would obtain a material with excellent performance and/or function.

The polymer chain in the melt or a solution changes its shape under an external field, such as elongation and shear. If we could induce significant elongation to the melt, the elongation should affect the bulky melt and the crystallization behavior and properties of polymer solids should significantly change. Hereafter, we will name the crystallization under melt elongation as “elongational (melt) crystallization.” However, the significant elongational crystallization has been difficult.

We succeeded in realizing an extreme melt elongation for the first time by developing a “compression method” [2]. Figure 1(a) shows the principle of the compression method. We compressed the supercooled melt by sandwiching it between two plates. By this method, the melt was stretched along a direction perpendicular to the compressed direction. Figure 1(b) shows a roll-type apparatus.

The purposes of this work are to show the formation of nano-oriented crystals (NOCs) with ultrahigh performance by elongational crystallization under an extreme elongational field and to clarify the structure and nucleation mechanism of NOCs.

We used isotactic polypropylene (iPP, $M_w = 34 \times 10^4$, $M_w/M_n = 30$) as a model polymer, where M_w is the weight-average molecular weight and M_w/M_n is the index of dispersion. The equilibrium melting temperature (T_m^0) in a quiescent field was 187°C [3]. The sample was melted at above T_m^0, cooled to the crystallization temperature (T_c = 150°C) and then compressed to elongate the supercooled melt into a sheet or plate. The former is one-dimensional (1D) compression-type crystallization and the latter is two-dimensional (2D) compression-type crystallization. Small/wide angle X-ray scattering (SAXS/WAXS) observation was carried out at **BL03XU** and **BL40B2**.

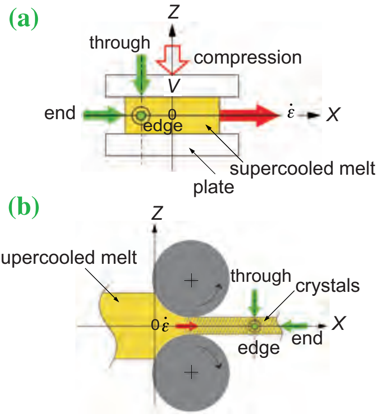

Fig. 1. Schematic illustration of principle of elongational crystallization by compression method. The *Z*-axis is along the direction of compression and the *X*-axis is parallel to the elongational direction. **(a)** Compression-type apparatus. Both 1D and 2D compression-type crystallizations are applicable. **(b)** Roll-type apparatus. It is 1D compression-type crystallization.

Figures 2(a) and 2(c) and 2(b) and 2(d) show typical SAXS and WAXS patterns for small and large elongational strain rates ($\dot{\varepsilon}$), respectively. Figures 2(a) and 2(c) for small $\dot{\varepsilon}$ mainly showed well-known unoriented long-period patterns (L1 and L2) and a

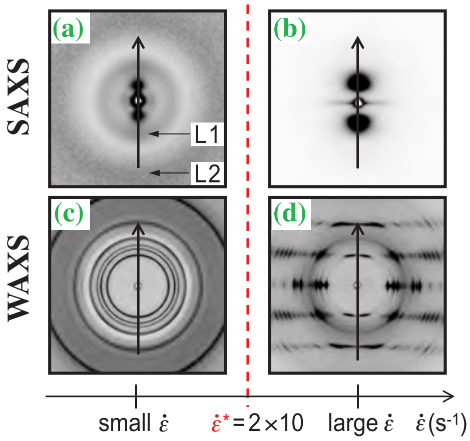

Fig. 2. $\dot{\varepsilon}$ dependence of scattering patterns for through-view. Samples were crystallized by 1D compression. Meridian arrows show the elongational direction. **(a)** SAXS pattern of small $\dot{\varepsilon}$. **(b)** WAXS pattern of small $\dot{\varepsilon}$. **(c)** SAXS pattern of large $\dot{\varepsilon}$. **(d)** WAXS pattern of large $\dot{\varepsilon}$.

Debye-Scherrer ring pattern, respectively. Therefore, the dominant structure was the conventional stacked lamellar structure. Figures 2(b) and 2(d) for large $\dot{\varepsilon}$ showed an oriented two-point pattern and a highly oriented fiber pattern along the melt-elongational direction, respectively. Since the NOCs showed a high crystallinity of about unity, the oriented two-point pattern means that the crystals are randomly oriented, such as 1D paracrystals or a 1D liquid-like packing of particles [4]. From the structural analysis of the SAXS and WAXS patterns, the structure model of the NOCs was obtained (Fig. 3(b)). Nanocrystals with sizes of 20-30 nm were linked and oriented along the elongational direction. Stems were also oriented along the elongational direction. Thus, the scattering pattern discontinuously changed at a critical $\dot{\varepsilon}$ ($\dot{\varepsilon}^*$).

$\dot{\varepsilon}^* = 2\times10^2$ s^{-1} was obtained from the NOC fraction f(NOCs) within the crystalline volume. Figure 4 shows f(NOCs) agains $\dot{\varepsilon}$, which was obtained by analyzing WAXS intensity. The basic viewpoint of this analysis is as follows: As the WAXS patterns of the NOCs and unoriented crystals show typical fiber and Debye-Scherrer patterns, respectively, these regions are well-known in the X-ray scattering theory [5]. When the NOCs and unoriented crystals are mixed, the scattering intensity (I_X) from the (hkl) reflection of NOCs can be estimated by subtracting the I_X of unoriented crystals from the observed I_X. With an increase in $\dot{\varepsilon}$, f(NOCs) increases slightly, then significantly at $\dot{\varepsilon} \cong 10^2$ s^{-1}, and finally saturates. We defined $\dot{\varepsilon}^*$ as $\dot{\varepsilon}$, where f(NOCs) becomes 0.6.

Figure 3 shows a schematic illustration of the nucleation mechanism and the structure model of the NOCs. Figure 3(a) is illustrated by focusing on one random coil of one polymer chain within the bulky melt. Polymer chains should be elongated along the elongational direction when the melt is compressed with a large $\dot{\varepsilon}$. Many parallel packings of chains would be generated, and an infinite number of nuclei would be formed. Then, they grow instantaneously into nanocrystals before the melt structure randomizes by entropic relaxation. During the growth, entanglements should be condensed to the interface between the nanocrystals (Fig. 3(b)). One chain should three-dimensionally interpenetrate and connect the nanocrystals more than 10^2 times, as the mean extended length of one polymer chain is about 2 μm. This model was called the "YOROI" model, as its structure is similar to the armor of samurai in ancient Japan.

The NOCs showed an ultrahigh performance: the tensile strength at break was about 2.3×10^2 MPa, which was comparable to that of metals, Young's modulus was 4.1 GPa. The thermal resistance was 176°C. The origin of these performance characteristics of the NOCs can be explained by the YOROI model. NOCs will be useful in a wide variety of applications and will contribute to the effort to construct a sustainable society by enabling the development of lightweight devices.

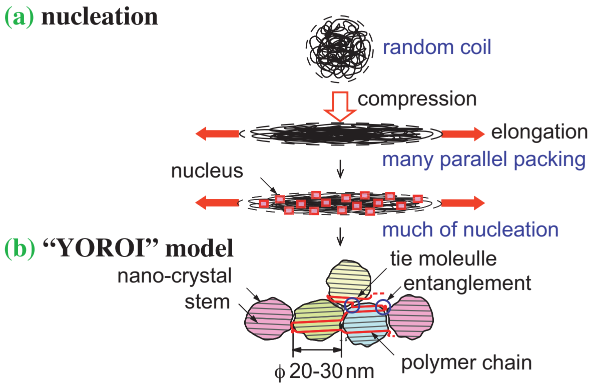

Fig. 3. Schematic illustration of crystallization of NOCs. **(a)** Nucleation mechanism of NOCs. **(b)** YOROI model of the NOC structure.

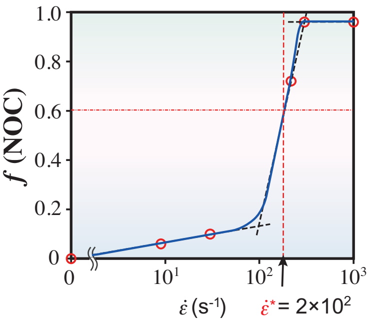

Fig. 4. f(NOCs) against $\dot{\varepsilon}$ including 1D and 2D compression-type crystallizations.

Kiyoka N. Okada and Masamichi Hikosaka*

Graduate School of Integrated Arts and Sciences,
Hiroshima University

*E-mail: hikosaka@hiroshima-u.ac.jp

References

[1] E.P. Moore: Polypropylene handbook Ch.3 (Kogyo Chosakai, Tokyo, 1998).
[2] *K.N. Okada, J. Washiyama, K. Watanabe, S. Sasaki, H. Masunaga and M. Hikosaka: Polymer J.* ***42*** *(2010) 464.*
[3] K. Yamada *et al.*: J. Macromol. Sci. Phys. B **42** (2003) 733.
[4] A. Guinier: Theorie et technique de la radiocristallographie Ch.10-11 (Dunod, Paris, 1964).
[5] I. Nitta: X-sen kessyougaku, the first volume 117-121 (Maruzen, Tokyo, 1959). (in Japanese)

Dual energy *K*-edge subtraction imaging of 3D inhomogeneous microstructure in highly alloyed aluminium foam

X-ray computed tomography (CT) gives unique chemical information within bulk materials in 3D/4D (i.e., 3D+time axis). In the case of pure binary systems in which two constituent atoms are relatively apart in atomic number, X-ray CT can provide chemical concentration distributions quantitatively. However, since the X-ray mass absorption coefficient is obtained simply from the sum of the absorption cross sections of constituent atoms, the quantitative measurement does not apply to ternary or more complex systems such as practical alloys.

K-edge subtraction imaging technique was originally developed for the diagnosis of neurovascular pathology with an iodine-containing contrast agent and later extended to lung imaging with an inhaled contrast agent containing xenon gas. After a couple of monochromatic images are acquired above and below the X-ray *K*-edge energy, logarithmically subtracting the two images enables the enhancement of the contrast of any structure containing a contrast agent. This technique was further extended by Ikeda *et al*. [1] to realize quantitative analysis in 3D Cs concentration demonstrations for partially molten granite.

In this work, dual energy *K*-edge subtraction imaging was performed to quantify the Zn distribution in Al-Zn-Mg foam. This foam, which is designed for ultra-lightweight energy absorption structures, is a newly developed metallic foam with a closed-cell structure. The fracture behavior of the cell wall has also been identified three-dimensionally, providing new insights into the damage evolution of metallic foams.

High-resolution X-ray tomography was performed at beamline **BL20XU**. A liquid nitrogen-cooled Si (111) double-crystal monochromator was used to produce monochromatic X-ray beams. Dual energies, 9.71 keV and 9.61 keV (above and below the *K* absorption edge of Zn, respectively), were chosen for subtraction imaging. The combination of the CCD detector (4000×2624 pixels, 2×2 binning mode, 5.9×5.9 μm^2 pixel size) and the optical lens (×20) provided an isotropic voxel with a 0.474 μm edge.

The 3D quantification of Zn concentration was obtained from the subtraction of the CT images corresponding to 9.71 keV and 9.61 keV. It is described as [2]:

$$g_{Zn} = \frac{\Delta\mu}{\Delta\mu_{Zn(above)} - \Delta\mu_{Zn(below)}} \times \frac{\rho_{Zn}}{\rho}$$

where g_{Zn} is the weight fraction of Zn, $\Delta\mu$ is the difference in linear absorption coefficient (LAC) between the two energies, ρ and ρ_{Zn} are the densities of bulk alloy and Zn, $\mu_{Zn(9.71)}$ and $\mu_{Zn(9.61)}$ are the LACs of Zn at 9.71 keV and 9.61 keV, respectively. The correction of LAC is necessary to ensure the accuracy of the LAC measurement [3]. It has been confirmed that when the same setup is used, the detection limit for Cu in Al alloys is similar to the EDS results in scanning electron microscopy (i.e., about 0.5 mass%), and a superior reproducibility of ±0.1 mass% is obtained [4].

Figures 1(a) and 1(b) show the reconstructed 3D image of a single cell wall and its 3D Zn distribution with a concentration map, as seen on the outside

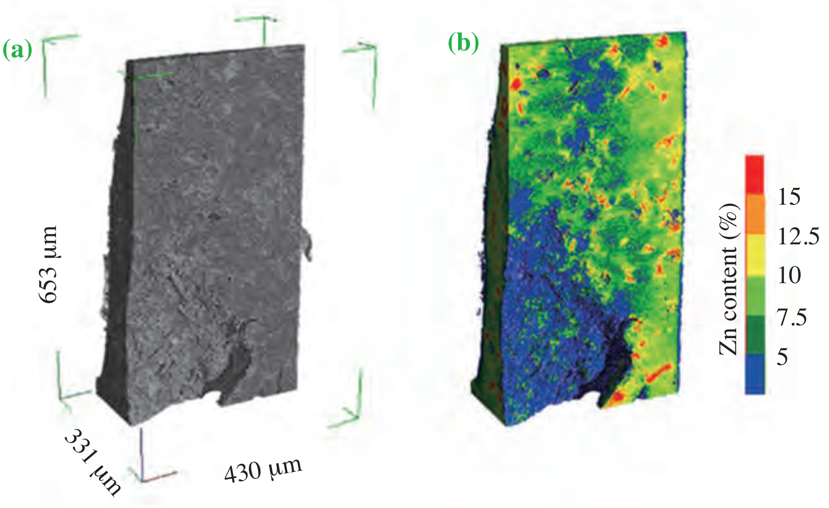

Fig. 1. 3D image of cell wall **(a)** and corresponding Zn distribution with concentration map on outside surface of cell wall **(b)**. [2]

surface of the cell wall. The quantitative visualization of Zn content is based on the $\Delta\mu$ information from two sets of CT image taken at 9.71 keV and 9.61 keV, respectively. A quite inhomogeneous distribution of Zn is found throughout the cell wall, which was cut from as-cast foam. The red regions indicate a higher Zn concentration, corresponding to Zn-bearing particles. The remaining aluminum matrix regions exhibit a wide variation in Zn concentration. The agglomeration of Zn-bearing particles would affect the fracture behavior of the cell wall.

In situ compressive tests of the cell walls were performed and 3D visualization was carried out to determine the fracture response and identify the interaction between fracture paths and Zn distributions or micropores. Figure 2 shows one representative crack path. In the 2D slice image in Fig. 2(a), some white areas and micropores are observed. In Fig. 2(b) showing the reconstructed Zn mapping by *K*-edge subtraction method, those white areas are proven to be highly concentrated Zn regions that are distributed non-uniformly in the foam. Particularly in the center part, the Zn-bearing particles agglomerate along a line. A crack is also observed in this region, and the fracture path is along the agglomerated Zn-bearing particles, which probably acted as sites for stress concentration, indicating an adverse effect of agglomerated particles on crack resistance. A 3D image of the crack's interaction with the Zn-bearing areas and micropores is shown in Fig. 2(c). The propagation of the crack along the particle agglomeration areas is visualized three-dimensionally. The crack approaches a coarse micropore at the crack tip, then the acceleration of crack propagation can be anticipated in this local area as a result of the anti-shielding effect. Our previous work [5] has shown that the brittle cracking of a cell wall is usually followed by the rapid collapse of the cell wall in the Al-Zn-Mg foam. The combination of local agglomerated particles and micropores is confirmed to exert an adverse effect on intrinsic crack propagation.

In summary, a highly heterogeneous distribution of Zn in the cell wall of Al-Zn-Mg foam was illustrated in 3D using dual energy *K*-edge subtraction technique. It has been clarified that the combination of local agglomerated Zn-bearing particles and micropores exerts an adverse effect on intrinsic crack propagation. The current element sensitive tomography has been proved to be an effective technique for determining the microstructure and property relationship of highly inhomogeneous foam materials in 3D.

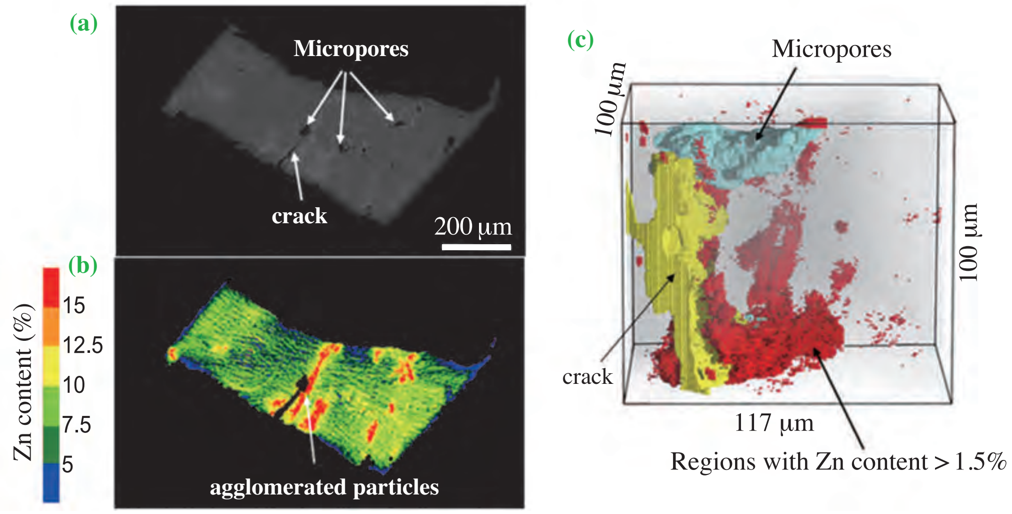

Fig. 2. Representative crack path through region of agglomeration of Zn-bearing particles and micropores: slice image taken at 9.61 keV **(a)**, Zn mapping **(b)** and 3D image **(c)**. [2]

Qiang Zhang[a,*] and Hiroyuki Toda[b]

[a] School of Materials Science and Engineering,
Harbin Institute of Technology, China
[b] Dept. of Mech. Eng., Toyohashi University of Technology

*E-mail: zhang_tsiang@hotmail.com

References

[1] S. Ikeda *et al*.: Am. Mineral. **89** (2004) 1304.
[2] *Q. Zhang, H. Toda, Y. Takami, Y. Suzuki, K. Uesugi, M. Kobayashi: Phil. Mag.* ***90*** *(2010) 1853.*
[3] H. Toda *et al*.: Mater. Trans. **51** (2010) 2045.
[4] H. Toda *et al*.: Acta Mater. **58** (2010) 2014.
[5] T. Ohgaki *et al*.: Phil. Mag. **86** (2006) 4417.

Three-dimensional electron density mapping of shape-controlled nanoparticle by focused hard X-ray diffraction microscopy

Metal nanostructures have been extensively studied for many decades because of their various applications. In general, the intrinsic properties of metal nanostructures can be tuned by controlling the shape as well as the structure of the nanostructures. Recently, extensive effort has been devoted to the synthesis of more complex structures, such as core-shell or hollow nanoparticles, because of their increased surface area, reduced densities, and localized surface plasmon resonance [1]. Determining the three-dimensional (3D) nano-mesoscopic structures is indispensable for a complete understanding of the structure-property relationship that guides the design and synthesis of nanomaterials with well-controlled sizes and shapes for specific applications.

X-ray diffraction microscopy is a lensless microscopy technique first demonstrated by Miao *et al.* in 1999 [2]. An object is illuminated with coherent X-ray beams and far-field diffraction data are collected by area detectors. Phase retrieval calculation is performed to reconstruct a 2D or 3D image. A number of applications of X-ray diffraction microscopy have emerged in biological and materials sciences. In principle, the spatial resolution of such diffraction microscopy is limited only by the wavelength of the incident beam. However, the spatial resolution achieved in experiments is effectively limited by the strong decay of the diffraction intensity with increasing scattering vector, and hence, high-flux-density coherent X-rays are crucial to improve the resolution. Recently, the spatial resolution has reached the sub-10-nm scale in two dimensions using focused high-density hard X-rays [3-5]. In addition, focusing technologies for diffraction microscopy are also necessary to realize single-shot imaging using X-ray free electron lasers in the near future. In the present study [6], we first demonstrated 3D hard X-ray diffraction microscopy with a sub-10-nm scale resolution and revealed the 3D nano-mesoscopic structures of a shape-controlled Au/Ag nanobox.

Ag nanocubes with an edge length of ~150 nm were prepared by a modified polyol synthesis technique. The nanocubes are single crystals with a face-centered-cubic structure. Then, the Ag nanocubes were titrated with an aqueous solution of $AuCl_4^-$. Au/Ag nanoboxes were formed by the galvanic replacement reaction between Ag and $AuCl_4^-$. The Au/Ag nanoboxes and Ag nanocubes used as reference samples were mounted on 100-nm-thick SiN membranes.

The coherent X-ray diffraction experiments were carried out at beamline **BL29XUL**. Figure 1 shows a schematic drawing of the apparatus used. The X-ray energy was tuned to 11.8 keV with an undulator gap and a Si (111) double-crystal monochromator. The X-ray beam was two-dimensionally focused to a spot of ~1 μm size by Kirkpatrick-Baez (KB) mirrors. An isolated Ag nanocube or Au/Ag nanobox was placed at the focus in each measurement and illuminated with the focused X-ray beam. Since the nanoparticles are much smaller than the focal spot size, the illuminated X-ray beam is considered to be an X-ray plane wave. The diffracted X-ray photons were detected by an in-vacuum front-illuminated charge-coupled device

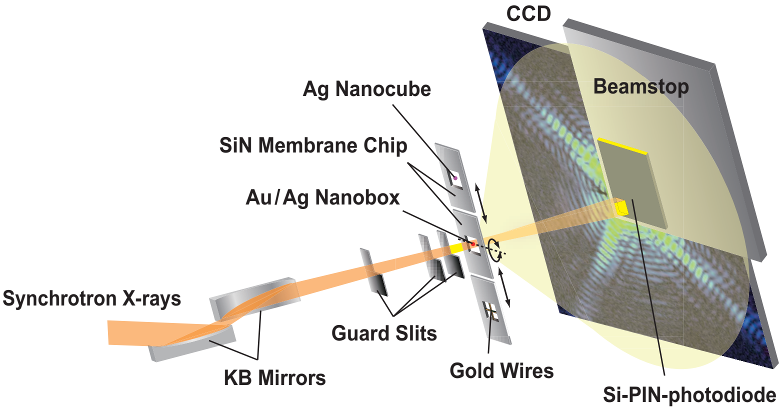

Fig. 1. Schematic view of coherent hard X-ray diffraction measurements of Ag nanocube and Au/Ag nanobox. KB mirrors were placed in air ~100 m downstream of the light source. X-rays with a beam size of 100 μm in both directions illuminated the first mirror. The X-ray beam was 2D focused in a vacuum chamber 445 mm downstream of the second mirror. The focal profile was measured by the wire scanning method using gold wires of 200 μm diameter. To interrupt parasitic scattering X-rays from the mirrors, three guard slits were placed between the mirrors and the focus. An isolated Ag nanocube or Au/Ag nanobox was placed at the focus in each measurement. Forward-diffracted X-ray photons were detected by the CCD detector with a pixel size of $20 \times 20\ \mu m^2$ placed 996 mm downstream of the sample. A direct X-ray beamstop was placed in front of the CCD detector. The intensity of the penetrating X-ray beams was monitored using a Si-PIN photodiode, which was assembled on the beamstop, during the measurement of diffraction intensity. The SiN membrane chip, supporting Au/Ag nanoboxes, was rotated for 3D diffraction microscopy.

(CCD) detector. In the data analysis, we used 1251×1251 pixel data, which provided a reconstructed image with a single pixel (or a voxel) size of 4.2 nm in each dimension. Diffraction data were collected at different incident angles ranging from −75° to +72.5° at intervals of 2.5° for the Au/Ag nanobox and of 0° for the Ag nanocube. The X-ray exposure times ranged between 250 s and 1650 s at each incident angle.

The reconstruction of a 3D image was performed by the hybrid input-output method with the Shrinkwrap algorithm. Using the intensities of the reconstructed image of the Ag nanocube used as the reference sample, the flux density at the focus was estimated to be 3.4×10^3 photons/nm^2/s. The image intensity of the Au/Ag nanobox is converted to electron units using the flux density. The maximum number of electrons per voxel in the 3D reconstruction was 3.4×10^5, which was in good agreement with the 3.5×10^5 electrons per $4.2 \times 4.2 \times 4.2$ nm^3, corresponding to the voxel size, calculated using the density of the gold crystal with the face-centered-cubic structure, atomic number, and Avogadro's number. Figure 2(a) shows the isosurface rendering of the reconstructed 3D image. The distinctive features of the nanobox are small pits indicated by blue arrows and a depression indicated by a green arrow. The other faces are relatively flat. In previous works, a pinhole was observed on one of the six faces of each cube in the initial stage of reaction, indicating that the reaction was initiated locally at a high-energy site rather than over the entire cube surface. It is possible that the pits on the surface are related to the reaction in the initial stage.

To quantitatively visualize the 3D internal structure, we produced cross-sectional images in the *A*-, *B*-, and *C*-planes parallel to the *xy*-plane. Figure 2(b) shows the cross-sectional images in the *A*-, *B*-, and *C*-planes indicated in Fig. 2(a), which are shown in electron units. The hollow interior is clearly visible in each image. In the *B*-plane crossing the center of the nanobox, the interior space is larger and the wall is thinner than those in the *A*- and *C*-planes. This indicates that the progression rate of the replacement reaction between Ag and $HAuCl_4$ differs depending on the site. The maximum value of the color bar is 3.4×10^5 electrons. We can roughly identify Au-rich and Au-poor regions in each slice. Areas from yellow to white are Au-rich regions, where more than 50% Ag atoms are replaced with Au atoms. The interesting feature observed is that the Au-rich region exists close to the edges. This suggests that dealloying and morphological reconstruction start from the edges of the nanobox. The spatial resolution of the present 3D diffraction microscope was estimated to be 10 nm or higher from the thinnest wall in the *B*-plane, which is the highest resolution achieved in 3D hard X-ray diffraction microscopy. In the near future, ultimate X-ray diffraction microscopy will be realized, which is high-resolution imaging on a short time scale for studying structural dynamics, which will be realized using focused hard X-ray free electron lasers.

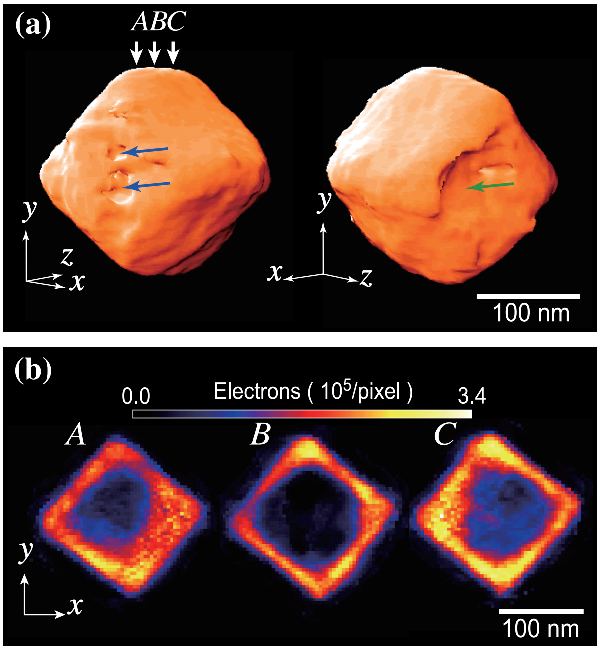

Fig. 2. **(a)** Isosurface rendering of reconstructed 3D Au/Ag nanobox observed from two directions, which was drawn with a threshold value of 20% of the highest electron density. The small pits and the depression on the surface of the nanobox are clearly visible, which are indicated by blue and green arrows, respectively. **(b)** Cross-sectional images of a 3D reconstruction of a Au/Ag nanobox. Each image is a cross-sectional image in the *A*-, *B*-, and *C*-planes parallel to the *xy*-planes shown in (a). The distance between two adjacent planes is 33.6 nm. The thickness of each slice is 4.2 nm, corresponding to voxel size.

Yukio Takahashi[a,*] and Nobuyuki Zettsu[b]

[a] Graduate School of Engineering, Osaka University
[b] Graduate School of Engineering, Nagoya University

*E-mail: takahashi@prec.eng.osaka-u.ac.jp

References

[1] Y. Xia and N. J. Halas: MRS Bulletin **30** (2005) 338.
[2] J. Miao *et al.*: Nature **400** (1999) 342.
[3] Y. Takahashi *et al.*: J. Appl. Phys. **105** (2009) 083106.
[4] Y. Takahashi *et al.*: Phys. Rev. B **80** (2009) 054103.
[5] Y. Takahashi *et al.*: Phys. Rev. B **82** (2010) 214102.
[6] *Y. Takahashi, N. Zettsu, Y. Nishino, R. Tsutsumi, E. Matsubara, T. Ishikawa and K. Yamauchi: Nano Letters **10** (2010) 1922.*

MATERIALS SCIENCE:

Spectroscopic studies in SPring-8 cover one of the most progressing research fields in materials science for the investigating of electronic and magnetic properties. Because relatively high energy photons with a high energy resolution are used for spectroscopy works, intrinsic bulk and buried interface properties are precisely investigated in these works. Hard-X-ray photoemission spectroscopy (at BL15XU, 29XU, 46XU and 47XU), so-called HAXPES, provides accurate bulk and interface information of materials. The report by Nagata and coworkers at BL15XU shows the results of a HAXPES study with bias voltage applied to the Pt/HfO_2/Pt interface. This extends the field for investigating realistic devices under operating conditions. Tanaka and coworkers presented the mechanism of the tunable metal-insulator transition of VO_2 by HAXPES.

The activities of angle-resolved photoelectron spectroscopy in the soft-X-ray regime at SPring-8 (BL17SU, BL23SU and BL25SU) are also leading the field in materials science for the investigating of electronic structures, which give us bulk-sensitive information of band structures. Not only bulk-sensitive measurements, but also thin film studies have been performed. The spin-spiral nature of ultrathin Fe/Cu(001) films was investigated by Miyawaki *et al*. at BL17SU.

ELECTRONIC & MAGNETIC PROPERTIES

The investigation of the anisotropy of magnetic materials is very important, because the phenomenon is directly related to the exchange bias effect and perpendicular magnetization among others, which are applied in recording devices. In the present volume, several investigations concerning magnetic anisotropy are reported. Sakurai and coworkers measured the magnetic Compton profile of the Co/Pd and Co/Pt multilayer systems at BL08W and discussed the mechanism of perpendicular magnetization.

The anisotropic phonon state of the *c*-axis-aligned $L1_0$-FePt nanoparticles was investigated by ^{57}Fe nuclear resonant inelastic scattering at BL09XU by Tamada *et al*.

The similar $\mathrm{L1_0}$ structure was found in an iron meteorite. Photoelectron emission microscopy observation for the Widmanstättenn structures in the meteorite was performed by Kotsugi *et al*., at BL25SU and BL39XU. They found out very strong anisotropy in the interface between the bcc- and fcc-FeNi structures, which corresponds to $L1_0$- FeNi.

PEEM observation is also performed on the antiferromagnetic materials. Arai and coworkers successfully determined the spin axes of each magnetic domain of NiO at BL17SU and BL25SU. This gives us fundamental knowledge of micro-antiferromagnetic structures.

Although the other activities based on other spectroscopic methods such as very high energy resolution inelastic X-ray scattering (IXS), magnetic circular dichroism in absorption spectroscopy (XMCD), and infrared spectroscopy are not introduced in this volume, the installation and setup of new apparatus are underway. It is expected that further challenges will produce a variety of activities. These show us the frontier of materials science.

Toyohiko Kinoshita

Study of oxygen migration at Pt/HfO_2/Pt interface by bias-application hard X-ray photoelectron spectroscopy

Resistive random access memory (ReRAM) has been proposed as a new application for oxides that have potential use in future functional devices with high-k, ferroelectric, magnetic, and optical properties. An oxide sandwiched between two metal electrodes shows reversible electric-field-induced resistance switching behavior [1]. Two switching mechanisms have been proposed for this behavior. One is the filament model, which describes the generation and rupture of a metal filament with a metal such as Ag or Cu acting as a fast mobile ion in oxide. The other is that of oxygen vacancy nucleation in oxide. Although oxygen migration toward the anode has been reported by several groups, there has been no direct observation at the metal/oxide interface under bias operation. To examine the interface electronic structure of a Pt/HfO_2/Pt structure, which shows resistance switching behavior, in an operating device [2], we used hard X-ray photoelectron spectroscopy (HAXPES) under bias operation [3]. With this method, bias-induced compositional changes around the metal/oxide interface (under device operation) have been directly observable.

The measurement setup is shown in Fig. 1(a). A 10-nm-thick Pt top electrode/30-nm-thick HfO_2/Pt bottom electrode structure was deposited on a sapphire substrate by physical vapor deposition techniques [2]. A bias voltage was applied to the sample with a DC voltage current source/monitor. HAXPES at beamline **BL15XU**, for which the incident X-ray energy was 5.95 keV and the total energy resolution was 240 meV, was performed at several take-off angles (TOAs) to obtain rough depth profiles; a TOA of 20° is surface/interface-sensitive, whereas a TOA of 85° is bulk-sensitive. Our measurement probes approximately 20 nm below the surface at a TOA of 85°.

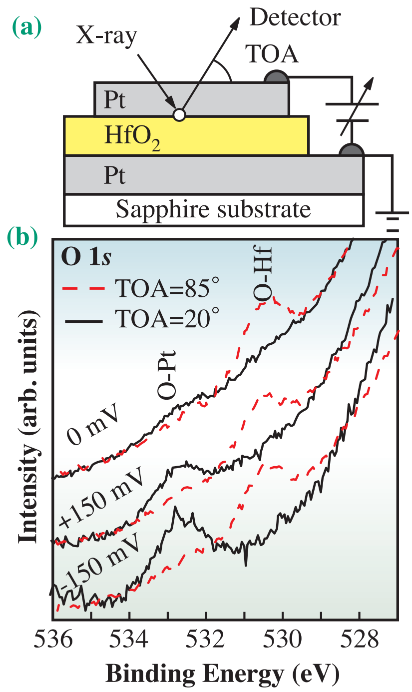

Fig. 1. **(a)** Schematic illustration of measurement setup. **(b)** HAXPES spectra of O 1*s* as a function of bias at TOAs of 20° and 85°.

For the O1*s* spectra (Fig. 1(b)), as the TOA increased, the intensity of the O-Hf peak decreased and a peak attributed to O-Pt bonding (532.8 eV) developed, indicating that there was PtO at the interface and/or surface. Note that when the thickness of the Pt layer increased, the intensities of both peaks decreased. Therefore, these states are predominantly formed at the interface. When a forward bias voltage was applied, the intensity of the O-Pt peak increased, whereas that of the O-Hf peak decreased, indicating that the Pt interface layer was oxidized and oxygen vacancies were formed in the HfO_2 layer. The O-Pt peak became more pronounced under a reverse bias than under a forward bias, suggesting that the PtO layer formed by the forward bias remained and the reverse bias formed an additional PtO layer at the interface.

In the Hf $3d_{5/2}$ spectrum, the peak at 1662.0 eV corresponds to HfO_2. Under a reverse bias, an additional peak appeared at the lower binding energy position (Fig. 2 inset) attributed to Hf-Pt bonding. The HfPt intensity showed a monotonic increase under the reverse bias, as shown in Fig. 2(a), indicating that the reverse bias drew hafnium toward the negatively biased anode and induced Hf-Pt bond formation. The Hf $3d_{5/2}$ intensity normalized by Pt $4f_{7/2}$ intensity at a TOA of 20°, which shows the variation in the Hf density at the interface, was plotted as a function of bias voltage in Fig. 2(b). With increasing forward and negative reverse biases, the intensity decreases and increases, respectively. At –150 mV, the intensity reverts to the initial intensity ratio. These results indicated that the forward and reverse biases drew hafnium toward the cathode and negatively biased anode, respectively. This suggests that the diffusion of Hf into the Pt anode produced a Pt-Hf mixed oxide and stabilized oxygen atoms in the negatively biased anode.

By using the results above, the relationship between the interface structures and the chemical states at the

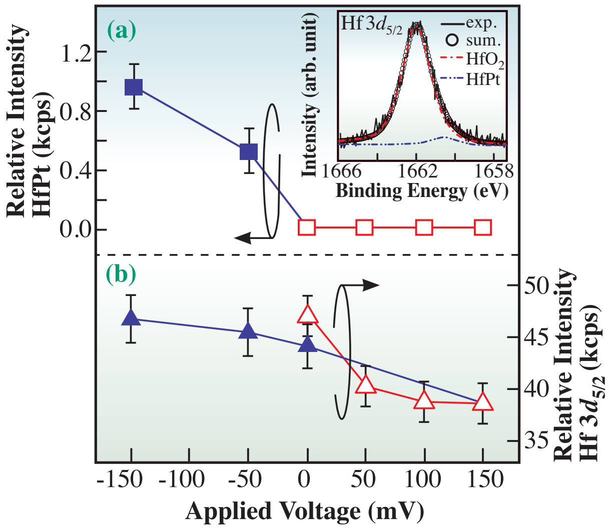

Fig. 2. Applied bias dependences of **(a)** Hf 3$d_{5/2}$ intensity ratio of HfPt (squares) and **(b)** intensity of Hf 3$d_{5/2}$ (triangles). All spectra were normalized by the Pt 4f intensity of Pt at 0 V (initial state). The inset shows HAXPES spectra of Hf 3$d_{5/2}$ at a bias of –150 mV (reverse bias) and a TOA of 20°. The solid line and open circles show the spectra and sum-fitted curve, respectively. Dashed lines are fitted curves for HfO_2 and HfPt bonds.

Pt/HfO_2/Pt interface under different biases is summarized as Fig. 3. The application of a forward bias causes oxygen to diffuse into the Pt layer, forming PtO (Fig. 3(b)). Under a reverse bias (Fig. 2(c)), the PtO layer remains at the interface, whereas hafnium moves to the interface, forming additional Pt-O and Pt-Hf bonds. Note that this oxygen vacancy formation behavior is consistent with the reported electrical properties, namely, oxygen vacancies form percolating conduction filaments during ReRAM applications. In this study, the biases were smaller than the threshold voltage at which the high resistance state changes to a low resistance state; therefore, our results did not describe the resistance-changing behavior. However, the most important implication of our results is that oxygen migration occurs at low bias voltages. The control of oxygen migration and the oxidization of the interface between metal and oxide have the potential to become key techniques for exploiting the electrical properties of metals on oxides.

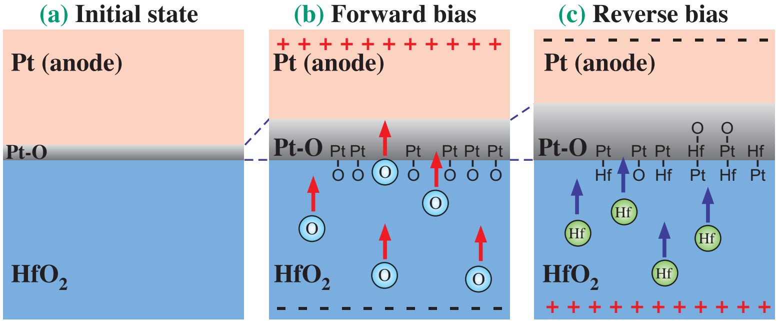

Fig. 3. Schematic illustration of Pt/HfO_2 interfaces at **(a)** initial state and under **(b)** forward and **(c)** reverse biases.

Takahiro Nagata[a,*], Yoshiyuki Yamashita[a,b] and Keisuke Kobayashi[b]

[a] Advanced Electric Materials Center,
National Institute for Materials Science
[b] NIMS Beamline Station at SPring-8,
National Institute for Materials Science

*E-mail: NAGATA.Takahiro@nims.go.jp

References

[1] M. Haemori *et al.*: Appl. Phys. Express **2** (2009) 061401.
[2] *T. Nagata, M. Haemori, Y. Yamashita, H. Yoshikawa, Y. Iwashita, K. Kobayashi and T. Chikyow: Appl. Phys. Lett.* ***97*** *(2010) 082902.*
[3] Y. Yamashita *et al.*: e-J. Surf. Sci. Nanotech. **8** (2010) 81.

Tunable strongly correlated oxide semiconductors revealed by hard X-ray photoemission spectroscopy

Transition metal oxides with strongly correlated electron systems are attracting considerable interest as one of the best candidates for constructing novel electronic devices owing to their rich functionalities such as high-T_C ferromagnetism, perfect spin polarization, and huge metal-insulator transition. Among them, vanadium dioxide (VO_2) exhibits electronically attractive properties, showing orders of magnitude changes in resistivity at its metal-insulator transition temperature ($T_{M\text{-}I}$) of 340 K. The Mott-Hubbard or Peierls transition mechanism has been discussed as one of the origins of these phenomena. From a practical viewpoint, an abrupt change of resistivity is expected to be applied to an uncooled bolometer because their temperature coefficient of resistance (TCR), defined as $(1/\rho)(d\rho/dT)$, becomes huge above room temperature (RT). The TCR of VO_2 is usually over 70%/K; however, the maximum TCR (TCR_{max}) is obtained only in a narrow range of high temperatures around 340 K. This makes VO_2 unsuitable for application in practical devices working at room temperature (RT). Control of the physical features, especially metal-insulator transition, of VO_2 by doping is a promising method of utilizing this attractive functionality at RT. $T_{M\text{-}I}$ is reduced by doping with transition metal elements, especially W. Therefore, information on the electronic structures and chemical states of W-doped VO_2 is quite important for understanding the origin of its excellent functionality. We investigated the electronic structures as above and chemical states of $V_{1\text{-}x}W_xO_2$ (VWO) thin films by hard X-ray core-level photoemission spectroscopy (HAXPES). HAXPES reveals the true bulk electronic structure up to a depth of about 10 nm, although conventional PES is surface-sensitive and sometimes yields contradictory results concerning the physical properties of the bulk.

HAXPES experiments were performed at beamline **BL15XU**, and HAXPES spectra were taken at $h\nu = 5.95$ keV. The W 4*d* core-level spectra of VWO and the V 2*p* core-level spectra of VO_2 and VWO were measured in the metal phase at 360 K [1].

Figure 1 shows the schematic illustration of the crystal structure of VWO and the temperature dependence of the resistivity for VO_2 and VWO films. As shown in Fig. 1(b), the resistivity rapidly decreased, changing VWO from a metallic state in a high temperature region to an insulating region crossing $T_{M\text{-}I}$. Doping a small amount of W effectively shifts $T_{M\text{-}I}$ and the temperature of the maximum TCR toward RT, while maintaining a high TCR of about 20%/K, as shown in Fig. 1(c). Figure 2(a) shows the W 4*d* core-level spectrum of the VWO film. The W $4d_{5/2}$ peak is located at E_B = 246.9 eV and the single fitting curve is in excellent agreement with the experimental spectrum, indicating that the valence of doped W takes the 6+ state without any other valence numbers. This implies that neighboring V^{4+} ions around the site of W^{6+} dopants change to V^{3+} ions to maintain charge neutrality in accordance with the formula $[V^{4+}]_{1-3x}[V^{3+}]_{2x}[W^{6+}]_xO_2$.

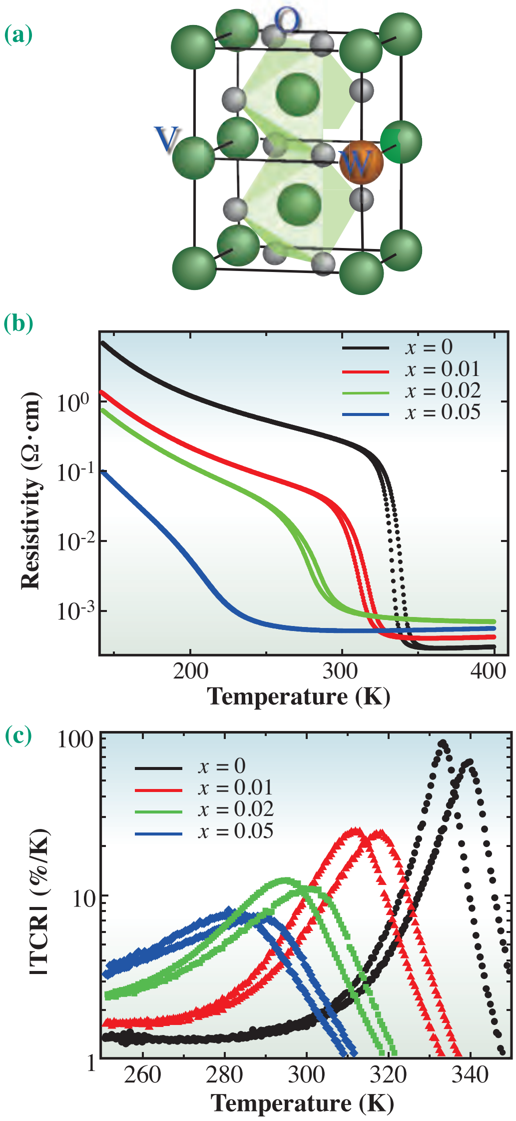

Fig. 1. **(a)** Schematic illustration of $(V_{1\text{-}x}W_x)O_2$ thin films. **(b)** Characteristics of metal-to-insulator phase transition for different W doping ratios. **(c)** Characteristics of temperature coefficient of resistivity (TCR).

To clarify this experimentally, Fig. 2(b) shows the V 2*p* core-level spectra of the VWO films with various W doping levels. Satellite shoulder structures were observed at E_B of 514 eV at the lower binding energy of the V $2p_{3/2}$ main peak, as shown in the dashed box in Fig. 2(b). It was explained by the well-screened states due to electrons in the vicinity of E_F, as observed only in metallic manganites [2,3] and vanadiates [4] and only through the use of HAXPES. This shoulder intensity I_s is related to the density of states of the cohered metallic band around E_F, $D(E_F)$, as expressed by $I_s \propto D(E_F)$. For the VWO film, with increasing W doping ratio, I_s is notably enhanced, indicating the enhancement of the carrier density and suggesting the presence of V^{3+} ($3d^2$) ions, as illustrated in Fig. 3, although the detection of V^{3+} in core-level spectra is difficult because the chemical shift of V $2p_{3/2}$ between V^{4+} and V^{3+} is only 0.15 eV. This effect breaks the half-filled insulating state (V^{4+}-V^{4+} ($3d^1-3d^1$)) electron configuration. As a result, the increase in carrier from W-doping into VO$_2$ is a dominant effect for changing $T_{M\text{-}I}$.

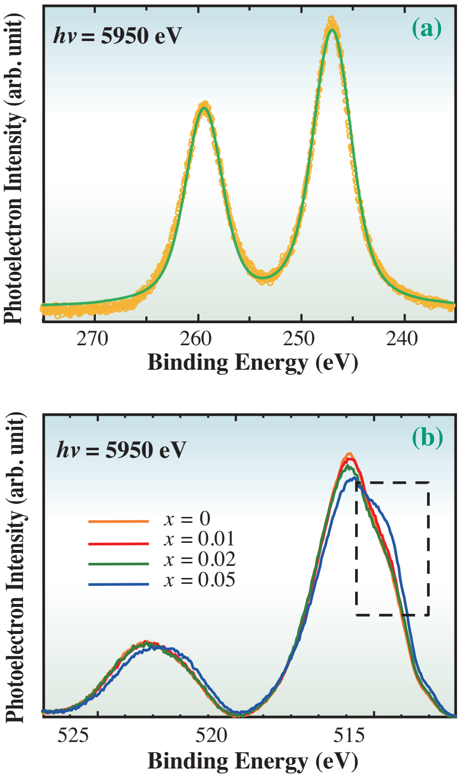

Fig. 2. Hard X-ray photoemission spectra of the $(V_{1-x}W_x)O_2$ thin films: **(a)** for W 4*d* core level (the solid line represents the fitting curve) and **(b)** for V 2*p* core level with various W doping levels.

The HAXPES study revealed that electron doping is an effective mechanism for controlling the metal-insulator transition in the $(V_{1-x}W_x)O_2$ system. Regarding the future significance of this study, the field effect control of transition metal oxides with strongly correlated electrons in heterostructures offers opportunities to create novel functional electronic devices such as electrically tunable colossal magnetoresistance, ferromagnetism, and high-T_C superconductivity devices with controlling interactions between charges with spins [5]; perovskite manganites and high-T_C superconductors are good candidates. The present study demonstrated that VO$_2$ is a candidate material for constructing functional oxide devices owing to its huge metal-insulator transition.

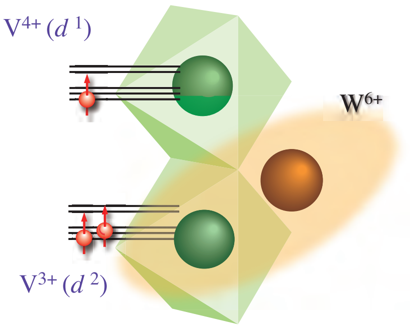

Fig. 3. Schematic illustration of the physical state of $(V_{1-x}W_x)O_2$ based on the mechanism of tunable strongly correlated oxide semiconductors.

Hidekazu Tanaka[a,*], Hidefumi Takami[a] and
Shigenori Ueda[b]

[a] Institute of Scientific and Industrial Research,
Osaka University
[b] NIMS Beamline Station SPring-8,
National Institute for Material Science

*E-mail: h-tanaka@sanken.osaka-u.ac.jp

References

[1] *H. Takami, T. Kanki, S. Ueda, K. Kobayashi and H. Tanaka: Appl. Phys. Exp.* **3** *(2010) 063201.*
[2] K. Horiba *et al.*: Phys. Rev. Lett. **93** (2004) 6401.
[3] H. Tanaka *et al.*: Phys. Rev. B **73** (2006) 094403.
[4] T. Miyamachi *et al.*: J. Magn. Magn. Mater. **310** (2007) E252.
[5] C.H. Ahn *et al.*: Nature **424** (2003) 1015.

Nesting driven spin spiral in ultrathin Fe/Cu(001) films

Iron is one of the most useful and familiar metals in our daily lives. However, its common physical properties are actually based on special features of its magnetism and crystal structure. Iron is delicately perched in terms of magneto-structural instability, with antiferromagnetic Cr and Mn to its left and ferromagnetic Co and Ni on its right in the periodic table. Its crystal structure is body-centered cubic (bcc) at room temperature, and it undergoes a structural transformation from bcc to face-centered cubic (fcc) at 1184 K. Since fcc is the highest density close-packed structure and expected to be more stable than the bcc form, the bcc phase at room temperature is "exceptional" from the viewpoint of structure. Thus, many studies have been performed to elucidate the correlation between structure and magnetism. Theoretical studies have predicted that, in spite of its ferromagnetism in the bcc form, fcc Fe can become nonmagnetic, ferromagnetic, antiferromagnetic or exhibit a spin spiral, sensitively depending on its lattice parameter. Experimentally, fcc Fe nanoparticle precipitates stabilized in a Cu matrix were found to exhibit a spin spiral with an ordering vector of $\boldsymbol{q}=(2\pi/a)(0.12,\ 0,\ 1.0)$ [1], and remarkable progress has been achieved in understanding the interplay of crystal structure and electronic instabilities in realizing spin order. Interestingly, despite extensive effort, the spin spiral associated with the bcc-fcc (α - γ) transition in elemental Fe and its momentum-resolved electronic structure have remained challenging unsolved problems for over 40 years.

As an alternative to experiments at high temperatures or using nanoparticles confined in a Cu matrix, a suitable system was developed to study structure-property correlations in Fe: epitaxial ultrathin Fe films on fcc Cu(001). Ultrathin Fe/Cu(001) films have a complex magnetic and structural phase diagram. It is known that (i) below a thickness of four monolayers (MLs), an Fe/Cu(001) film is ferromagnetic and has the face-centered tetragonal (fct) structure (Region I). (ii) Between 5 and11 ML, it has the fcc structure and a spin spiral, with a top ferromagnetic bilayer (Region II, Fig. 1). The spin spiral ordering temperature is T_{SS}~200 K. (iii) Above 12 ML, it transforms to the bulk ferromagnetic bcc structure (Region III). In this work, we focused our interest on the spin spiral phase of Region II [2]. The spin spiral in ultrathin Fe/Cu(001) films was determined by the magneto-optic Kerr effect (MOKE) to have an ordering vector of $\boldsymbol{q} = (2\pi/a)(0,\ 0,\ \sim0.75)$ [3]. According to theoretical calculations, the ordering vectors $\boldsymbol{q}_1 = (2\pi/a)(0,\ 0,\ 0.6)$ and $\boldsymbol{q}_2 = (2\pi/a)(0.5,\ 0,\ 1.0)$ may be stable [4]; however, $\boldsymbol{q}_1$ and $\boldsymbol{q}_2$ do not match the $\boldsymbol{q}$ obtained by MOKE measurements. The most serious limitation to date, however, is the absence of experimental results relating the momentum (k)-resolved electronic structure to the spin spiral in epitaxial ultrathin Fe/Cu(001) films.

To discuss this relation, it is essential to obtain the in-plane and out-of-plane Fermi surfaces of Fe/Cu(001) films. Although in-plane Fermi surfaces are routinely measured by angle-resolved photoelectron spectroscopy (ARPES) at a fixed photon energy, to extract the q_z component of a spin spiral from out-of-plane Fermi surfaces, we require bulk-sensitive ARPES with a tunable energy. Thus, we chose soft-X-ray (SX) ARPES as our technique: its larger probing depth is typically 10-20 Å.

SX-ARPES was performed with a Gammadata-Scienta SES2002 electron energy analyzer at the undulator beamline **BL17SU** using a spectrometer with a grazing incidence geometry (<5°). Such a spectrometer makes SX-ARPES highly efficient and also ensures that the X-ray photon momentum imparted to the electrons is accounted for easily. Circularly polarized X-rays were used to avoid the symmetry selectivity of linearly polarized X-rays. The measurement was carried out at 50 K, which is considerably below T_{SS}~200 K, to minimize indirect transition losses.

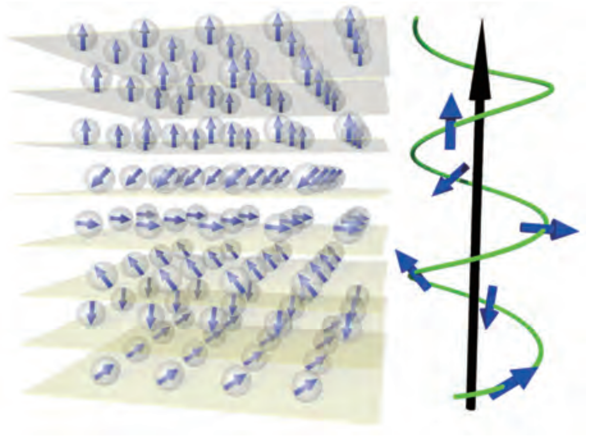

Fig. 1. Schematic representation of 8 ML Fe/Cu(001) thin films with spin spiral order (left). A Cu substrate lies just beneath the Fe thin films, but only Fe thin films are shown for simplicity. The gray balls represent Fe atoms in the thin films and the blue arrows depict spin moments of the Fe atoms. The periodic modulation of the angle of the spins in each Fe layer (blue arrows) is highlighted (right). The black arrow indicates the direction of propagation of the spin spiral.

Fe thin films were grown on Cu(001) using electron beam deposition at room temperature. The thickness of the Fe films was controlled to 8 ML by monitoring reflection high-energy electron diffraction (RHEED) oscillations. The crystallinity and crystal orientation of the Cu(001) substrate and the deposited Fe thin films were also verified by low-energy electron diffraction (LEED).

Figure 2(a) shows the Brillouin zone of fcc Fe. We measured in-plane and out-of-plane band maps along the directions indicated by blue and red lines, respectively. First, we compared experimental band maps with calculated band dispersions for fcc Fe with ordering vectors of both $\boldsymbol{q}_1$ and $\boldsymbol{q}_2$ [4] but they did not give a satisfactory match with our results. We then tried to obtain the in-plane and out-of-plane Fermi surfaces of the Fe thin films in order to determine the spin spiral vector. The in-plane and out-of-plane intensity maps at E_F were obtained from polar angle scans at $h\nu$ = 430 eV and as a function of energy at $h\nu$ = 385–595 eV, respectively. The raw data was measured over one-quarter of the Brillouin zone and symmetrized to obtain the experimental in-plane (Fig. 2(b)) and out-of-plane (Fig. 2(c)) Fermi surfaces for the full Brillouin zone. From peaks in MDCs, we have determined the Fermi surface crossings (Figs. 2(d) and 2(e)). Since the k_x, k_y, and k_z directions are equivalent in the fcc structure, the in-plane and out-of-plane Fermi surfaces should be the same in the absence of electronic/magnetic anisotropies. However, the results show distinct differences between the in-plane and out-of-plane Fermi surfaces. The in-plane Fermi surfaces exhibit fourfold symmetry, whereas the out-of-plane Fermi surfaces exhibit twofold symmetry. Although the in-plane Fermi surfaces show no evidence of nesting, the out-of-plane Fermi surfaces show clear nesting. From the distance between the nestings in the out-of-plane Fermi surfaces, we identified the q_z component of the nesting vector to be $(2\pi/a)\times(0.86\pm0.1)$. This identification is based on precise reciprocal space maps along k_z in successive Brillouin zones. Subsequently, we identified an associated real space compressive strain of 1.5±0.5% along the c-axis. To determine the in-plane component of the nesting vector, we carried out an autocorrelation analysis. Since the autocorrelation analysis using a full Brillouin zone did not give a meaningful result, we applied the autocorrelation analysis to a restricted area of the Brillouin zone (red dashed boxes in Fig. 2(e)) and obtained q_x=0.0. Thus, the spin spiral vector was experimentally quantified as $\boldsymbol{q} = (2\pi/a)(0, 0, 0.86\pm0.1)$. These results are consistent with MOKE [2] and surface X-ray diffraction [5] results for Fe/Cu(001) films, and suggest the importance of in-plane and out-of-plane Fermi surface mappings for ultrathin films.

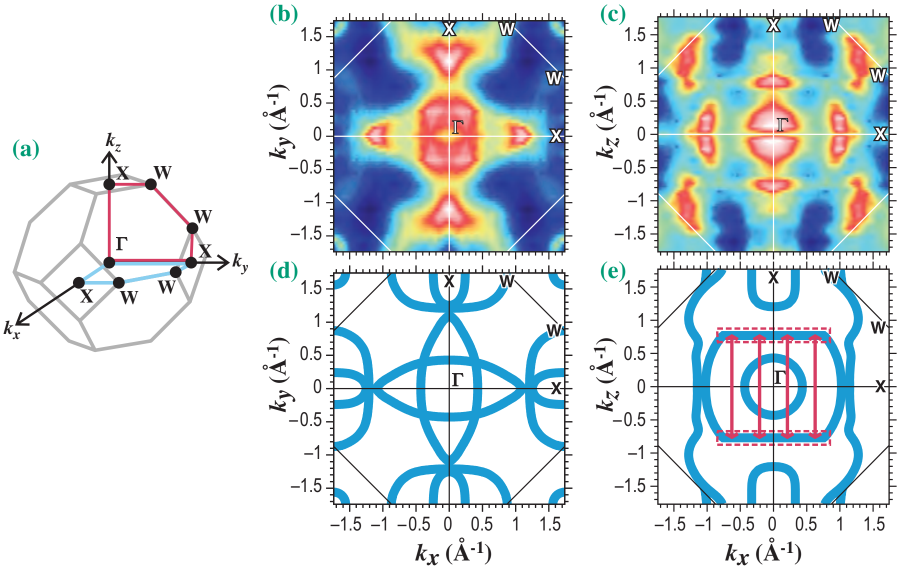

Fig. 2. In-plane and out-of-plane Fermi surfaces of Fe(8ML)/Cu(001). **(a)** Volume Brillouin zone of fcc Fe. **(b)** and **(c)** In-plane and out-of-plane Fermi surfaces for the full Brillouin zone, respectively, which were obtained by symmetrizing data from 1/4 of the Brillouin zone. **(d)** and **(e)** In-plane and out-of-plane Fermi surface crossings extracted from MDCs, respectively. The regions indicated by the red dashed lines are nesting parts and were used for the autocorrelation analysis.

Jun Miyawaki[a,*], Ashish Chainani[a] and Shik Shin[a,b]

[a] SPring-8/RIKEN
[b] Institute for Solid State Physics,
The University of Tokyo

*E-mail: miyawaki@spring8.or.jp

References

[1] Y. Tsunoda: J. Phys. Condens. Matter **1** (1989) 10427.
[2] *J. Miyawaki, A. Chainani, Y. Takata, M Mulazzi, M. Oura, Y. Senba, H. Ohashi and S. Shin: Phys. Rev. Lett.* ***104*** *(2010) 066407.*
[3] D. Qian *et al.*: Phys. Rev. Lett. **87** (2001) 227204.
[4] M. Körling and J. Ergon: Phys. Rev. B **54** (1996) R8293.
[5] H.L. Meyerheim *et al.*: Phys. Rev. B **71** (2005) 035409.

Symmetry of wavefunction in perpendicular magnetic anisotropy films

Recent high-density magnetic storage has been made possible by perpendicular magnetic recording (PMR) techniques. The first application of PMR to hard disk drives was achieved in Dec. 2005 [1]. PMR can achieve 5-10 times higher recording density than the previous conventional magnetic recording. The key material for PMR is a film with perpendicular magnetic anisotropy (PMA), which has a large positive magnetic anisotropy energy perpendicular to the film plane.

Metallic multilayers, such as Co/Pd and Co/Pt, exhibit large PMA energies when their magnetic layer thickness is reduced to a few monolayers [2-5]. In spite of many experimental and theoretical studies toward the understanding of magnetic anisotropy, the origin of PMA in multilayered magnetic thin films remains to be clarified.

Previous theoretical investigations [6,7] have shown the following. The orbital hybridization between Co-3*d* and Pd-4*d* (Pt-5*d*) at the interface increases the population of symmetric Co-3*d* states with $|m|=2$. Here, *m* denotes the magnetic quantum number. The angular momentum induced by the increased number of $|m|=2$ states gives enhanced orbital magnetic moments perpendicular to the film plane. The enhanced orbital magnetic moments perpendicular to the film plane induce PMA. X-ray circular magnetic dichroism (XMCD) experiments have shown the presence of enhanced Co *3d* orbital magnetic moments perpendicular to the film plane at the Co/Pd (or Pt) interface [8,9]. However, the contributions of the $|m|=2$ symmetry to PMA have not yet been confirmed experimentally.

A magnetic Compton profile (MCP), $J_{mag}(p_z)$, is expressed by a projection of a spin density map to the p_z axis in momentum space. Here, p_z denotes the z component of the electron momentum $\boldsymbol{p}$ in a solid. Because the symmetries of a wavefunction are the same in real space and momentum space, the symmetry of the spin-dependent wavefunction can be determined if MCPs are observed from different directions [10].

Recently, we have applied MCPs to the analysis of Co/Pd and Co/Pd multilayers to directly observe the $|m|=2$ symmetry of Co 3*d* states in multilayers with PMA. In this paper, we report the symmetry of the wavefunction in multilayers with PMA [11].

Five multilayer films (Co(0.8 nm)/Pd(*x* nm), x = 0.8, 1.6, 4.0, Co(0.8 nm)/Pt(*x* nm) *x* = 0.8, 4.0) were fabricated on PET film substrates of 4 μm thickness by RF sputtering. The total film thickness of the multilayers was adjusted to about 1 μm. The thin-film samples were folded 16 times to increase their effective thickness, and the effective thicknesses of the films and PET substrate were 16 μm and 64 μm, respectively.

The crystal structure was confirmed by $\theta-2\theta$ X-ray diffraction measurement. The (111) texture of the fcc structure was observed in the intermediate-angle region. Satellite peaks, which were observed around the intermediate-angle region, confirm the designed period of the multilayers. The lattice constant obtained from the peak position of (111) has a linear relation with the thickness fraction of the Co layer.

Magnetization was measured in an out-of-plane configuration (applied fields were perpendicular to the sample surface) and an in-plane configuration (applied fields were parallel to the sample surface). Figure 1 shows the lattice constants and PMA energies. The present results reproduce those of previous studies [2-5]. Magnetic anisotropy changes from in plane magnetic anisotropy to PMA at a lattice constant of more than 0.372 nm.

MCPs were measured at the high-energy beamline **BL08W**. The circularly polarized X-ray energy was set to be 174 keV. The degree of circular polarization was about 0.76. The scattered X-rays were detected by a 10-segmented Ge solid-state detector (SSD) with a scattering angle of 178° that was installed 1 m from the sample. The momentum resolution was 0.43 atomic units (a.u.). The applied magnetic field, which was supplied by a superconducting magnet, was ±2.5 T for magnetization saturation in both the in-plane and out-of-plane configurations. All the measurements were carried out under vacuum at room temperature.

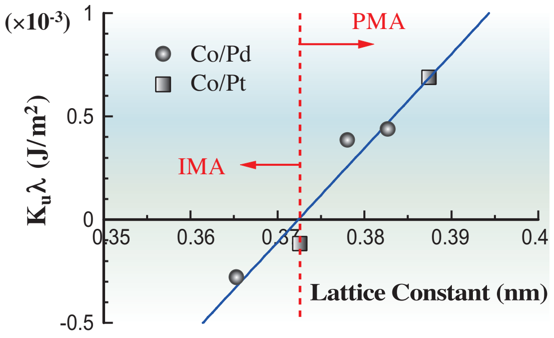

Fig. 1. Perpendicular magnetic anisotropy (PMA) energy density per bilayer against the lattice constants of fcc Co/Pd and Co/Pt multilayers. The blue solid line denotes a least squares fitting result as a visual guide. The red vertical dashed line denotes the boundary of PMA and in-plane magnetic anisotropy (IMA).

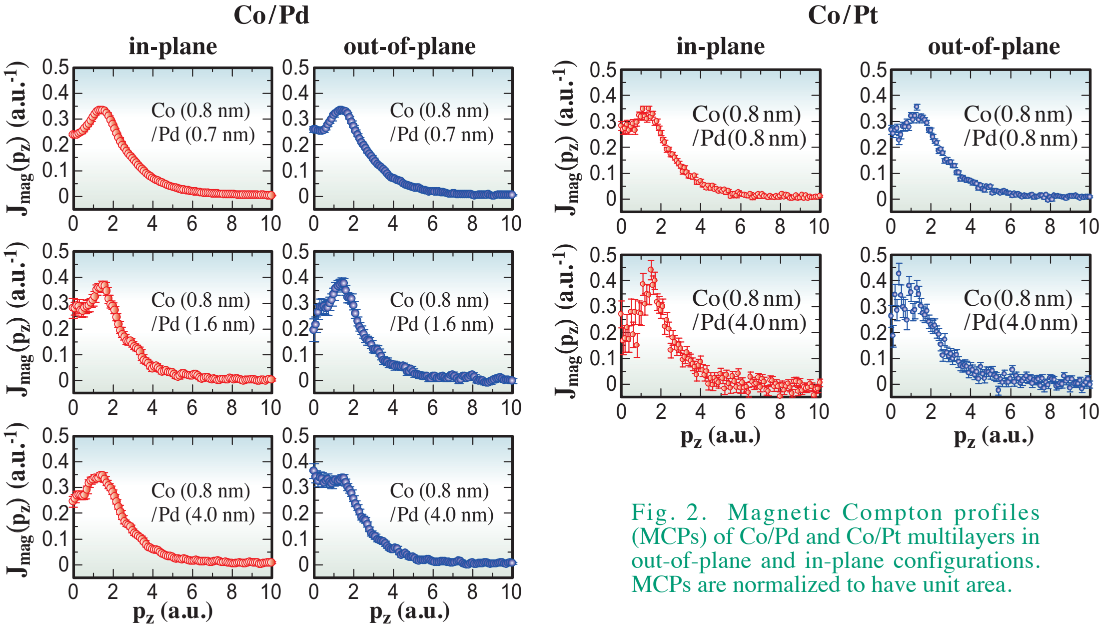

Fig. 2. Magnetic Compton profiles (MCPs) of Co/Pd and Co/Pt multilayers in out-of-plane and in-plane configurations. MCPs are normalized to have unit area.

Figure 2 shows the MCPs of the (Co(0.8 nm)/Pd(x nm) and (Co(0.8 nm)/Pt(x nm) multilayers with the in-plane and out-of-plane configurations. Differences in the MCP between the in-plane and out-of-plane configurations, which we call the anisotropies of the MCP, are observed for the Co/Pd and Co/Pt multilayers within the momentum region 2 a.u. The anisotropies depend on the Pd and Pt thickness, x. This dependence originates from the changes in the populations of $|m|$ = 0, 1, and 2 states, and hence from the change in the symmetry of the wavefunctions. Then the MCPs are decomposed using the model calculation, and the populations of $|m|=0$, 1, and 2 states are obtained.

Figure 3 shows the lattice constants and populations of $|m|=0$, 1, and 2 states. $|m|=2$ states dominate above 0.380 nm. This indicates that $|m|=2$ states contribute to PMA. $|m|=1$ states dominate between 0.372 nm and 0.380 nm. This indicates that $|m|=1$ states also contribute to PMA on the boundary region.

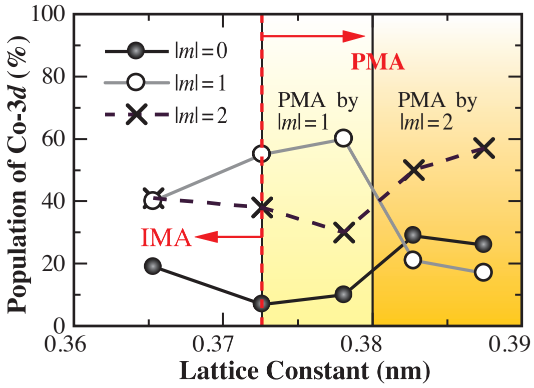

Fig. 3. Population of $|m|=0$, 1, and 2 states in the spin-projected Co 3d electrons against the lattice constants of fcc Co/Pd and Co/Pt multilayers. The red vertical dashed line denotes boundary of PMA and in-plane magnetic anisotropy (IMA).

In conclusion, the lattice constants change the PMA energy and the symmetry of the wavefunction. The contributions of the $|m|=2$ symmetry to PMA are confirmed experimentally. The contributions of the $|m|=1$ symmetry to PMA are also experimentally observed for the first time.

Hiroshi Sakurai

Department of Production Science and Technology,
Gunma University

E-mail sakuraih@gunma-u.ac.jp

References

[1] Y. Shiroishi: Magnetics Jpn. **5** (2010) 312. (in Japanese)
[2] P.F. Carcia *et al.*: Appl. Phys. Lett. **47** (1989) 178.
[3] F.J.A. den Broeder*et al.*: Appl. Phys. A **49** (1989) 507.
[4] F.J.A. den Broeder *et al.*: Phys. Rev. Lett. **60** (1988) 2769.
[5] P.F. Carcia: J. Appl. Phys. **63** (1988) 5066.
[6] G.H.O. Daalderop *et al.*: Phys. Rev. B **50** (1994) 9989.
[7] K. Kyuno *et al.*: Phys. Rev. B **54** (1996) 1092.
[8] D. Weller *et al.*: Phys. Rev. B **49** (1994) 12888.
[9] N. Nakajima *et al.*: Phys. Rev. Lett. **81** (1998) 5229.
[10] N. Sakai: "X-Ray Compton Scattering" edited by M.J. Cooper *et al.*, Oxford (2004).
[11] *M. Ota, M. Itou, Y. Sakurai, A. Koizumi and H. Sakurai: App. Phys. Lett.* ***96*** *(2010) 152505.*

Anisotropic phonon density of states in FePt nanoparticles with $L1_0$ structure

Ferromagnetic FePt with an $L1_0$ structure is composed of alternating stacked layers of Fe and Pt atoms along the *c*-axis (AuCu-type structure with *P4/mmm* space group), as shown in Fig. 1(a). The structure gives rise to a marked crystal anisotropy, which is responsible for the uniaxial magnetic easy axis along the *c*-axis (i.e., perpendicular to the Fe and Pt layers). Since the uniaxial magnetic anisotropy energy (K_u) of approximately 6×10^6 J/m^3 is extremely large, the superparamagnetic limit at room temperature can decrease to approximately 3 nm in particle size [1,2].

It is interesting to determine whether the phonon states of $L1_0$-FePt also have an anisotropy as large as its magnetic energy. We investigated the phonon states of $L1_0$-FePt utilizing ^{57}Fe nuclear resonant inelastic scattering with synchrotron radiation [3]. By developing the chemical method named the "SiO$_2$-nanoreactor method" [4], we prepared $L1_0$-FePt nanoparticles that have a well-ordered $L1_0$ single-crystalline structure with a single magnetic domain. $L1_0$-FePt nanoparticles synthesized by this method can be made dispersible in various solvents, and the orientation of the easy axis (i.e., *c*-axis) of the dispersed nanoparticles can be controlled by applying an external magnetic field [5]. By taking these advantages of the method, we prepared $L1_0$-FePt nanoparticle/polystyrene composites, in which *c*-axis aligned nanoparticles are well dispersed and tightly fixed. These composites are suitable for observing an anisotropic phonon state along different directions of the lattice using ^{57}Fe nuclear resonant inelastic scattering with synchrotron radiation. Indeed, we observed the anisotropic partial density of states (PDOS) in $L1_0$-FePt and compared it with the PDOS calculated in the bulk state by the first-principles method.

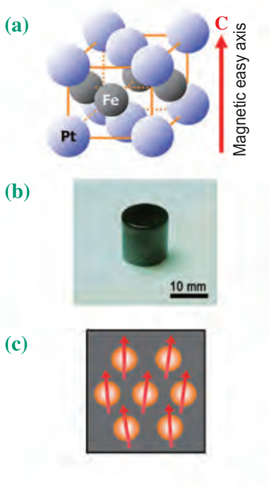

Fig. 1. **(a)** Schematic illustration of the $L1_0$ structure of FePt. **(b)** Photograph of the $L1_0$-FePt nanoparticles /polystyrene composite. **(c)** Schematic illustration of the cross-sectional view of the composite.

The average particle diameter of the prepared $L1_0$-FePt nanoparticles and its standard deviation were 5.1 and 1.2 nm, respectively. To prepare an $L1_0$-FePt nanoparticles/polystyrene composite, $L1_0$-FePt nanoparticles (3.2 wt.%) were dispersed in a styrene monomer solution with azobisisobutyronitrile (1.0 wt.%), which acts as an initiator of the radical polymerization of styrene. The solution was then kept at 60°C for 18 h in argon atmosphere while applying an external magnetic field of 9 T. During this process, the free radical polymerization of styrene proceeds almost completely and the thus-formed polystyrene matrix acts as a binder to fix $L1_0$-FePt nanoparticles with the *c*-axis aligned parallel to the external magnetic field. A photograph of the obtained $L1_0$-FePt nanoparticles/polystyrene composite is shown in Fig. 1(b). The cylindrical composite is 10 mm in diameter and 12 mm in height. The direction of the aligned *c*-axis of the $L1_0$-FePt nanoparticles was perpendicular to the top and bottom faces of the composite. Figure 1(c) shows the schematic illustration of a cross-sectional view of the composite. The orientation of the *c*-axis of the nanoparticles in the composite has a finite distribution because the fixation process using an external field was affected by the thermal effect [6].

The phonon states of the c-axis aligned $L1_0$-FePt nanoparticles were investigated by ^{57}Fe nuclear resonant inelastic scattering at beamline **BL09XU**. The storage ring was operated in the 11-bunch train mode. An SR of 14.41 keV with a bandwidth of 2.5 meV excited ^{57}Fe nuclei in the sample. By detuning the energy of the SR within approximately 100 meV at approximately the ^{57}Fe nuclear resonant energy, we can obtain the probability of the creation and annihilation of phonons at the energies. Four avalanche photodiode detectors were use to collect the intensity scattered into a large solid angle. The energy spectra of the composite were measured under the conditions in which the direction of incident X-rays was set parallel or perpendicular to the direction of the aligned *c*-axis of the $L1_0$-FePt nanoparticles. We call these the parallel and perpendicular geometries, respectively.

The energy spectra measured for the composite at 300 and 10 K in the parallel geometry are shown in Figs. 2(a) and 2(b), respectively. The spectra measured under the perpendicular geometry are shown in Figs. 2(c) and 2(d). The intense central peaks are due to the zero-phonon scattering by ^{57}Fe Mössbauer resonance. The side parts of the spectra show the probability of inelastic excitation with the creation (right-hand side) or annihilation (left-hand side) of phonons in the $L1_0$-FePt nanoparticles. The intensities of the spectra in the side parts show the PDOS at the energies in the lattice. The contribution of the zero-phonon Mössbauer resonance effect was subtracted and the multiphonon contributions were also subtracted using an iterative procedure [7]. The thus-obtained PDOS, which were determined from the phonon energy spectra measured at 10 K in the parallel and perpendicular geometries, are shown in Figs. 3(a) and 3(b), respectively. It is clearly shown that the PDOS observed in the parallel and perpendicular geometries are significantly different from each other. In Fig. 3(a), the spectrum consists of a strong peak at about 28 meV, which can be observed in the original experimental spectra of Figs. 2(a) and 2(b). In Fig. 3(b), the PDOS from the *a*-axis in the $L1_0$-FePt lattice has a distribution from 17 to 32 meV. These measurements also imply that the Debye temperature of $L1_0$-FePt along the *c*-axis is higher than that along the *a*-axis. This can be ascribed to the chain structure with alternating Fe and Pt atoms, which have very different masses, located only along the *c*-axis. To study the results from a theoretical point of view, we calculated the PDOS of the $L1_0$-FePt in the bulk state by the first-principles method [8]. Figures 3(c) and 3(d) show the results of the calculation along the *c*- and *a*-axes, respectively. The calculated PDOS along the *c*-axis shown in Fig. 3(c) consists of a strong peak at about 28 meV, which is consistent with the experimental result. The calculated PDOS along the *a*-axis shown in Fig. 3(d) consists of two strong peaks at 18 and 24 meV. The results were in good agreement with the experimental results.

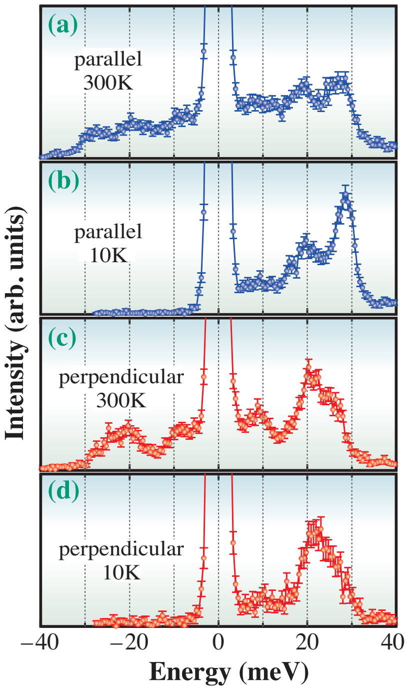

Fig. 2. Phonon energy spectra of the composite measured at **(a)** 300 and **(b)** 10 K in the parallel geometry. Corresponding spectra measured at **(c)** 300 and **(d)** 10 K in the perpendicular geometry.

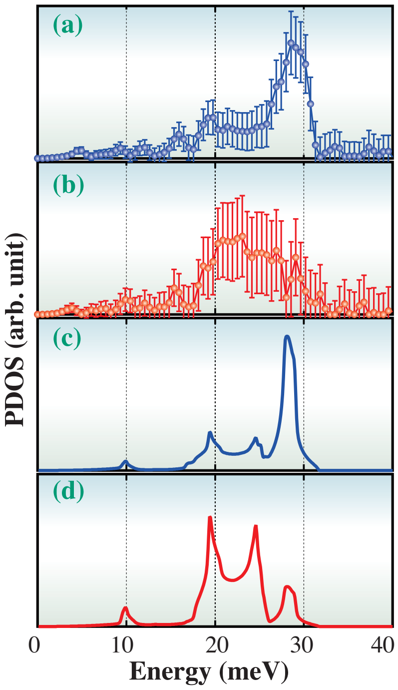

Fig. 3. Phonon densities of states (PDOSs) determined from the phonon energy spectra measured at 10 K in the **(a)** parallel and **(b)** perpendicular geometries. PDOSs calculated in the bulk state by the first-principles method for the **(c)** parallel and **(d)** perpendicular geometries.

Yoshinori Tamada, Teruo Ono* and Saburo Nasu

Institute for Chemical Research, Kyoto University

*E-mail: ono@scl.kyoto-u.ac.jp

References

[1] K. Inomata *et al.*: J. Appl. Phys. **64** (1988) 2537.
[2] T. Klemmer *et al.*: Scr. Metall. Mater. **33** (1995) 1793.
[3] *Y. Tamada, R. Masuda, A. Togo, S. Yamamoto, Y. Yoda, I. Tanaka, M. Seto, S. Nasu and T. Ono: Phys. Rev. B* ***81*** *(2010) 132302.*
[4] S. Yamamoto *et al.*: Appl. Phys. Lett. **87** (2005) 032503.
[5] S. Yamamoto *et al.*: Chem. Mater. **18** (2006) 5385.
[6] Y. Tamada *et al.*: Phys. Rev. B **78** (2008) 214428.
[7] M. Seto *et al.*: Phys. Rev. Lett. **74** (1995) 3828.
[8] A. Togo *et al.*: Phys. Rev. B **78** (2008) 134106.

Novel magnetic domain structure of iron meteorite observed by photoelectron emission microscopy (PEEM)

Iron meteorites show an extraterrestrial pattern called the Widmanstätten structure (Fig. 1(a)). Their metallographic features have been of great benefit to planetary scientists in their study of the history of the solar system. On the other hand, they also show unique magnetic properties significantly different from those of common FeNi alloys. Namely, iron meteorites have remarkably large magnetic anisotropy and strong coercivity, but no explanation has been proposed for how these magnetic properties are associated with the Widmanstätten structure. The important basic question is how the spins of hard magnetic tetrataenite ($L1_0$-FeNi) thin films couple with the surrounding soft magnetic Fe-Ni alloys in the Widmanstätten structure. From the viewpoint of materials science, the heterogeneous structure near the boundary can be considered as a type of magnetic multilayer system composed of α-FeNi, $L1_0$-FeNi, and γ-FeNi (Fig. 1(b)). It is also remarkable that the crystallographic orientation of these FeNi phases maintains a certain relationship, in which the $\{110\}_\alpha$ axis maintains a parallel orientation to the $\{111\}_\gamma$ axis [1]. Here, we studied the magnetic properties of iron meteorites associated with the Widmanstätten structure for the first time.

Photoelectron emission microscopy (PEEM) was carried out to study the magnetic domain structure and metallographic structure of iron meteorites [2]. PEEM is a type of electron microscopy, that can reveal the chemical composition, bonding state, and magnetic domain structure at a resolution of several tens of nanometers. PEEM together with the magnetic circular dichroism (MCD) technique provides a magnetic domain image by the helicity reversal of circularly polarized light. PEEM together with the X-ray absorption fine structure (XAFS) technique provides lattice and composition information by the continuous scan of excitation photon energy. Although PEEM has been mainly used in the study of synthetic nanomaterials, it is also a powerful investigation tool for natural materials. Experiments were performed at beamlines **BL25SU** and **BL39XU**.

Figure 2(a) shows the obtained composition map in the interface region between the α- and γ-lamellae. The Ni composition in the γ-lamella rapidly increased toward the interface, and the crystallographic structure gradually changes from the bcc structure to the fcc structure as the Ni composition increases. Such structural alteration may be associated with the chemical composition suggesting that $L1_0$-FeNi is segregated at the boundary from the metallurgical viewpoint. The magnetic domain structure obtained in the same region is shown in Fig. 2(b). The magnetizations on both sides of the interface are aligned opposite to each other and orthogonal to the domain wall; this magnetic domain eventually forms a ''head-on'' structure. Such a magnetic domain structure is unfavorable for synthetic Fe–Ni alloys, because it requires a large amount of magnetostatic energy for a demagnetizing field. For a typical 180 domain structure, the magnetization is oriented parallel to the domain wall so as to reduce the static magnetic energy; thus, such a structure in iron meteorites is a unique magnetic domain.

To verify such a magnetic domain structure, we performed micromagnetic simulation, solving the Landau-Lifshitz-Gilbert equation for the Fe/$L1_0$-FeNi/Ni system. The magnetic domain structure is disarranged and a head-on magnetic domain structure is clearly revealed near the interface. According to the concept of technical magnetization, a magnetic domain structure is determined so as to minimize the total energy. The magnetic anisotropy energy of $L1_0$-FeNi is much larger than that of the surrounding soft

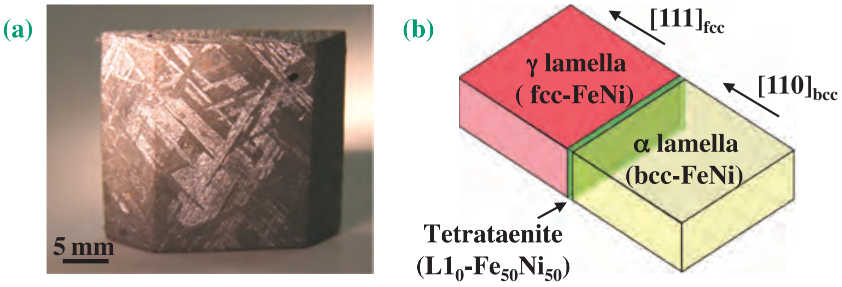

Fig. 1. Widmanstätten structure of iron meteorite **(a)** and model of structure in the interface region **(b)**.

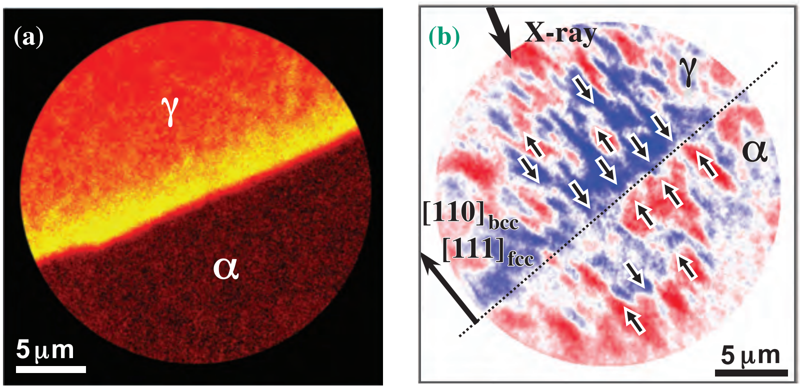

Fig. 2. Composition map **(a)** and magnetic domain image **(b)** in the interface region of iron meteorite obtained by PEEM.

magnetic Fe and Ni. The magnetization of $L1_0$-FeNi remains in the direction of an easy axis that produces the magnetic pole at the surface. To cancel the increase in magnetostatic energy at the surface, the magnetic moments of soft-magnetic Fe and Ni at both sides can be easily disarranged, resulting in the formation of a head-on magnetic domain structure (Fig. 3). Such a head-on magnetic domain structure is commonly reproduced for $L1_0$-FeNi films of various thicknesses; moreover, no head-on magnetic domain structure is observed for a simple Fe/Ni interface. It is finally concluded that head-on magnetic domains are induced by the $L1_0$-FeNi phase segregation at the boundary in the Widmanstätten structure.

It is also remarkable that the magnetic anisotropy energy of 3.2×10^5 J/m^3 in the $L1_0$-FeNi phase is significantly large compared with that in the common FeNi phase. From the viewpoint of reducing environmental impact, new important insights into the synthesis of the $L1_0$-FeNi phase have recently been attracting much attention [3]. The abundance of Fe and Ni opens a new possibility of rare-metal-free $L1_0$-type ferromagnets that will provide further magneto-electronic applications.

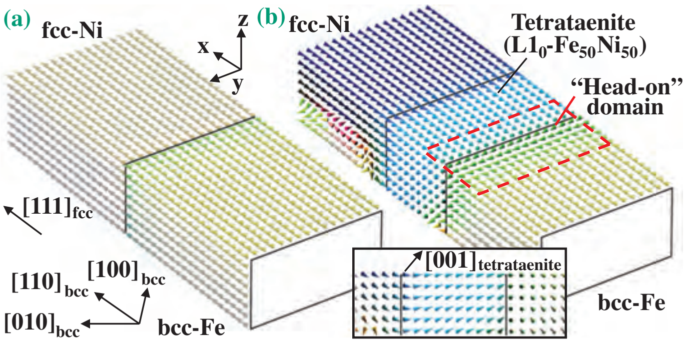

Fig. 3. Micromagnetic simulations of Fe/Ni and Fe/$L1_0$-FeNi/Ni.

Masato Kotsugi

SPring-8/JASRI

E-mail: kotsugi@spring8.or.jp

References

[1] H.J. Bunge *et al.*: J. Appl. Crystallogr. **36** (2003) 137.
[2] *M. Kotsugi, C. Mitsumata, H. Maruyama, T. Wakita, T. Taniuchi, K. Ono, M. Suzuki, N. Kawamura, N. Ishimatsu, M. Oshima and M. Taniguchi: Appl. Phys. Express.* **3** *(2010) 013001.*
[3] T. Shima *et al.*: J. Magn. Magn. Mater. **310** (2007) 2213.

Complete assignment of 3D spin axes of antiferomagnetic domain structures of NiO: Combined study of MLD-PEEM and cluster model calculation

Micromagnetic structures, i.e., magnetic domain structures, are strongly correlated with the magnetic nature of materials. The investigation of magnetic domain structures is very important not only for ferromagnetic (FM) materials but also for antiferromagnetic (AF) materials, from both applied and fundamental scientific points of view, for example, exchange bias. NiO is considered to be one of the typical AF materials. A detailed study of NiO will enable a complete understanding of AF domain structures. NiO has a relatively high Néel temperature (T_N = 523 K) and a collinear spin structure. Owing to their magnetostriction caused by AF ordering, NiO samples below T_N consist of many twinned crystals. Crystallographic twinning leads to four different possible domains, the so-called twin domains (T-domains), with different contractions along the <111> axes. Each T-domain has three easy spin axes, i.e., the <112> directions. Thus, in a single T-domain, three different spin domains (S-domains) can exist. These 12 possible types of easy spin axis make the domain structures in NiO complicated. To understand the AF domain structures, both the T- and S-domains should be assigned. Although many studies have been carried out to observe the domain structures of NiO over the past five decades, no complete determination of the spin axes in each domain structure has been achieved. In the present study, we have successfully assigned the three-dimensional (3D) spin axes of these domain structures completely for the first time by a combined method of X-ray magnetic- and nonmagnetic linear dichroism (XMLD and XLD, respectively), photoemission electron microscopy (PEEM), and cluster model calculation including crystal symmetry [1].

The experiments were performed using two PEEM apparatuses installed at beamlines **BL17SU** and **BL25SU**. Here, we show the results obtained mainly at BL17SU, where *s*- and *p*-linearly polarized light is used. The PEEM apparatus at BL17SU is a spectroscopic photoemission and low-energy electron microscope (SPELEEM). A single-crystal NiO sample was cleaved at the (100) plane in atmosphere and then immediately transferred into a vacuum chamber.

Figure 1 shows the X-ray absorption spectra (XAS) obtained at the (a) O *K* and (b) Ni L_2 edges. It is confirmed that large XLD and XMLD arise at the photon energies indicated by arrows in Figs. 1(a) and 1(b), respectively. Thus, we obtained XLD- and XMLD-PEEM images at these photon energies by both *s*- and *p*-polarized lights. It was reported in Ref. [2] that an XLD image reflects T-domain structures and an XMLD image reflects T- and S-domain structures. It is also known that the XMLD contrast depends on the angle between the polarization vector and the magnetization (spin axis). This means that we can determine the spin axis from the detailed angle dependence of XMLD-PEEM images. As shown in Fig. 1(c), we observed the azimuthal angle dependence (AAD) of the intensity ratio of the two peaks at the Ni L_2 edge in the S-domains with *s*- and *p*-polarized light sensitive to both parallel and perpendicular magnetization components, respectively, by rotating the sample around the [100] direction. We assigned the S-domains correctly by comparing the AAD with a cluster model calculation including the crystal symmetry.

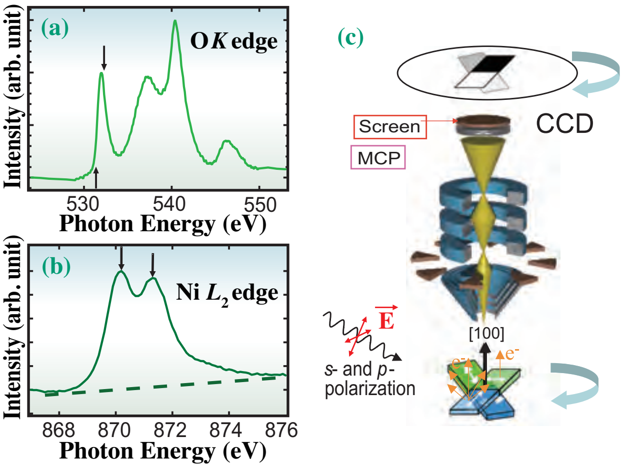

Fig. 1. **(a)** X-ray absorption spectrum (XAS) of NiO in O *K* edge region. PEEM images were acquired at photon energies indicated by arrows. **(b)** As (a) but in Ni L_2 edge region. The dashed line indicates the linear background considered in the observed absorption spectrum. **(c)** Schematic experimental setup for XLD- and XMLD-PEEM studies. The NiO(100) single crystal surface is azimuthally rotated around the [100] axis against the polarization vector. The AF domain contrast changes as a function of rotational angle.

The images shown in Fig. 2 are acquired with *p*-polarized light. At the O *K* edge, four types of contrast are observed corresponding to the four types of T-domain due to <111> crystal distortion, as shown in Fig. 2(a). The four colored lines in Fig. 2(b) indicate the boundaries of the four T-domains in the image. Here, we focus on the T-domain surrounded by the black line shown in Fig. 2(b). The three types of XMLD contrast at the Ni L_2 edge can be seen in the T-domain in Fig. 2(c). This suggests that the observed contrasts originate from the different S-domains. Therefore, the areas surrounded by three solid lines (green, blue, and red) in Fig. 2(d) correspond to the three types of S-domain (S1, S2, and S3), i.e., three types of S-domain exist within a single T-domain. The observed XMLD in the three types of S-domain in the T-domain can easily be compared with the theoretical results in contrast to that in one type of S-domain in the T-domain, because the spin axes should exist within a specified (111) plane. As shown in Fig. 2(c), the boundaries of the S-domains are curved or unclear unlike the T-walls in Fig. 2(a).

Figures 3(a) and 3(b) show the Ni L_2 intensity ratio (higher/lower photon energy) dependence on azimuthal angle observed in the three types of S-domain in Fig. 2 with (a) *s*- and (b) *p*-polarized light. It has been considered for a long time that the XMLD contrast follows the $(3\cos^2\theta - 1)$ dependence, where θ is the angle between a polarization vector and a spin. However, this was refuted very recently [3]. The AAD should be explained by considering the crystal symmetry. Therefore, we performed an analysis using a NiO_6 octahedral cluster model, where the crystal symmetry and the full multiplet splitting of the Ni ion are considered [4]. Figures 3(c) and 3(d) show the results obtained by NiO_6 cluster calculation for *s*- and *p*-polarized light excitations, respectively. The details of the model and the parameters for NiO are described in Refs. [1] and [4]. In Figs. 3(c) and 3(d), the intensity ratios of the three types of easy axis ($[\bar{1}21]$ (green), $[2\bar{1}1]$ (blue), $[112]$ (red)) in the $[11\bar{1}]$ T-domain are calculated. As shown in Fig. 3, the AADs of the relative intensity ratios are in qualitative agreement between the experiments and the calculations. From these comparisons, the easy axes for S1, S2, and S3 can be determined as above. Thus, the observed AAD of XMLD in the three S-domains can be explained by the cluster calculation.

An analytic formula that relates the intensity ratio to the spin axis was also derived. This formula is essential for understanding the behavior of XMLD in NiO. We further observed all types of the T- and S-walls. The results gave us an important basis for understanding antiferromagnetism and ferromagnetic/AF exchange coupled systems.

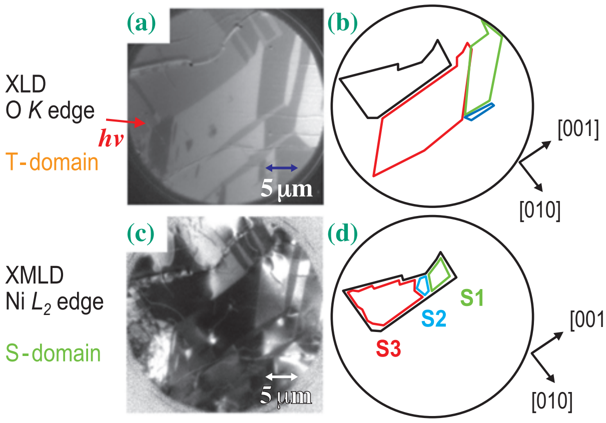

Fig. 2. PEEM images obtained by dividing two images acquired at two photon energies (higher *hν* image/lower *hν* image) with the *p*-polarized light shown in Fig. 1. **(a)** T-domain structures observed by XLD-PEEM. The red arrow indicates the incident soft X-ray direction projected onto the surface plane. **(b)** Schematic domain structures of (a). The four colored solid lines indicate the boundaries of the four T-domains. The area surrounded by a black solid line corresponds to the single T-domain discussed here. **(c)** S-domain structures observed by XMLD-PEEM observed at the same locations as (a). **(d)** Schematic domain structures of (c). The areas surrounded by solid lines (S1, S2, and S3) correspond to the three S-domains in the single T-domain indicated by the black line shown in (b).

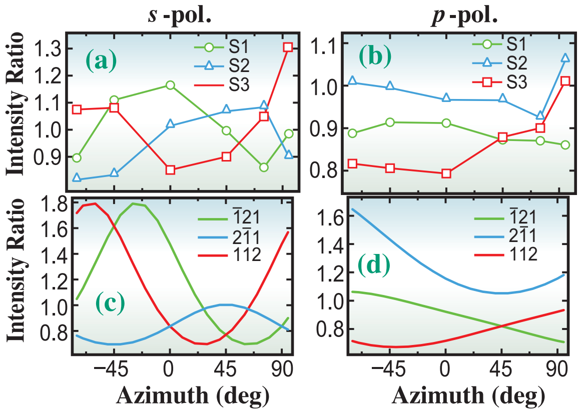

Fig. 3. **(a)** AAD (see text) of absorption intensity ratios at Ni L_2 edge in three domains [shown in Fig. 2(d)] observed with *s*-polarized light. The projective components of the propagation vector of the incident light to the surface plane are the [001] direction at 0° and $[0\bar{1}0]$ direction at 90°. **(b)** As (a) but with *p*-polarized light. **(c)** Calculated absorption intensity ratios (higher/lower energy) of Ni L_2 edge with *s*-polarized light by the cluster calculation containing full multiplet splitting including crystal symmetry. The results of the three spin easy axes, namely, $[\bar{1}21]$, $[2\bar{1}1]$, and $[112]$, are presented. **(d)** As **(c)** but with *p*-polarized light.

Kuniaki Arai[a], Arata Tanaka[b] and Toyohiko Kinoshita[c,d,*]

[a] SRL-ISSP, The University of Tokyo
[b] ADSM, Hiroshima University
[c] SPring-8/JASRI
[d] CREST, JST

*E-mail: toyohiko@spring8.or.jp

References

[1] *K. Arai, T. Okuda, A. Tanaka, M. Kotsugi, K. Fukumoto, T. Ohkouchi, T. Nakamura, T. Matsushita, T. Muro, M. Oura, Y. Senba, H. Ohashi, A. Kakizaki and T. Kinoshita: J. Phys. Soc. Jpn.* ***79*** *(2010) 013703 and Errattum J. Phys. Soc. Jpn.* ***79*** *(2010) 038001.*
[2] T. Kinoshita *et al.*: J. Phys. Soc. Jpn. **73** (2004) 2932.
[3] For example, E. Arenholz *et al.*: Phys. Rev. Lett. **98** (2007) 197201.
[4] A. Tanaka and T. Jo: J. Phys. Soc. Jpn. **63** (1994) 2788.

CHEMICAL

In recent years, great interest is being focused on exotic materials such as two-dimensional sheet-type layers, caged atoms/molecules, and three-dimensional assemblies of small molecules or polymers, as well as on conventional gas, liquid, and solid state materials. Many excellent articles have been published this year by SPring-8 users. Some representative topics are selected in this Chemical Science category. First, the photoelectron-recoil-induced rotational excitation following photo-ionization of gas molecules is introduced. When a photoelectron is ejected from a molecule, recoil momentum is imparted to the remaining ions. In general, the recoil energy is shared among translational, rotational, and vibrational motions. The research team of Prof. K. Ueda (Tohoku University) has shown that the degree of rotational excitation depends on the type of molecular orbital. Their technique, employed at BL27SU, provides information on the atomic orbital composition of molecular orbitals. A JAEA joint research team has successfully studied water under the multiply-extreme conditions of high pressure and high temperature – similar conditions to the Earth's interior. The structural and dynamical properties of water under these conditions were investigated with *in situ* X-ray diffraction experiments at BL14B1, backed up by advanced first principles molecular dynamics simulations. A crossover from a hydrogen-bonded liquid to a simple-liquid-like liquid was observed when the temperature of the molecular liquid phase was raised to 400 K - 500 K. As a typical 2D material, graphene, a honeycomb network constructed by

SCIENCE

sp^2-bonded carbon atoms, has attracted considerable attention as a potential material for electronics and photonics. Epitaxial graphene formation on an SiC thin film on an Si substrate (graphene-on-silicon), developed by the research team of Prof. M. Suemitsu (Tohoku University), has been proved to be effective for forming high quality and large area graphene films. Graphene formation was confirmed using real-time *in situ* photoemission spectroscopy of the C 1*s* core level at BL23SU, probing the *sp*^{2}-bonded carbon atoms. The encapsulation of a Li cation inside a C_{60} cage was observed by the research team of Prof. H. Sawa (Nagoya University) using X-ray diffraction at BL02B1. A single crystal of $[Li@C_{60}](SbCl_6)$ was grown by the diffusion of CS_2 vapor, and the positively charged $Li@C_{60}$ ions were found to be periodically assembled on a 2D negatively-charged sheet of $SbCl_6$ ions. Since the Li cation can move within the C_{60} cage, an external field can be used to control its position, suggesting applications such as single molecular switches and ferroelectric sheets. Controlling the size of porous objects on the nanoscale and aligning them on various substances is currently a hot topic. The fabrication of a preferentially-oriented metal-organic framework nanofilm was achieved by the research teams of Prof. R. Makiura (Osaka Pref. University) and Prof. H. Kitagawa (Kyoto University). Detailed insight into the crystallinity was obtained from X-ray diffraction at BL13XU. The versatility of the solution-based growth strategy is expected to allow the fabrication of various well-ordered metal-organic nanofilms. The large-area 3D molecular ordering of a graft polymer sandwiched between Teflon sheets lead to photo-actuating capability. Exposure to light releases the strain within the material, resulting in a photo-mechanical bending motion. This discovery provides a new design concept for photomechanical soft materials. To determine the structure of the polymer, small-angle X-ray scattering measurements were made at BL45XU by the research team of Prof. N. Hosono (The University of Tokyo/RIKEN). Porous coordination polymers (PCPs), or metal-organic frameworks possessing design-ability that provides host–guest interactions, as well as flexibility that allows guest-responsive dynamic accommodation, have attracted attention as candidates for enhancing molecular recognition ability. A PCP with selective sorption properties for O_2 and NO has been found by the research team of Prof. S. Kitagawa (Kyoto University/RIKEN) at BL02B2. PCPs are expected to provide a new platform for developing selective adsorption systems for small gas molecules. Liquid crystal semiconductors attract increasing attention due to their potential applications in solution-processable and self-repairable organic electronics. Triphenylene derivatives carrying paraffinic side chains with ionic liquid termini were applied to form a liquid crystal mesophase. The relevant phase diagrams have been re-investigated at BL02B2 and BL44B2 by the research team of Prof. Y. Yamamoto (University of Tsukuba). They found that the optically isotropic phase is not amorphous, but a liquid crystal mesophase. This unexpected observation has led to the design of new triphenylene derivatives with different paraffinic spacers and ionic liquid pendants. A combination of neutron and X-ray diffraction techniques has been applied to measure the full set of partial structure factors for liquid and glassy $ZnCl_2$ by the research team of Prof. P. S. Salmon (University of Bath, UK). The high energy X-ray diffraction measurements were conducted at BL04B2. The diffraction patterns were used to construct three-dimensional models for liquid and glassy $ZnCl_2$ by employing the reverse Monte Carlo method. Finally, several kinds of textile fabrics containing silk fibers have recently been found from archaeological sites in Japan. The characteristics of the degraded fibers have been analyzed using FTIR micro-spectroscopy at BL43IR by the research team of Prof. N. Akada (Kyoto Institute of Technology). This research on organic archaeological samples demonstrates the power and usefulness of synchrotron radiation infrared spectroscopy.

Yuden Teraoka

Photoelectron-recoil-induced rotational excitation

When a photoelectron is ejected from an atom or molecule, the remaining ion has a momentum that is equal and opposite to that of the ejected electron. For a free atom this so-called "recoil" momentum appears entirely as translational motion and the atomic ion has a kinetic energy (the "recoil" energy) that is easily calculated by conservation of momentum from the kinetic energy of the electron and the masses of the electron and the atom. In a molecule, however, the recoil energy can be shared among the various normal modes of the molecule – translational, rotational, and vibrational [1]. The fraction of the energy that goes into translational motion is easily calculated from the kinetic energy of the electron and the masses of the electron, the atom, and the molecule. The interesting point is that the division of the recoil energy between vibrational and rotational motion depends on the location of the atom in the molecule and the angular distribution of the photoelectron with respect to the molecular frame.

In the previous experiments, we have investigated the recoil-induced vibrational excitation in carbon 1*s* ionization of CH_4 [2] and CF_4 [3]. These were special cases where recoil-induced rotational excitation is completely suppressed and recoil-induced vibrational excitation is limited to the asymmetric modes. We then have investigated the recoil-induced rotational excitation of the B state in the valence ionization of N_2 [4]. We found that the photon energy dependence of the excitation was well described by a classical model in which the photoelectron is ejected isotropically from a localized atom. In this case the partitioning of the internal excitation between vibrational and rotational motion is given by the number of degrees of freedom for each mode, i.e., 1:2.

We have now extended these studies to include results for the X and A states in N_2, for which the angular distributions are not expected to be isotropic, and for the X, A, and B states of CO^+, where the photoelectron might originate from either the carbon or the oxygen atom [5]. The low-energy measurements were carried out on beamline I411 of the MAX II and the high energy measurements on beamline **BL27SU** of the SPring-8. The photoelectron spectrum of N_2 measured at SPring-8 at photon energy of 500 eV is shown in Fig. 1. We see that the widths are broader for the N_2 peaks (90–92 meV) than they are for the krypton peaks (66 meV). After correcting for the difference of Doppler broadening there remains about 45 meV of width in the N_2 peaks that is not accounted for by either instrumental width or Doppler broadening. This excess width presumably represents rotational broadening. The individual rotational lines cannot be resolved. In this case, the recoil-induced excitation is reflected in a shift in the centroid of the peak. Our analysis, therefore, involves determining the energy spacing between the centroid of the calibration line and the centroid of the v=0 peaks for the transitions to the X, A, and B states of the ions. This difference is corrected for the difference between translational recoil energies of the molecule and the reference atom to give the apparent differences in ionization energies between the molecule and the atom.

In the very simplest approximation, the molecular-frame angular distribution depends on the nature of the atomic orbital from which the electron is ejected. In the plane-wave approximation, ejection from an *s* orbital of a cylindrically symmetric molecule is isotropic in the molecular frame, ejection from a p_σ orbital has a distribution that goes as $\cos^2\theta$, and emission from a p_π orbital has a distribution that goes as $\sin^2\theta$, where θ is the angle between the electron emission direction and the molecular symmetry axis. Each of these angular distributions leads to a different sharing of the recoil-induced internal excitation between the vibrational and rotational modes, with the result that measurements of

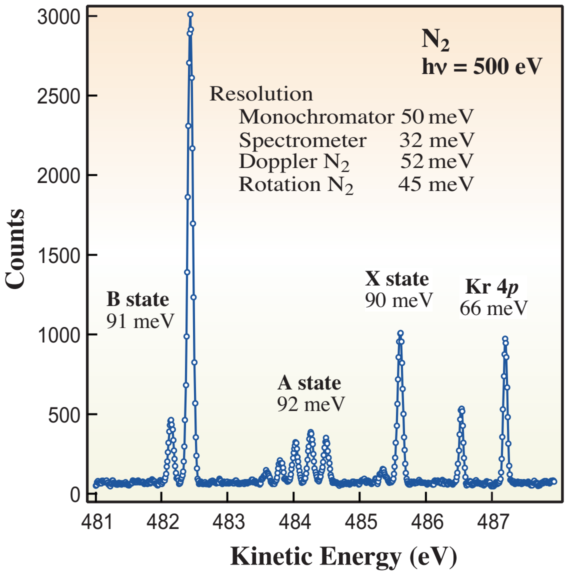

Fig. 1. Valence photoelectron spectrum of N_2/krypton mixture measured at a photon energy of 500 eV. Open circles show the data and the solid line shows a least-squares fit of Gaussian functions to the data. The widths (FWHM) determined from the fitting procedure for each group of peaks are shown. Also listed are the various components that contribute to the resolution.

the degree of recoil-induced rotational excitation can lead to information on the atomic orbital composition of the molecular orbital from which the electron is ejected.

The results of these measurements for the X, A, and B states of N_2^+ are shown in Fig. 2, where we have plotted the apparent ionization energy to form each of these states as a function of the kinetic energy of the photoelectron. The open circles show the experimental data and the solid lines show the results of weighted least-squares fits of straight lines to the data. The slopes of these lines are indicated in the figure. These slopes are generally in accord with a simple model that treats the electrons as if they were emitted from isolated atoms. This treatment takes into account the atom from which the electron is emitted, the molecular-frame angular distribution of the electron, and the dependence of the photoelectron cross section on photon energy, on atomic identity, and on the type of atomic orbital from which the electron is ejected. The results for the X and A states in N_2 and similar results for the X, A, and B states of CO^+ (not shown here) show that the degree of rotational excitation does depend on the type of molecular orbital, and that this technique can provide information on the atomic orbital composition of the molecular orbitals.

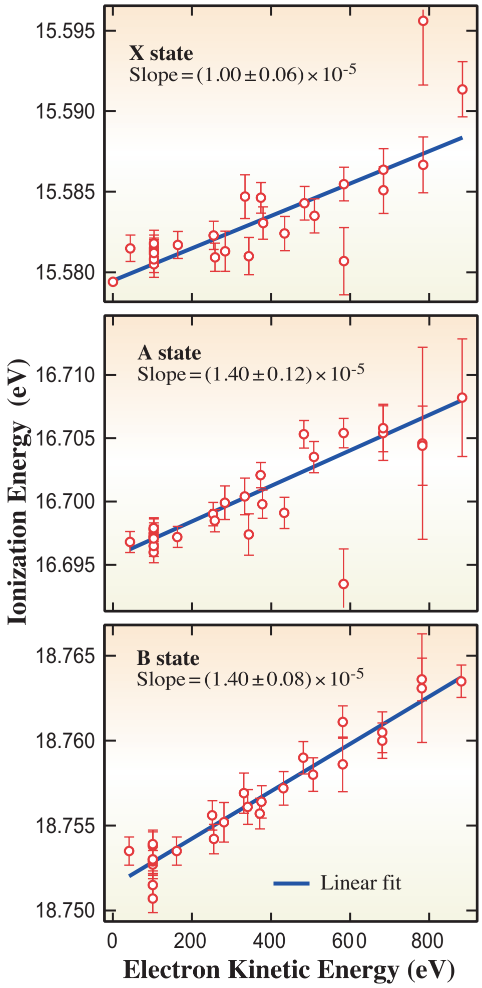

Fig. 2. Apparent energies for the X, A, and B states in N_2^+ (relative to N_2) as a function of photoelectron kinetic energy. The open circles show the data and the solid lines show straight lines fit to the data by weighted least-squares.

Additional information on the atomic orbital composition of the molecular orbitals can be obtained from the relative probabilities of ionization to form the X, A, and B states in N_2^+ and CO^+, that is, from the relative intensities of the lines observed in spectra such as that in Fig. 1. For example, at high photon energies the cross section for ionization of 2*s* electrons in a nitrogen atom is about nine times larger than the cross section for ionization of 2*p* electrons. In N_2 the X and A states are either predominantly or exclusively of 2*p* character, whereas the B state is predominantly of 2*s* character. As a consequence, the cross sections to form the X and A states are much smaller than the cross section to form the B state. In addition, the valence photoelectron spectrum of N_2 at high photon energy shows a stronger peak for the X state, which has some nitrogen 2*s* character, than for the A state, which is exclusively nitrogen 2*p*. Thus the measurement of these relative cross sections provides a potential additional tool for determining the atomic orbital character of the molecular orbitals. An analysis of these intensities to obtain such information is reported in Ref. [5].

T. Darrah Thomas[a], Edwin Kukk[b] and Kiyoshi Ueda[c,*]

[a] Dept. of Chemistry, Oregon State University, USA
[b] Department of Physics and Astronomy,
University of Turku, Finland
[c] Institute of Multidisciplinary Research for
Advanced Materials, Tohoku University

*E-mail: ueda@tagen.tohoku.ac.jp

References

[1] W. Domcke and L.S. Cederbaum: J. Electron Spectrosc. Relat. Phenom. **13** (1978) 161.
[2] E. Kukk *et al.*: Phys. Rev. Lett. **95** (2005) 133001.
[3] T.D. Thomas *et al.*: J. Chem. Phys. **128** (2008) 144311.
[4] T.D. Thomas *et al.*: Phys. Rev. A **79** (2009) 022506.
[5] *T.D. Thomas, E. Kukk, T. Ouchi, A. Yamada, H. Fukuzawa, K. Ueda, R. Püttner, I. Higuchi, Y. Tamenori, T. Asahina, N. Kuze, H. Kato, M. Hoshino, H. Tanaka, A. Lindblad, and L.J. Sæthre: J. Chem. Phys.* ***133*** *(2010) 174312.*

Structural and dynamical properties of water under high temperatures and pressures revealed by combining first principles molecular dynamics simulations and *in situ* X-ray diffraction experiments

Although liquid water is one of the most abundant materials on earth and one of the most familiar to all of us, the present understanding of liquid water that exhibits various anomalous properties around ambient conditions is still far from satisfactory. Recently, it is found that water also exists in the Earth's interior in the form of hydrous minerals; it plays crucial roles, e.g., in the formation of magma etc. Hence, water is certainly vital for the global environment. A joint research team of the Quantum Beam Science Directorate of JAEA has successfully studied fluid water at multi-extreme conditions of pressures (~1 GPa) and temperatures (>700 K) corresponding to the Earth's interior at a depth ~30 km, by both advanced first principles molecular dynamics simulations [1] and *in situ* X-ray diffraction experiments [1,2]. Thus we gained a novel insight into water under such multi-extreme conditions.

In situ X-ray diffraction experiments of fluid water under high temperatures and pressures were conducted at beamline **BL14B1**, where the cubic-type multianvil press is installed as shown in Fig. 1. On the other hand, first principles molecular dynamics simulations for fluid water at almost the same temperature-pressure conditions as the experimental ones were performed using supercomputer facilities of JAEA. Figure 2 compares the theoretical radial distribution functions $g_{XY}(r)$ in isochore conditions of

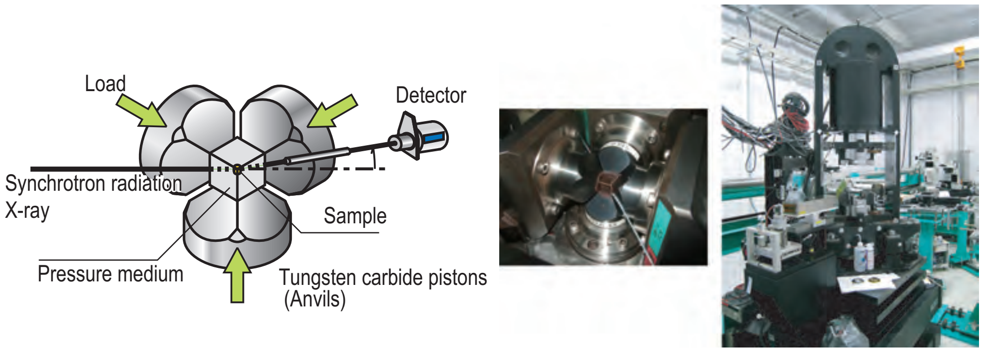

Fig. 1. Apparatus for high temperature and pressure X-ray diffraction experiment. Schematic view (left) and photograph (right) of the cubic-type multianvil press installed at BL14B1, where the present diffraction experiment was conducted.

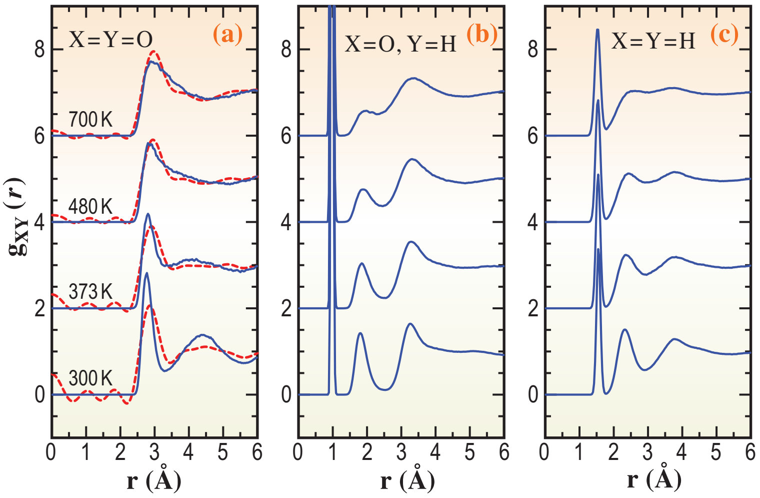

Fig. 2. Comparison of theoretical and experimental radial distribution functions. Radial distribution functions **(a)** $g_{OO}(r)$, **(b)** $g_{OH}(r)$, and **(c)** $g_{HH}(r)$ for 1.0 g/cm^3 obtained from our first principles molecular dynamics simulation and *in situ* X-ray diffraction experiment are shown as solid and dashed lines, respectively. For clarity, the vertical axis for data of different temperatures is shifted up.

1.00 g/cm^3 computed from the molecular dynamics simulations with our experimental ones. Both the theoretical and experimental results show that with raising temperature the second peak of the oxygen-oxygen radial distribution function $g_{OO}(r)$ located for ambient water at ~4.5 Å (bottom of Fig. 2(a)) represents an inward shift, which ends up merging the first and second peaks, thus leading to the increase in coordination number up to 12-14. Moreover, close examination of the coordination structure of water produced in the simulations reveals that with increasing temperature the tetrahedral coordination characteristic of ambient water tends to be diminished from 373 K and finally it is completely collapsed at high temperatures of ~700 K, although the intermolecular peak of $g_{OH}(r)$ which can be traced back to hydrogen bonds is still visible at around 1.8 Å as shown in Fig. 2(b).

The apparent inconsistency of the collapsed tetrahedral coordination with intact hydrogen bonds yet inferred at high temperatures turns out to be reconciled by unusual dynamical properties of high-temperature water. Our simulations show that high-temperature water under pressure exhibits a characteristic structure of simple liquids, resulting from anomalously fast rotational motions, which are found to be typically two orders of magnitude faster than in ambient water irrespective of density as shown in Fig. 3.

Our conclusions derived from a series of systematic studies via first principles molecular dynamics combined with *in situ* X-ray diffraction are summarized schematically in Fig. 4. The crossover is found to occur from hydrogen-bonded to simple-liquid-like liquids by raising temperature within molecular liquid phase at around 400-500 K. The resulting high-temperature water is characterized by very rapid molecular reorientation, which is hardly affected by compression, contrary to molecular diffusion, which is found to be much more easily quenched.

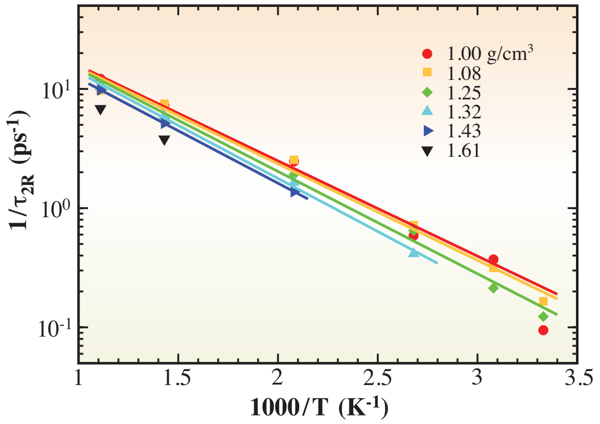

Fig. 3. Temperature dependence of rotational correlation time τ_{2R} estimated for various densities from first principles molecular dynamics simulations. High-temperature water under pressure exhibits anomalously fast rotational motions, which are suggested to be typically two orders of magnitude faster than in ambient water irrespective of density.

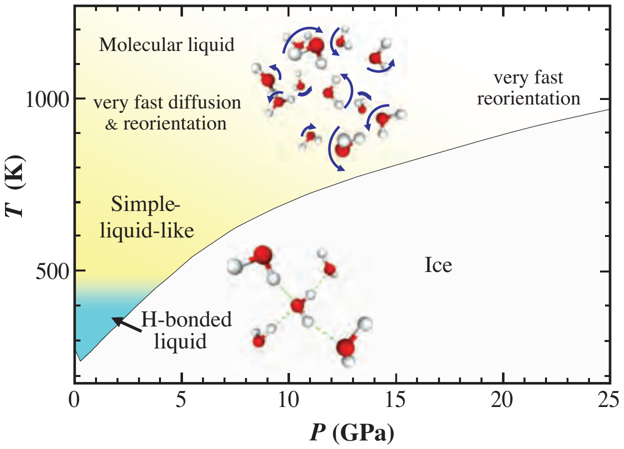

Fig. 4. Schematic *P*-*T* phase diagram of water representing the crossover between hydrogen-bonded and simple-liquid-like liquids in molecular liquid phase. Typical structures of water under high temperature-pressure and ambient conditions are shown at the top and bottom of the figure, respectively.

Takashi Ikeda* and Yoshinori Katayama

SPring-8/JAEA

*E-mail: tikeda@spring8.or.jp

References

[1] *T. Ikeda, Y. Katayama, H. Saitoh and K. Aoki: J. Chem. Phys.* ***132*** *(2010) 121102.*
[2] *Y. Katayama, T. Hattori, H. Saitoh, T. Ikeda, K. Aoki, H. Fukui and K. Funakoshi: Phys. Rev. B* ***81*** *(2010) 014109.*

Epitaxial graphene on silicon substrates

Graphene, a 2D honeycomb network of sp^2-bonded carbon atoms, has been attracting considerable attention as a material for electronics as well as for photonics. Graphene expresses multifunctionality in response to the breakage of the time-reversal symmetry of its honeycomb structure [1], as conceptually described in Fig. 1. Moreover, conventional lithographic techniques for Si-ULSI are easily applicable to graphene owing to its planar structure, in contrast to the structure of carbon nanotubes. Graphene is therefore one of the most promising materials to realize the next-generation multifunctional integrated circuits can be the successor to Si.

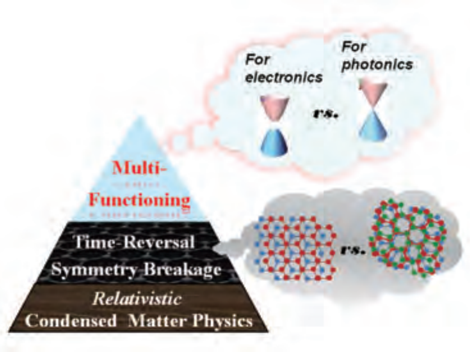

Fig. 1. Schematic of expression of multifunctionality of graphene.

Methods of growing large-scale epitaxial graphene on suitable substrates should, however, be developed in order for graphene to be the successor to Si. Among various epitaxial methods, the epitaxy of graphene on SiC bulk crystals has been considered the most promising technology. The epitaxial graphene method on SiC bulk crystals can produce high-quality films, which can be directly used for devices. In contrast, chemical-vapor-deposition-grown graphene on metal substrates needs to be transferred to insulating substrates for device applications. Unfortunately, however, epitaxially grown graphene on SiC bulk crystals has a crucial drawback: its high production cost.

To solve this drawback, we have chosen Si as the suitable substrate for the epitaxy of graphene. Namely, we have attempted and in fact succeeded for the first time in the epitaxy of graphene on Si (GOS) [2,3], as shown in Fig. 2. In fabricating GOS, a SiC thin film is grown by gas-source molecular beam epitaxy using monomethylsilane, followed by high-temperature annealing to sublimate silicon atoms from the SiC surface for graphitization [2,3]. The GOS fabrication processes were confirmed by C 1*s* core level photoelectron spectroscopy to probe the formation of sp^2-bonded carbon atoms and by Raman-scattering spectroscopy to probe the network consisting of sp^2-bonded carbon atoms. Finally, cross-sectional transmission electron microscopy (XTEM) clearly images the planar structure of GOS. It can thus be concluded that graphene can definitely be grown on a Si substrate.

Field-effect transistors using GOS as a channel can be readily fabricated by standard lithography of Si, and the highest carrier mobility has been estimated to be 6,000 cm^2/Vs [4]. This high carrier mobility clearly demonstrates the availability of GOS for the next-generation devices. Furthermore, the photoresponsivity of GOS using the field effect has recently been demonstrated. GOS is thus a promising electronic and photonic material, as anticipated.

Very intriguingly, the interface properties and therefore the electronic properties of GOS can be tuned in terms of the crystallographic orientation of the Si substrate (Fig. 3) [5]. The tunability of the interface between graphene and the SiC thin film is clearly demonstrated by high-resolution C1*s* core level photoelectron spectroscopy co-performed at **BL23SU**, as shown in Fig. 3(a). The main features of graphene and SiC are observed in the spectra of graphene on both Si(111) and Si(100). In contrast, a peak due to the buffer layer, which is partially bonded to the underlying SiC top surface, is only observed in the spectrum of graphene on SiC(111)/Si(111).

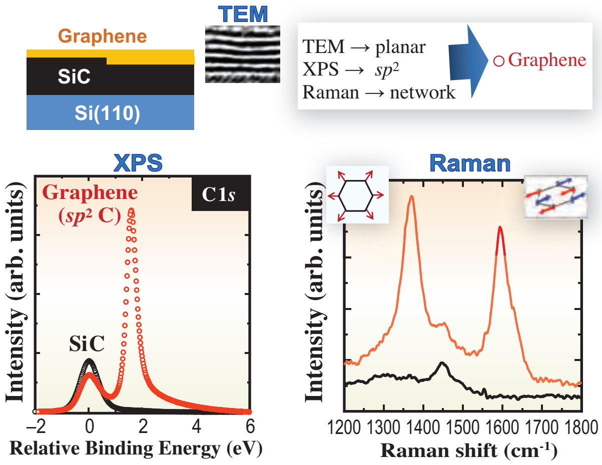

Fig. 2. C1*s* core level photoelectron spectra of graphene, XTEM image and Raman spectra probing epitaxial processes in GOS.

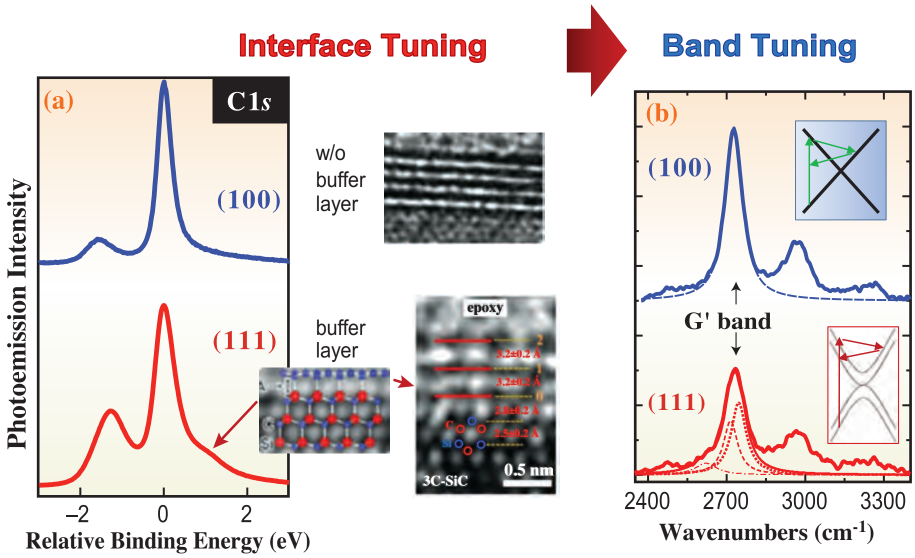

Fig. 3. **(a)** C1*s* core level photoelectron spectra of graphene and XTEM images, and **(b)** Raman spectra, revealing the mechanism of the expression of multifunctionality.

This result of the C1*s* core level spectroscopy is validated by XTEM (Fig. 3(b)). In GOS using Si(111) as the substrate, the buffer layer is clearly imaged by that of XTEM, while the absence of the buffer layer is confirmed by XTEM in GOS using Si(100) as the substrate. The tunability of the interface structure of GOS affects the electronic structure of GOS. In Fig. 3(b), the G' bands in the Raman spectra are shown for graphene on Si(111) and Si(100). On Si(111), the G' band is multiply split as a result of the coupling between photons and multiple electronic bands. In contrast, the G' band possesses a single component in the spectra of graphene on Si(100), due to the coupling between photons and an electronic band.

This tunability of an electronic structure should be one of the most unique points of GOS. By virtue of this property, GOS can play various roles in either electronic or photonic application, just by changing the crystallographic orientation of the Si substrate, as shown in Fig. 4. GOS using Si(111) as the substrate can serve as the channel for the FET of digital operation, particularly at the terahertz frequency. On the other hand, GOS using Si(100) and Si(110) as the substrates can serve as laser components for ultrahigh-speed optical communication. In the near future, we anticipate GOS-based electronic-photonic fusion integrated circuits; therefore, we are exerting effort to fabricate nanostructured GOS, owing to our collaborative work at BL17SU on spectroscopic low-energy electron microscopy (SPELEEM).

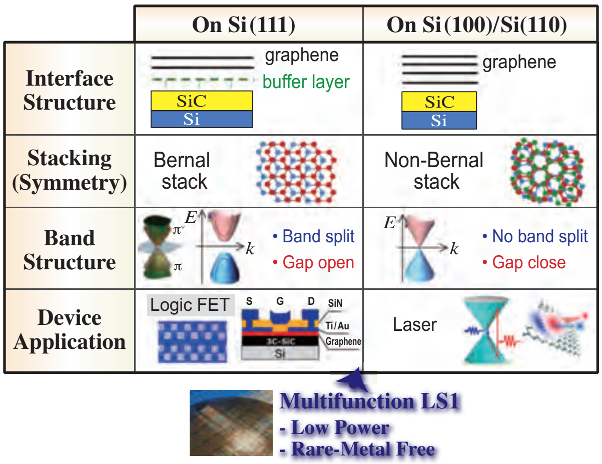

Fig. 4. Multifunctionality of GOS depending on the orientation of the substrate.

Hirokazu Fukidome* and Maki Suemitsu

Research Institute of Electrical Communication,
Tohoku University

*E-mail: fukidome@riec.tohoku.ac.jp

References

[1] A. Bostwick *et al.*: New J. Phys. **9** (2007) 35.
[2] M. Suemitsu *et al.*: e-J. Surf. Sci. Nanotech. **7** (2009) 311.
[3] H. Fukidome *et al.*: Jpn. J. Appl. Phys. **49**(2010) 01AH03.
[4] H.C. Kang *et al.*: Jpn. J. Appl. Phys. **49** (2010) 04DF17.
[5] *M. Suemitsu and H. Fukidome: J. Phys.* ***D*** *43 (2010) 374012.*

Observation of Li cation encapsulated in C_{60} fullerene cage by single-crystal charge density analysis

C_{60} fullerene is the most promising nanocarbon material for a wide range of practical applications owing to its high productivity and flexible electrical and chemical properties. The encapsulation of atoms and molecule in C_{60} fullerene is a promising method of developing application field. Various endohedral C_{60} fullerenes have been synthesized since the discovery of the first metallofullerene La@C_{60} in 1985. The macroscopic synthesis and molecular structures of the gas molecule endohedral C_{60}, H_2@C_{60} and Ar@C_{60}, have been reported [1,2]. The physical and chemical properties of H_2@C_{60} and Ar@C_{60} are similar to those of empty C_{60}. The encapsulation of a metal atom is expected to change the properties of C_{60} by metal ionization. However, the isolation and structure determination of M@C_{60} (M: metal) have been precluded by the insolubility and high reactivity of M@C_{60}.

Recently, the bulk synthesis and complete isolation of Li@C_{60} have been successfully carried out by researchers of idealstar Inc. and Tohoku University. A single crystal of [Li@C_{60}]($SbCl_6$) with typical dimensions of $60 \times 40 \times 10$ μm^3 was grown by the diffusion of CS_2 vapor into solution. However, it is generally difficult to determine the position of a Li cation from small crystals by X-ray diffraction analysis. We observed an encapsulation of a Li cation inside a C_{60} cage by a single-crystal X-ray diffraction analysis of [Li@C_{60}]($SbCl_6$) crystals at **BL02B1** beamline [3].

The single-crystal X-ray diffraction experiment was performed using a large cylindrical imaging plate camera [4]. The camera rapidly collects diffraction peaks over a wide diffraction angle range ($2\theta < 145°$) using an imaging plate with a wide dynamic range of 10^6 and a three-axis goniometer ($-130 < \omega < 220°$, $-5 < \chi < 60°$, $-180 < \phi < 360°$). The wavelength of X-rays used is 0.35 Å. The sample temperature was controlled using a He/N_2 gas flow system. The [Li@C_{60}]($SbCl_6$) crystal had a twinned monoclinic structure below room temperature. A phase transition from a twinned monoclinic structure to a single-domain orthorhombic structure was observed at ~320 K. The crystal structure of the orthorhombic [Li@C_{60}]($SbCl_6$) was determined at 370 K (space group $Amm2$, a = 12.30 Å, b = 9.95 Å, c = 29.05 Å, V = 3555 Å^3). The orientations of C_{60} cages and the position of a Li cation inside a cage were determined on the basis of charge density distributions by the maximum entropy method (MEM).

A charge density map for a [Li@C_{60}]$^+$ is shown in Fig. 1(a). Two charge density peaks (red arrows) inside the C_{60} cage were regarded as disordered Li cation occupying two off-centered sites that are crystallographically equivalent. This off-centered structure is quite different from the on-centered structure of the encapsulated gas molecule inside the C_{60} cage [1,2]. The distance from the center of the C_{60} cage to the Li cation is 1.34 Å, which is close to the theoretically predicted values. The inhomogeneous charge density distribution of the C_{60} cage (shown as green in Fig. 1(a)) demonstrates the ratchet-type disorder of the cage with four orientations. In any orientation of C_{60} fullerene, the Li cation lies in the vicinity of one of the six-membered rings (Fig. 1(b)) of the cage. This suggests the presence of an attractive force exerted between the six-membered ring and the Li cation.

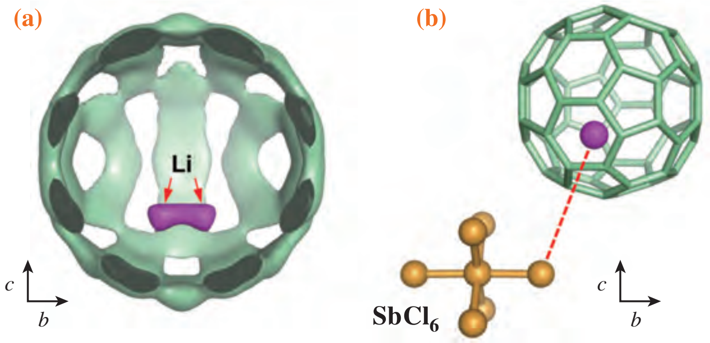

Fig. 1. **(a)** MEM charge density map of Li@C_{60} cation in [Li@C_{60}]($SbCl_6$) crystal at 370 K. A 0.25 e/Å^3 equi-charge density surface for a Li cation inside a C_{60} cage is shown as magenta. A 2.0 e/Å^3 equi-charge density surface is shown in green. The charge density at the two peaks for the Li cation (red arrows) is 0.38 e/Å^3. **(b)** Geometrical relationships between Li@C_{60} cation and adjacent $SbCl_6$ anion (orange). The structure of one molecular orientation for a Li@C_{60} cation extracted from a disordered structure is shown. The nearest Li-Cl distance is 5.58 Å (red dashed line).

An electrostatic attractive interaction between a Li cation and $SbCl_6$ anions should be crucial to determining the position of the Li cation in the C_{60} cage. Figure 1(b) shows the arrangement of an $SbCl_6$ anion around a Li@C_{60} cation. The Li cation is close to a negatively charged Cl atom of the $SbCl_6$ anion. The electrostatic attractive interaction between Li^+ and Cl^- through the cage should localize the Li cation at the two sites. The restriction of the free rotation of the C_{60} cage even at a high temperature of 370 K is regarded as a result of the attractive interaction between the localized Li cation and the six-membered rings.

The three-dimensional molecular arrangement of the $[Li@C_{60}]^+$ and $SbCl_6^-$ units (Fig. 1(b)) constructs the layered crystal structure, as shown in Fig. 2. The slab structure formed by two-dimensional arrays of the $[Li@C_{60}](SbCl_6)$ units (Fig. 1(b)) perpendicular to the *c*-axis is clearly seen. In the slab, the first- and second-nearest intermolecular distances of the Li@C_{60} cations are 9.95 and 10.03 Å, respectively. The shorter distance (9.95 Å) between the adjacent Li@C_{60} cations is almost exactly the same as that of the close-packed pristine fcc C_{60} structure, whereas the interslab distance of the Li@C_{60} cations is 10.30 Å. The positively charged Li@C_{60} ions are periodically assembled on the two-dimensional negatively charged sheets of $SbCl_6$ ions by the electrostatic attractive force between the Li cation and the Cl atom. This unique structural feature may exhibit interesting solid-state properties. The ^{13}C NMR spectrum of $[Li@C_{60}](SbCl_6)$ in solution shows that the Li cation is rapidly moving inside the C_{60} cage. These facts suggest that the position of the Li cation can be varied and controlled by adjusting the external field outside the C_{60} cage. Such position control by an external field can be widely used in electronics applications such as in single molecular switches and ferroelectric sheets.

The most striking feature of Li@C_{60} revealed in the present study, which has never been observed in conventional metallofullerenes, is the extremely high tendency of Li@C_{60} to form ion-pair states (species) such as $[Li@C_{60}](SbCl_6)$. Li@C_{60} can only be stabilized significantly under ambient condition when it coexists with an appropriate counteranion. The present methodology for the isolation and crystallization of *M*@C_{60} can be widely applied to the existing Groups 2, 3, and 4 and all lanthanide metallofullerenes such as La@C_{60} and Gd@C_{60} [5].

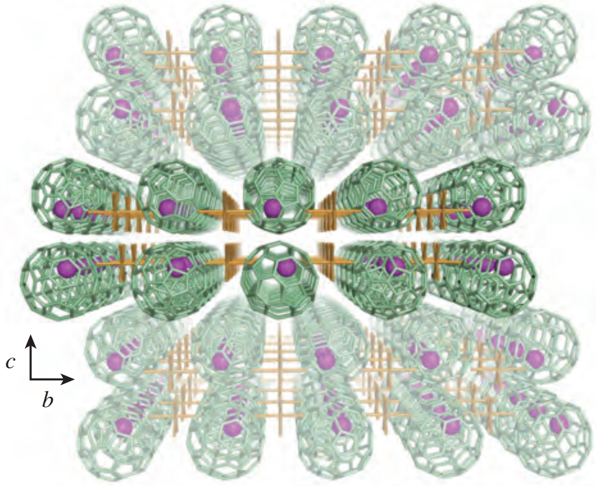

Fig. 2. Layered crystal structure of $[Li@C_{60}](SbCl_6)$. Slabs formed by two-dimensional arrays of $[Li@C_{60}](SbCl_6)$ units (Fig. 1(b)) are stacked along the *c*-axis. Three slabs (one layer in dense color and two outer layers in light colors) are shown in the figure.

Shinobu Aoyagi, Eiji Nishibori and Hiroshi Sawa*

Department of Applied Physics, Nagoya University

*E-mail: hiroshi.sawa@cc.nagoya-u.ac.jp

References

[1] Y. Kohama *et al.*: Phys. Rev. Lett. **103** (2009) 073001.
[2] K. Yakigaya *et al.*: New. J. Chem. **31** (2007) 973.
[3] *S. Aoyagi, E. Nishibori, H. Sawa, K. Sugimoto, M. Takata, Y. Miyata, R. Kitaura, H. Shinohara, H. Okada, T. Sakai, Y. Ono, K. Kawachi, K. Yokoo, S. Ono, K. Omote, Y. Kasama, S. Ishikawa, T. Komuro and H. Tobita: Nature Chem.* **2** *(2010) 678.*
[4] K. Sugimoto *et al.*: AIP Conf. Proc. **1234** (2010) 887.
[5] R.D. Bolskar *et al.*: J. Am. Chem. Soc. **125** (2003) 5471.

Surface molecular architecture : Highly crystalline metal-organic framework nanofilms assembled by Langmuir-Blodgett and layer-by-layer methods

The recent remarkable research activities and interest in new metal-organic frameworks (MOFs), porous coordination polymers (PCPs) or related porous hybrid solids arising from the virtually unlimited structural possibilities involving combinations of inorganic and organic building components have implications for general fundamental crystal growth techniques and for a number of potential applications in a wide range of fields from materials science to life science. In many cases of the targeted synthesis of polycrystalline or single-crystalline bulk MOFs using solvothermal reactions, the desired structures with well-defined pores were generated following rational molecular design routes, strategic choice of the combination of molecular components based on coordination chemistry knowledge and exploration of reaction conditions. On the other hand, controlling the size of porous objects at the nanoscale and aligning such objects on/with various substances in certain desired ways (e.g., sequentially layered on top of each other, patterned on surfaces) has remained a challenge that needs to be addressed, especially when we consider that such thin-film architectures are necessary for applications of these porous materials in nanotechnological devices. In addition, understanding the roles played by the nanoscale size and by the interfacial conditions in integrated systems in defining the properties of such porous solids can lead to the optimization of their potential functionalities.

Here, we introduce our recent study on the facile bottom-up fabrication at ambient temperature of a perfect preferentially oriented MOF nanofilm on a solid surface (NAFS-1), consisting of metalloporphyrin building units [1,2]. The construction of NAFS-1 was achieved by an unconventional integration in a modular manner of a layer-by-layer growth technique coupled with the Langmuir-Blodgett (LB) method. NAFS-1 is endowed with highly crystalline order in both the out-of-plane and in-plane orientations relative to the substrate, as demonstrated by synchrotron X-ray surface crystallography.

The fabrication strategy we developed is based on the principle of attempting first to prepare well-ordered 2D arrays of the desired building blocks on liquid surfaces by the LB method. In this way, we were able to remove any influence of the solid substrate on the in-plane molecular arrangement – such an influence can be of paramount (and often detrimental) importance when conventional epitaxial growth techniques on solid surfaces are undertaken. Having fabricated ordered monolayers at the air-water interface, these can then be deposited on appropriate substrates and sequentially stacked by following an LbL growth protocol (Fig. 1). We selected as the molecular component in our attempted formation of 2D arrays the CoTCPP metalloporphyrin (5,10,15,20-tetrakis(4-carboxyphenyl) porphyrinato-cobalt(II)) together with a source of copper(II) ions to serve as secondary building units and pyridine (py) as a coordination-saturating ligand (CoTCPP-py-Cu). The fabrication protocol was initiated by spreading a solution of CoTCPP and py onto an aqueous solution of $CuCl_2\cdot 2H_2O$ at room temperature. The 2D array of CoTCPP-py-Cu formed on the liquid surface was transferred to the solid substrate at room temperature. The substrate with the CoTCPP-py-Cu sheet was then rinsed with flowing distilled water, immersed in distilled water for 3 min, and finally dried by blowing nitrogen. To stack additional layers, CoTCPP-py-Cu monolayers

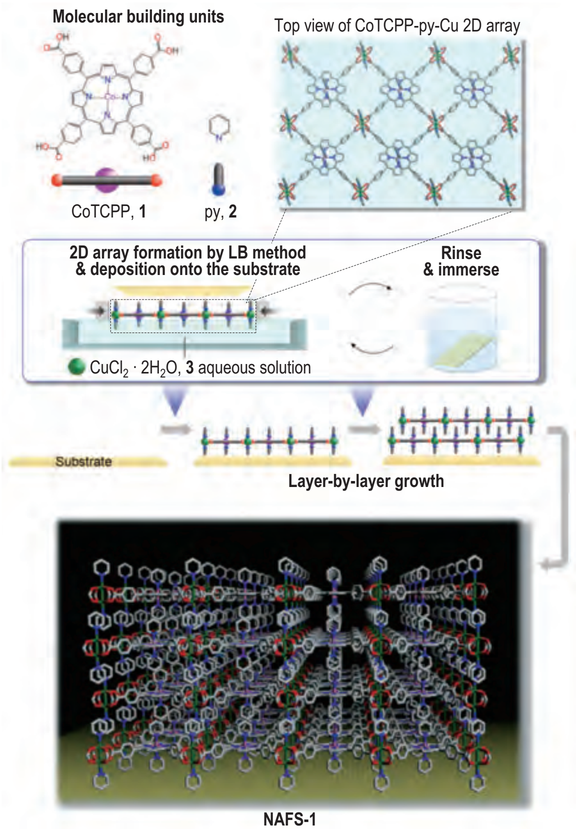

Fig. 1. Schematic illustration of the fabrication method of NAFS-1. The solution mixture of 5,10,15,20-tetrakis(4-carboxyphenyl) porphyrinato-cobalt(II) (CoTCPP), **1** and pyridine (py), **2** molecular building units is spread onto $CuCl_2\cdot 2H_2O$ **3** aqueous solution in a Langmuir trough. Pressing the surface with barrier walls leads to the formation of a copper-mediated CoTCPP 2D array (CoTCPP-py-Cu) (LB method). The 2D arrays are deposited onto the substrate by the horizontal dipping method at room temperature. The substrate is then immersed in the pure solvent to remove excess starting materials or physisorbed components and dried. The repetitive process of successive sheet deposition and rinsing/solvent immersion leads to the sequential layer-by-layer growth of NAFS-1 with any desired thickness.

on the subphase were repeatedly transferred onto the substrate. The number of layers deposited is controlled by the number of cycles of sheet deposition and rinsing/solvent immersion/drying. The successive LbL growth procedure of NAFS-1 was monitored by UV-vis spectroscopy [1,2]. The linear increase in the absorbance of the CoTCPP Soret band indicates that roughly the same amount of CoTCPP is deposited in each step of the layer stacking protocol.

Detailed insight into the crystallinity, preferred orientation and homogeneity of the fabricated NAFS-1 films was obtained by synchrotron X-ray (λ = 1.554 Å) diffraction, carried out in two different scattering geometries – out-of-plane mode, which is sensitive to the lattice parameter in the growth direction, and in-plane (grazing incidence) mode, which is sensitive to the in-plane lattice dimensions. Figure 2 shows the XRD pattern recorded in the out-of-plane geometry for NAFS-1 with 20 stacking cycles fabricated on a Si(100) substrate. Three diffraction peaks are observed, revealing the highly oriented nature of the material. They can be indexed as (001), (002), and (003), leading to a 0.9380(3) nm interlayer spacing. Figure 3(a) shows the in-plane XRD pattern for the NAFS-1 sample measured at an incident angle α = 0.1°. Seven diffraction peaks are observed up to a scattering angle 2θ of 45° and index as (110), (200), (320), (400), (330), (440), and (550)/(710) on a metrically tetragonal unit cell with basal plane dimensions, $a = b = 1.6460(3)$ nm. An important point to note here is that none of the Bragg reflections observed in grazing incidence geometry coincides with any of the peaks measured in the out-of-plane XRD pattern and that all the in-plane XRD peaks indexed as (hk0) – no (hkl) ($l \neq 0$) reflections are present. This signifies not only that NAFS-1 is characterized by highly crystalline order in the in-plane orientation but also that it grows in a perfect preferentially oriented directionally controlled manner. Our structural model for NAFS-1 consists of a 2D "checkerboard" motif of CoTCPP units linked by binuclear $Cu_2(COO)_4$ paddle-wheels for each stacked sheet (Fig. 3(b)). In the NAFS-1 structural model, two monodentate pyridine molecules axially coordinate to both the copper dinuclear block and CoTCPP to complete the coordination sphere and retain two-dimensionality (Fig. 3(c)). As shown in Fig. 3(a), the simulation of the in-plane XRD pattern (including only (hk0) peaks) is in excellent agreement with experiments for this structural model. We expect that the versatility of the solution-based growth strategy presented here will enable the fabrication of various well-ordered MOF nanofilms, the way for their use in a range of important applications.

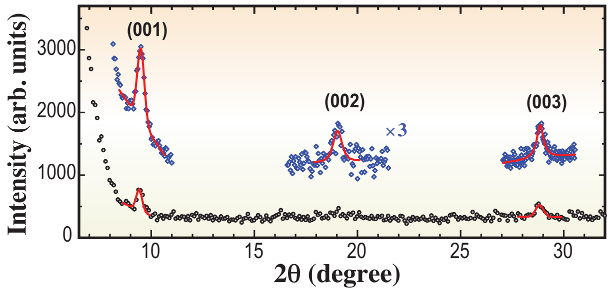

Fig. 2. Out-of-plane synchrotron XRD patterns of NAFS-1. Observed (solid circles) and fitted (red solid line) out-of-plane synchrotron X-ray diffraction profiles (λ = 1.554 Å) for an NAFS-1 thin film (20 deposition cycles) on a Si(100) substrate. The inset shows additional higher statistics fine scans collected in the vicinity of the three diffraction peaks.

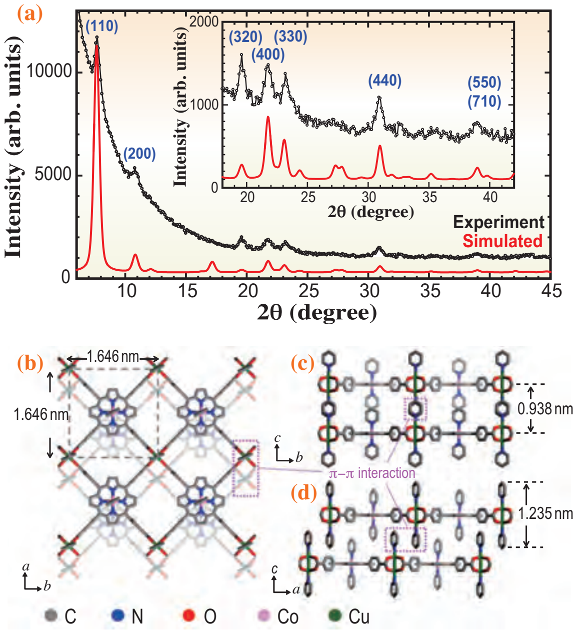

Fig. 3. In-plane synchrotron XRD patterns and the derived structural model for NAFS-1. **(a)** Observed (solid circles) and calculated (red line) in-plane synchrotron X-ray diffraction profiles (λ = 1.554 Å) for a NAFS-1 thin film (20 deposition cycles) on a Si(100) substrate. **(b)** Basal plane projection of the proposed crystalline structure for NAFS-1. **(c, d)** Schematic diagrams of the proposed crystalline structure for NAFS-1 viewed along the *a*- and *b*-axes, respectively. The interdigitated layer stacking can be driven by attractive π–π interactions between adjacent Cu^{2+}-coordinated pyridine molecules that protrude from the 2D sheets.

Rie Makiura[a,b,*] and Hiroshi Kitagawa[b,c]

[a] Nanoscience and Nanotechnology Research Center, Osaka Prefecture University
[b] JST-CREST
[c] Division of Chemistry, Kyoto University

*E-mail: r-makiura@21c.osakafu-u.ac.jp

References

[1] *R. Makiura, S. Motoyama, Y. Umemura, H. Yamanaka, O. Sakata and H. Kitagawa: Nature Mater.* **9** *(2010) 565.*
[2] *R. Makiura and H. Kitagawa: Eur. J. Inorg. Chem.* **24** *(2010) 3715.*

Photoresponsive soft material by large-scale molecular ordering of a polymer brush

As exemplified by skeletal muscles, living organisms make use of long-range three-dimensional (3D) molecular orders to achieve particular biological functions. This notion has prompted chemists to develop effective methods for tailoring elaborate molecular assemblies over a macroscopic length scale. Such a technology is considered essential for creating high-performance organic materials and devices. Although several approaches, including the use of shear forces, external electric fields, and patterned surfaces, enable the one-dimensional (1D) macroscopic ordering of liquid crystalline molecules and polymers, no rational molecular design strategy or processing methodology has yet been developed for the 3D ordering of large and/or complex molecules in macroscopic solid materials.

In this report, we describe our recent finding that a one-step hot pressing of a certain graft polymer, sandwiched by uniaxially stretched Teflon sheets, affords a free-standing film, where a 3D molecular order with a remarkably high structural integrity develops widely on its both sides over a macroscopic size regime [1]. The graft polymer that makes the unique structuring event possible is a polymer brush consisting of a polymethacrylate backbone wrapped with densely grafted paraffinic side chains containing three azobenzene units (poly-**1**, Fig. 1). The azobenzene functionality serves as a mesogenic core of liquid crystalline molecules and is capable of reversible photochemical transformation between its *trans* and *cis* forms with a large structural change.

Poly-**1** was prepared by the free-radical polymerization of **1** (M_n = 1.5 × 10^5 g/mol). This polymer brush showed two exothermic peaks at 120 and 103°C on cooling from its isotropic melt. To determine the structure of poly-**1** at the mesophase, we measured synchrotron radiation small-angle X-ray scattering (SAXS) using beamline **BL45XU**. The SAXS pattern, thus obtained (Fig. 2(a)), showed multiple reflection peaks assignable to a 2D rectangular lattice (space group; $P2_1/a$) with lattice parameters *a* and *b* of 218(5) and 147(1) Å, respectively. This observation suggests that poly-**1** molecules adopt an elliptically cylindrical structure and align parallel to one another without the entanglement of their side chains.

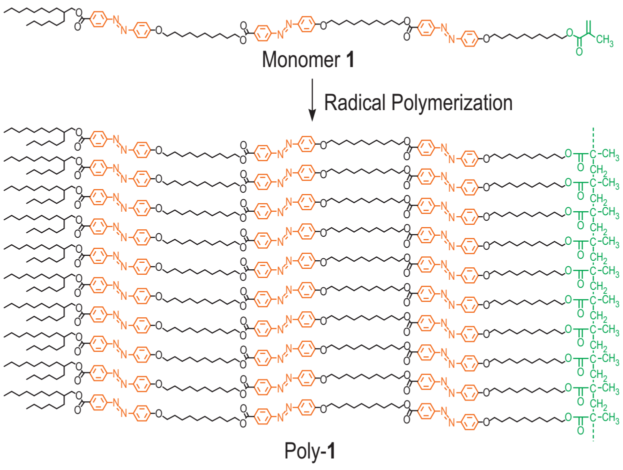

Fig. 1. Molecular formulae of monomer **1** and poly-**1**.

We found an interesting phenomenon that the polymer molecules, upon hot pressing with commercially available Teflon sheets, orient in a macroscopic regime to yield a free-standing film. When the resultant film was exposed to a synchrotron X-ray beam in a direction perpendicular to the film plane, a through-view 2D SAXS image, characteristic of a rectangular structure ($P2_1/a$), was obtained (Fig. 2(b)). The diffuse spots were successfully

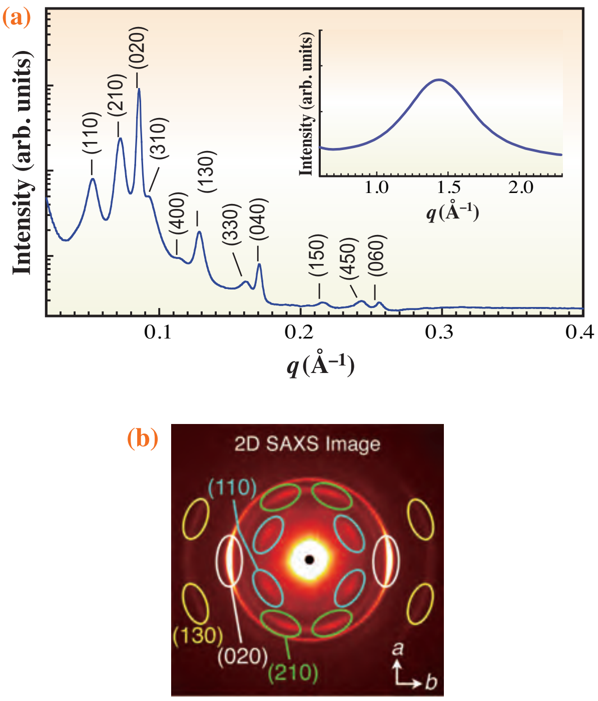

Fig. 2. SAXS data of poly-**1**. Miller indices are given in parentheses. **(a)** 1D SAXS pattern of a powdery sample of poly-**1** in a capillary, measured at 115°C on cooling from its isotropic melt. (Inset) Scattering profile in wide-angle region. **(b)** Through-view 2D SAXS images of hot-pressed film of poly-**1**.

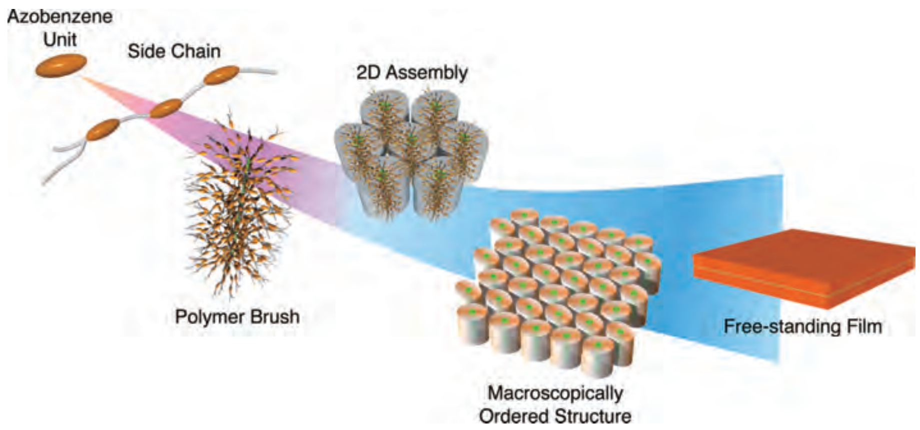

Fig. 3. Schematic illustration of 3D molecular order in hot-pressed polymer brush film.

assigned to the reflections from the (*hkl*) = (110), (210), (020), and (130) planes. Through detailed structural investigation, we revealed that the hot pressing enables the unidirectional alignment of the polymer brush in such a way that the backbone of the polymer brushes orients perpendicular to the film plane, while the side chains align horizontally along the drawing direction of the Teflon sheets (Fig. 3). The 3D molecular ordering thus observed most likely originates from the polymer brush-mediated structural transfer at the contact interface. In the Teflon sheet, polytetrafluoroethylene (PTFE) molecules are oriented along the drawing direction, and this structural information is transferred to bulk poly-**1** at the interface, so that the azobenzene-containing side chains of poly-**1** are oriented along the direction of PTFE molecules.

The large-area 3D molecular ordering of poly-**1** endows a hot-pressed polymer film with photoactuating capability. Thus, the film rolls up and flattens upon alternate irradiation with UV and visible light (Fig. 4). By detailed investigations, we found that the film possesses competing strains on its both sides. Upon exposure to light, the strain on the photoirradiated side of the film is released, so that the competing strain on the other side prevails, thereby resulting in a photomechanical bending motion.

The present achievement provides a new design concept for photomechanical soft materials and may update the common perception on such materials that the covalent crosslinking of photoactive molecular components is always essential for exerting macroscopic motions. More importantly, the processing method using a polymer brush and Teflon sheets, which enables large-area 3D molecular ordering, has great potential in the development of high-performance organic materials including electronic materials for thin-film organic transistors and solar cells.

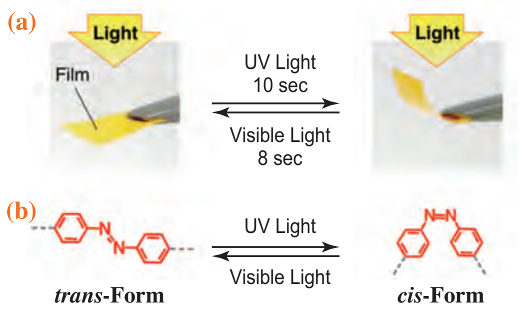

Fig. 4. **(a)** Photomechanical bending motion of hot-pressed polymer brush film. **(b)** Structural deformation of azobenzene molecule upon exposure to UV and visible light.

Takashi Kajitani

RIKEN Advanced Science Institute (Wako)

E-mail: kajitani@riken.jp

References

[1] *N. Hosono, T. Kajitani, T. Fukushima, K. Ito, S. Sasaki, M. Takata and T. Aida: Science* ***330*** *(2010) 808.*

Highly selective sorption of oxygen and nitric oxide by an electron-donating flexible porous coordination polymer

The recognition and selective accommodation of gas molecules are vital challenges in the environmental and industrial fields, and fascinating subjects for scientific study. Enhancing the molecular recognition ability of the microporous domain is an important aim of such research; achieving this aim requires providing good affinity for the target molecule and a means to avoid the uptake of other molecules. In the cases of conventional porous materials, there are few molecules applicable to selective accommodation because of the difficulty in designing structures having the properties mentioned above. On the other hand, porous coordination polymers (PCPs) or metal organic frameworks (MOFs) possessing designability that provides various kinds of host–guest interaction, as well as flexibility that allows guest-responsive dynamic accommodation, have attracted much attention as strong candidates for this purpose [1,2]. The design of the pore surfaces to increase the affinity for target molecules is recognized as a good approach to attaining some positive results for selective accommodation. Furthermore, structural flexibility, causing the closed/open-type structural transformation, is the linchpin for the exclusion effect, which enhances the selectivity. For many conventional porous materials, their selective gas sorption properties depend on the size and shape effects, and the dispersion force. Therefore, it is difficult to achieve the retrograde tendency of the selectivity to these factors. Focusing on O_2 as a target adsorbate molecule presents some difficulties in designing the mechanism of O_2 recognition from N_2 and Ar, which have similar molecular shape or size to O_2. Here, we report a PCP having an exceptional selective sorption property for O_2 and NO utilizing the charge transfer interaction between the guest and the host.

A potential mechanism of the gate-opening properties for selective accommodation of target molecules is the structural transformation. The synthesized [Zn(TCNQ-TCNQ)bpy](**1**) has a flexible three-dimensional structure constructed from a Zn(II) cation, 4,4′-bipyridyl (bpy), and a TCNQ dimer, which is the interactive dianion unit for the guest molecule (Fig. 1), and shows the closed/open-type structural transformation accompanying the adsoption/desorption process. These properties make **1** a good candidate adsorbent for selective separation. The channels delimited by the TCNQ dimer have an undulating form, which is unique, comprising an alternating arrangement of two types of tubes of large and small diameters. The electron-rich pore surfaces of **1** should have a good affinity for electron-accepting molecules. This tendency can be observed in the case of gas molecules.

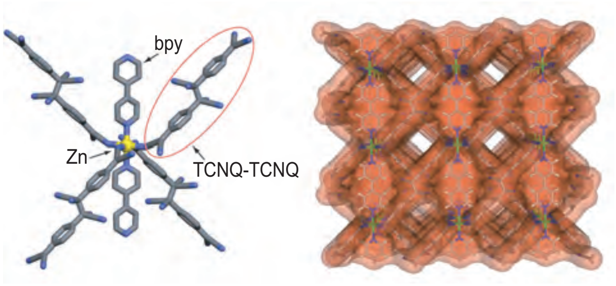

Fig. 1. Crystal structure of **1**. The geometry around the Zn ion (left) and the whole network structure (right) are shown.

The sorption isotherms of several kinds of gas molecule were measured in the closed form **1** (Fig. 2). Interestingly, only in the cases of O_2 and NO did this compound show the sorption phenomena characteristic of the gate-type sorption behavior: no uptake in the low-concentration region and an abrupt enhancement of adsorption after the threshold concentration. This behavior based on the closed/open-type structural transformation was detected by X-ray powder diffraction (XRPD) analysis. The synchrotron XRPD patterns of the open form and the closed form are distinctly different from each other. Accompanying the accommodation of O_2 and NO, the patterns from the closed form to the new phases with almost the same unit cells as those of the open form was observed. The saturation-adsorbed amount of O_2 was 268 cm^3 (at STP)g^{-1}, and that of NO was 322 cm^3 (at STP)g^{-1}. In contrast, no sharp uptake over one molecule per

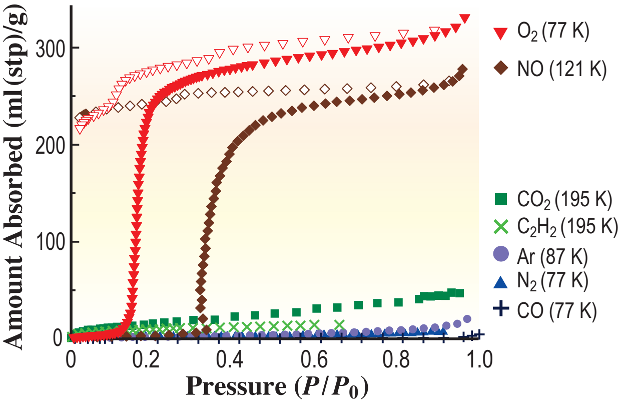

Fig. 2. Adsorption isotherms of several gas molecules on **1**.

formula was observed in the other gas molecules (N_2, CO, CO_2, C_2H_2, and Ar). In this phenomenon, the closed/open transition is important because the trigger of the transformation—the interaction between the host and guest—is an overriding factor for this selectivity. Considering the case of the lack of uptake of CO_2 and C_2H_2, the quadrupole moment and polarizability, which have a strong effect on the dispersion force of the molecule, have no bearing on this selectivity. In contrast to that in the case of NO, no uptake of CO indicates that the electric dipole moment of guest molecules is not associated with this phenomenon. From these results and background, **1** seems to respond to and recognize some sort of properties common to O_2 and NO.

The Raman spectrum of **1** under the O_2 sorption condition was measured to elucidate the state of **1** and O_2 in the sorption process. The ν(O=O) stretch band, which is the index of the physical and chemical states of the O_2 molecule, can be detected directly. As the sorption of the $^{16}O_2$ molecule progressed, two peaks were observed: a sharp peak at 1454 cm^{-1} and a broad peak at 1449 cm^{-1}. When O_2 was adsorbed on a microporous compound, a slight blue shift of the ν(O=O) stretching band by about 10 cm^{-1} was induced by physical stress in nanospace, the so-called confinement effect. On the other hand, the case of **1** shows a propensity different to that shown in the previous result. The large redshift of the ν(O=O) band by about 100 cm^{-1} cannot be induced by the confinement effect. Compared with the reported peak positions of ν(O=O) stretching in the various electronic states, the band suggests that O_2 molecules accommodated in **1** have a partial negative charge and that there is no redox reaction with one-electron transfer. This is direct evidence of the existence of the CT interaction between the framework and O_2 molecules and that they are in an exceptional state with an electronic effect and a confinement effect.

We have discovered that **1** shows the selective recognition of O_2 and NO molecules. This specific sorption ability is ascribed to the closed/open-type structural transformation triggered by the CT interaction between the host framework and guest molecule (Fig. 3). The key to this selectivity is the combination of structural dynamics and electron-donating function of the framework, which can be induced by the soft crystallinity and designability of PCPs. PCPs will provide a new platform for selective adsorption systems for small gas molecules.

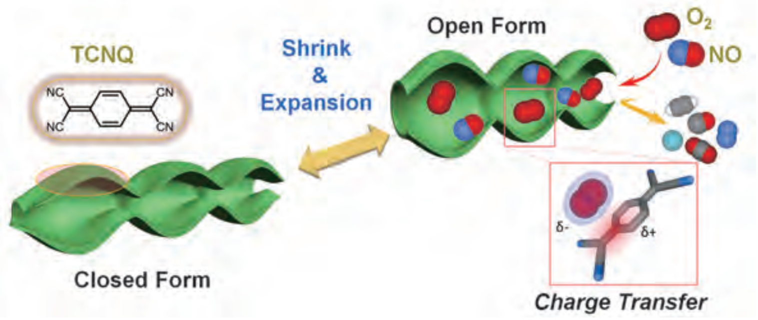

Fig. 3. A schematic representation of the concept shown in this work. The channel formed in TCNQ-based PCP (green tube) shows an expanding/shrinking structural transformation for the NO and O_2 guests, which is induced by the partial charge transfer interaction between the host and the guest.

Ryotaro Matsuda[a,b,c,*], Satoru Shimomura[b] and
Susumu Kitagawa[a,b,c]

[a] Exploratory Research for Advanced Technology (ERATO),
Japan Science and Technology Agency (JST)
[b] Institute for Integrated Cell-Material Sciences,
Kyoto University
[c] SPring-8/RIKEN

*E-mail: ryotaro.matsuda@kip.jst.go.jp

References

[1] S. Kitagawa *et al*.: Coord. Chem. Rev. **251** (2007) 2490.
[2] R. Matsuda *et al*.: Nature **436** (2005) 238.
[3] J. Seo *et al*.: J. Am. Chem. Soc. **131** (2009) 12792.
[4] *S. Shimomura, M. Higuchi, R. Matsuda, K. Yoneda, Y. Hijikata, Y. Kubota, Y. Mita, J. Kim, M. Takata, S. Kitagawa: Nature Chem.* ***2*** *(2010) 633.*

Discovery of 'bicontinuous cubic' liquid crystalline mesophase from discotic molecules

Liquid crystalline (LC) semiconductors have attracted increasing attention owing to their potential use in solution-processable and self-repairable organic electronics. Toward this goal, extensive studies have been performed on hexagonal columnar (Col_h) assembly of discotic LC molecules, since their π-stacked columnar arrays are expected to serve in electrical conduction. However, in a practical sense, the macroscopic alignment of such conducting columns with a desired configuration requires much effort to realize. From this point of view, discotic LCs with a bicontinuous cubic (Cub_{bi}) geometry might work, if their three-dimensionally interconnected networks serve as π-electronic channels.

Here, we report that triphenylene (TP) derivatives (Fig. 1(a)) carrying paraffinic side chains with ionic liquid (IL) termini form an LC mesophase with a Cub_{bi} geometry over a wide temperature range including room temperature. In 2005, we reported that $\mathbf{1}_{10}$ (see Fig. 1) forms an LC assembly with a Col_h geometry [1]. The phase sequence upon cooling displayed, after the Col_h mesophase (111–47°C), an optically isotropic phase, which however was not identified because of the lack of clear diffractions obtained in our conventional diffractometer for X-ray analysis (XRD). Recently, we have reinvestigated the phase diagram of $\mathbf{1}_{10}$ using a synchrotron radiation beam (**BL02B2** and **BL44B2**) and found that the optically isotropic phase is not amorphous but an LC mesophase with a Cub_{bi} geometry (Fig. 1(b)) [2]. This unexpected observation prompted us to design 19 new TP derivatives with different paraffinic spacers and IL pendants (Fig. 1(a)). Interestingly, two of them with a long tetradecyl spacer between the TP core and IL pendants, i.e., $\mathbf{1}_{14}$ and $\mathbf{2}_{14}$, exclusively form a Cub_{bi} LC mesophase over a very wide temperature range (~200°C).

The optically isotropic phase of $\mathbf{1}_{10}$ at 30°C displayed 14 distinct diffraction peaks in a small-angle region (2θ = 1.8–5.6°, Fig. 2(a)). The reciprocal spacing ratios of these diffraction peaks ($\sqrt{6}:\sqrt{8}:\sqrt{14}:\sqrt{16}:\sqrt{20}:\sqrt{22}:\sqrt{24}:\sqrt{26}:\sqrt{30}:\sqrt{32}:\sqrt{38}:\sqrt{42}:\sqrt{46}:\sqrt{50}$) agreed well with those expected for the cubic symmetry with the space group $Ia\bar{3}d$. Upon heating to 87°C, these peaks disappeared completely, and instead, a set of new diffractions with d-spacings of 17.0, 14.7, and 11.2 Å appeared (Fig. 2(b)). As previously reported [1], these new peaks were indexed as the (110), (200), and (210) diffractions of a Col_h mesophase (Fig. 1(b)). As summarized in Fig. 3, the phase transition behaviors of the other TP derivatives (Fig. 1(a)) on heating were likewise determined by synchrotron radiation XRD analysis. Ten TP derivatives formed a Cub_{bi} mesophase, which in every case appeared in a lower temperature range than the Col_h mesophase. In the comparison of $\mathbf{1}_{10}$ with $\mathbf{1}_8$, $\mathbf{1}_{12}$, and $\mathbf{1}_{14}$ with BF_4^- counterions, note that their phase behaviors are highly dependent on the length of the paraffinic side chains. Compound $\mathbf{1}_8$ with the shortest side chains among the family showed only a glass-to-isotropic transition (Fig. 3(a)). On the other hand, analogously to $\mathbf{1}_{10}$, $\mathbf{1}_{12}$ with dodecyl chains exhibited a bicontinuous $Ia\bar{3}d$ cubic phase, although, in a much wider temperature range (16–160°C, on heating) than that observed for $\mathbf{1}_{10}$. To our surprise, a further increase in the side-chain length from dodecyl ($\mathbf{1}_{12}$) to tetradecyl ($\mathbf{1}_{14}$) resulted in the exclusive formation of a Cub_{bi} mesophase from 24 up to 221°C. To the best of our knowledge, there are no LC molecules that form a Cub_{bi} mesophase in

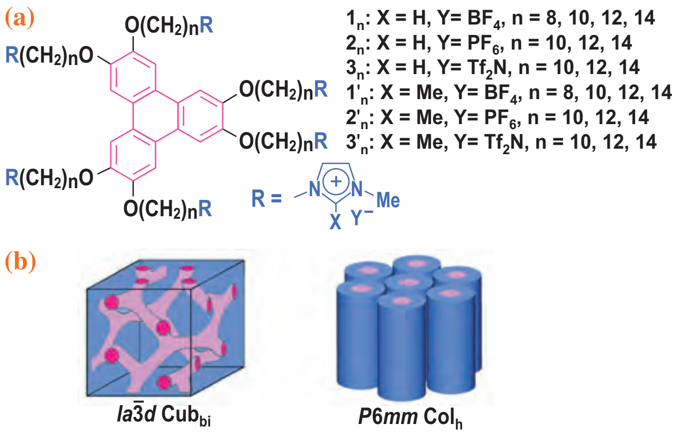

Fig. 1. Schematic structures of **(a)** imidazolium ion-appended triphenylene derivatives and **(b)** bicontinuous cubic ($Ia\bar{3}d$) and hexagonal columnar ($P6mm$) liquid crystalline assemblies.

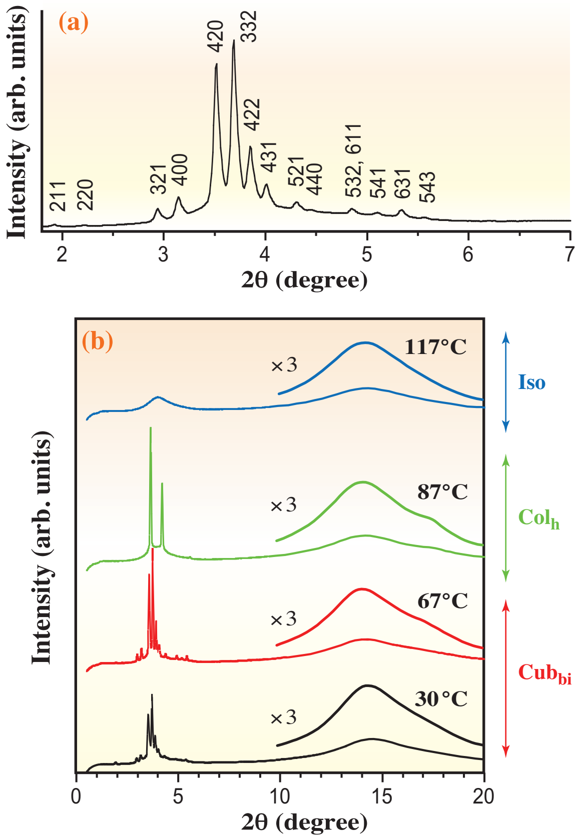

Fig. 2. **(a)** XRD pattern of **1**$_{10}$ at 30°C. The numbers indicate the Miller indices. **(b)** Temperature-dependent XRD patterns of **1**$_{10}$ on heating in 2θ ranges of 0–20°. The wavelength of the X-ray was set at 1.08 Å.

such an extremely wide temperature range (~200°C) from room temperature. When the counteranions were changed from BF_4^- to larger ones such as PF_6^- (**2**), an essentially identical side-chain dependence of the phase transition emerged, where **2**$_{14}$ exclusively formed a Cub$_{bi}$ LC mesophase over a very wide temperature range (21–177°C, upon heating). Nonetheless, **2**$_{10}$ with decyl chains, in contrast to its BF_4^- analogue (**1**$_{10}$), did form no LC assembly. When much larger counteranions such as bis(trifluoromethanesulfonyl)imide (Tf_2N^-) were employed, no LC assembly was obtained from **3**$_{12}$ with dodecyl side chains, and even **3**$_{14}$ with the longest side chains among the family formed not only Cub$_{bi}$ mesophase but also gave Col$_h$ mesophase. Nevertheless, as an overall tendency, TP with larger counteranions ($BF_4^- \rightarrow PF_6^- \rightarrow Tf_2N^-$) requires longer paraffinic side chains (decyl → dodecyl → tetradecyl) to form the Cub$_{bi}$ mesophase. Having this trend in mind, we also investigated the phase behaviors of **1’–3’** with bulkier imidazolium ion pendants than **1–3**. As shown in Fig. 3(b), only four TP derivatives showed, though not exclusively, the Cub$_{bi}$ LC mesophase. With respect to the effects of paraffinic side chains and counteranions, the trends observed for **1’–3’** appear to be similar to those for **1–3**. Possibly owing to the larger IL pendants in **1’–3’**, the formation of the Cub$_{bi}$ LC assembly required much longer paraffinic side chains than that in the case of **1–3**. Typically, **1’**$_{10}$ and **2’**$_{12}$, in contrast to **1**$_{10}$ and **2**$_{12}$, showed no Cub$_{bi}$ mesophase, only a Col$_h$ mesophase, between the glassy and melt states.

Overall, both Col$_h$ and Cub$_{bi}$ LC mesophases are most likely composed of π-stacked TP columns. We consider that (1) the π-stacking of the discotic core and (2) the interionic interaction of IL pendants are two major parameters for determining the phase diagram. When the paraffinic chains are sufficiently long, LC mesophases result, where the core and IL pendants can undergo π-stacking and interionic interactions, respectively. Meanwhile, when the paraffinic chains are rather short, LC mesophases hardly emerge unless the IL pendants are sufficiently small, since the columnar π-stacking of the discotic core is sterically disturbed. Semiconducting Cub$_{bi}$ LC materials, unveiled in the present work, are quite attractive for many applications.

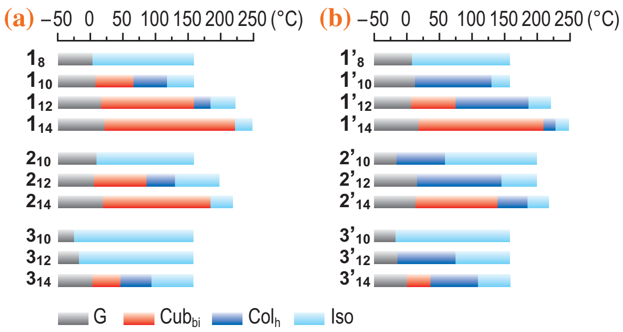

Fig. 3. Phase transition behaviors of imidazolium ion-appended triphenylene derivatives upon heating. G: glass, Cub$_{bi}$: bicontinuous cubic, Col$_h$: hexagonal columnar, and Iso: isotropic liquid. Compound **1’**$_{14}$ showed a $Pn\bar{3}m$ cubic-to-$Ia\bar{3}d$ cubic transition at 129°C.

Yohei Yamamoto

Graduate School of Pure and Applied Sciences,
University of Tsukuba

E-mail: yamamoto@ims.tsukuba.ac.jp

References

[1] J. Motoyanagi *et al*.: Chem. Commun. (2005) 101.
[2] *M.A. Alam, J. Motoyanagi, Y. Yamamoto, T. Fukushima, J. Kim, K. Kato, M. Takata, A. Saeki, S. Seki, S. Tagawa, T. Aida: J. Am. Chem. Soc.* ***131*** *(2009) 17722.*

Structure of liquid and glassy $ZnCl_2$

A basic question in glass science concerns the nature of the glass transition and, while this process is intimately related to the dynamical properties of a system on cooling [1], it is nevertheless important to understand the atomic ordering in the liquid and glass. Within the family of binary network glass forming systems, $ZnCl_2$ is an exemplar whose basic properties can be understood in terms of an ionic interaction model, provided that anion polarisation effects are taken into account, i.e. it is possible to model this material by using large scale molecular dynamics methods [2]. We have therefore applied a combination of neutron and X-ray diffraction techniques to measure the full set of partial structure factors for liquid and glassy $ZnCl_2$, thus maximising the information that can be obtained at the pair correlation function level [3,4].

The neutron diffraction experiments employed the method of isotope substitution and were made using the instrument D4c at the Institut Laue-Langevin in Grenoble, France. The high energy X-ray diffraction experiments used beamline **BL04B2** at SPring-8 with an incident wavelength of 0.2 Å. The sample for the X-ray experiments was held in a silica capillary tube which was loaded by using the “Hummingbird” method in which anhydrous beads of $ZnCl_2$ are first sealed under vacuum in a silica tube connected to the capillary (Fig. 1). The beads are then evaporated in an oven, condensed into a liquid within the capillary, and quenched to form a glass. The capillary containing the sample is finally sealed under vacuum. The full set of partial structure factors were extracted from the neutron diffraction data sets by using the method of singular value decomposition [4]. Their accuracy was assessed by using them to reconstruct the expected X-ray diffraction pattern, making a correction for the effect of the resolution function of the neutron diffractometer [5]. A comparison between the measured and reconstructed X-ray diffraction patterns for liquid and glassy $ZnCl_2$ is shown in Fig. 2.

The diffraction patterns were used to construct three-dimensional models (Fig. 3) for liquid and glassy $ZnCl_2$ by employing the reverse Monte Carlo (RMC) method [4]. The results show that the predominant structural motif in both phases is the corner sharing $ZnCl_4$ tetrahedron where the average

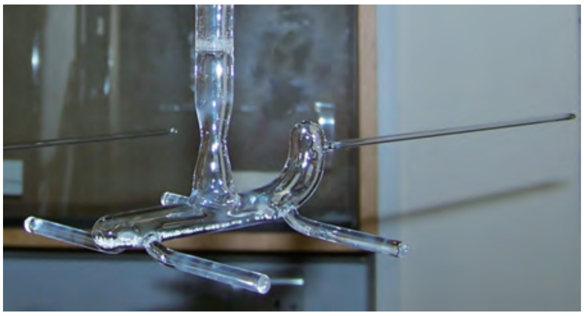

Fig. 1. The “Hummingbird” apparatus, made from silica, which was used to load a capillary tube with the $ZnCl_2$ sample for the X-ray diffraction experiments. The sample is initially in the form of white anhydrous beads which can be seen in the “body” of the bird while a long thin capillary tube forms the “beak” of the bird on the right hand side. The vertical tube, which is used to load the beads into the bird, is initially connected to a vacuum line but is sealed prior to placing the apparatus into an oven.

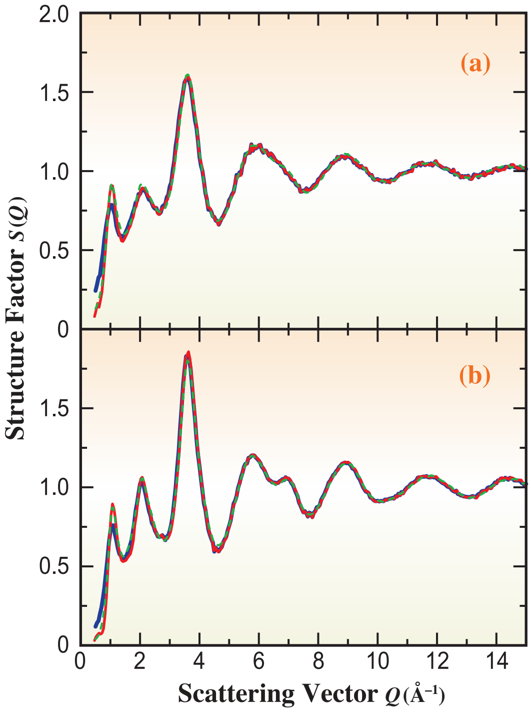

Fig. 2. Comparison between the X-ray and neutron diffraction results for **(a)** liquid $ZnCl_2$ at 330°C and **(b)** glassy $ZnCl_2$ at room temperature. For each panel, the broken (green) curve corresponds to the structure factor $S(Q)$ measured by using X-ray diffraction, the solid dark (blue) curve corresponds to the X-ray structure factor reconstructed from the neutron diffraction results, and the solid light (red) curve corresponds to this data after correction for the resolution function of the neutron diffractometer. The resolution function correction improves agreement between the neutron and X-ray data sets, especially in the region around the first sharp diffraction peak at $Q \approx 1$ Å^{-1}.

Zn-Cl coordination number is 3.96 for the liquid and 3.99 for the glass. There is also a small number of edge sharing configurations, these being more abundant in the liquid. The fraction of fourfold coordinated Zn atoms in corner and edge sharing configurations was estimated at 82% and 18% for the glass and at 63% and 37% for the liquid, respectively. The tetrahedra organize on an intermediate length scale to give a so-called first sharp diffraction peak in the measured diffraction patterns at a scattering vector $Q \approx 1$ Å^{-1} that is most prominent for the Zn-Zn correlations i.e. this peak arises from the ordering associated with the tetrahedron centres. An analysis of the connectivity profiles for the models shows an absence of odd membered rings which is a characteristic of a chemically ordered network (Zn-Cl-Zn-Cl connections), as befits an ionic system. Sixfold rings containing three Zn and three Cl atoms are a significant feature of both the liquid and glass networks.

The relative ‘‘fragility’’ of glass forming materials is a measure of the rate at which the dynamical properties of a liquid change on approaching the glass transition. In the case of $ZnCl_2$, the temperature dependence of the liquid viscosity shows behavior that is intermediate between “strong” glass forming systems such as SiO_2 and GeO_2 and “fragile” glass forming systems such as $KCl\text{-}BiCl_3$ and $Ca_2K_3(NO_3)_7$. Recent molecular dynamics work on tetrahedral glass forming liquids with the MX_2 stoichiometry suggests that the fragility of a melt increases with the number of edge sharing configurations [2]. The present results for liquid $ZnCl_2$ are consistent with this notion since they show the presence of edge sharing units, these conformations being absent in strong liquids such as SiO_2 and GeO_2.

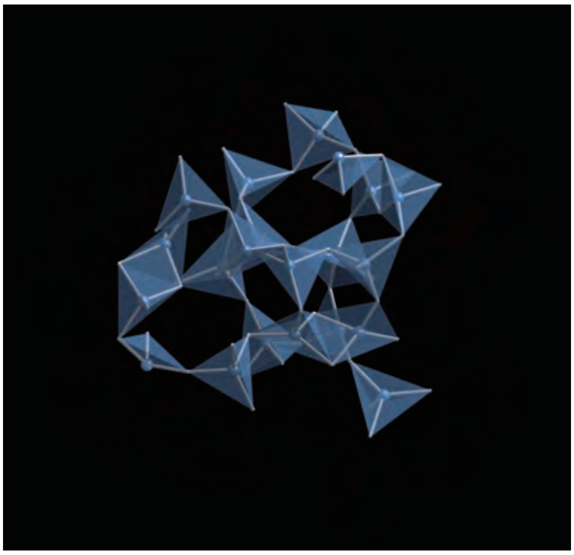

Fig. 3. A representative atomic configuration in glassy $ZnCl_2$ as extracted from the RMC model. Corner sharing $ZnCl_4$ tetrahedra are the predominant structural motifs where a Zn atom (large sphere) resides at the centre of a tetrahedron and four Cl atoms (small spheres) reside at its vertices. A few edge sharing $ZnCl_4$ tetrahedra also occur.

Anita Zeidler[a], Philip S. Salmon[a,*] and Takeshi Usuki[b]

[a] Department of Physics, University of Bath, UK
[b] Department of Material and Biological Chemistry, Yamagata University

*E-mail: P.S.Salmon@bath.ac.uk

References

[1] A. Cavagna: Phys. Reports **476** (2009) 51.
[2] M. Wilson and P.S. Salmon: Phys. Rev. Lett. **103** (2009) 157801.
[3] P.S. Salmon *et al.*: Nature **435** (2005) 75.
[4] *A. Zeidler, P.S. Salmon, R.A. Martin, T. Usuki, P.E. Mason, G.J. Cuello, S. Kohara and H.E. Fischer: Phys. Rev. B* ***82*** *(2010) 104208.*
[5] W.S. Howells: Nucl. Instrum. Meth. Phys. Res. **219** (1984) 543.

Studies of the degraded state of excavated archaeological silk fibers using infrared microspectroscopy

Several kinds of textile fabric made of silk fibers have been found in many archaeological sites in Japan. However, almost all of them were heavily degraded owing to their long-term exposure to the elements underground. Therefore, the identification of textile materials is often difficult. Besides, only a small amount of sample is available.

The objective of this research is to enable the characterization of degraded archaeological silk fibers using FTIR microspectroscopy. The samples used were excavated from the *Fujinoki* tumulus (6th century AD) and the *Shimoikeyama* tumulus (3rd century AD) in Nara Prefecture. Both archaeological sites are famous for several excavated remains including textile fabrics. Since organic subjects are almost all in a heavily degraded state, it is very difficult to identify the original textile fibers.

The degraded archaeological silk fibers of the Fujinoki tumulus (6th century AD) are shown in Fig. 1 and were gifted by the Kashihara Archaeology Institute, Nara Prefecture. The degraded silk fibers show diverse characteristics: collapsed fibers, absolutely pulverized, etc. First, suitable fiber samples were selected using a stereomicroscope. All of the selected fibers showed a distinct direction of the fiber axis and a clear cross-sectional pattern.

The infrared microspectroscopy of beamline **BL43IR** was used. To identify the fiber material, a stereomicroscope and a super high-resolution scanning electron microscope were also used. A high-brilliance infrared synchrotron radiation beam was focused on the surface of a very small amount of sample fibers.

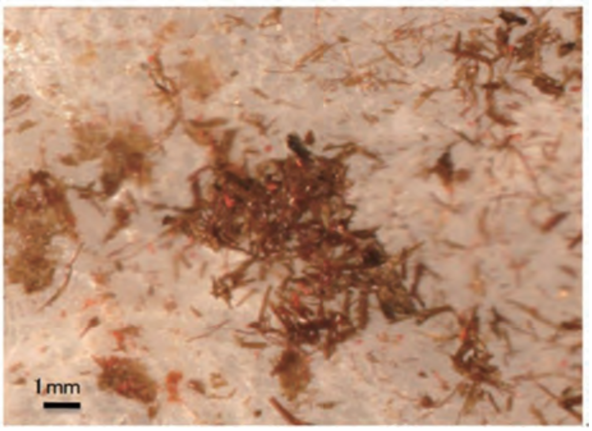

Fig. 1. Photograph of degraded archaeological silk fibers of the *Fujinoki* tumulus.

FTIR microspectroscopy was used since it requires only a small amount of sample, and its sample preparation is easy. The infrared spectra obtained show deformed profiles due mainly to the degradation of the silk fibers. The second derivative of the spectrum is useful for the analysis of the change in the secondary structure of silk fibroin molecules. Curve fitting analysis was also performed by combining established procedures for research.

Prior to the measurement, the silk fibers were pressed on a diamond cell to produce a thin-film sample. The sample prepared on the diamond cell was transferred to the measurement compartment, and measured by the transmittance mode. The measurement conditions are as follows: resolution, 4 cm^{-1}; numbers of scans, 1024 or 2048; wavenumber range, 4000-700 cm^{-1} for several absorption peaks in which each peak is further composed superposed component peaks.

As a preliminary identification of the fiber material, the infrared spectrum of each sample was measured. Since all of the samples showed distinct absorption peaks of the secondary amide, the samples were unequivocally determined to be animal fibers. The observation using a scanning electron microscope showed that the diameter of the cross section of the fibers was about 20 μm, and that their forms were oval or distorted triangles. In summary, the fiber material was identified as silk even in its degraded state.

The FT-IR spectra of reference modern silk samples and ancient silk samples are shown in Fig. 2. As a result of the analysis of the excavated silk fibers, with the advance of the degradation from the peak intensity ratio of each spectrum, it turned out to be that amides **II** and **III** are preferentially decomposed rather than amide **I**. In the spectra of the excavated silk, the peaks of amides **I** and **II** are overlapped and appear as one broad peak. This is due to the effect of oxidation or hydrolysis in the environments where the fibers were found buried [1,2] because amides **II** and **III** belong mainly to the N-H and C-N combinations and amide **I** belongs mainly to the C=O combination.

The second derivative spectra of the (a) reference modern silk and (b) ancient silk samples are shown in Fig. 3. It was found that the amides **II** and **III** peaks preferentially decrease in area as compared with the amide **I** peak with progress of the degradation.

The difference between the behaviors of amides **II** and **III** is due to the difference in binding energy, namely, amides **II** and **III** (N-H and C-N) are relatively

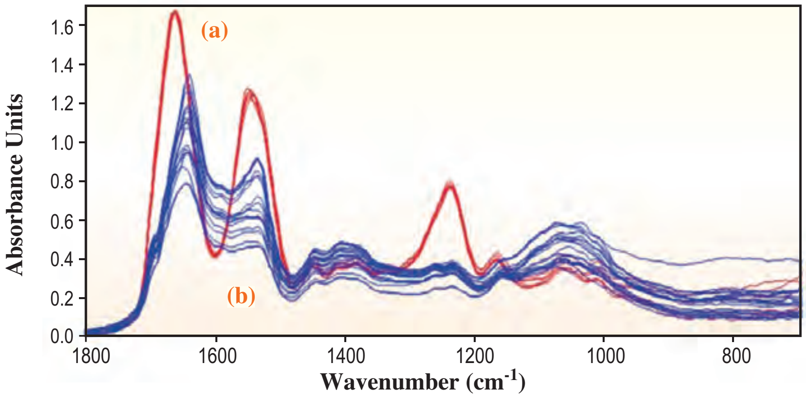

Fig. 2. FT-IR spectra of **(a)** reference modern silk samples and **(b)** ancient silk samples.

weaker than amide **I** (C=O); hence, their bonds degrade relatively easily by oxidation or hydrolysis in environments under long-term burial. Although the apparent form of the amide **I** peak showed no remarkable change with degradation, it was found that the analysis of secondary component structures showed an evident increase in the amount of crystalline components (1660 and 1650 cm^{-1}, β-sheet /disorder), as compared with that of modern reference silk fibers.

As the sample amount that can be used for the analysis is severely limited, it is usually difficult to obtain sufficient data by repeating the measurements using an IR microscope with a glover-lamp light source [3]. Throughout the IR research on the organic archaeological samples, the availability of the synchrotron radiation infrared microscope used was approved.

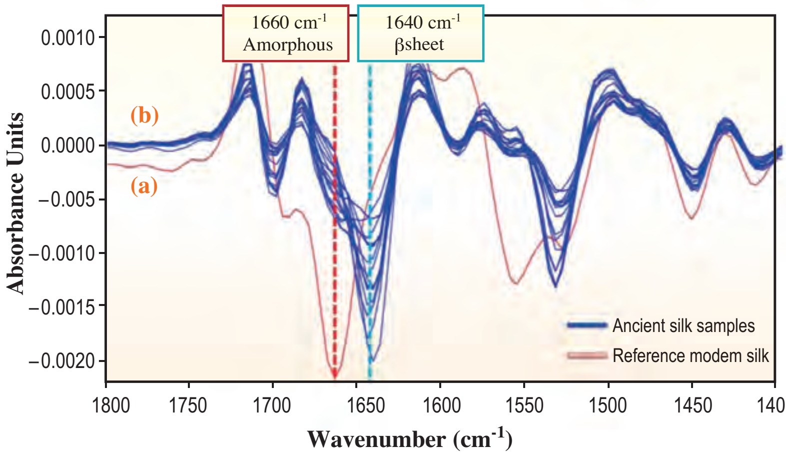

Fig. 3. Second derivative spectra of **(a)** reference modern silk and **(b)** ancient silk samples.

Masanori Akada[a,*], Masanori Sato[b] and
Masayoshi Okuyama[c]

[a] Division of Advanced Fibro-Science,
Kyoto Institute of Technology
[b] Nara National Research Institute for Cultural Properties
[c] Archaeological Institute of Kashihara, Nara Prefecture

*E-mail: akada004001@hotmail.com

References

[1] *M. Akada, M. Sato, M. Okuyama and S. Imazu: J. Textile Engineering **55** (2009) 155. (in Japanese)*
[2] M. Akada *et al.*: J. Textile Engineering **55** (2009) 171. (in Japanese)
[3] M. Akada *et al.*: Sen'i Gakkaishi **65** (2009) 262. (in Japanese)

EARTH & PLANETARY

"Tyulipu"- *Tulip*

Synchrotron radiation-based techniques have become an essential tool for fields as wide-ranging as mineral physics, geology, and environmental matters. Advances in synchrotron radiation instruments and techniques and the upgrade of scientific applications have made it possible to measure many physical and chemical properties of deep Earth materials under extreme conditions and those of extraterrestrial matters. In 2010, new research findings came from *in situ* X-ray diffraction and high-resolution synchrotron imaging through cutting-edge techniques and analysis in earth science. Here, we introduce five outstanding topics in the research field of Earth and Planetary Science.

Tateno *et al*. presented the successful result for generating 377 GPa and 5700 K, corresponding to the high-pressure and high-temperature conditions in the center of the Earth, using the laser-heated diamond anvil cell. *In situ* X-ray diffraction observation of materials under such extreme conditions has been one of the absolute goals in the high-pressure research program at SPring-8. They found that solid iron, the main element in the Earth's core, at the center of the Earth has a hexagonal close-packed (hcp) structure and suggested that the Earth's inner core anisotropy in seismic velocities may be caused by the texturing of aggregate hcp iron crystals.

Irifune *et al*. expanded the measurable pressure range at high-temperature in X-ray studies using a combination of a recently developed large-volume press of a multianvil apparatus (MA) with sintered diamond anvils and synchrotron radiation. The feature of uniform P-T conditions with large sample volumes in MA has made it possible to study complex systems and accurate bulk physical properties. Using the new technique, they investigated the detailed phase relations, density change, and element partitioning of a lower mantle material up to 50 GPa and 220 K and indicated that pyrolite, a hypothetical representative bulk composition for the mantle, is a reasonably good model composition for the upper part of the lower mantle.

SCIENCE

Nishi *et al*. studied the kinetics of high-pressure back transformation in the Earth's mantle mineral of majoritic garnet, for the purpose of experimentally constraining the ascent speed of diamonds from deep Earth to the surface of the Earth. They carried out time-resolved X-ray diffraction measurements with energy-dispersive method by combining a Kawai-type high-pressure apparatus and synchrotron radiation and revealed that diamonds would be transported by magma with an ascent rate of over 60 km/s.

Uesugi *et al*. studied the texture of extraterrestrial materials of meteorites nondestructively using synchrotron radiation X-ray microcomputed tomography (CT) and applied the X-ray CT data to quantitative analysis of the chemical compositions of individual minerals in meteorites by combining the textural information. By increasing the number of data, the new method using X-ray CT can provide reliable classification of extraterrestrial materials, including meteorites and interplanetary dust.

Asahara *et al*. reported the elastic properties of high-pressure ice VII using Brillouin spectroscopy with simultaneous X-ray diffraction at high pressure. They observed the discontinuity of volume, bulk modulus, and shear modulus at high pressure on the structural phase transition of ice VII to X, suggesting that the hydrogen bonding state is closely related to the elastic properties. Because of the existence of ice within deep Earth as well as icy satellite interiors, the change of elastic properties of ice would have an influence on their structures and dynamics.

Yasuo Ohishi

Structure of iron in Earth's inner core

The inner core, the most remote part of our planet, is composed of solid iron. A number of observations show anisotropy in seismic wave speed, which is most likely caused by the preferred orientation of iron. The crystal structure in the inner core provides key information for deciphering such observations and understanding the inner core dynamics. Owing to limited accessibility in an ultrahigh pressure and temperature (*P*-*T*) experiment to the real conditions of the inner core (reaching >330 GPa and ≥5000 K), the crystal structure of iron at the inner core has long been under debate.

Iron adopts a body-centered-cubic (*bcc*) structure under ambient condition and transforms into the hexagonal close-packed (*hcp*) phase above 15 GPa. While *hcp*-Fe can persist to core pressures at 300 K [1], a phase transition at elevated temperature is a possibility. Both theory and experiments proposed different forms of iron at simultaneously high *P*-*T* conditions, which include *bcc*, face-centered-cubic (*fcc*), and *hcp* structures. The structure of iron has never been examined experimentally under the inner core *P*-*T* conditions, because such extreme conditions could only be achieved by dynamical shock-wave experiments on a microsecond order. On the basis of a combination of static compression experiments in a laser-heated diamond-anvil cell (DAC) and synchrotron X-ray diffraction (XRD) measurements, we first determined that the hexagonal *hcp* structure is a stable form of iron up to 377 GPa and 5700 K, corresponding to inner core conditions [2].

Angle-dispersive X-ray diffraction (XRD) measurements were conducted at the dedicated beamline **BL10XU**, for high-pressure research. The XRD patterns were collected *in situ* at high *P*-*T* on a CCD detector (Bruker APEX) with a typical exposure time of 10 sec. A monochromatic incident X-ray beam was focused by stacked compound refractive lenses (CRLs) and collimated to about 6 μm (full width at half maximum) in diameter on the sample. For experiments beyond 300 GPa, double-beveled diamond anvils with 40 μm culets were used, and accordingly, the sample size was limited to about 20 μm. Heating was performed from both sides of the sample by employing a couple of 100 W single-mode Yb fiber lasers (SPI). We used beam shaping optics, which converts a Gaussian beam to one with a flatter energy distribution in an attempt to reduce the radial temperature gradient in the sample. The laser-heated spot was ~15 μm across. Temperature was measured by the spectroradiometric method.

To construct the phase diagram of iron to core conditions, we conducted six separate sets of experiments. The first experiment at 303 GPa and room temperature resulted in an XRD pattern that included peaks from *hcp*-Fe and Re (gasket material). Subsequently, we heated this sample to 4820 K at 332 GPa (Fig. 1(a)). The one-dimensional XRD pattern did not change except the appearance of the *hcp* 002 line. On the other hand, the two-dimensional image became spotty, indicating crystal growth, and hence, the stability of *hcp*-Fe under these *P*-*T* conditions. Following these measurements, the sample was temperature-quenched and then further compressed to 321 GPa at room temperature. We again heated the sample to 5520 K at 356 GPa. The XRD pattern was still dominated by the *hcp* phase, but minor peaks assigned to pyrite-type SiO_2 (pressure medium) and Fe_3C cementite appeared (Fig. 1(b)). The measured lattice parameters and

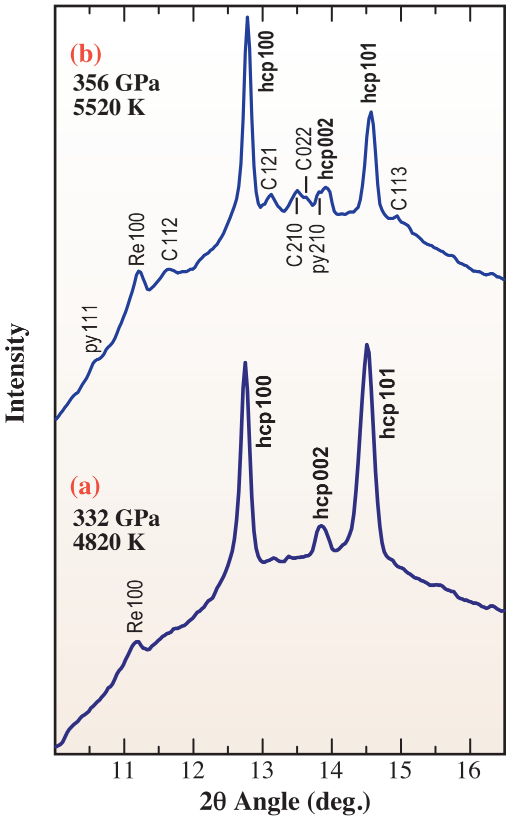

Fig. 1. Representative XRD patterns of *hcp*-Fe at **(a)** 332 GPa and 4820 K and at **(b)** 356 GPa and 5520 K. Labels indicate *hcp*, *hcp*-iron; py, pyrite-type SiO_2 (pressure medium); C, Fe_3C cementite; Re, rhenium (gasket).

volumes of Fe_3C are in agreement with earlier experimental results to 187 GPa. Similar observations were made in five other experiments, which were conducted in a wide *P*-*T* range from 135 GPa and 2690 K to 377 GPa and 5700 K. In all the measurements, we obtained no evidence of a phase transition to *bcc* or *fcc* iron phases.

These results indicate that *hcp* is a stable form of iron up to 377 GPa and 5700 K, compatible with previous *ab initio* calculations (Fig. 2). The estimation of temperature at the inner-outer core boundary ranges from 4850 to 5700 K, depending on the melting temperature of iron and the effect of light alloying elements. The temperature gradient should be very small within the inner core. Our experiments thus represent the range of inner core *P*-*T* conditions. One limitation of these experiments is that chemical impurities such as silicon and sulfur, which have the ability to change the stable crystal structure, were not accounted for.

Strong seismic anisotropy exists in the inner core, with longitudinal waves traveling ~3% faster along the polar axis than in the equatorial plane. This was originally attributed to the preferred orientation of *hcp*-Fe, which exhibits a strong single-crystal elastic anisotropy, at least, at low temperature. However, recent calculations [3,4] reported that the *c*/*a* ratio approaches the value of 1.6299 for the ideal *hcp* structure at high temperature, and consequently, elastic anisotropy of *hcp*-Fe no longer exists under inner core conditions (Fig. 3). On the other hand, experimental evidence previously suggested a weak temperature dependence of the *c*/*a* ratio at 140 GPa [5], as do our data at ~330 GPa. The *c*/*a* ratio of 1.602 at 332 GPa and 4820 K, which is substantially lower than the ideal value, suggests that *hcp*-Fe should be elastically anisotropic even under the high temperature conditions of the inner core. The observed seismic anisotropy may therefore result from the preferred orientation of the *hcp* phase with the *c*-axis parallel the Earth's rotation axis.

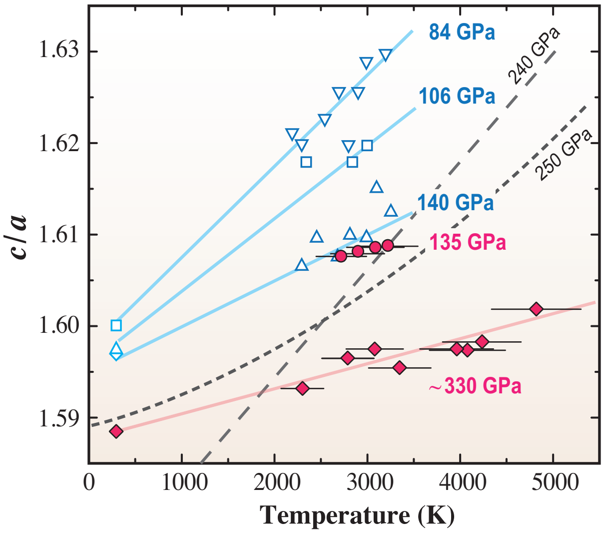

Fig. 3. Temperature dependence of the *c*/*a* axial ratio of *hcp*-Fe collected at 135 GPa and ~330 GPa (red). The results of theoretical calculations are also shown by a dashed curve [3] and a dotted curve [4]. Previous experimental results at 84, 106, and 140 GPa are from Boehler *et al.* [5] (blue).

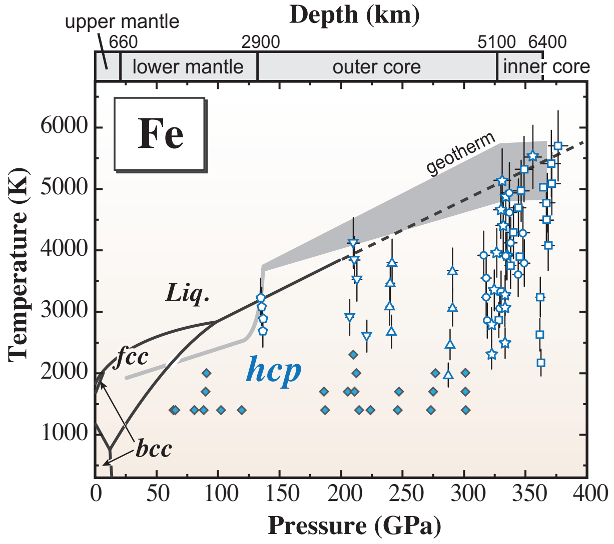

Fig. 2. Phase diagram of iron and the inferred temperature profile inside the Earth. Open symbols indicate present results, and filled diamonds are from previous experimental work [1].

Shigehiko Tateno

Dept. of Earth & Planetary Sciences,
Tokyo Institute of Technology

E-mail: tateno.s.aa@m.titech.ac.jp

References

[1] Y. Kuwayama *et al*.: Earth Planet. Sci. Lett. **273** (2008) 379.
[2] *S. Tateno, H. Hirose, Y. Ohishi, Y. Tatsumi: Science* ***330*** *(2010) 359.*
[3] A.B. Belonoshko *et al*.: Nature **424** (2003) 1032.
[4] R. Boehler *et al*.: J. Phys. Conf. Ser. **121** (2008) 022018.
[5] X. Sha and R.E. Cohen: Phys. Rev. B **74** (2006) 064103.

Phase transitions, element partitioning, and density changes in a model lower mantle composition

Pyrolite is the name of a hypothetical rock, which was proposed as a model mantle material nearly 50 years ago [1]. Detailed phase relations and associated density changes in this composition have been studied using a multianvil apparatus (MA), which demonstrated that pyrolite is certainly an excellent model for the upper mantle (30-410 km), the mantle transition region (410-660 km), and the uppermost part of the lower mantle (660-2900 km) of the Earth. This kind of study, however, has been limited up to about 30 GPa, equivalent to a depth of ~800 km in the lower mantle, because of the limitation of pressures available in MA [2].

Recent developments in high-pressure generation in MA using sintered diamond (SD) anvils enabled us to extend this pressure limit toward those approaching 100 GPa, although experiments at high temperatures of the Earth's lower mantle (2000-3000 K) under such high pressures have still been quite difficult (e.g., Ref. [3]). We have firstly conducted detailed studies on phase transitions, element partitioning, and density changes in pyrolite at pressures up to 50 GPa and temperatures along an appropriate geotherm (1900-2200 K) [4] using a combination of synchrotron radiation and MA techniques with SD anvils at **BL04B1**. Mössbauer spectroscopy and electron energy-loss spectroscopy (EELS) measurements were also conducted on the recovered samples to analyze the iron valence state in the coexisting major high-pressure phases, in addition to the chemical composition measurements using a conventional scanning electron microscope with an EDX analyzer.

Figure 1 shows phase and density changes in pyrolite as a function of pressure (or depth) along the geotherm. It is seen that pyrolite consists of $MgSiO_3$-rich orthorhombic perovskite (Mg-Pv; 75 vol%), (Mg,Fe)O ferropericlase (Fp; 17 vol%), and $CaSiO_3$-rich cubic perovskite (Ca-Pv; 8 vol%) in virtually constant volume proportions down to a depth of 1200 km in the lower mantle, which is consistent with earlier reconnaissance studies with a laser-heated diamond anvil cell (LHDAC). The density change of the pyrolite remarkably agrees with the model density profile (PREM) based on seismological observations, suggesting that this composition is a good model for the upper part of the lower mantle.

The partition coefficients (K_D) of iron between Fp and Mg-Pv in pyrolite were determined as a function of pressure from the chemical composition data of these phases, which are plotted in Fig. 2, where the K_D values lower than 1 indicate that iron is preferentially partitioned in Fp. The K_D values between Fp and Mg-Pv in San Carlos olivine composition (SC olivine) are also shown in this figure for comparison. It is seen that the K_D values in pyrolite are larger than those in SC olivine, which are attributed to the presence of ferric iron in Mg-Pv in the former composition, as a result of a coupled substitution of Mg^{2+} and Si^{4+} by Fe^{3+} and Al^{3+}.

The increase in K_D in pyrolite at pressures up to ~30 GPa is due to the enrichment of Al^{3+} and Fe^{3+} in Mg-Pv as a result of the smeared-out phase transition of majorite garnet to Mg-Pv, which stays constant above this pressure, where the majorite-perovskite transition is completed (Fig. 1). However, we noted a sudden decrease in K_D in pyrolite at pressures above ~40 GPa. Some recent experimental and theoretical studies demonstrate that ferrous iron in Fp undergoes a high-spin to low-spin transition at pressures around 40-60 GPa. This should result in the enrichment of ferrous iron in this phase and thereby a decrease in K_D, as observed in Fig. 2. Thus, we confirmed

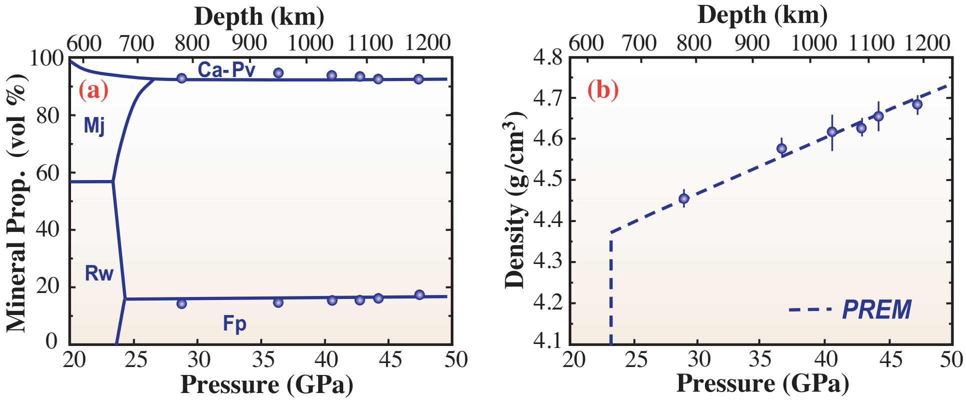

Fig. 1. Mineral proportion **(a)** and density **(b)** changes in pyrolite at pressures up to 50 GPa along a geotherm. PREM is a representative seismological model proposed by A. Dziewonski and D.L. Anderson. Mj = majorite garnet, Rw = ringwoodite, Mg-Pv = $MgSiO_3$ perovskite, Ca-Pv = $CaSiO_3$ perovskite, Fp = (Mg,Fe)O ferropericlase.

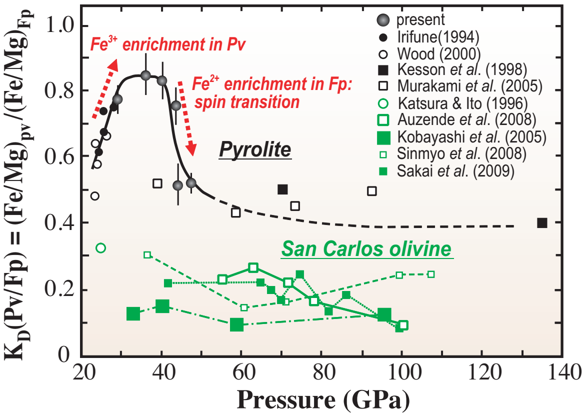

Fig. 2. Changes in iron partition coefficient (K_D) between Mg-Pv and Fp in pyrolite and San Carlos olivine compositions as a function of pressure along a geotherm.

that the spin transition in Fp causes the enrichment of iron in Fp and a significant decrease in K_D in the realistic mantle composition, although this yields no notable anomalous changes in the density profile of pyrolite (Fig. 1).

Figure 3 shows schematic illustrations of two typical models of the compositions of the Earth's interior. It has been shown that pyrolite is a good model for the compositions of the upper mantle and the mantle transition region, except for the bottom part of the latter region, where we proposed the existence of a layer of harzburgite material on the basis of sound velocity measurements at high pressure and temperature [5]. The chemical composition of the lower mantle, however, has not been well constrained; some believe that pyrolite is a reasonable model also in this region (Fig.3 (a)), while others claim that further Si-rich compositions, such as chondritie or perovskitite, are more feasible (Fig. 3(b)). As the lower mantle occupies more than half of the Earth's entire volume, elucidating its chemical composition is important to address the evolution and dynamics of the Earth's interior.

The present study suggests that pyrolite is a reasonably good model composition for at least the upper part of the lower mantle, in light of the density profile. However, the density profile in the Earth's interior is derived from observed seismic wave velocities with some assumptions, while the latter velocity data are more directly constrained by seismological observations. Thus, we need to compare laboratory sound velocity data of pyrolite and other compositional models with those by seismological observations. Researchers in our laboratory and those of JASRI have developed techniques to measure the sound velocities under P-T conditions of the uppermost lower mantle, which should provide important data to constrain the chemical composition of this region of the Earth's mantle in the near future.

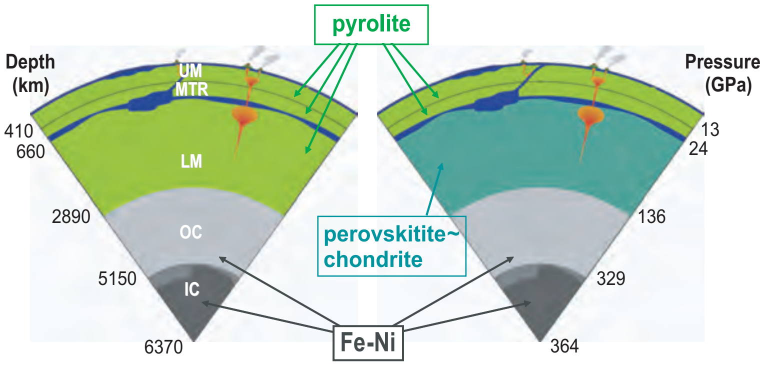

(a) pyrolite model
(Si deficient primordial mantle)

(b) chondrite model
(chondritic primordial mantle)

Fig. 3. Two representative models of the Earth's interior with pyrolite **(a)** and perovskitite/chondrite **(b)** compositions for the lower mantle. The core material is believed to be composed of mainly Fe-Ni alloys. UM = upper mantle, MTR = mantle transition region, LM = lower mantle, OC = outer core, IC = inner core. Illustration courtesy of Jun Tsuchiya.

Tetsuo Irifune

Geodynamics Research Center, Ehime University

E-mail: irifune@dpc.ehime-u.ac.jp

References

[1] A. E. Ringwood: Advances in Earth Sciences, MIT Press, Cambridge (1966) 287.
[2] T. Irifune: Nature **370** (1994) 131.
[3] E. Ito: Treatise on Geophysics, Elsevier, Amsterdam, vol.2 (2007) 198.
[4] *T. Irifune, T. Shinmei, C.A. McCammon, N. Miyajima, D.C. Rubie, D.J. Frost: Science **327** (2010) 193.*
[5] T. Irifune *et al.*: Nature **451** (2008) 814.

Elastic properties of ice VII and its high-pressure polymorphs

Ice shows rich polymorphism under various pressure and temperature conditions due to the variation of hydrogen bonds linking the H_2O molecules. This is one reason why the properties of H_2O ice under pressure are of great interest in a broad range of fields including physics, chemistry, and earth and planetary sciences. At room temperature, compressed liquid water transforms to tetragonal ice VI at 1.05 GPa and with further compression, ice VI transforms to cubic ice VII at 2.1 GPa. The structure of ice VII consists of a body-centered cubic (bcc) lattice of oxygen and each oxygen atom covalently bonded to two hydrogen atoms occupying two of four tetrahedral sites (see Fig. 1). The phase X, in which the proton is at the center position between two oxygen atoms with a bcc framework of oxygen, was predicted as a following phase of ice VII by Holzapfel (1972) [1]. Infrared and Raman spectroscopic studies suggest that a sluggish translation of ice VII with pressure to the atomic phase X starts at approximately 60 GPa and ends at approximately 100 GPa. The possible existence of intermediate phases, in which protons distribute dynamically into double potential wells along the axis of hydrogen bond, has been suggested from theoretical studies (e.g., [2]).

In this study [3], longitudinal and transversal velocities in polycrystalline ice were measured at room temperature and a pressure range of 6–60 GPa by Brillouin scattering method. Synchrotron X-ray diffraction measurements were also conducted simultaneously with Brillouin scattering measurements at the pressure range from 40 to 60 GPa to clarify the change in elastic properties across the expected transitions of ice. Experiments were conducted with the Brillouin scattering measurement system equipped with a CO_2 laser heating system installed at beamline **BL10XU** [4].

Polycrystalline ice directly frozen from water by compression usually consists of several anisotropic large grains and it is difficult to obtain precise aggregate acoustic velocity for material using such samples because the acoustic velocity is sensitively affected by crystallographic orientation. Therefore, we quenched ice VII from water using a CO_2 laser in a diamond anvil cell at 14 GPa to obtain an isotropic aggregate of ice VII. We could obtain nearly isotropic spectra from the polycrystalline ice by this quenching process. Then, we compressed the sample with a pressure interval of 2–3 GPa and collected Brillouin spectrum at room temperature and each pressure up to 60 GPa. Measurements were also taken along a decompression path until reaching 6 GPa. Measured acoustic velocities for longitudinal and transversal modes of ice are plotted as a function of pressure in Figs. 2(a) and 2(b), respectively. Velocities collected along compression and decompression paths were in good agreement with each other except the pressures between approximately 40 GPa and 55 GPa. The pressure dependence of the longitudinal acoustic velocity of ice above 58 GPa is clearly different from that below 50 GPa, although an intermediate pressure region was hidden by the transversal mode of a single-crystal diamond. We conducted measurements with the χ angles of upper and lower velocity limits for the transversal mode of a single-crystal diamond, at 40–63 GPa. Therefore, the longitudinal velocities of ice should be in the shadow range of Fig. 2(a) at 48–57 GPa. Figure 3 shows the volumes of ice against pressure obtained in this study in the pressure range of

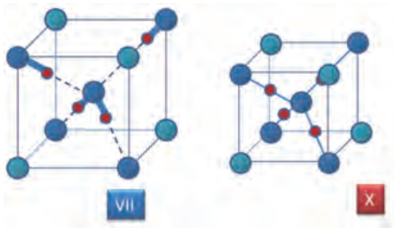

Fig. 1. Crystal structures of high-pressure dense ice: Oxygen atoms are represented by large blue spheres and hydrogen atoms by small red spheres.

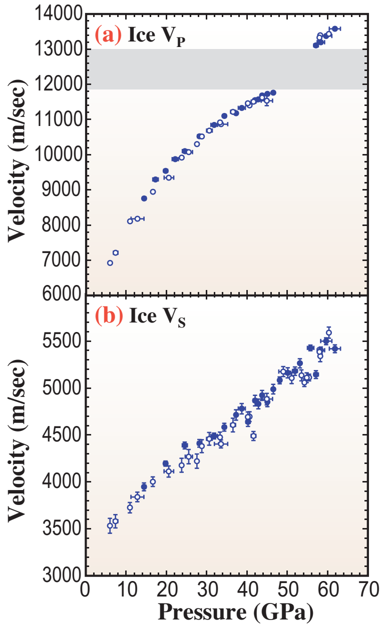

Fig. 2. Acoustic velocities in polycrystalline H_2O ice measured in this study as a function of pressure: **(a)** Transversal velocities, **(b)** longitudinal velocities. Filled and open circles represent acoustic velocities measured along compression and decompression paths, respectively. The velocity region is shadowed in which the spectrum of transversal mode for single-crystal diamond hides other spectra.

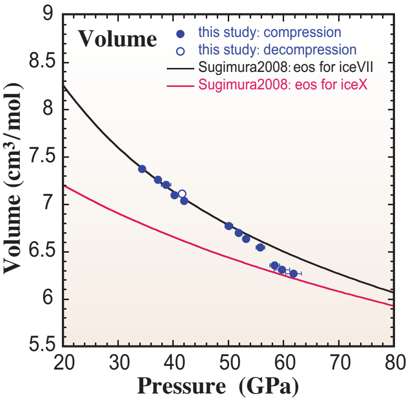

Fig. 3. Measured volumes of ice as a function of pressure: Filled and open blue circles represent volumes measured in this study along compression and decompression paths, respectively. A black line and a red line are predicted with the equations of state of ice VII and ice X, respectively, proposed by [5].

40–60 GPa. Volumes of ice seem that they were on the line predicted using the equation of state of ice VII suggested by a density-functional calculation combined with synchrotron X-ray diffraction measurements [5] until 58 GPa and approached that of ice X above 58 GPa.

It has been debated whether the compression behavior of bcc ice should be expressed with one equation of state. In this study, we could calculate the adiabatic elastic moduli of bcc-structured ice from a set of longitudinal and transversal velocities and volume, which are measured simultaneously in the pressure range of 40–60 GPa, independent of the debate. The slope of the shear modulus against pressure changes at approximately 35–40 GPa, and we also observed that there is a small discontinuity of the shear modulus against pressure at approximately 55–60 GPa (see Fig. 4(a)). There is no distinct discontinuity in bulk modulus at 40 GPa, but the pressure dependence is clearly different below 50 GPa and over 58 GPa (see Fig. 4(b)). It is plausible that the pressure dependence of the bulk modulus changes at approximately 58 GPa accompanied by discontinuities of shear modulus and other vibration properties, which have been observed in previous studies. We consider that these observed changes at approximately 58 GPa are comparable to the transition from a statically disordered state to a dynamically disordered state of the hydrogen bond in bcc-structured ice, which is proposed by theoretical studies. This change in pressure dependence of the bulk modulus could support the argument that bcc-structured ice is expressed better with two sets of thermodynamic parameters.

We demonstrated that a change in the hydrogen bonding state clearly affects the elastic properties of the bcc-structured ice. A temperature effect on the change of elastic properties was not clarified in this study, but the discontinuous change of thermodynamic properties across the transition should exist at a whole temperature range of the transition. The high-temperature bcc-structured ice could exist in cold subducting slabs of the Earth and in interiors of icy planets and satellites. The elasticity difference between ice VII and the dynamically disordered ice X may affect the dynamics of the interiors of these planets. Further investigation in a wide range of temperature is required for more detailed modeling; however, the thermoelastic properties of high-pressure polymorphs of ice obtained in this study could contribute to clarifying the dynamics and evolution of the Earth and icy planets and satellites.

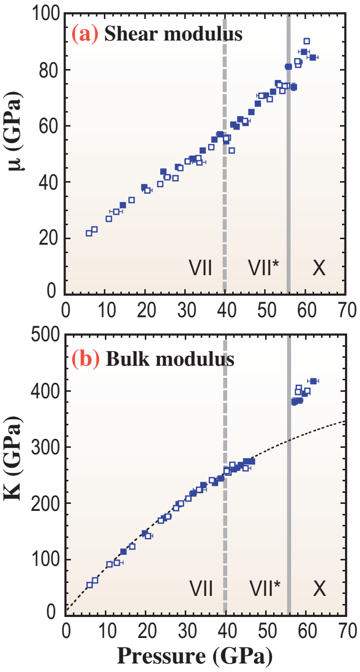

Fig. 4. Pressure dependence of the elastic moduli obtained from measured velocity: **(a)** shear moduli and **(b)** bulk moduli as functions of pressure: Filled and open blue squares represent elastic moduli measured in this study along compression and decompression paths, respectively. The estimated boundary between ice VII and the transitional state of ice VII (VII*) and that between the transitional phase to the dynamically disordered ice X (X) are shown as a bold grey dashed line and a bold grey solid line, respectively. Black dotted lines in (b) are predictions from specific heats obtained in this study and an isothermal equation of state for ice VII.

Yuki Asahara

Department of Earth and Space Science, Osaka University

E-mail: asaharay@anvil.ess.sci.osaka-u.ac.jp

References

[1] W.B. Holzapfel: J. Chem. Phys. **56** (1972) 712.
[2] M. Benoit *et al.*: Phys. Rev. Let. **89** (2002) 145501.
[3] *Y. Asahara, K. Hirose, Y. Ohishi, N. Hirao, M. Murakami: Earth Planet Sci. Let.* ***299*** *(2010) 474.*
[4] M. Murakami *et al.*: Phys. Earth Planet. Int. **174** (2009) 282.
[5] E. Sugimura *et al.*: Phys. Rev. B **77** (2008) 214103.

Back transformation kinetics of majoritic garnet and implication for ascending rate of diamond

Mineral inclusions in diamonds provide important information on the depth of diamond source regions and mineralogy of the Earth's deep interior. We have successfully presented the strongest constraint on the ascent speed of diamond from the deep interior of the Earth [1].

Majoritic garnet is a stable mineral in the Earth's deep mantle at a depth of ~400-700 km [2], which is discovered as diamond inclusions in several localities [3]. The presence of majoritic garnet in diamonds indicates that they have been formed in such extremely deep regions. Majoritic garnet should transform to other minerals (i.e., low-pressure minerals) during transportation to the Earth's surface because it is unstable at depths shallower than ~300-400 km. Therefore, diamonds containing majoritic garnet should have been transported quickly before the majoritic garnet inclusions were converted to other low-pressure-type minerals. We considered that the transformation rate of majoritic garnet can be potentially used as a unique speedometer of diamonds rising from a depth of ~400 km.

We determined the transformation rate of majoritic garnet into low-pressure minerals (back transformation of majoritic garnet) by time-resolved *in situ* synchrotron X-ray diffraction measurement at 3.0-7.5 GPa (depth of ~100-200 km) and 1020-1300°C using a Kawai-type high-pressure apparatus SPEED-1500 at beamline **BL04B1**. White X-rays from synchrotron radiation were used as the incident X-ray beam, which was collimated to 0.05 mm×0.2 mm. The diffracted beam was measured by the energy dispersive method with a fixed 2θ angle of 5.0° using a Ge solid state detector.

We observed the transformation kinetics of majoritic garnet to its low-pressure minerals (pyropic garnet + clinopyroxene) from the increase in integrated intensity of the diffraction line of clinopyroxene. The time dependence of the transformed volume fraction is shown in Fig. 1. Back-scattered electron image and element mappings of partially transformed sample after the transformation experiment are shown in Fig. 2. Textural observation revealed that decomposed low-pressure minerals (clinopyroxene and pyropic garnet) were formed along grain boundaries of parental majoritic garnet.

The kinetic data were analyzed on the basis of the one-dimensional growth of the reaction rim, which is observed to be a predominant process of the back transformation. In this case, the rate equation is given by [4]

$$V = 1 - \exp[-2SX(t)] \qquad (1)$$

$$X(t) = kt^n \qquad (2)$$

where V is the transformed volume fraction, S is the area of the grain boundary, $X(t)$ is the growth distance from the original grain boundary at time t, and k and n are constants. The area of the grain boundary S can be expressed as $3.35/d$, where d is the grain size of the parental phase. The k and n values were optimized by fitting of the kinetic data to these rate equations using a nonlinear least-squares procedure. Results of these fittings are shown in Fig. 1.

Figure 3 shows the time needed for 5 μm and 50 μm growths for the back transformation as a function of temperature. The kinetic parameters obtained at 6.7-7.5 GPa (~200 km depth) were used in the calculation ignoring the pressure effect on the diffusion rate. Figure 3 indicates that, if we consider the grain size of 100 μm for the parental

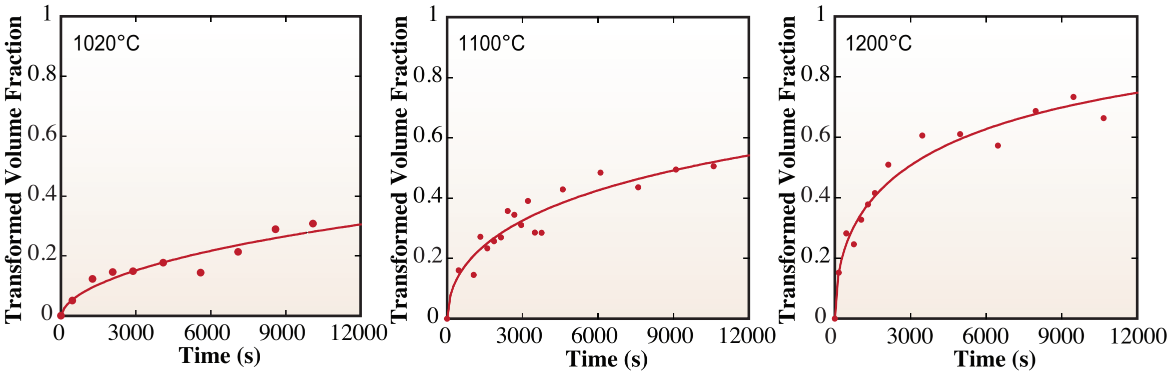

Fig. 1. Changes in the transformed volume fraction with time in the back transformation from majoritic garnet to clinopyroxene+majoritic garnet at 1020-1200°C. Curves obtained by least-squares fits of the kinetic data to eqs. (1) and (2) are also shown.

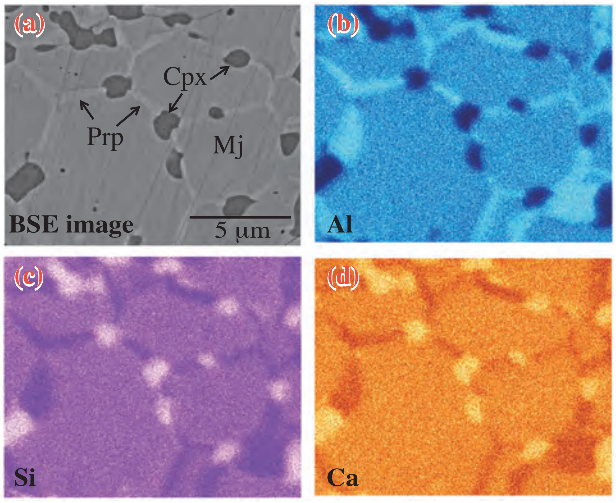

Fig. 2. **(a)** Back-scattered electron image and **(b)**-**(d)** element map of Al, Si and Fe showing textures of the recovered sample transformed at 3.0 GPa and 1100°C after 180 min of heating. Pyropic garnet (Prp, light gray) and clinopyroxene (Cpx, dark gray) precipitate along grain boundaries of parental majoritic garnet (Mj, gray).

majoritic garnet as typically observed in diamond, the majoritic garnet trapped in diamond can be brought to the Earth's surface through the upper mantle within ~600 hours at 1300°C. The average ascent rates of diamond are also shown in Fig. 3. When considering the temperature of 1300°C, the ascent rate of more than 60 km/h is required to preserve the untransformed majoritic garnet. In case that the ascent rate is slower than 0.6 km/h, the majoritic garnet completely transforms into pyropic garnet and clinopyroxene. We found that the velocity of the typical convective mantle flow (1-20 cm/year) is far too slow to satisfy the time limitation for the survival of majoritic garnet, indicating that such diamonds with majoritic garnet inclusions have been transported directly from the deep mantle by the rapid movement of "kimberlite" magma. Kimberlite magma is known to transport diamond to the surface quickly, but such activities have been considered to be restricted to the depths of the uppermost part (~150-200 km) of the Earth's mantle. Our experimental results suggest that such a rapid ascent mechanism as kimberlite magma activity may exist at greater depths than once thought.

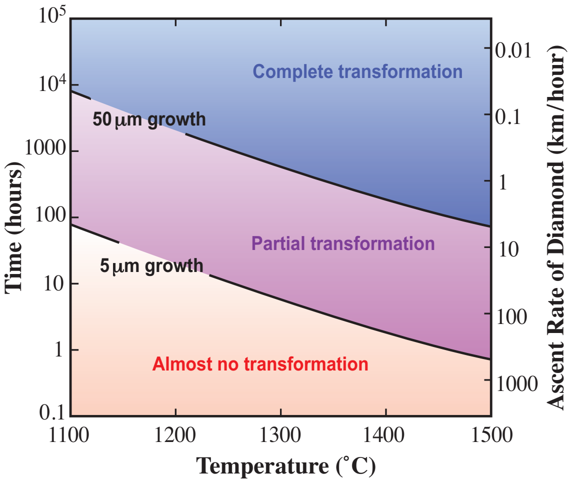

Fig. 3. Plots of the time needed for the 5 and 50 μm growths in the back transformation as a function of temperature based on the growth kinetics in this study. The ascent rates of diamond are also shown assuming that the back transformation proceeds at depth ranges of 50-400 km (right-hand scale).

Masayuki Nishi[a,b,*], Tomoaki Kubo[c] and Takumi Kato[c]

[a] Geodynamics Research Center, Ehime University
[b] Dept. of Earth and Planetary Sciences,
Graduate School of Sciences, Kyushu University
[c] Dept. of Earth and Planetary Sciences,
Faculty of Sciences, Kyushu University

*E-mail: nishi@sci.ehime-u.ac.jp

References

[1] *M. Nishi, T. Kubo, T. Kato, A. Tominaga, A. Shimojuku, N. Doi, K. Funakoshi and Y. Higo: Geophys. Res. Lett.* ***37*** *(2010) L09305.*
[2] T. Irifune *et al.*: Earth Planet. Sci. Lett. **77** (1986) 245.
[3] B. Harte and N. Cayzer: Phys. Chem. Miner. **34** (2007) 647.
[4] J.W. Cahn: Acta Metall. **4** (1956) 449.

Quantitative analysis of minerals in meteorite chips by SR-X-ray microcomputed tomography

Recently, X-ray micro-CT has become one of the important methods of observing extraterrestrial materials such as meteorites, Antarctic micrometeorites, interplanetary dust particles, and materials of sample-return missions [1]. Synchrotron radiation (SR) provides particularly high flux density monochromatic X-rays, which enables the quantitative determination of materials with a spatial resolution of approximately 1 μm. We applied SR-X-ray CT to the non-destructive analyses of meteorites including the quantitative analysis of chemical composition using Linear Attenuation Coefficient (LAC, μ) [2].

Experiments were carried out at beamline **BL20B2**. The X-ray beam is monochromatized using a double-crystal monochromator. Samples were fixed on a rotational stage by clay. Transmitted and direct X-ray images were converted into visible light by a powder P43 ($Gd_2O_2S:Tb^+$) scintillator with thicknesses of 7 μm and 10 μm in the X-ray beam monitor. The effective pixel sizes of the detector, δ, were 2.74 μm and 3.14 μm.

Figure 1 shows CT images of meteorites. The spherical shape of chondrules, which are igneous spherules in meteorites, as well as their texture and fine grained rims around them are well defined in the CT images, with a few microns of spatial resolution. In Fig. 1B, the radial texture of a chondrule is clearly visible in an enlarged image and a 3D cut-off image.

CT images of differentiated meteorites (ureilite, shergottite, and iron) are also shown in Fig. 1. Figure 1G displays an image of a Martian meteorite, DaG 476 (shergottite). The CT image displays distinct crystals such as olivine phenocryst (large light-gray objects), groundmass of pyroxene (gray matrix in CT image), and plagioclase (dark gray objects between pyroxene), and opaque phases including chromite grains (white objects). Figure 1H shows a bird's eye view image of the Gibeon iron meteorite. Gibeon shows no structure in the CT image, but the 3D distribution of voids (~20 μm in diameter) inside the meteorite is visible. A previous study has suggested the possibility that these voids are the carriers of noble gases in iron meteorites.

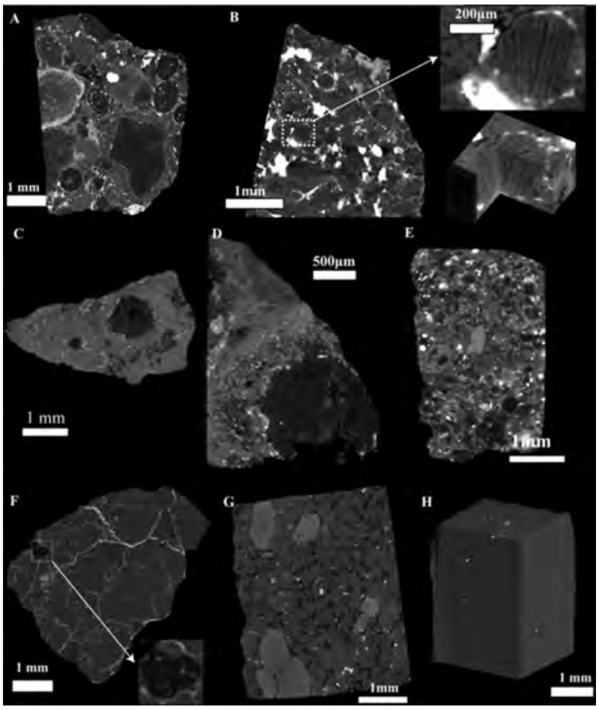

Fig. 1. CT images of various meteorite chips obtained using optimized experimental conditions. Except for D and H, the X-ray energy is 30 keV. A: Y-790448 (ordinary chondrite, LL3), B: ALH 78084 (ordinary chondrite, H3), enlarged image of a radial chondrule and 3D cut-off image of the radial chondrule, C: Allende (carbonaceous chondrite, CV3), D: Allende (23 keV), E: Y-81020 (carbonaceous chondrite, CO3), F: Y-791538 (Ureilite), G: DaG 476 (Martian meteorite, Shergottite), H: 3D distribution of voids in Gibeon (iron meteorite, 60 keV).

Figure 2 shows a magnified image of Fig. 1G (DaG 476) with a line profile of μ taken along the rectangle in the CT image. The line profile is the average value of 10 pixels perpendicular to the long side in the rectangle. We can observe the zoning of the olivine phenocryst, roughly from 8.1 to 10.0 cm^{-1} in μ. This range of μ is equivalent to a fayalite range (the iron content of olivine ranges from 0 to 100) of Fa_{29-39} for μ of olivine crystal. From a previous study, it appears that an olivine phenocryst in DaG 476 shows igneous zoning as Fa_{24-37} [3]. The range of Fa number shows good agreement with the Fa number obtained with μ.

Figure 3 shows the histograms of μ obtained using 30 keV X-rays. The count number is normalized to the total number of voxels of the meteorite chip. From the peak position of the histograms, we can deduce the internal components and their chemical composition. All the histograms of LL chondrites show peaks at almost the same position. For example, the histogram of Y-790448 shows peaks at 4.9 and 6.4 cm^{-1}. The peaks correspond to low-Fe silicates, which are mainly included in chondrules. The value of 6.4 cm^{-1} is equivalent to Fa_{20} for olivine and Fs_{29} for low-Ca pyroxene (Fs shows iron contents of low-Ca pyroxene), and 4.9 cm^{-1} is equivalent to Fa_{12} for olivine and Fs_{17} for low-Ca pyroxene. Peaks of iron inclusions, such as troilite (FeS, ~29 cm^{-1}) and metallic iron (~64 cm^{-1}), also appear in Fig. 3.

The histogram profile of DaG 476 shows a peak at around 6.4 cm^{-1}, which is equivalent to Fs_{29}. From polished section observations, the groundmass pyroxene in DaG 476 is Fs_{21-30} [3] and is consistent with the peak. The peak of the groundmass pyroxene is associated with two different peaks, 3.9 cm^{-1} (plagioclase, 3.5 cm^{-1} for anorthite) and 9.1 cm^{-1} (olivine phenocryst, equivalent to Fa_{34}). The compositional range of olivine crystals obtained by polished section observation is Fa_{24-42}. The peaks of chromite can be observed in the histogram. We can also observe a peak of ferrihydrite, which would be products of terrestrial weathering.

These results show that we can observe the texture in CT images, and obtain chemical compositions of individual minerals quantitatively by combining the textural information without destruction of the samples. We can also estimate the average chemical compositions of major and minor minerals in the meteorites from the peak position of the histogram. The method can be applied effectively to the initial observation of materials that will be obtained by future sample-return missions. CT data in this paper lacks higher and lower petrologic types and some reduced chondrites, such as E and CR. By increasing the number of data, we can increase the reliability of the classification of meteorite using X-ray CT.

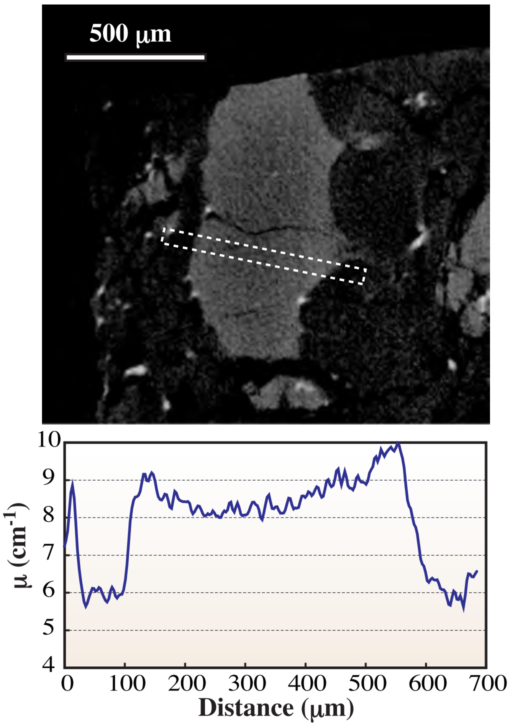

Fig. 2. An enlarged CT image of Fig. 1G (DaG 476) together with a line profile along the white rectangle in the image. The line profile is averaged perpendicular to the long side of the rectangle. We can observe igneous zoning of the olivine phenocryst in the range of 8.1–10.0 cm^{-1}, which is equivalent to Fa_{29-39}.

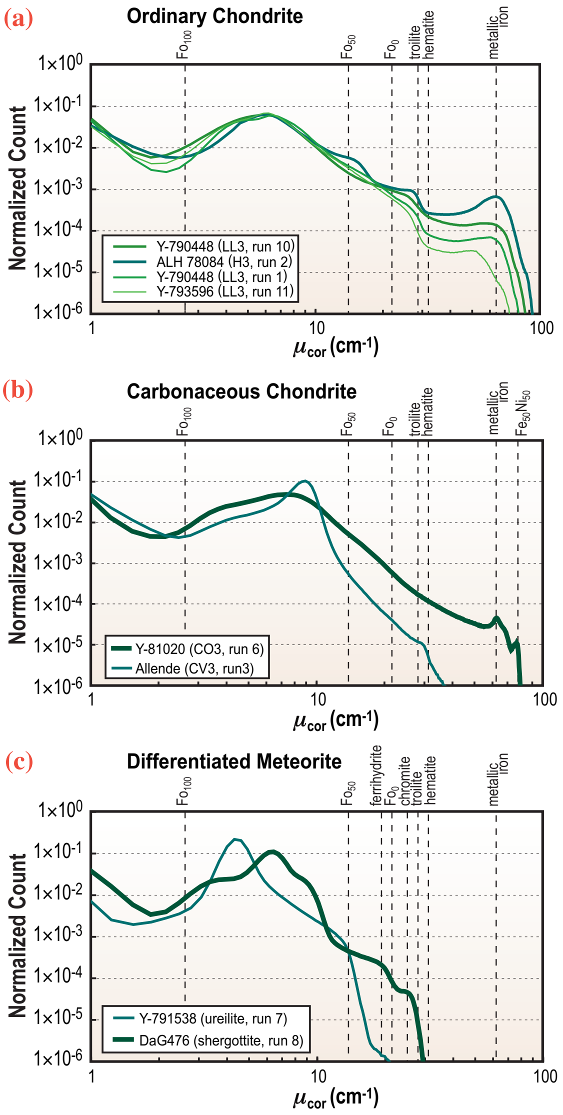

Fig. 3. Histograms of various classes of meteorites, obtained from CT data recorded using 30 keV X-rays. **(a)** Ordinary chondrites. **(b)** Carbonaceous chondrites. **(c)** Differentiated meteorites.

Masayuki Uesugi[a,*,†], Kentaro Uesugi[b] and Mayumi Oka[c]

[a] Dept. of Adaptive Machine Systems, Osaka University
[b] SPring-8/JASRI
[c] Dept. of Earth and Space Science, Osaka University

*E-mail: uesugi@planeta.sci.isas.jaxa.jp

† Present address: JAXA/JSPEC

References

[1] T. Nakamura *et al*.: Science **321** (2008) 1664.
[2] *M. Uesugi, K. Uesugi, M. Oka: Earth and Planetary Science Lett.* ***299*** *(2010) 359.*
[3] T. Mikouchi *et al*.: Meteorit. Planet. Sci. **36** (2001) 531.

ENVIRONMENTAL

Environmental science covers various research fields, such as environmental problems, environmental enhancement using new techniques or functional materials and geochemistry. Recently, the amount of research on practical use or product development seems to be increasing in the field of Environmental Science. This trend matches social demands for solving environmental problems, such as pollution and the low-carbon economy. Also, the amount of research on the dynamical change of molecules or nanoparticles under *in situ* conditions is increasing, as seen in topics selected in this section. This bulk of research could be realized by effectively utilizing well-developed measurement techniques using synchrotron radiation X-rays, and databases and know-hows have been accumulated so far.

The first three topics are about spatial distribution or path of harmful elements and compounds from natural or artificial products using micro-XRF/XAFS techniques. The first topic, is about Mitsunobu *et al.*'s measurement of the spatial distributions of Sb oxidation states within a soil particle by the μ-XANES method. They clarified that the more toxic species Sb(III) has a higher affinity to the solid phase than Sb(V), and that the oxidation state is an important factor controlling the mobility and solubility of Sb.

The second topic is about the tracking of nanomaterials that invade the body through the nose. Nanosized particles are now widely used in industrial and medical products, which are more dangerous than micronsize particles. Matsui *et al.* revealed a pathway of diesel exhaust particles (DEPs) from the nose to the brain of mice after whole-body DEP exposure by measuring the major metal elements included in DEPs, such as Fe, Ni and Zn, using the micro-XRF method.

SCIENCE

The third topic is about phosphorus-amended immobilization technologies for metals in soil by plants, so called phytoremediation. Hashimoto *et al*. investigated the effect of phosphorus amendment on the solubility and speciation of Pb in a highly contaminated shooting range soil using the XAFS method.

The fourth topics is about Takahashi *et al*.'s study of the cause of the enrichment of heavy rare earth elements (HREEs) on bacterial cell surfaces using the EXAFS method. They found that the cause is the formation of multiple phosphate surface complexes. The results showed that bacterium-related materials that have phosphate sites can be used as separation agent of HREEs.

The fifth topic is about the mechanism of a newly developed convenient and versatile chemical sensor for sick house gas detection. This sensor consists of organic crystals, which show vapochromism, a reversible color change upon the absorption/desorption of volatile organic compound vapor. Takaya *et al*. revealed the mechanism of these dynamic vapochromic behaviors using XRD and DFT calculations.

The last topic concerns a remarkably active catalyst, which is important from the viewpoint of environmental friendliness and low energy consumption. Okumura *et al*. developed Pd catalysts loaded on zeolites exhibiting excellent catalytic activity in the Suzuki coupling reactions. He studied the formation of Pd a catalyst interacting with zeolites by the time-resolved *in situ* XAFS method, and revealed that atomically dispersed Pd is the active species in this catalytic reaction.

Tomoya Uruga


"Ajisai"- *Hydrangea*

Mechanism of antimony immobilization in contaminated soil under reducing condition

Antimony (Sb) is the ninth most mined metal worldwide. It is frequently used in a variety of industrial products such as flame retardants, catalysts in the synthesis of plastics, and alloys for ammunition. In general, the natural abundance of Sb in soils and sediments is low (less than 1 mg/kg) and it ranges from 10^{-3} to 10^{-6} mg/L in fresh water [1]. However, elevated concentrations of Sb have been detected in soils near mining and smelter areas and at shooting ranges [2,3]. However, the geochemical and environmental behaviors of Sb in natural aquifers are still largely unknown, while Sb and its compounds have recently been considered as pollutants of priority interest [2 and references therein].

The oxidation states of Sb observed in the environment are Sb(III) and Sb(V). It is considered that the geochemical fate and toxicity of Sb depend on the oxidation state; Sb(III) compounds are more toxic than Sb(V) compounds [1]. Recent studies have shown that the Sb concentration in pore water decreases under reducing conditions in contaminated soil, where the reductive dissolution of Fe(III) hydroxides (the host phase of Sb in soil) took place in soil (ex. [3]). However, the mechanism of this Sb immobilization in reductive soil is still unclear. Accordingly, to understand the chemical processes associate with Sb behavior, we have characterized Sb and Fe species in soil collected under reducing conditions at the microscale by micro-X-ray absorption fine structure (μ-XAFS) and electron probe microanalyzer (EPMA) techniques. In particular, the spatial distributions of Sb oxidation states within a soil particle were examined, since the oxidation state is an important factor controlling the mobility and solubility of Sb.

Natural soil samples in mine tailings were collected near the Ichinokawa mine pithead in Ehime, Japan. The redox condition of the soil was highly reductive (Eh = –107, pH 7.7; gray zone in Fig. 1), and Sb was accumulated in the soil. For μ-XAFS and EPMA, we prepared a thin section of the soil sample. Antimony *K*-edge μ-XANES experiments were performed at beamline **BL37XU**, a third-generation synchrotron facility. The incident beam was monochromatized with a Si(111) double-crystal monochromator and focused to 0.9 (V) μm × 1.3 (H) μm.

The chemical maps for Sb, Fe, and Si of two soil grains based on EPMA (Fig. 2) showed that Sb was accumulated into Fe oxides secondarily deposited on the rim of silicate minerals in grains A-B. Quantitative analyses indicated that the rims in grains A and B contain 4–15 wt.% Sb_2O_5, suggesting that Sb was highly concentrated in these parts. Figure 3(a) shows the normalized Sb *K*-edge XANES spectra of Sb hot spots in the rims of grains A and B. As presented in Figs. 3(b) and 3(c), the XANES spectra were measured at seven hot spots for each grain, including interior and surface points. The absorption edge of Sb shifted to lower energy at the surface (hot spots A5–7 and B4–7). These findings suggest that Sb(III) exists at the surface parts in both grains A and B. This partial Sb reduction to Sb(III) on the surface of the soil grain was also supported by XANES theoretical fittings (Figs. 3(d) and 3(e)). Previous studies reported that Sb(III) is adsorbed at the surface of Fe(III) hydroxides (the host phase of Sb in this soil) by inner-sphere surface complexation of the soil at pH 7.7 and it is adsorbed more strongly on the solid phase than Sb(V) [4]. Hence, Sb(III) has a higher affinity to the solid phase than Sb(V). In addition, the solubility of Sb(III) species in the soil is much lower (more than 10^5 times) than that of Sb(V) species, because Sb(III) forms neutral (or no anionic) hydroxide species, $Sb(OH)_3^0$, in this pH range.

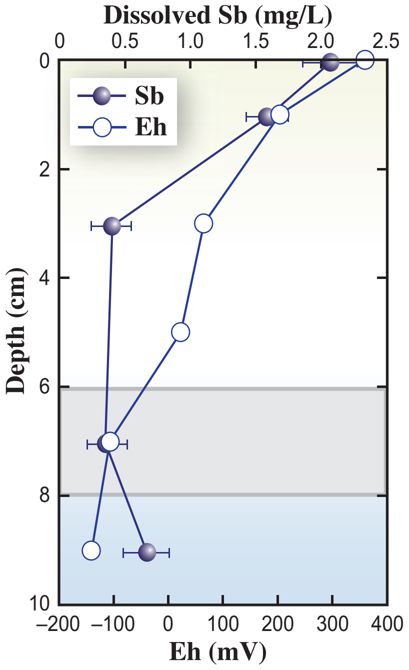

Fig. 1. Depth profile of Sb concentration and Eh (indicator of redox condition) in Ichinokawa soil. The gray box shows the depth of soil investigated in this study.

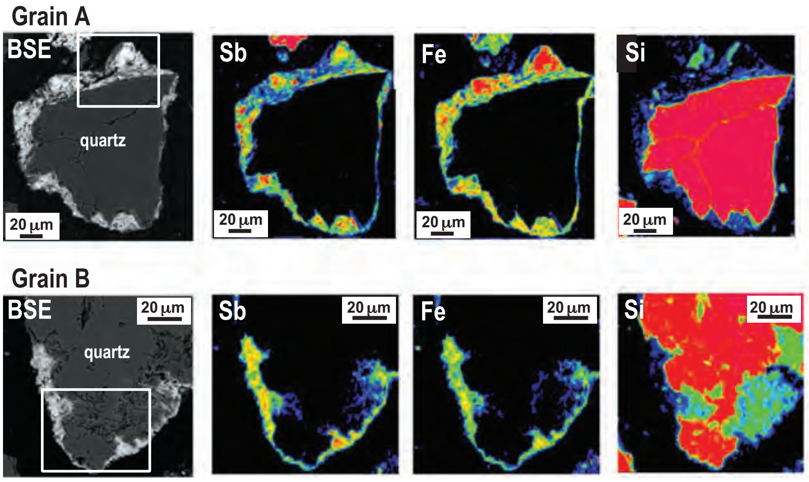

Fig. 2. Backscattered electron photomicrographs (BSEs) and element distribution maps for Sb, Fe, and Si of three soil particles (grains A-B) in Ichinokawa soil. The white frames in BSEs of grains A and B correspond to the images enlarged in Figs. 3(b) and 3(c), respectively.

These results suggest that the reduction to Sb(III) in the system can be a significant factor for Sb distribution for the solid phase observed under reducing conditions, considering both adsorbed and precipitated species. This study emphasized the importance of speciation in environmental samples in understanding the fate of Sb in the aquatic environment.

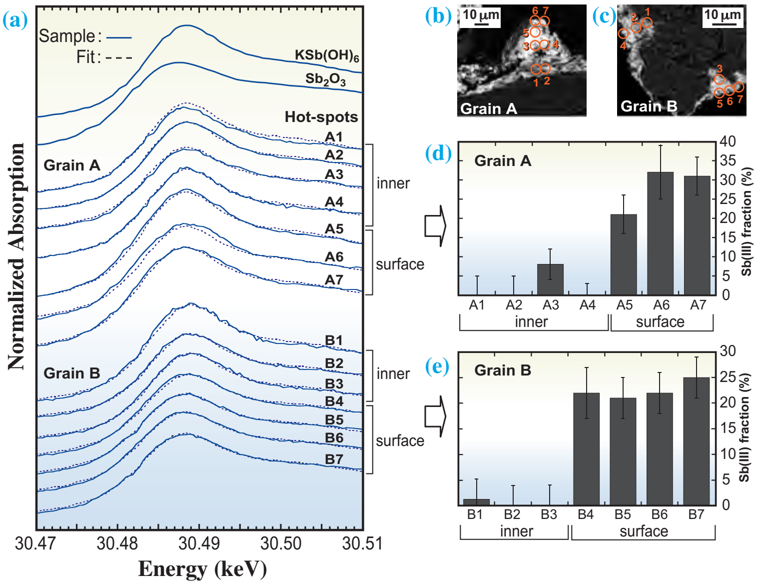

Fig. 3. **(a)** Normalized Sb *K*-edge μ-XANES spectra (solid lines) of the reference materials (Sb_2O_3 and $KSb(OH)_6$) and the points of interest (Sb hot spots) in grains A and B. Dashed lines overlapped on solid lines indicate the linear combination fits. Spectra of hot spots are shown in (a) according to "inner" or "surface" areas in each grain. **(b)** and **(c)** BSE images in grains A and B, respectively. The letters next to the orange circles indicate spots measured in (a). **(d)** and **(e)** Sb(III) fractions estimated by the simulation of Sb μ-XANES in spots of grains A and B, respectively.

Satoshi Mitsunobu

Institute for Environmental Sciences,
University of Shizuoka

E-mail: mitunobu@u-shizuoka-ken.ac.jp

References

[1] M. Filella *et al.*: Earth-Sci. Rev. **57** (2002) 125.
[2] S. Mitsunobu *et al.*: Environ. Sci. Technol. **40** (2006) 7270.
[3] A.C. Scheinost *et al.*: Geochim. Cosmochim. Acta **70** (2006) 3299.
[4] K. Oorts *et al.*: Environ. Sci. Technol. **42** (2008) 4378.
[5] *S. Mitsunobu, Y. Takahashi and Y. Terada: Environ. Sci. Technol.* ***44*** *(2010) 1281.*

Tracking the pathway of diesel exhaust particles from nose to brain by micro-X-ray florescence analysis

The work presented here is the result of tracking diesel exhaust particles (DEPs) in the olfactory nerve by detecting the metal elements included in those particles using micro-X-ray fluorescent analysis based synchrotron radiation (SR-XRF). Nanomaterials are already being widely used in medical products, such as dressings for injuries and wounds, dental-bonding agents, sunscreens, and cosmetics. It is also common in industrial products such as fuel cells, tires, tonal cartridges, clothing, and electronics. Nanosized particles (NPs) are more dangerous than microsized particles [1]. DEPs are well known for containing many NPs. Most of the particles emitted by engines are NPs with a diameter less than 50 nm in the nuclei mode. Most of the mass is from 50 nm to 1 μm in the accumulation mode. DEPs consist mainly of a highly agglomerated solid carbonaceous material and ash, as well as volatile organic and sulfur compounds. Metal compounds in the fuel and lube oil result in a small amount of inorganic ash. Recent studies have shown that after inhalation of metal NPs, an increase in the quantity of metal is evident in both the olfactory bulb and olfactory cortex [2]. These facts suggest that NPs can invade the olfactory nerve from the olfactory mucosa and are consequently transported to the central nervous system (CNS) via olfactory nerves (Fig. 1). However, recent studies have not shown that the NPs actually exist in olfactory nerves, which leads to the possibility that metal NPs could have been ionized in the nasal mucosa first, and then transported to the CNS as metal ions afterwards. It is proposed in further studies that NPs reach the olfactory bulb through cerebrospinal fluid enveloped by olfactory ensheathing cells [3]. The purpose of this study was reveal whether metal elements in DEPs are detectable in the olfactory epithelium and olfactory bulb after whole-body exposure to DEPs. By employing the method of micro-XRF, we were able to identify the metal elements included in DEPs and generate gradation maps showing the levels of metal elements within the minute tissue layers of the olfactory organ.

The 3D image in Fig. 1 (left: sagittal plate, right: coronal plate) is a micro-CT image measured using the table top system (inspeXio SMX-90CT, Shimadzu). The coronal section in the 3D image clearly shows the otherwise complex anatomy of the nasal cavity. The main area of the olfactory epithelium consists of three major cell types: (1) the olfactory cell, which forms the most superficial layer with support cells (olfactory cell layer: OCL), (2) one type of basal cell, which is a stem cell, and (3) another type of basal cell, which makes up the basal membrane (BM). The lamina propria (LP) consists of Bowman's glands, bundles of olfactory axons, and blood vessels of both small arteries and veins. The main olfactory bulb consists of six types of tissue layer: olfactory neuron layer (ONL), glomerular cell layer (GL), external plexiform layer, mitral cell layer (ML), internal plexiform layer, and granular cell layer. The first olfactory neurons at the olfactory epithelium form a bundle at the lamina propria, projecting to the glomerular cell layer at the olfactory bulb. Many synapses are in the glomerular cell layer and connect to higher neurons. Their cell bodies line up at the mitral cell layer and project to the nucleus of the amygdala and the piriform cortex in the brain. Given the invasion of the NPs into the olfactory nerves from their dendrites, the NPs can be transported to the olfactory bulb by axonal flow. Furthermore, in case the NPs pass the synapses in the glomerular cell layer according to the neurotransmission, the NPs could be transported to the amygdala and the piriform cortex.

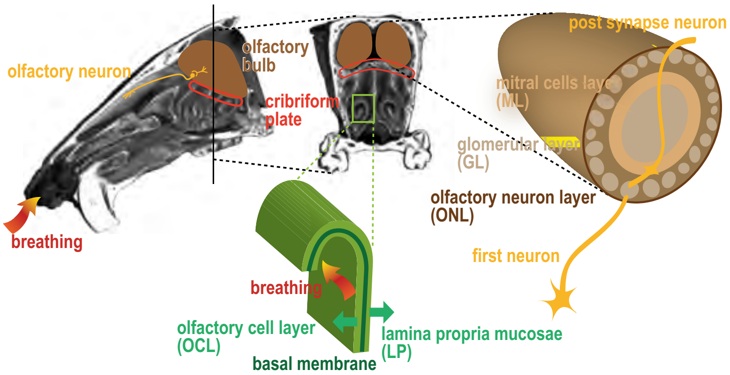

Fig. 1. Anatomy of the olfactory organ. CT image shows sagittal plate (left) and dose coronal plate (right) in lab mouse.

After the whole-body DEP exposure for four weeks, the mice were anesthetized by pentobarbital sodium, at which point they were transcardially perfused with phosphate-buffered saline and then fixed with 4% formaldehyde. DEPs were generated by a four-cylinder light-duty diesel engine (2740 cc, Isuzu) removed from a truck in the DEP inhalation facility at the National Institute for Environmental Studies, Japan [4]. The DEP concentration in the chamber was 0.1 mg/m^3 and the count median diameter was 40 nm. The olfactory bulb and epithelium were removed and prepared using a microslicer to a sectional thickness of 100 μm. Micro-XRF imaging was performed at beamline **BL37XU**. A white X-ray from the undulator was monochromatized to 10 keV using a Si (111) double-crystal monochromator and then was adjusted to a fine beam (1.6 H × 2.0V μm^2) using a Kirkpatrick-Baez (K-B) mirror. A silicon drift detector (SDD) was used to measure fluorescence X-ray intensity [5].

The major metal components measured in the Teflon filter that is used for removing NPs or viruses and for collecting the diesel exhaust particles were calcium, copper, iron, nickel and zinc. Figure 2 shows an SR-XRF spectrum of the filter. Figure 3 shows micro-XRF images of the olfactory epithelium and bulb. The gradation maps of iron (a,c) and nickel (b,d) were superimposed on optical microscope images. Fluorescence intensities in high level areas observed in the exposure group were more than 7 times stronger than those observed in the non-DEP exposure group. High-concentration areas marked by arrows appear as red in the LP in the exposure group (arrows, Fig. 3(a)). It is suggested that these high-concentration areas were caused by DEP exposure because all the elements were observed in those areas but not in the non-exposure group. These high concentration areas possibly correspond to the axon bundle of the first olfactory neurons in the LP and perhaps move to the olfactory bulb by axonal transport. In the result of the olfactory bulb, iron shows high-level areas at the ONL and GL, and nickel is observed on the ONL. One nickel high-level area was observed in the GL (arrow, Fig. 3(d)). Something probably existed as organic compounds or remained as DEPs at the terminal of the first neuron in the GL. In addition, the concentrations of iron and zinc were slightly higher in the ML after DEP exposure, showing that these metal elements were transported to the second neurons just beyond the synapse.

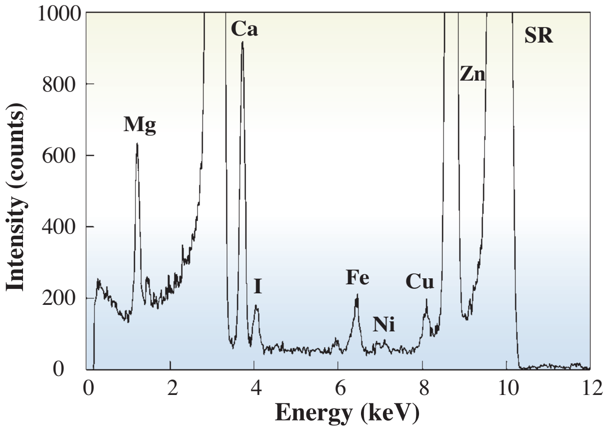

Fig. 2. XRF spectra of diesel exhaust nanosized particles (median diameter: 40 nm).

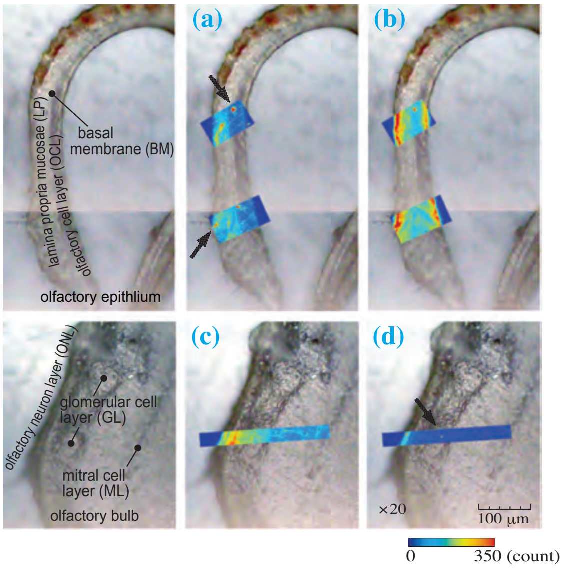

Fig. 3. Elemental mapping images of iron **(a, c)** and nickel **(b, d)** at the olfactory epithelium (upper) and olfactory bulb (lower) after DEP exposure. Exposure air included gaseous components.

Yasuto Matsui[a,b,*] and Nobumitsu Sakai[c]

[a] Department of Urban and Environmental Engineering, Kyoto University
[b] Occupational Health, Safety and Environmental Management Center, Kyoto University
[c] Department of Urban and Environmental Engineering, Kyoto University

*E-mail: ymatsui@risk.env.kyoto-u.ac.jp

References

[1] G. Oberdörster *et al*.: Environ. Health Persp. **113** (2005) 823.
[2] A. Elder *et al*.: Environ. Health Persp. **114** (2006) 1172.
[3] S.V. Dhuria *et al*.: J. Pharm. Sci. **99** (2010) 1654.
[4] H. Fujimaki *et al*.: Immunopharm. Immunot. **28** (2006) 703.
[5] *Y. Matsui, N. Sakai, A. Tsuda, Y. Terada, M. Takaoka, H. Fujimaki, I. Uchiyama: Spectrochim. Acta Part B* ***64*** *(2009) 796.*

Transformations of soil Pb species by plant growth and phosphorus amendment: Phytoremediation and metal immobilization technologies

Shooting range areas are one of the highly concerns of heavy metal contamination. Over 400 shooting ranges are present in Japan. The environmental impact of soil contamination around shooting ranges is closely related to chemical speciation of lead (Pb) in spent pellets. If Pb species present in the soil are readily soluble, then these species are predicted to be bioavailable. When a spent pellet has been released in the soil, the surface of the metallic Pb(0) is gradually oxidized to Pb(II) (e.g. PbO) and subsequently transformed into carbonate phases (e.g., $PbCO_3$). These species are labile and have been recognized as a primary phase controlling Pb solubility and availability in shooting range soils. Recent investigations using synchrotron-based X-ray spectroscopy have revealed that organically bound Pb is one of the predominant species in a shooting range soil with abundant organic matter [1]. Lead sorbed to pedogenic Fe and Mn (oxy)hydroxides is another important phase for moderating solubility and bioavailability [2]. These Pb phases occurring in soil systems are illustrated in Fig. 1.

The success of *in situ* remediation programs of Pb contaminated shooting range soil relies on the transformation of comparably soluble Pb species into thermodynamically more stable species. A technology attracting attention concerning the remediation of contaminated shooting range soil is the immobilization of Pb using phosphorus-containing amendments. The mechanism of Pb immobilization using phosphorus (P) amendments is based on the rapid kinetic formation of Pb phosphates [e.g., $Pb_5(PO_4)_3Cl$], which are thermodynamically the most stable in a wide range of pH and redox status under earth surface conditions. Used in conjunction with plant growth, phosphorus-amended immobilization technologies can be used to reduce the leaching potential of both dissolved phosphorus and metal contaminants in the soil profile [3]. This remediation technology is called phytostabilization, which reduces the risk of metal toxicity and mobility by transforming metal speciation in the soil. However, it remained unclear how chemical speciation of preexisting Pb is affected in the soil surrounding plant roots (i.e., rhizosphere soils).

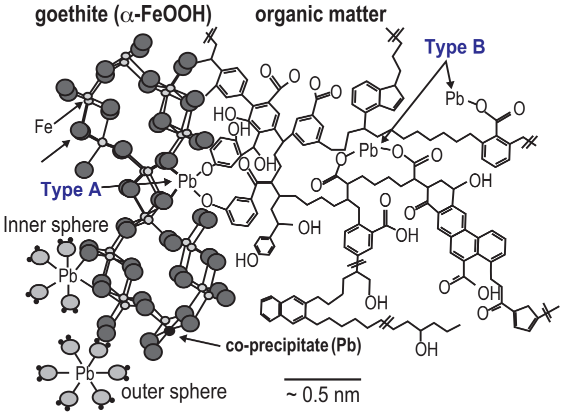

Fig. 1. Molecular mechanisms of Pb(II) bonding to an Fe oxide-organic matter assemblage. Mechanisms involving the mineral component include inner- and outer-sphere surface complexes, and coprecipitation by isomorphic substitution into the mineral structure. A Type A ternary complex is a bridging cation between the organic and mineral components, and a Type B ternary complex involves the mineral-bound organic matter. Figure modified based on Hesterberg *et al*. [5].

Plant roots can alter metal speciation via rhizosphere processes that physically and biochemically modify the properties of the soil at root interfaces. Plants and mycorrhiza (fungi) closely associated with roots locally modify the chemical properties of rhizosphere soils by exuding exchanging ions and organic acids. From the perspective of Pb immobilization, biochemical alternation of rhizosphere soils compared with the bulk soils may have a distinct effect on the solubility of amendment and Pb minerals, which eventually promotes transformations of preexisting Pb species. For the development and evaluation of phosphorus-amended phytostabilization technology for shooting ranges, it is necessary to assess how the plant rhizosphere affects the speciation and solubility of Pb in soil.

We investigated the effect of phosphorus amendment on the solubility and speciation of Pb in a highly contaminated shooting range soil under rhizosphere conditions. A Pb-contaminated soil collected from a shooting range was treated with a phosphorus amendment, and buckwheat plants were grown in the pot. After 100 days, the soil was collected and analyzed for Pb L_{III}-edge EXAFS spectroscopy at beamline **BL01B1** in a fluorescent mode. To provide qualitative and quantitative estimates of Pb speciation, the Pb-EXAFS spectra of soil samples were modeled by least-squares fitting using a linear combination (LCF) of known standard Pb species. Knowledge from soil mineralogical and chemical properties and related studies [2] was employed to narrow down the standard spectra used for the fitting procedure. Detailed information is available in Hashimoto *et al.* [4].

To assess the effect of root growth and P amendment on the soil Pb speciation, Pb L_{III}-edge EXAFS spectra of selected soil samples were simply compared (Fig. 2). The P amendment modified the overall spectral shape, which differed from that of unamended soil (Fig. 2(a)). In addition to the molecular spectroscopic analysis, a soil extraction procedure showed a significant reduction of soluble Pb concentration in the P-amended soil, indicating the modification of soil Pb species to less soluble phases. In the soil growing buckwheat, the overall shape of the Pb L_{III}-edge EXAFS spectrum was altered as compared with that of bulk soil (Fig. 2(b)). These results indicate the modifications of preexisting soil Pb species by the P amendment and plant root growth. The overall structure of EXAFS spectrum was also different among the plant species [4], suggesting that modifications of soil Pb species could be dependent on biochemical processes of plant roots.

The LCF procedure on the EXAFS spectra revealed that Pb in the *bulk* soil was present in the form of $PbCO_3$ (37%), and Pb sorbed on Fe minerals (Pb-Fe, 36%) and on organic matter (Pborg, 15%) (Fig. 3). The predominance of these Pb species could be supported by the soil chemical constraints, including the abundance of Fe (oxy)hydroxides, organic matter and carbonate minerals [3]. The *buckwheat* soil contained more Pb-Fe (51%) and less $PbCO_3$ (25%) than the *bulk* soil. These notable modifications of Pb species occurred due to acidification of buckwheat rhizosphere soil whose pH value was significantly lower than that of the *bulk* soil. The reduced Pb solubility in the *buckwheat + P* soil resulted from the transformation of preexisting $PbCO_3$ and Pborg into thermodynamically more stable $Pb_5(PO_4)_3Cl$ (26%) and Pb-Fe (57%) phases. It was expected that the mechanism of Pb immobilization by P amendments relies entirely on the formation of Pb phosphate compounds. Our study, however, concluded that the inner-sphere complex of Pb with Fe minerals is an alternative mechanism of soil Pb immobilization [4]. This study demonstrated that root growth modifies Pb speciation in P-amended soils, and for the purpose of phytostabilization, some plant species with strong rhizosphere processes may impair the efficiency of Pb immobilization by P amendments.

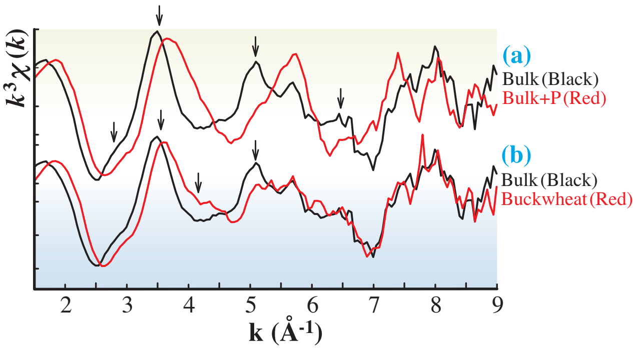

Fig. 2. Pb L_{III}-edge EXAFS spectra of soil samples comparing **(a)** the effect of the P amendment in the bulk (non-rhizosphere) soils, and **(b)** the effect of plant growth in the unamended soils. Arrows point to spectral modifications caused by the amendment or the plant growth.

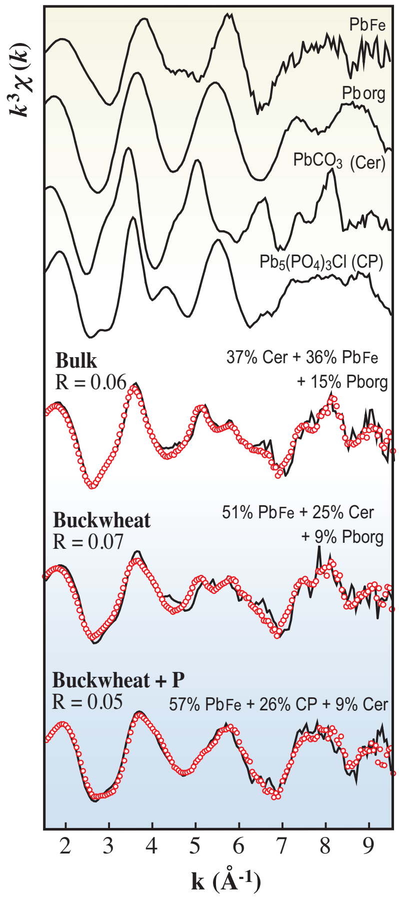

Fig. 3. Pb L_{III}-edge EXAFS spectra (solid line) of soil samples and their best linear combination fits (circle) using the standard spectra of known Pb species. Cer, cerussite ($PbCO_3$); CP, chloropyromorphite [$Pb_5(PO_4)_3Cl$]; PbFe and Pborg, Pb sorbed on ferrihydrite and on organic matter, respectively.

Yohey Hashimoto[a,*] and Masaki Takaoka[b]

[a] Department of Bioresource Science, Mie University
[b] Department of Urban and Environmental Engineering, Kyoto University

*E-mail: yhashim@bio.mie-u.ac.jp

References

[1] Y. Hashimoto *et al.*: J. Environ. Qual. **38** (2009) 1420.
[2] A.W. Schroth *et al.*: Environ. Sci. Technol. **42** (2008) 3627.
[3] Y. Hashimoto *et al.*: Chemosphere **73** (2008) 643.
[4] *Y. Hashimoto, M. Takaoka and K. Shiota: J. Environ. Qual. 40 (2011) 696.*
[5] D. Hesterberg *et al.*: J. Environ. Qual. **40** (2011) 667.

EXAFS study on the cause of enrichment of heavy rare earth elements on bacterial cell surfaces

In our previous studies [1,2], we investigated the adsorption of rare earth elements (REEs) on a bacterial cell surfaces in bacterial suspension system in water. As a result, we found that REEs consisting of lanthanides and yttrium have high affinities to bacterial cell surfaces. In particular, peculiar enrichment to the cell surfaces was found for heavy REEs such as Dy, Tm, Yb, and Lu in the REE distribution patterns between bacteria and water (Fig. 1(a)). These findings are noteworthy from various viewpoints. In the cycle of rare metal resources, the results suggested that bacteria and bacteria-related materials can be used to recover REEs from a solution containing REEs in refining and recycling systems. The high selectivity of HREEs may enable us to use the bacteria for the mutual separation of REEs, since REEs are usually recovered as a mixture from mineral ores. From the biogeochemical point of view, the HREE-enriched REE pattern can be unique, which can be used as a biomarker in natural samples, since other adsorbents of REEs in nature do not exhibit such HREE enrichment signature. To develop applications of our previous results to the engineering field of REE resources using bacteria and also to the biogeochemical field using REE distribution pattern as a biomarker, it is essential to understand the interaction of REE and bacteria from the atomic scale, which must be linked to the high affinity of REEs and the high selectivity of HREEs to bacteria. Thus, we employed extended X-ray absorption fine structure (EXAFS) spectroscopy to reveal the binding site of REE on bacterial cell surfaces.

EXAFS spectra at L_{III}-edge of various REEs were measured at beamline **BL01B1** for REEs adsorbed on a Gram-positive bacterium (*Bacillus subtilis*). The EXAFS data showed that the HREE form complexes with multiple phosphate sites (including phosphoester sites) with a larger coordination number (CN) at lower REE-bacteria ratios ([REE]/[bac]), whereas light and middle REEs form complexes to the phosphate site with a lower CN. The fraction coordinated to carboxylate increased for all REEs with increasing [REE]/[bac] ratio (Fig. 2). On the other hand, the enrichment of HREEs in the REE distribution patterns of the bacteria was less marked with increasing [REE]/[bac] ratio. This result is consistent with the EXAFS data, because the REE pattern of the surface complex with multiple phosphate sites in a reference material (Ln-resin) exhibits a monotonic increase for heavier REEs, whereas the phosphate surface complex with a low CN (cellulose phosphate) and a carboxylate site (carboxylmethyl cellulose) reach a maximum around Sm and Eu. On the basis of

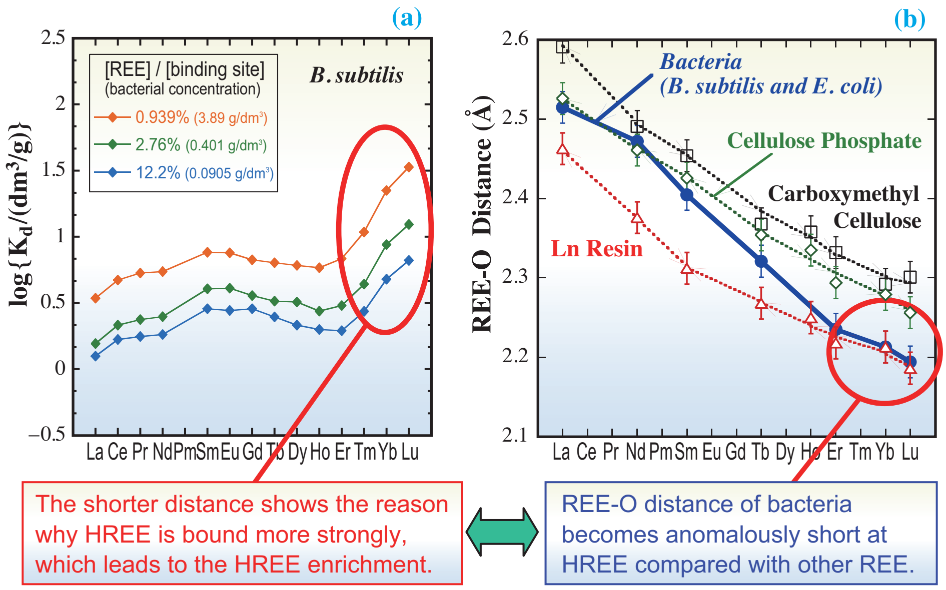

The shorter distance shows the reason why HREE is bound more strongly, which leads to the HREE enrichment.

REE-O distance of bacteria becomes anomalously short at HREE compared with other REE.

Fig. 1. **(a)** REE distribution pattern of adsorption coefficient (= Kd) at various [REE]/[bac] ratios. **(b)** Average REE-O bond length of REEs sorbed on reference materials, *B. subtilis*, and *E. coli* determined by EXAFS.

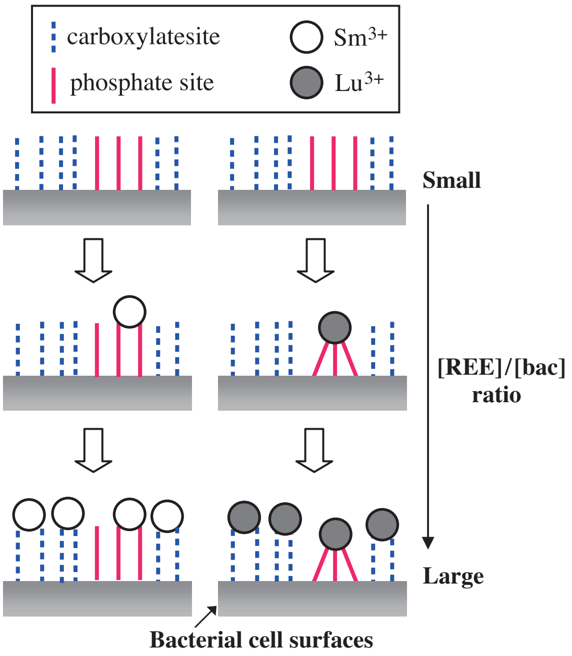

Fig. 2. Schematic of the variation of binding site with increasing in the [REE]/[bac] ratio for Sm^{3+} and Lu^{3+} ions representing middle REEs and HREEs, respectively.

these results, it is clear that the REEs are primarily bound to the phosphate site and subsequently to the carboxylate site on the bacterial cell surface. The variation of the binding sites described above is depicted in Fig. 2.

The results obtained for *B. subtilis* were also valid for *Escherichia coli*, a Gram-negative bacterium, showing that similar phosphate and carboxylate sites are also available in the cell walls of *E. coli*, or other Gram-negative bacteria. The fact that similar adsorption behaviors of REEs were obtained for both Gram-positive and Gram-negative bacteria showed that the high affinity of REEs and enrichment of HREEs are common features for REE adsorption on any bacteria in nature.

In all of our results, the variation in the shape of REE distribution pattern correlated with the binding site indicated by EXAFS, which showed that the REE distribution pattern itself reflects the binding site of REEs on the bacterial surface. Thus, the REE distribution pattern can be used to estimate the binding sites for lower [REE]/[bac] ratios, where spectroscopic techniques such as EXAFS cannot be applied.

The average bond length between the REEs and oxygen was compared for various REEs sorbed on bacteria, showing that the bond length for HREEs (Er to Lu) was much shorter than those extrapolated from the trend between La and Dy, because of the selective binding of the HREEs as multiple phosphate surface complexes. Our results are consistent with the selective enrichment of the HREEs on the bacterial cell surfaces, considering that chemical species with a shorter bond length are more stable. Thus, it is clear that the HREE enrichment on the bacterial cell surfaces is caused by the formation of multiple phosphate surface complexes (Fig. 1). On the basis of these results, it is suggested that materials having such phosphate sites such as bacteria and bacteria-related materials can induce anomalous HREE enrichment in natural systems.

The finding that REEs are associated with phosphate sites on bacterial cell surfaces has various implications both on the technology of REE recovery and separation by bacteria and also on the possibility of the REE distribution pattern as a biomarker. The results showed that bacteria-related materials that have phosphate sites can be used as adsorbents and separation agents of REEs. On the other hand, the fact that the anomalous HREE enrichment is caused by the formation of multiple phosphate sites, which are not usually found in other important REE host phases such as Fe and Mn oxides and humic substances in nature, makes REE patterns a potential tool as a biomarker.

Yoshio Takahashi

Department of Earth and Planetary Systems Science,
Hiroshima University

E-mail: ytakaha@hiroshima-u.ac.jp

References

[1] Y. Takahashi *et al*.: Chem. Geol. **219** (2005) 53.
[2] Y. Takahashi *et al*.: Chem. Geol. **244** (2007) 569.
[3] *Y. Takahashi, M. Yamamoto, Y. Yamamoto and K. Tanaka: Geochim. Cosmochim. Acta* ***74*** *(2010) 5443.*

Vapochromic behaviors of organic crystals: A convenient and versatile chemical sensor for sick house gas detection

The development of highly sensitive and selective detection colorimetric reagents for volatile organic compounds (VOPs) including so-called sick house syndrome gases has been one of the urgent social demands. A variety of transition-metal-based colorimetric reagents have been reported for VOP detection. The large *d*-orbitals of an electron-rich metal can interact effectively with VOP molecules to provide a highly sensitive and versatile color change toward the adsorption/desorption of VOP molecules. However, some of the heavy metals used for colorimetric reagents are environmentally unfriendly and expensive. The development of metal-free organic colorimetric reagents with sustainability is becoming an urgent social demand, which motivated and guided us.

Recently, our research group has found that the organic crystal of the PI-NDI molecule, in which 1,4,5,8-naphthalenetetracarboxylic diimide (NDI) is connected to two 4-*t*-butylpyrroleimine (PI) tethers, shows remarkable sensing ability for VOP detection, including typical sick house syndrome gases such as methanol, toluene, and formaldehyde (Fig. 1) [1]. The red-purple powder crystal of PI-NDI changed to orange upon exposure to methanol vapor. Vapochromism, a reversible color change upon absorption/desorption of VOP vapor, was observed on the PI-NDI system, as shown in Fig. 1. The methanol-absorbed orange powder crystal reverts to the original red-purple powder under vacuum condition where the vapochromic process can be repeated without crystal decomposition. The visible detection of typical sick house syndrome gases that are emitted from building materials, which cause chronic health problems and allergy symptoms such as headache, chills, and eye, nose, throat irritation, was demonstrated upon exposure of PI-NDI to toluene, DMSO, THF, and formaldehyde. The distinct and wide range of color change from the original red-purple to orange to yellow guarantee the effectiveness and usefulness of PI-NDI as an organochemical sensor.

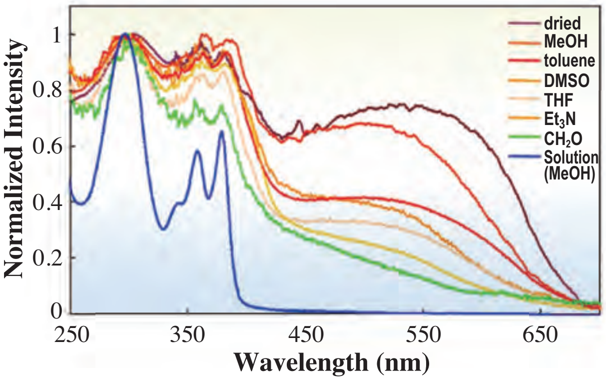

Fig. 2. Solid-state UV-*vis* spectra of PI-NDI exposed to various VOPs.

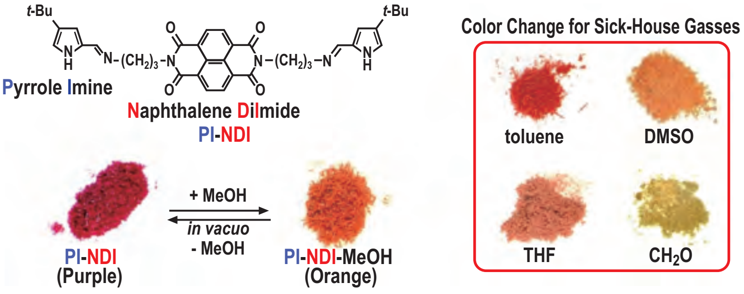

Fig. 1. PI-NDI molecule and colorimetric changes for VOP detection.

The mechanistic investigation of the vapochromic color change of PI-NDI was carried out by solid-state UV-*vis* spectroscopy in $BaSO_4$ as matrix (Fig. 2). The significant change of the 400-650 nm region ascribed to the charge transfer of the PI unit to the NDI unit suggested that the gas molecules introduced into the crystalline PI-NDI affect the charge transfer interaction. The lack of solvation-induced color change in methanol solution (blue line in Fig. 2) supports the fact that the molecular structure and assembly formed in the crystal state are keys for the vapochromic behavior.

The molecular structure of PI-NDI in crystal was unequivocally determined by synchrotron X-ray powder diffraction at beamline **BL19B2**. The X-ray structure of the methanol absorbed PI-NDI definitely demonstrated that methanols trapped in the crystal lattice occupy the interstitial cavity between the PI and NDI units affecting the perturbation of PI-NDI charge-transfer interactions (Fig. 3). The molecular structure of guest-VOP-free PI-NDI was also obtained from the powder X-ray structure analysis at the same beamline. The *S*-shaped sandwich structure of PI-NDI well retained with the cavity for VOP trap and detection. The interspatial distance of PI and NDI unit shortened from 3.319 Å of PI-NDI·2MeOH to 3.292 Å of guest-free PI-NDI qualifies as evidence for VOP-inclusion-induced perturbation change of PI-NDI interaction. The relationship of color change and PI-NDI geometry was confirmed by DFT calculation based on these X-ray structures within

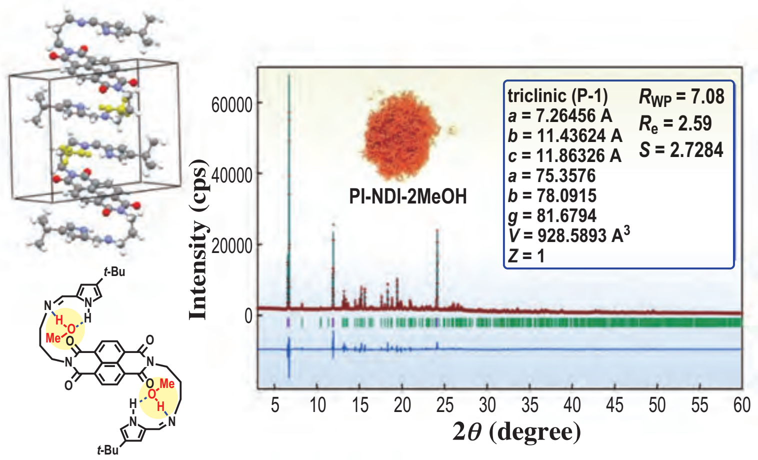

Fig. 3. Molecular structure of methanol absorbed PI-NDI.

periodic boundary condition using GGA-PBE pseudopotential. The DFT-based simulation clearly exhibits the decrease in the 450-650 nm signal intensity corresponding to the color change from red-purple to orange as observed in the methanol absorption of PI-NDI. The calculated changes in the interspatial distances of PI-NDI were 3.322 Å for PI-NDI•2MeOH and 3.296 Å for guest-free PI-NDI, being in good agreement with the results of powder X-ray structure analysis. The combination of strong electron donor and acceptor of PI and NDI would lead to the observed susceptibility to microenvironmental change in the PI-NDI crystal lattice and molecular geometry to afford a versatile color change dependent on various VOP molecules. These results clearly indicate the effectiveness of the molecular design based on the charge transfer system for the creation of metal-free organochemical sensors.

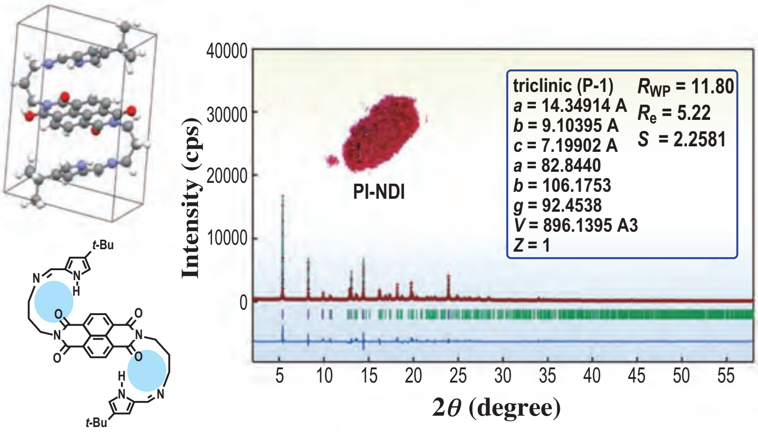

Fig. 4. Molecular structure of guest-free PI-NDI.

Hikaru Takaya[a,b,*], Eiji Takahashi[c] and Takeshi Naota[c]

[a] International Research Center for Elements Science,
Kyoto University
[b] PREST, Japan Science and Technology Agency
[c] Division of Chemistry, Osaka Univeristy

*E-mail: takaya@scl.kyoto-u.ac.jp

References

[1] *E. Takahashi, H. Takaya and T. Naota: Chem. Euro. J.* ***16*** *(2010) 4793.*

XAFS studies on the formation of atomic Pd active in the Suzuki coupling reactions

Cross-coupling reactions, such as Suzuki, Negishi and Heck reactions, are very important in the field of organic synthesis and are utilized for the production of pharmaceuticals, organic electroluminescent devices, and liquid crystals. These reactions attract much attention these days; as a matter of fact, the 2010 Nobel Prize in Chemistry was awarded to the discoverers of these reactions. In the Suzuki coupling reactions, selective formation of C-C bond occurs through the reaction between halogenated aromatics and derivatives of phenylboronic acids. On the other hand, C=C bond formation occurs between halogenated aromatics and olefins with high selectivity and yield in Heck reactions. To date, numerous Pd complexes, such as palladacycles and *N*-heterocyclic carbenes, have been developed as catalysts for use in these reactions. However, these Pd(0) or Pd(II) complexes cause difficulties in the synthesis and purification of the final product. Another class of catalysts for these reactions, namely, heterogeneous catalysts, are easy to prepare and readily separated from the products. Therefore, heterogeneous catalysts that show high activity are more beneficial than homogeneous ones from the viewpoint of environmental friendliness and low energy consumption. Among these supported catalysts, there are several reports on supported Pd catalysts that are nearly as active as the best homogeneous ones. These highly active heterogeneous catalysts have been realized when well-dispersed active sites with a homogeneous structure are fabricated on supports. Moreover, well-dispersed metals having surface atoms with a low coordination number are anticipated to exhibit high activity; this behavior is different from that of a bulk-type catalyst.

Zeolites have a large surface area and uniform micropores, which can accommodate dispersed metal clusters, leading to a high surface-to-volume ratio. Using zeolites as supports for Pd is therefore expected to lead to high catalytic activity. Among the various zeolites, faujasite-type zeolites are the most promising for use as a support for Pd because they have a large supercage with diameters of *ca*. 1.3 nm. Indeed, we found that Pd loaded on ultra-stable Y (USY) zeolites exhibited excellent catalytic activity in a Suzuki reaction when H_2 was bubbled through the system prior to the reaction [1]. Evolution of the extremely high activity was found only when o-xylene and Pd ammine complexes were used as the solvent and the Pd precursor, respectively. The catalytic activity was improved significantly by continuously bubbling H_2 through the system during the reaction, as shown in Fig. 1 [2]. A similar enhancement of the catalytic activity by H_2 was also found in Heck reactions [3]. To reveal the reason for the evolution of such high catalytic activity, we have tried to analyze the structure and valence of active Pd species generated by H_2 bubbling in *o*-xylene using extended X-ray absorption fine structure (EXAFS) analysis under *in situ* conditions.

EXAFS experiments were performed at beamlines **BL14B2** and **BL01B1**. Figure 2 illustrates the equipment for *in situ* measurements of Pd/USY immersed in *o*-xylene. The Pd/USY catalyst and *o*-xylene were mounted in the plastic cell connected to the condenser. The 6% H_2 diluted with He was introduced to the Pd/USY while the solution was stirred with a magnetic stirrer. The Pd *K*-edge EXAFS

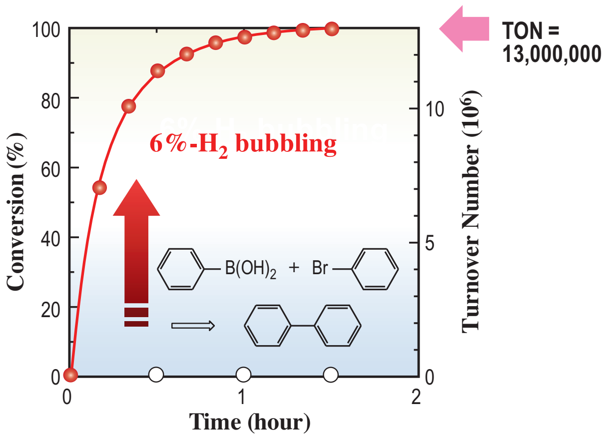

Fig. 1. Time course of the conversion of bromobenzene over 0.4 wt% Pd/USY with or without 6% H_2 bubbling.

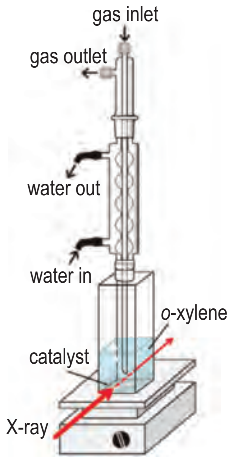

Fig. 2. Equipment for *in situ* XAFS measurements of Pd/USY in *o*-xylene with H_2 bubbling.

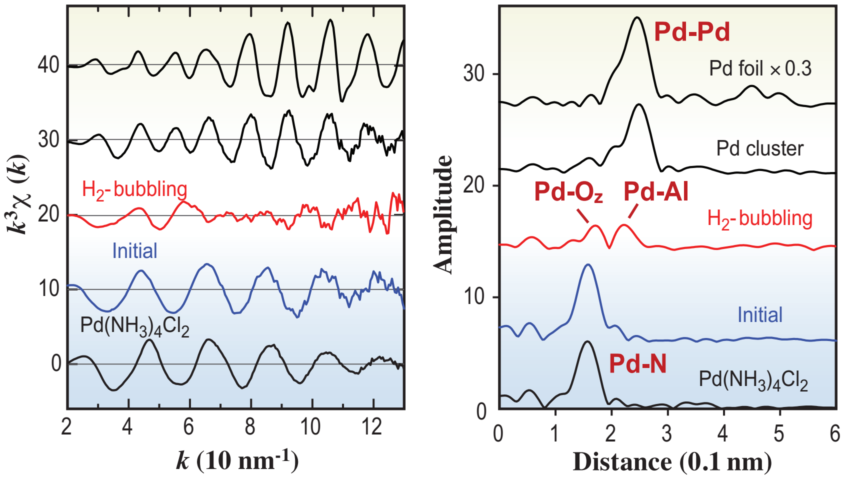

Fig. 3. Pd K-edge EXAFS $k^3\chi(k)$ and their Fourier transforms (FT) of Pd/USY measured after H_2 bubbling in o-xylene and reduction with H_2 in the gas phase, together with reference samples.

spectrum of Pd/USY measured in *o*-xylene using this *in situ* cell is given in Fig. 3. The spectrum showed Pd-O_z and Pd-Al bonds arising from the framework of USY zeolites. The feature was much different from that of the Pd cluster where an intense Pd-Pd bond was observed. Pd L_3-edge XANES spectra measured at Rits-BL10 indicated that the valence of the Pd reduced with bubbling H_2 was +0.3. These facts indicate the formation of atomically dispersed Pd species with a slightly cationic character when Pd/USY was reduced with bubbling H_2 in *o*-xylene, which was considered to be the active species in Suzuki coupling reactions [4]. In addition to studying the active sites, it is important to obtain insights into the role of the support, taking into account that the catalytic performance of Pd varies significantly depending on the type of support. For this purpose, the acid character of USY zeolites was analyzed by IRMS-TPD methods [5]. The detailed analysis of acid properties of USY zeolites in correlation with catalytic performance revealed that the strong acid sites characteristic of USY zeolites had a profound effect on the catalysis of Pd/USY [4]. On the basis of the catalytic activity, Pd *K*-edge and Pd L_3-edge XAFS analyses, and IRMS-TPD studies, the active species was proposed to be the atomic Pd with a partially cationic character, which was anchored to the strong acid sites induced by extra-framework Al species, as shown in Fig. 4.

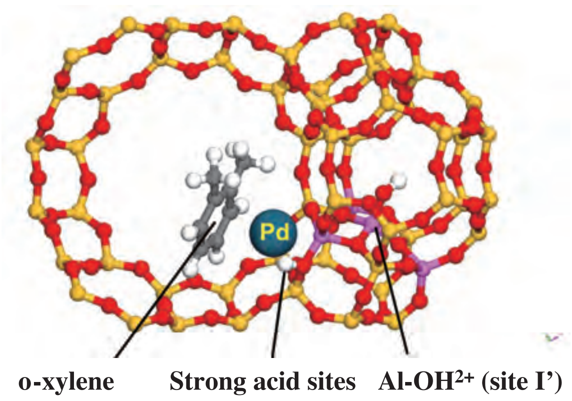

Fig. 4. Proposed structure of the atomic Pd generated in the supercage of USY zeolite.

Kazu Okumura

Department of Materials Science, Tottori University

E-mail: okmr@chem.tottori-u.ac.jp

References

[1] K. Okumura *et al.*: J. Catal. **265** (2009) 89.
[2] K. Okumura *et al.*: Chem. Phys. Chem. **10** (2009) 3129.
[3] *K. Okumura, T. Tomiyama, S. Moriyama, A. Nakamichi and M. Niwa: Molecules* ***16*** *(2011) 38.*
[4] *K. Okumura, T. Tomiyama, S. Okuda, H. Yoshida, M. Niwa: J. Catal.* ***273*** *(2010) 156.*
[5] *T. Tomiyama, K. Okumura and M. Niwa: Chem. Lett.* ***40*** *(2011) 49.*

INDUSTRIAL


"Niseakashia"- *Robinia*

In 2009, two contract beamlines for industrial application were in operation. The Toyota beamline BL33XU, which is the first beamline in SPring-8 with a tapered undulator, was designed for the dynamic observation of chemical reactions through the XAFS technique. The Frontier Soft Matter Beamline (FSBL) BL03XU was established by the Advanced Softmaterial Beamline Consortium consisting of 19 research groups from both commercial corporations and universities.

On the other hand, the industrial application of SPring-8 in 2009 was largely influenced by the "Lehman Shock", and the number of companies using SPring-8 decreased from 190 to 171 in 2008. In 2009A (the first term of the fiscal year 2009), the number of non-proprietary proposals at public beamlines by companies was as many as that in 2008B (the second term of the fiscal year 2009). However, proprietary proposals markedly decreased in 2009A. In particular, measurement service proposals in 2009A drastically decreased to 22% of that in 2008B. The recovery of the number of proprietary proposals to the normal level occurred in 2009B.

In the present issue, five topics were chosen to represent the works carried out in Industrial Applications. In particular, we focused on outputs using X-ray imaging techniques in this issue, since the last two issues mainly introduced topics obtained by diffractometric or spectroscopic techniques.

APPLICATIONS

The first topic by Koike *et al*. is about the application of microcomputed tomography (μ-CT) at BL47XU for the development of laser fusion technology for splicing optical fibers. It was clarified that origin of splicing loss was the presence of small inclusions detected by μ-CT at BL47XU. Considering that the result of X-ray fluorescence analysis at BL19B2 elucidated the inclusion to be zirconium compounds, a new splicing process was developed to reduce inclusions.

In the second topic, I am very happy to introduce the output obtained at newly established contract beamline BL03XU. Senoo *et al*. revealed that silica particles of 45 and 110 nm diameters are uniformly dispersed without any aggregation in transparent plastic substrates by SAXS observations at BL03XU and BL08B2.

In the third topic, Sano *et al*. proposed the technique for detecting fatigue cracks inside materials by CT observation at BL19B2. A newly developed holder, which loads tension on specimens to open fatigue cracks, was introduced to visualize inside cracks.

Matsui *et al*. introduced equipment for CT installed at the Hyogo prefectural contract beamlines BL08B2 and BL24XU. The high-speed CT with an acquisition time of 0.144 s should be a very powerful technique for industrial applications.

The technique for elucidating the inner strain of individual steel grains was proposed by Kajiwara *et al*. in the last topic. It was clearly observed that the responses of strain to external stress differed from grain to grain. These four topics show that X-ray imaging is very useful in industrial application for characterizing various types of material.

Ichiro Hirosawa

Zr inclusions revealed by microcomputed tomography observations on the CO_2 laser fusion splicing interface between single-mode optical fibers

Throughout the communications equipment hierarchy from cabinet-level to board-level interconnection, optical interconnection technologies have recently attracted much attention as the solution for the interconnection bottleneck [1], such as the limits of the interconnection density in future high-performance computing systems, routers and servers. In applying many optical fiber interconnections to board-level interconnections, the technical difficulties related to entanglement of optical fibers wired on circuit boards need to be solved.

We have proposed the laser fusion splicing technology for fiber buckling (Ref. [2]). The technology has advantages in terms of efficient integration of a large number of optical fibers on circuit boards, because it does not require the same complicated optical fiber positioning mechanism and large electrodes for melting down fibers as in the currently used electric arc discharge method [3].

Figure 1 shows the experimental setup for CO_2 laser fusion splicing for single-mode silica optical fibers with the external diameter of 125 micrometers using the fiber buckling. The single-mode optical fiber cores (about 10 μmϕ) inside both fiber#1 and fiber#2 are aligned by inserting the optical fibers into the conventionally used zirconia-ceramics V-shaped grooves and by closing the arms attached to the plate, as shown in Fig. 1. After butting both optical fiber end faces, the optical fiber buckling force can be generated by making optical fiber#1 go forward with a small offset of Δy. The adjustment to the buckling force results in the splicing interface with the suitable volume of silica optical fiber material, when the spliced interface of silica is melted by CO_2 laser irradiation. Thus, the laser system installed at the remote position from the circuit board and the fiber buckling force can replace the large fiber fusion splicing system. However, new characteristics of the laser-fusion-spliced optical fiber, such as mechanical fracture strength and splicing loss distribution, have not yet been fully elucidated [4].

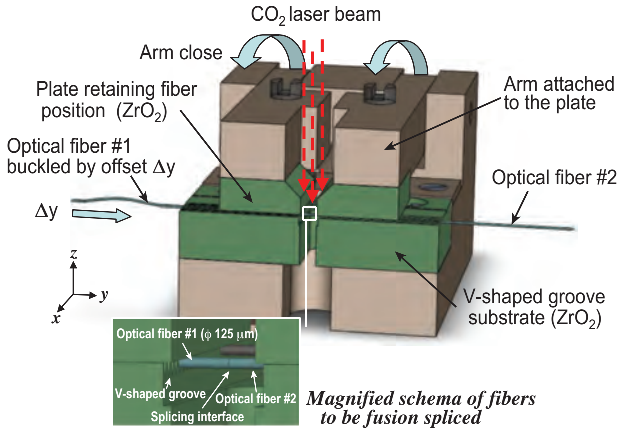

Fig. 1. Isometric cross-sectional view of experimental apparatus for stabilizing optical fibers to be laser-fusion-spliced for fiber buckling.

SPring-8 microcomputed tomography (SP-μCT) installed at beamline **BL47XU** is a powerful method of nondestructive investigation that enables even the cross-sectional structure of the spliced optical fiber with a high signal-to-noise ratio to be visualized with the proper choice of X-ray energy and an intensive photon dose using a ring accelerator and an undulating magnet field system [5]. It also enables the precise linear absorption coefficient (LAC) distribution with one-micrometer-space resolution that is suitable for observing optical fiber structure changes to be obtained. The SP-μCT clarified the existence of some inclusions with high LAC at the interface between optical fibers spliced using a CO_2 laser. The observation results implied that the laser fusion splicing losses increased with the volume of the inclusions lying behind the fusion splicing interface.

Figure 2 shows the fluorescent X-ray spectroscopy results obtained at the splicing interface and at a position away from the splicing interface. Fluorescent X-ray spectroscopy measurement was carried out with a germanium single-element solid-state detector (Ge SSD) installed at beamline **BL19B2**. As shown in this experimental result, detection of Zr K_α fluorescence at the interface implies that the inclusions were the material including zirconium. After this analysis, the newly proposed cleaning process using micro-polyester nylon fiber textiles and air blowing with a microstatic eliminator have been introduced to clean up the V-shaped groove substrate and the plate retaining the fiber position as shown in Fig. 1 [6].

Figure 3 shows the effect of the zirconium inclusions on the structural changes of the optical fiber core and cladding observed from the classification of LACs. The structural relationship between the zirconium inclusions, optical fiber core and optical fiber external structure was successfully visualized by SP-μCT. We could observe clearly a large volume of zirconium inclusions in the sample fabricated before the introduction of the cleaning process as shown in this figure, whereas only a small volume of zirconium inclusions could be observed in the sample fabricated after the introduction of the cleaning process [6].

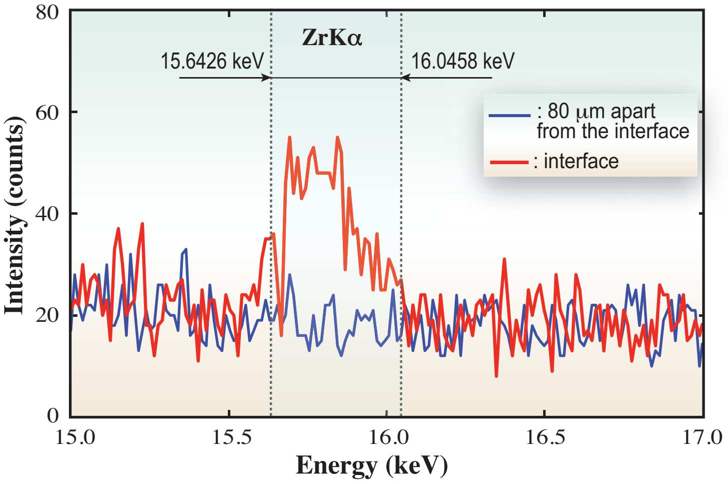

Fig. 2. Results of fluorescent X-ray spectroscopic microbeam analysis at the interface of the laser-spliced fiber and a position away from the interface.

Thus, the proposed cleaning process is considered to enable the reduction of the volume of zirconium inclusions at the fusion-splicing interface [6]. On the other hand, the observation results implied that the large volume of zirconium inclusions caused defects on the optical fiber external structure and core-structure changes as shown in Figs. 3(a) and 3(b). These structural changes would affect the laser-fusion-spliced fiber qualities including the mechanical fracture strength and splicing loss distribution.

On the basis of the described analytical results of having unveiled the laser-fusion spliced optical fiber structure, the analytical performance of SP-μCT for observing optical fiber devices' structures is expected to be clarified further with the deployment of optical microdevices.

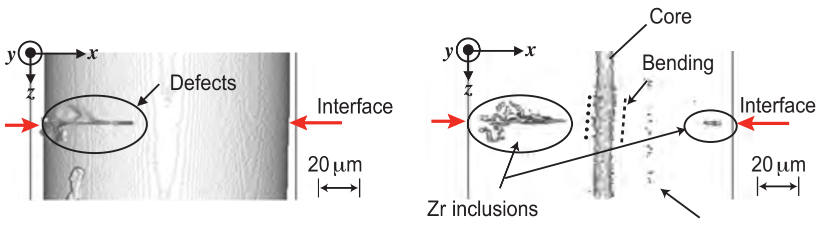

(a) External **(b) Inside**

Fig. 3. Structural changes of the optical fiber external structure and the core due to Zr inclusions revealed by SP-μCT at the laser-fusion-spliced interface. ((**a**) External structure of a spliced optical fiber reconstructed from SP-μCT images. (**b**) Optical fiber core and Zr inclusions revealed after the extraction calculation. The x-y-z coordinates and scale in (a) correspond to those in (b).)

Shinji Koike*, Shuichiro Asakawa and Junya Kobayashi

NTT Photonics Laboratories, NTT Corporation

*E-mail: koike.s@lab.ntt.co.jp

References

[1] C. Tocci and H.J. Caulfield, "Optical Interconnection - Foundations and Applications-," (Artech House, London 1994).
[2] M. Kobayashi *et al.*: IEEE J. Sel. Top. Quant. Electron. **5** (1999) 1271.
[3] A.D. Yablon: "Optical Fiber Fusion Splicing," (Springer, Berlin 2005).
[4] S. Koike *et al.*: Int. Conf. Electronics Packaging (ICEP) **12B4-1** (2008) 421.
[5] K. Uesugi *et al.*: Nucl. Instrum. Meth. Phys. Res. A **467-468** (2001) 851.
[6] *S. Koike, S. Asakawa, M. Kobayashi, R. Nagase, J. Kobayashi, K. Uesugi, K. Kajiwara, A. Takeuchi, Y. Suzuki, I. Hirosawa and Y. Watanabe: IEEE Transactions on CPMT,* ***1*** *(2011) 100.*

Structure analysis of nanoparticle dispersed in transparent resin using synchrotron X-ray scattering

A flexible transparent plastic substrate is attracting attention in the field of photovoltaic power generation and display [1,2]. Plastic substrates have not only molding processability and lightweight properties but can also easily control transmission and reflectivity of the visible light ray by changing their molecular structure and composition. Although substrates consisting of acryl and cycloaliphatic group-based polymers have a high light transmittance in general, they are difficult to employ for products such as displays and solar batteries because of their low heat resistance and high coefficient of expansion [3]. Recently, we have developed a novel transparent plastic substrate with a heat resistance of over 200°C and a coefficient of expansion under 40 ppm/°C by dispersing inorganic nanosilica particles into the substrate resin [4]. Moreover, we found that the transparency was increased by increasing the content of nanosilica particle to over 50 vol%. From the results of synchrotron small-angle X-ray scattering measurements (SAXS), it was suggested that the increased content of nanosilica particles resulted in the formation of a para-crystal structure. In this study, we elucidate the effects of the content and diameter of nanosilica particles on their regular arrangement structures in the transparent plastic substrates using a field-emission-type scanning electron microscope (FE-SEM) and synchrotron small-angle X-ray scattering (SAXS) [5].

In the experiment section, norbornene diacrylate, an isopropanol solution containing a colloidal silica of 45 and 110 nm diameters, an additive, and an initiator were mixed under vacuum. A transparent film less than 150 μm thickness was obtained by removing a solvent at 40°C and crosslinking with ultraviolet in the mold at room temperature (r.t.). An average heat coefficient of expansion from 30 to 250°C was measured by thermomechanical analysis (TMA) using a SEIKO instruments SS6000. Haze and parallel light transmittance were measured with a haze meter using a Nippon Denshoku Kogyo Corporation NDH2000. The regular arrangement of structures of nanosilica particles was determined using synchrotron small-angle X-ray scattering at beamlines **BL08B2** and **BL03XU**. The distance and shape of the nanoparticles were observed with FE-SEM in 5 kV at r.t. using a JEOL JSM-7401.

Figure 1 shows the effect of the colloidal silica content on the light transmittance. The light transmittances have a local minimum with an increase in the content of colloidal silica of both 45 and 110 nm diameters. It indicates that the substrate becomes transparent again after becoming opaque with increasing content of colloidal silica. The film becomes transparent at a content of 55 vol% colloidal silica when the particle diameter is 45 nm, while it becomes transparent at a content of 33 vol% when the particle diameter is 110 nm. From these results, we suggest that there is a correlation between the particle diameter of the colloidal silica and re-transparence of the film.

Figure 2 shows the SAXS profile with varying content of the colloidal silica of 110 nm diameter in a resin network film. Several peaks scattered from isolated silica particles were observed in the range of q (nm^{-1}) > 0.08 in all profiles. It indicated that no cohesion of the particle was observed with the increase in the content of colloidal silica because the provided peaks were consistent with those of a dilute solution at 0.1 vol% colloidal silica. In addition, a peak due to the scattering from the interparticle distance of the colloidal silica was observed in the range of a small angle, q (nm^{-1}) = 0.02 – 0.06, where it was difficult to observe using a conventional SAXS with a rotating-anode generator. The peak was found to shift to the wide-angle side with increasing content of colloidal silica. The correlation between the content

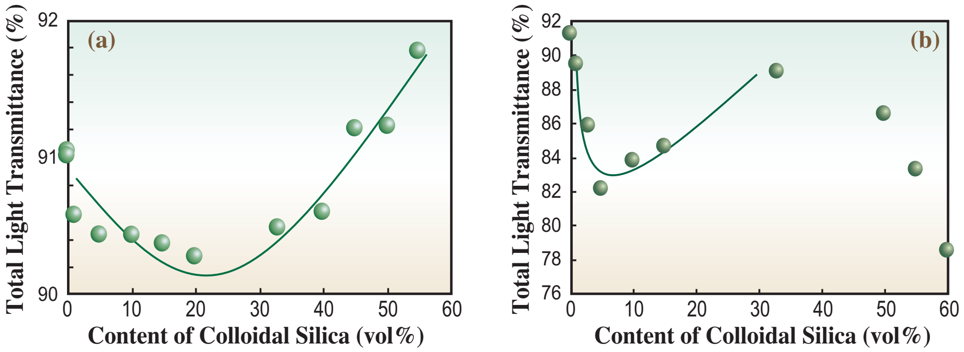

Fig. 1. Effect of colloidal silica content on light transmittance, **(a)** colloidal silica of 45 nm diameter, **(b)** colloidal silica of 110 nm diameter.

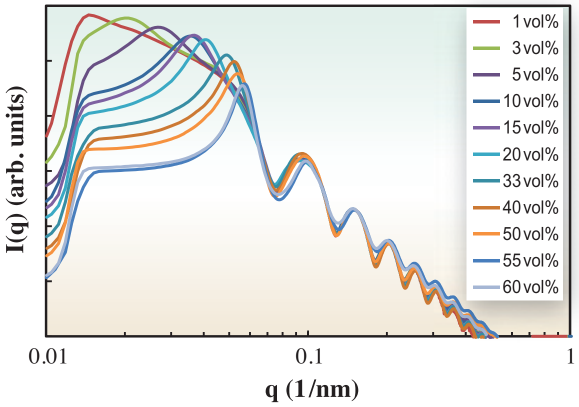

Fig. 2. SAXS profile with varying content of colloidal silica of 110 nm diameter in resin network film.

of colloidal silica and the lattice spacing calculated from the shifted peak top according to Bragg diffraction is plotted. The lattice spacing was found to decrease from 280 to 110 nm, which corresponded to the diameter of silica with increasing content of the colloidal silica. From these results, highly filled particles were suggested to exist individually in the film.

Figure 3 shows the results of SEM observations of films with varying colloidal silica contents. As the content of colloidal silica increased, their filling rate was observed to increase without the aggregation of the colloidal silica. A hexagonal close-packed structure was observed for 60 vol% colloidal silica content, which was almost equal to the theoretically predicted maximum value of the packing. Distances between particles in SEM images are consistent with the lattice spacing obtained from the SAXS profile.

In summary, highly filled nanosilica particles of 45 and 110 nm diameters resulted in a transparent film without any silica aggregation. In addition, the distances between particles calculated from SEM images agreed with those determined from the SAXS profiles. These results suggest that the SAXS measurement in SPring-8 is effective for the observation of the particle dispersion state in the nanoparticle high-filling system. A mechanism of the expression of transparency is still being elucidated from the observation of a submicron ordered structure using an ultra-small-angle X-ray scattering such as a Bonse & Hart optical system.

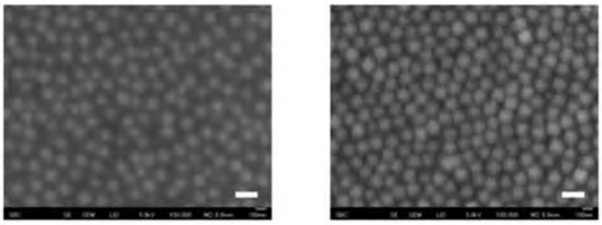

110 nm - 15 vol% **110 nm - 33 vol%**

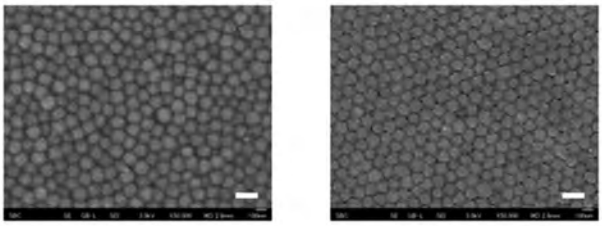

110 nm - 50 vol% **110 nm - 60 vol%**

Fig. 3. SEM images with varying content of colloidal silica of 110 nm diameter in resin network film.

Kazunobu Senoo

Kobe Fundamental Research Laboratory,
Sumitomo Bakelite Corporation

E-mail: senoo@sumibe.co.jp

References

[1] H. Kanamori: "Advanced Technology of Transparent Resin", Toray Research Center (2008).
[2] G.P. Crawford: "Flexible Flat Panel Displays", John Wiley & Sons, Ltd. (2005) 462.
[3] T. Nakao *et al.*: IDW'03 Proc., 2003, p. 621.
[4] K. Senoo *et al.*: J. Network Polymer **30** (2009) 16. (in Japanese)
[5] K. *Senoo, T. Takeuchi, W. Oka, Y. Shimobe, S. Kuwamoto, Y. Urushihara, J. Matsui and K. Nakamae: J. Network Polymer* ***31*** *(2010) 19. (in Japanese)*

Observation of fatigue crack propagation in laser-peened aluminum alloy by computed tomography with synchrotron radiation

Fatigue is a major cause of reduced structural integrity, and fatigue fracture usually starts from the surface of components. Therefore, various technologies have been developed to enhance surface properties, and laser peening is an emerging technology that effectively prolongs the fatigue life of structures [1]. However, it is not thoroughly understood how these technologies work on resisting fatigue because of the difficulty in directly observing fatigue cracks propagating inside opaque materials. To overcome this situation, we have made an ambitious challenge to visualize fatigue cracks inside materials and their propagation by computed tomography (CT) with synchrotron radiation [2]. Even if we utilized CT, we could not expect a clear image of fatigue cracks since they are almost closed without external loading. After attempting to open a fatigue crack with a newly devised specimen holder to obtain a clearer image without obstructing X-ray paths, we performed imaging experiments of fatigue cracks developing inside materials.

The holder was introduced on a rotation stage at beamline **BL19B2**, as shown in Fig. 1. The holder keeps a fatigue specimen and controls the tension load on it to slightly open the fatigue crack, which could enhance the contrast of the crack image. The specimen is pulled using a driving nut on a tension bolt at the top of the holder without torsion on the specimen. The load is measured with a compact load cell placed between the tension bolt and the specimen. The reacting compression load is supported by a thin pipe of polycarbonate, which is almost transparent for high energy X-ray. The holder is equipped with a dummy pipe under the specimen, which is used to compensate for the slight absorption by the pipe by substituting the background collected through the dummy pipe. While the holder or supporting pipe is outside the reconstructed area, the quality of the images is not affected because of the concentric arrangement of the supporting pipe with the axis of the rotating motion.

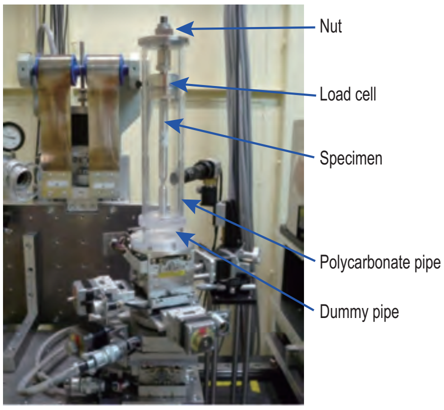

Fig. 1. Specimen holder on a rotation stage at BL19B2 for CT experiment.

Figure 2 shows the reconstructed image of a fatigue crack in a specimen of AC4CH cast aluminum alloy under different tension loads of 0 and 40 MPa. White shadows are the 2D expressions of the 3D image of the fatigue crack projected onto a plane perpendicular to the axis of the specimen. The imaging conditions are almost the same as in the previous study [2]: White X-ray from a bending magnet was monochromatized by a silicon double-crystal and the energy was adjusted to 28 keV. The distance between the specimen and an X-ray area detector was set to 0.8 m to incorporate the phase contrast effect into the image. A series of 2D slice images were reconstructed by convolution back projection algorithm, and the 3D image was retrieved by stacking the 2D slice images sequentially. The fatigue crack developed from a small drilled hole that is intentionally made to control the crack initiation position. The image of 40 MPa tension load is clearer than that of 0 MPa, suggesting the crack opening as expected and the enhancement of the image due to phase and/or absorption contrast. The crack image would not change in shape or size even with increasing the tension load onto the specimen beyond 40 MPa, and the crack length on the surface deduced from the image agreed well with the surface observation. These results imply that the crack front could be most likely determined by controlling the tension load.

It is self-evident that defects inside the material could not be detected by external observation such as replication method or optical microscopy. Actually, we could not identify the defects through external observation; however, CT revealed an internal defect as indicated by the arrow in Fig. 3 [3]. It happened that the defect existed just below the surface. The fatigue crack is clearly visualized as well, showing the propagation from the defect with the increase in the number of fatigue loading cycles of 160 MPa stress amplitude. Figure 4 is a replica of the surface covering the position of the internal defect, which of course

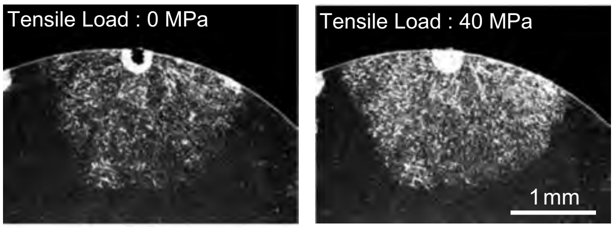

Fig. 2. Images of a fatigue crack under different axial tensile loads.

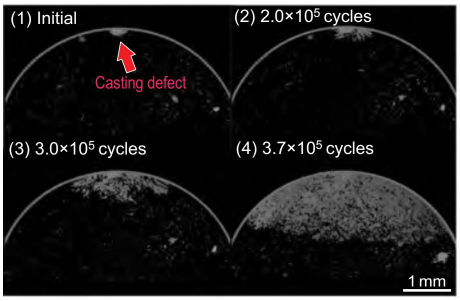

Fig. 3. Propagation of a fatigue crack from a defect beneath the surface.

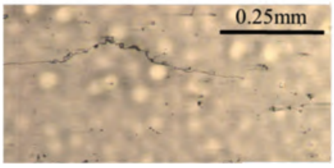

Fig. 4. Replica of the fatigue crack appearing on a surface at 1.5×10^5 loading cycles.

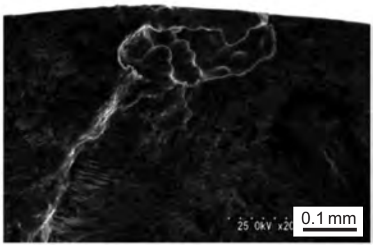

Fig. 5. SEM image of the defect on the fracture surface.

could not be observed on the replica. Figure 5 is a SEM image of the fractured surface of the specimen, showing a casting defect near the surface, which agreed with the results in Fig. 3. The inside defect and fatigue crack developing from the defect were successfully observed [3], which is the world's first 3D imaging of a fatigue crack developing from an inside defect, to the best of our knowledge.

The experiment was extended to evaluate the interference between two fatigue cracks closely located on a specimen. The two cracks were generated and propagated by fatigue loading with a stress amplitude of 120 MPa from two drilled holes separated by 0.5 mm axially and 30° azimuthally. Laser peening was applied to the specimen just before the overlapping of the two cracks. Then, additional 10^5 fatigue cycles were loaded to the specimen with a stress amplitude of 220 MPa because at a lower stress amplitude the cracks would not sufficiently propagate on the specimen toughened by laser peening within the available time of the experiment. The reconstructed 3D image of the cracks is shown in Fig. 6. Here, the surface of the specimen was deleted from the image. Figure 6(a) shows the entire view of the two cracks in a manner where the axis of the specimen is tilted by 30°. It is found that the drilled holes are distorted in shape to some extent, suggesting that the surface layer of the specimen deformed plastically by laser peening. The shape of the cracks is different from semi-ellipsoidal probably because of the interference between cracks and/or residual stress induced by laser peening. The two cracks can be divided virtually as shown in Figs. 6(b) and 6(c), which allows us to evaluate each crack separately and precisely. Such treatment would be hardly conceivable without utilizing the benefit of CT.

Computed tomography (CT) was performed for cast aluminum alloy AC4CH specimens at BL19B2. Taking advantage of highly parallelized synchrotron radiation, fatigue cracks and the propagation inside the specimens were successfully visualized by incorporating the edge enhancement arising from phase contrast. The results are summarized as follows: (i) The crack front was identified by introducing a newly devised holder and controlling the tension load on the specimen. (ii) The growth of a fatigue crack from an internal defect was visualized, which could not be attained without CT and is greatly expected to elucidate the mechanism of giga-cycle or ultrahigh-cycle fatigue, since the internal fracture is the major cause of the failure in the giga-cycle regime. (iii) The 3D shape of fatigue cracks was determined, which contributes to the verification and advancement of fracture mechanics, especially on FEM analysis.

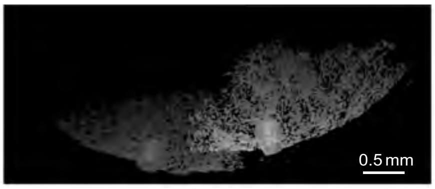

(a) Whole view (crack-1 and crack-2)

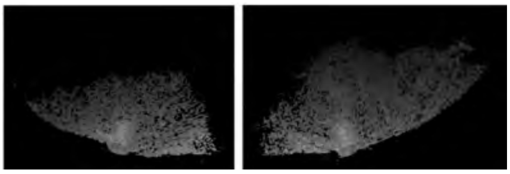

(b) Crack-1 **(c)** Crack-2

Fig. 6. Three-dimensional images of fatigue cracks on a laser-peened specimen.

Kiyotaka Masaki[a,*] and Yuji Sano[b]

[a] Okinawa National College of Technology
[b] Toshiba Corporation

*E-mail: masaki-k@okinawa-ct.ac.jp

References

[1] Y. Sano *et al*.: Mat. Sci. Eng. A **417** (2006) 334.
[2] Y. Sano and K. Masaki: SPring-8 Research Frontiers 2006, p.151.
[3] *K. Masaki, Y. Sano, Y. Ochi, K. Akita and K. Kajiwara: J. Sol. Mech. Mat. Eng.* ***2*** *(2008) 1104.*

High-resolution three-dimensional computed tomography for materials from industrial field

Three-dimensional synchrotron-radiation-based imaging has been defined as one of the new global technologies for the visualization of internal features of biological, chemical and material substances. With the recent developments in X-ray detectors and personal computers, three-dimensional computed tomography (3D CT) has generated interesting images with no additional data treatments like Fourier transformation, this fact being very attractive even for non-experts of X-rays.

Hyogo Prefectural contract beamlines, **BL08B2** and **BL24XU**, have provided opportunities for various users from industries to perform 3D CT experiments for fairly large samples (at BL08B2) and small samples (at BL24XU) to observe very local volumes.

CT systems utilizing highly brilliant undulator emission at BL24XU are available based on simple projection imaging with absorption and/or refraction contrast using a visible-ray-conversion-type X-ray imager. The X-ray energy is discretely selectable from 10 to 30 keV for every 5 keV using a silicon double-crystal monochromator. The field of view is limited by the incoming beam size of 2 mm (horizontal) by 1.5 mm (vertical). The typical X-ray intensity of 10 keV is about 1×10^{13} photons/s.

Two types of system are open for industrial users. One is for high-spatial-resolution CT combined with a YAG single-crystal scintillator. The spatial resolution of about 1 μm is possible with a typical measurement time of 1 h. The other system is for high-speed CT introducing a P46-type high-speed phosphor screen and a high-speed CMOS sensor. The acquisition time for single CT is 0.14 sec with the spatial resolution of 14 μm. This system can work with continuous sample rotation and image acquisition up to 2 gigabytes of data, so that 4D (3D + time) CT measurement to observe the dynamics of the internal structure is available.

The thermal change or solution reaction in a sample can be observed with this system. Figure 1 shows typical images obtained with both systems with 10 keV X-rays. Figure 1(a) shows volume-rendering images of a casting of carbon fibers of 7 μm diameter obtained by the high-spatial-resolution system. The image is reconstructed using 1200 projections with the effective pixel size of 0.95 μm. In the right figure (a magnified figure of the left), the local orientation of the fibers can be clearly seen. Figure 1(b) shows a rendering image and a sliced image of the solution with the bubbles of detergent in a glass capillary obtained by the high-speed system. The CT reconstruction is made using 361 projections with the acquisition time of 0.144 sec (2500 frames/sec). In this setting, continuous measurement of about 5000 images, corresponding to 14 CTs, is achievable.

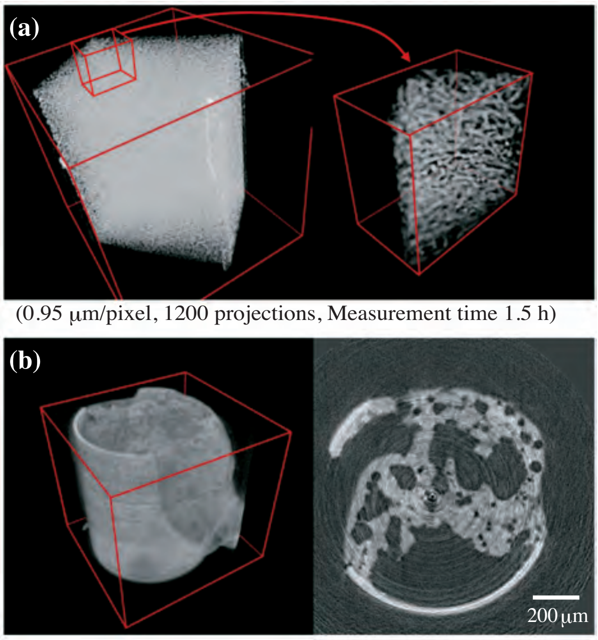

(0.95 μm/pixel, 1200 projections, Measurement time 1.5 h)

(3.6 μm/pixel, 361 projections, Measurement time 0.14 s)

Fig. 1. Typical CT images obtained at BL24XU. **(a)** Volume-rendering images (right: magnified image of the left image) of a casting of carbon fibers of 7 μm diameter obtained by the high-spatial-resolution system. **(b)** A volume-rendering image and a sliced image of a bubbling solution of detergent in a glass capillary obtained using the high-speed system.

Furthermore, other CT systems for ultrahigh resolution are under development using X-ray optical devices as scientific research at the University of Hyogo. A micro-interferometer system based on X-ray imaging microscopy for phase contrast CT with 200 nm resolution and a phase contrast scanning CT system using an X-ray focusing beam have been developed. Figure 2 shows typical images obtained

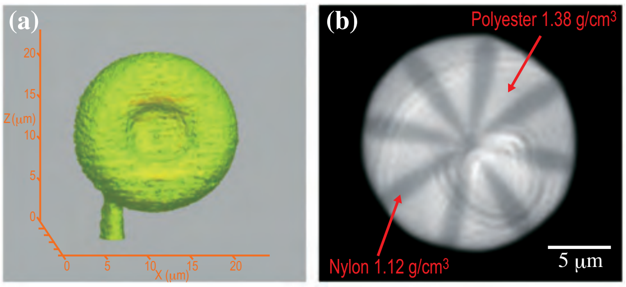

(33 nm/pixel, 180 projections)

(200 nm/pixel, 300 projections)

Fig. 2. Typical CT images obtained by the ultrahigh-resolution system in BL24XU. **(a)** A volume-rendering image of a diatom obtained using the micro-interferometer. **(b)** A sliced image of a composite fiber of polystyrene and nylon obtained using the scanning system.

using both systems with 10 keV X-rays. A volume-rendering image of a diatom obtained using the micro-interferometer is shown in Fig. 2(a), and a sliced image of a composite fiber of polystyrene and nylon obtained using the scanning system with a focusing beam of 0.4 μm size is shown in Fig. 2(b).

In BL08B2, on the other hand, a new experimental station for a large-viewfield CT exploiting a characteristic in wide X-ray beams from a bending magnet light source has been constructed at 2010A. The monochromated X-ray beams with an energy ranging from 5 to 30 keV are selectable for the CT experiments. To achieve both the large viewfield and the high spatial resolution, a visible-ray-conversion type X-ray imager with a 4008×2672-element CCD camera is employed. Two types of scintillators, a cerium-doped lutetium oxyorthosilicate (LSO) single-crystal screen for a high-spatial-resolution CT and a P43-type powder phosphor screen for the large-viewfield CT, are available in this imager. The viewfield ranges from a few mm with the effective pixel size of sub-μm to 20 mm (horizontal) by 10 mm (vertical) with the effective pixel size of 5 μm. The CT measurement takes typically 0.5 – 2 h.

The large-viewfield CT system can be used to observe many industrial materials without any prior processes. Typical images obtained with this system are shown in Fig. 3. The observed samples are drug tablets of 5 – 10 mm size. The CT reconstructions are made using 1000 projections with the effective pixel size of 4.28 μm. Active substances, excipients and outer coating layer were clearly visible. The CT can provide crucial information about the tabletting formulations such as uniformity of the active substances and thickness of the coating layer.

We have carried out a CT experiment of a resin foam as an example for industrial use [1]. The resin foam exhibits excellent impact and shock absorption properties, and is utilized as a cushion materials, for instance, as a shoe sole. The CT observations of the resin foam under compressive deformation were carried out to interpret cell deformation behaviors in the resin foam, which is directly linked to the impact and shock absorption properties. Figure 4 shows the CT images of the resin foam before and after applying uniaxial compressive deformation. It is seen that the cells are collapsed with the increase in the compressive strain. The deformation behaviors of each cell can also be tracked out by the sequential measurements. To elucidate the deformation mechanism more in detail, further analysis combining the obtained CT data and a finite element method is now in progress.

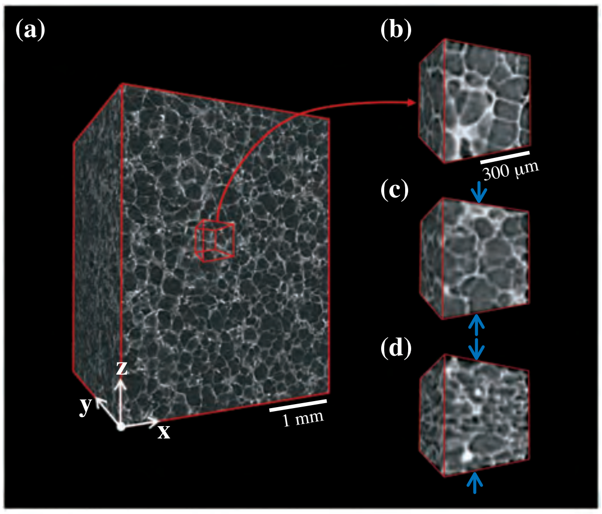

(4.28 μm/pixel, 1000 projections, Measurement time 1.2 h)

Fig. 4. Volume-rendering images of a resin foam. **(a)** Overview image of the sample before compression. Magnified images around the center of the sample **(b)** before and under the compressive strains of **(c)** 20% and **(d)** 40%. The sample was compressed parallel to the z-axis.

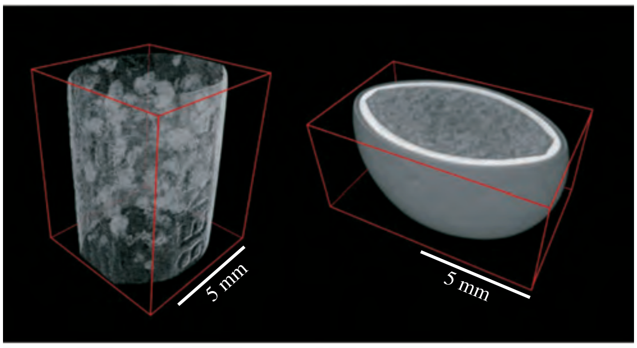

(4.28 μm/pixel, 1000 projections, Measurement time 1.2 h)

Fig. 3. Volume-rendering images of drug tablets.

Hidekazu Takano[a,*], Yoshimasa Urushihara[b] and Junji Matsui[b]

[a] Graduate School of Material Science,
University of Hyogo
[b] Synchrotron Radiation Nanotechnology Lab.,
Hyogo Science and Technology Association

*E-mail: htakano@sci.u-hyogo.ac.jp

References

[1] J. Tateishi *et al*.: in preparation.

Measurement of the internal stress distribution in grains of stainless steel using white X-ray microbeam diffraction

The mechanical strength of a structural metallic material depends on the distribution of internal stress in crystalline grains controlled by their metallographic factors such as the dislocation density. In the development of stainless steel for the structural material of a nuclear reactor, it is important to inhibit the stress corrosion cracking in the presence of high-temperature and high-pressure water. Recently, it has been revealed that the susceptibility to intergranular stress corrosion cracking (IGSCC) of stainless steel of SUS316 tends to depend on its level of cold working. It has been suggested that the cold working affects the internal stress distribution generated by the external stress. To clarify the effect of the cold working on the internal local stress around the grain boundary, we developed the X-ray diffraction measurement technique with white X-ray microbeam for the observation of the internal stress distribution in individual grains of polycrystalline metal [1].

The internal stress can be evaluated from crystal lattice spacing determined by X-ray diffraction. The technique we developed measures crystal lattice spacing on a point-by-point basis by scanning X-ray irradiated position. This development had two technical problems. One was how to detect the diffraction signal from each single crystalline grain whose crystalline orientation is unknown. The other was that a visualizing technique of the grain boundary is needed for identifying the grain irradiated with the microbeam. The former problem can be solved using a white X-ray microbeam. The white X-ray microbeam must contain some X-ray photons with wavelengths fitting the Bragg condition of some crystalline planes of the irradiated grain. As the solution to the latter problem, we developed the technique of visualizing the grain structure by detecting the grain boundary from the change in the X-ray diffraction pattern during the scan of the irradiated position in the sample [2]. When the irradiated position on the sample crosses a grain boundary during the scanning of the sample position, the diffraction patterns must be drastically changed. The grain boundary can be recognized by evaluating this change in the diffraction patterns quantitatively.

This technique was developed at the white beam X-ray diffraction beamline **BL28B2**. The schematic of the experimental setup is shown in Fig. 1. The white X-ray microbeam was formed by a slit set at the upstream side of the sample. The minimum size of the beam we could obtain was about 10 μm. Data on the diffraction angle and wavelength of the X-ray diffraction peak are necessary to determine the crystal lattice spacing of their diffraction plane using the Bragg equation. The fundamental procedure of the measurement is as follows. At first, the two-dimensional (2D) detector was set downstream of the sample to detect the diffraction angle of the X-ray diffraction peak. We used a complementary metal oxide semiconductor (CMOS) flat-panel imager (FPI) made by Hamamatsu Photonics as the 2D detector. The Laue pattern of X-ray diffraction from each grain was detected as an image using the FPI. An example of the image data is shown in Fig. 1. The diffraction angle and azimuthal angle of each diffraction peak were geometrically determined from its position in the image data. Secondly, the solid-state detector (SSD) was set at the position of the diffraction peak determined from the image data to detect its wavelength. A slit is

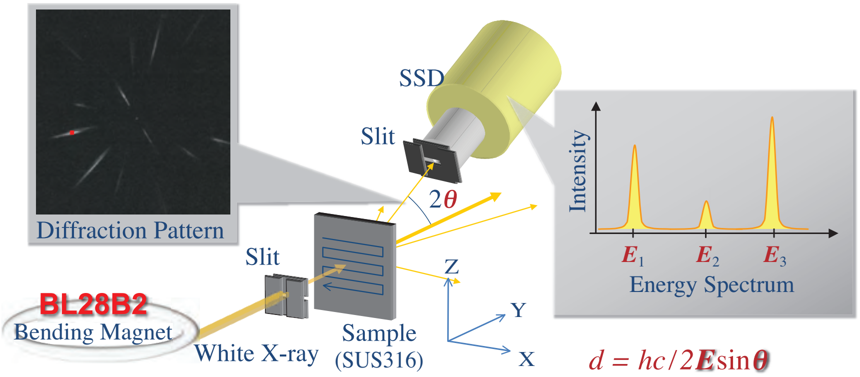

Fig. 1. Schematic of experimental setup. The applied stress is in the x-axis direction.

set at the upstream side of the SSD to keep the angle resolution for the restriction of the diffraction angle of the diffracted X-ray detected by the SSD. The accuracy of the determination of the lattice spacing of the system was estimated at $\delta d/d \cong 4\times10^{-4}$ by the measurement of the crystal lattice spacing of an undistorted silicon single crystal.

Here, we will introduce the result of the experiments performed on the specimen of 20% cold-rolled stainless steel of SUS316 applied with external tensile stress. Stainless steel of SUS316 is used for the nuclear reactor because of its high corrosion resistance. The thickness of the specimen was 0.3 mm. The average size of the grains in the specimen was estimated to be about 0.1 mm from the electron backscatter diffraction (EBSD) image. This specimen was mounted on the tensile testing machine set on the sample stage of the diffractometer. In this experiment, we applied the tensile stresses of 300 and 380 MPa to the specimen, where the former was the yield stress and the latter was the 0.1% proof stress. The direction of the external tensile stress is in an x-axial direction, as shown in Fig. 1.

Firstly, the grain boundary image of the specimen is shown in Fig. 2(a). The dark contrast in the image indicates the grain boundary. It was confirmed by comparison with the EBSP image (Fig. 2(b)) that this image was reasonable. Secondly, we evaluated the internal stress that occurred in 7 grains selected among the grains indicated in this image. The grains are indicated by the numbered-filled circles in Fig. 2(a). We measured more than three crystal lattice spacings to fully determine the component of the stress tensor.

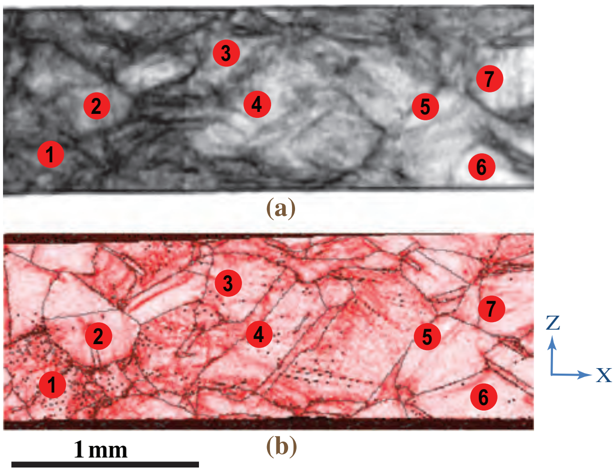

Fig. 2. Image of grain distribution obtained by the developed technique **(a)** and kernel average misorientation map of EBSP **(b)**.

Figure 3 shows the dependence of the internal stress measured at the selected grains on the external tensile stress. This data indicates that normal stress occurred on the plane perpendicular to the direction of the applied stress. The average value of the measured stress of seven grains is indicated by the red broken line. As shown in Fig. 3, the values of the internal stress that occurred in the grains were dispersed in a wide range and the increments of internal stress were almost proportional to the external stress. It suggested that the distribution of the internal stress in the grains of the cold rolled stainless steel was affected by the residual stress due to the cold rolling, which was dispersed in a wide range from tensile to compressive.

The measurement technique of internal stress in individual grains was successfully developed as the first step to clarify the mechanism of IGSCC. We will apply this technique to the measurement of the stress distribution around the grain boundary as the next step.

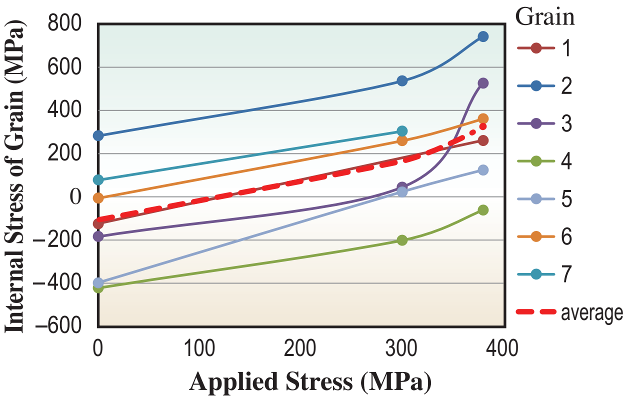

Fig. 3. Relation between applied stress and measured stress of individual grains. The grain number corresponds to that in Fig. 2.

Kentaro Kajiwara[a,*], Masugu Sato[a] and Takuyo Yamada[b]

[a] SPring-8/JASRI
[b] Institute of Nuclear Safety System, Inc.

*Email: kajiwara@spring8.or.jp

References

[1] K. Kajiwara *et al.*: to be submitted (2011).
[2] *K. Kajiwara, M. Sato, T. Hashimoto, I. Hirosawa, T. Yamada, T. Terachi, T. Fukumura and K. Arioka: Phys. Status Solidi A* ***206*** *(2009) 1838.*

NUCLEAR


"Goyo-tsutsuji" - *Five-leaf Azalea*

PHYSICS

The linearly polarized photon beam is produced by backward-Compton scattering of laser photons from 8 GeV electrons at BL33LEP. The current LEPS facility studies photoproduction of hadrons in the forward angles, where the high linear polarization plays an essential role to decompose various reaction processes.

The beam polarization is high and can be changed easily by changing the laser polarization. The LEPS covers the photon energy region from 1.5 GeV to 2.9 GeV, which is suitable to study the creation of excited baryons containing a strange quark or an anti-strange quark near the production thresholds. The production and decay properties of the excited hadrons shed lights on their structure in terms of confined quark.

In 2010, we reported two unexpected results. The first article shows the unexpected reduction of the ϕ photoproduction cross section from a deuteron, which is a loosely bound system of two nucleons. Since the nuclear density effect is expected to be small, the reduction must be due to the nuclear structure such as correlation of two nucleons. The second article shows an unexpected bump structure found in the backward η photoproduction cross section just above 2 GeV. One possible interpretation of the structure is that the enhancement is due to the presence of missing resonances (N*), which contain large $s\bar{s}$ components, which preferably decay into ηN. Both results are new and not theoretically well understood yet. Further studies, both experimental and theoretical, will be needed.

Takashi Nakano
Research Center for Nuclear Physics
Osaka University

Incoherent ϕ-meson photoproduction from deuterium

A strong attenuation was observed in the ϕ-meson photoproduction from the Li, C, Al and Cu nuclei, compared to its production from hydrogen, the free proton case. It has been interpreted as the nuclear density effect due to a large ϕ-N cross section in nuclear matter. To clarify the underlying physics, it is essential to construct a baseline in a low density region, using the simplest nucleus –the deuteron– made of one proton and one neutron.

We measured the differential cross sections and decay asymmetries of incoherent ϕ-meson photoproduction from a liquid deuterium target near threshold in the very forward direction with linearly polarized photons using the LEPS spectrometer at beamline **BL33LEP**. Highly polarized photons were produced by backward Compton scattering with an ultra-violet Ar laser from 8 GeV electrons in the storage ring of SPring-8. The photon energy was event-by-event determined by measuring the scattering angle of recoil electrons. A liquid deuterium target with an effective length of 16 cm was employed. Charged particles produced at the target were detected at forward angles with the LEPS spectrometer, which consisted of a dipole magnet, a silicon-strip vertex detector, three multi-wire drift chambers, a plastic scintillator behind the target, and a time-of-flight hodoscope placed downstream of the tracking detectors.

The production of ϕ mesons was identified via the charged kaon decay mode with detection of K^+ and K^- in the final state. A clear signal of ϕ mesons could be identified in the invariant mass of K^+K^- pairs. The separation of coherent ($\gamma d \rightarrow \phi d$) and incoherent ($\gamma d \rightarrow \phi pn$) interactions were done by fitting the missing mass spectrum, where the reaction of coherent production from deuterons, $\gamma d \rightarrow \phi d$, is peaking at the mass of deuterons 1.875 GeV/c^2. Figure 1 shows the disentanglement done in the missing mass spectra for 8 bins of photon energy in the range of 1.57-2.57 GeV. The overall shapes were nicely reproduced by the sum of individual ones generated by Monte Carlo simulations.

The zero-degree cross sections of incoherent production from deuterium as a function of the photon energy are shown in Fig. 2(a), together with data from hydrogen. The nuclear transparency ratios for deuterium, $Td = \sigma d/(2^* \sigma p)$, is evaluated by the ratio of cross sections at zero degrees and are shown in

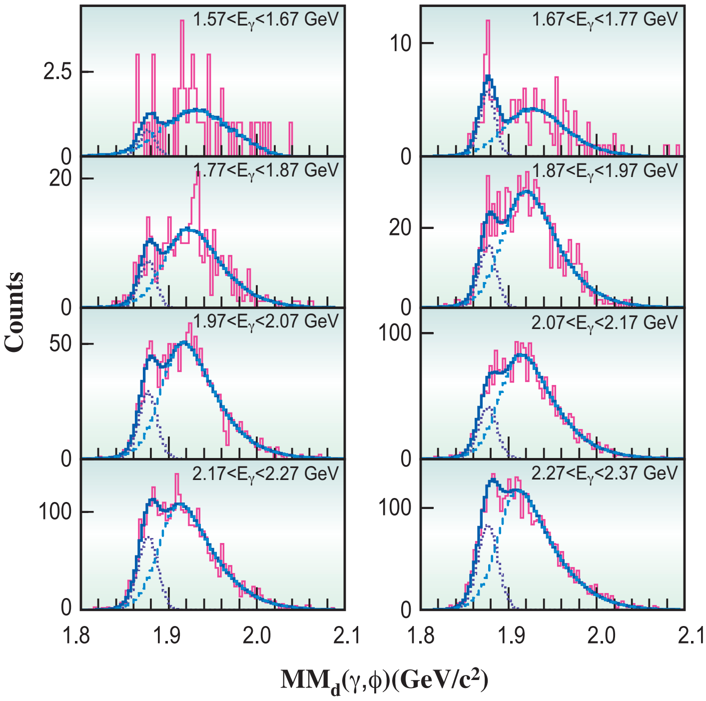

Fig.1. Missing mass spectra assuming the whole deuteron as target, at 1.57<Eγ<2.37 GeV. Each spectrum is fitted with the sum (solid line) of MC-simulated components of coherent (dotted line) and incoherent (dashed line) events.

Fig. 2(b). Compared with the ϕ production from a free proton, a significant 25-30% reduction of the ϕ yield per nucleon is observed for the incoherent production from deuterium.

Because the nuclear transparency ratio is associated with the production from the protons, the most naïve speculation of the observed suppression of nuclear transparency ratio for deuterium is because of a smaller cross section for ϕ-mesons produced from neutrons. We examined this scenario by studying the exclusive ϕ events whose final state of a K^+K^- pair and a proton is fully detected in the spectrometer; the kinematics of these events is dominated by interactions with the proton inside deuterium. Though limited by statistics, Fig. 3 clearly shows a similar degree of reduction for quasi-free events from the proton as compared with inclusive reactions. Therefore, the reduction in ϕ yield occurs on a similar scale for the incoherent production either from the proton or the neutron inside deuterium. Further supporting evidence was obtained in the measurement of decay asymmetry.

In summary, the differential cross sections and decay asymmetries of incoherent ϕ-meson photoproduction from deuterons were measured at forward scattering angles near threshold. In comparison with those from proton, the production cross section per nucleon shows a significant reduction. The reduction is found to be common for the production from both the proton and the neutron inside deuterium. The present work suggests that the nuclear transparency ratio of ϕ-meson photoproduction is sensitive to the details of the nuclear structure. It should work as an important baseline used for differentiating the nuclear density effects.

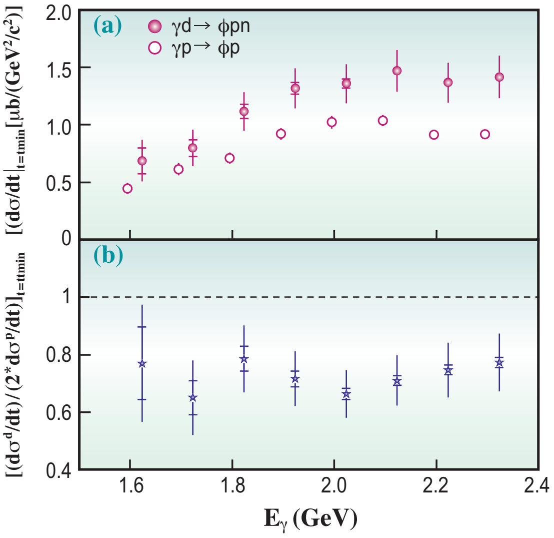

Fig. 2. **(a)** Differential cross section at zero degree as a function of photon energy for incoherent production from deuterium and that from hydrogen. The horizontal bars represent the range of statistical errors. The $\gamma p \rightarrow \phi p$ data are shifted by –50 MeV for clarity of display. **(b)** Nuclear transparency ratios of ϕ-meson photoproduction from deuterium (A=2) are shown as a function of the photon energy.

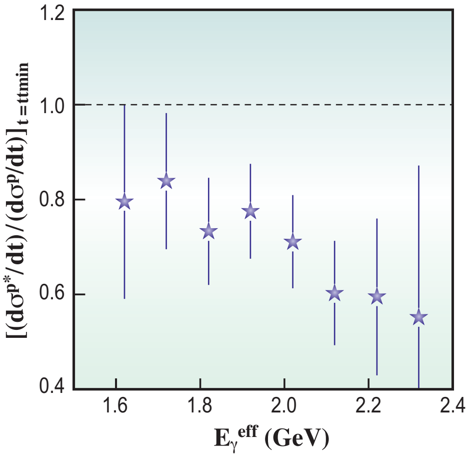

Fig. 3. Ratio of ϕ-meson photoproduction from the proton inside deuterium and hydrogen as a function of photon energy. The error bars are statistical only.

Wen-Chen Chang for the LEPS Collaboration

Institute of Physics, Academia Sinica, Taiwan.

E-mail: changwc@phys.sinica.edu.tw

References

[1] *W.C. Chang, M. Miyabe, T. Nakano, D.S. Ahn, J.K. Ahn, H. Akimune, Y. Asano, S. Daté, H. Ejiri, S. Fukui, H. Fujimura, M. Fujiwara, S. Fukui, S. Hasegawa, K. Hicks, K. Horie, T. Hotta, K. Imai, T. Ishikawa, T. Iwata, Y. Kato, H. Kawai, K. Kino, H. Kohri, N. Kumagai, S. Makino, T. Matsuda, T. Matsumura, N. Matsuoka, T. Mibe, Y. Miyachi, N. Muramatsu, M. Niiyama, M. Nomachi, Y. Ohashi, H. Ohkuma, T. Ooba, D.S. Oshuev, C. Rangacharyulu, A. Sakaguchi, P.M. Shagin, Y. Shiino, H. Shimizu, Y. Sugaya, M. Sumihama, Y. Toi, H. Toyokawa, M. Uchida, A. Wakai, C.W. Wang, S.C. Wang, K. Yonehara, T. Yorita, M. Yoshimura, M. Yosoi, R.G.T. Zegers: Phys. Lett. B* ***684*** *(2010) 6.*

Backward-η meson photoproduction at BL33LEPS

In this study, new baryon resonances were investigated via η photoproduction. Baryons are composed of quarks, which are fundamental constituent particles of matter. Although various dynamical models (e.g., the constituent quark-model and the deformed oscillator quark model) have been developed to describe baryon resonances, the internal structure of baryons has not been fully understood yet.

The constituent-quark model, which describes a baryon as a three-quark state, predicts many baryon resonances. However, there are considerably many baryon resonances not observed experimentally [1]. Two possible explanations are given for understanding the missing baryon resonances. One possibility stems from oversimplifications of the model. Several pictures are proposed to describe the internal structure of baryons instead of the simple structure of three-quarks. For example, a picture of five-quark components (three constituent quarks and a large admixture of an extra quark-antiquark pair) explains the characteristic of the $S_{11}(1535)$ resonance, which is heavier than the $P_{11}(1440)$ and $\Lambda(1405)$ resonances [2]. In this model, the $S_{11}(1535)$, $P_{11}(1440)$, and $\Lambda^*(1405)$ particles are composed of $uud[s\bar{s}]$, $uud[d\bar{d}]$, and $uds[u\bar{u}]$ quarks, respectively. This picture can also explain the strong coupling of $S_{11}(1535)$ to an ηN channel because the η meson is the lightest meson with an $s\bar{s}$ component.

The other explanation for the missing baryon resonances is that missing baryon resonances are still not observed in conventional experiments for measuring the pion induced or pion production reactions. Some of the missing baryon resonances may couple to other channels, like ηN, $\eta' N$, ωN, ρN, ϕN, KY, etc. and have higher masses of around 2 GeV, which have not been studied well experimentally. Therefore, experiments to study various meson-coupled resonances at around 2 GeV would give us a new insight into the internal structure of baryons.

We measured differential cross sections for η photoproduction ($\gamma p \rightarrow p\eta$) at **BL33LEPS** [3]. The LEPS beamline provides a laser-electron photon beam with an energy range from 1.5 to 2.4 GeV. The laser-electron photon beam was produced by backward-Compton scattering between Ar-ion laser photons with a 351nm wavelength and electrons with an 8 GeV energy. The beam intensity was typically 10^6 photons/s. The target was a liquid hydrogen target with a thickness of 15 cm. Scattered protons were detected by a magnetic spectrometer, which covers forward angles. Mass identification was made using momentum, path length, and time-of-flight. The proton mass resolution was 46 MeV/c^2 at 2 GeV/c momentum. Proton events were selected in the reconstructed mass spectrum within 4σ of the nominal value. Contaminations from pions and kaons were estimated to be less than 0.1%. The produced η mesons were identified by calculating the missing-mass of protons. Figure 1 shows the missing-mass spectrum for the reaction of $\gamma p \rightarrow pX$ ('X' is unknown particles). Peaks due to π^0, η, η', and ω mesons are

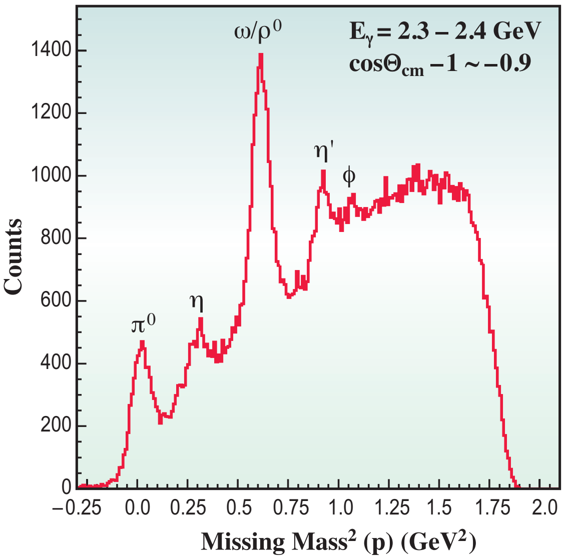

Fig. 1. Missing-mass spectrum of protons.

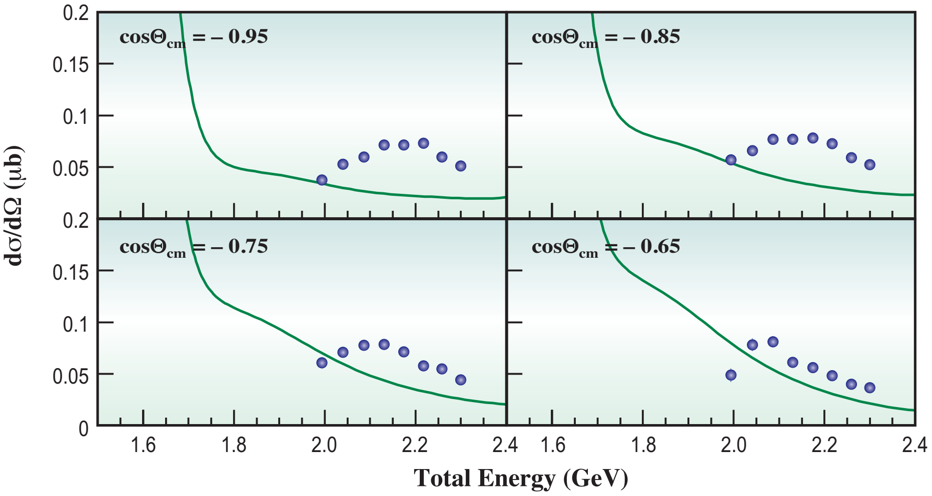

Fig. 2. Differential cross sections for η photoproduction.

clearly observed. There are background events of multipion photoproduction under signal peaks. The yield of η photoproduction was obtained by estimating the distributions of each reaction using Monte Carlo simulation. Differential cross sections were calculated by correcting for the acceptance and detection efficiency of the spectrometer and the numbers of beam photons and target protons.

Figure 2 shows differential cross sections as a function of the total energy for η photoproduction. The closed circles are the present data. The curves correspond to the theoretical model including non-resonant processes and known resonances with significant contributions. A wide bump structure has been observed above 2.0 GeV in total energy [4]. In order to explain such a large bump structure, the contribution of new resonances is required. The central position of the bump structure shifts to higher energies at backward angles. This may be attributed to the interference between resonances and diffractive processes that, in general, depends on the scattering angles. The other possibility is that the bump structure consists of more than one resonance, whose angular distributions are different. We measured differential cross sections for π^0, η', and ω photoproductions as well in the same kinematical range as that in the present study. No such structure was observed in the reaction channels. Therefore, it is inferred that this unique structure in ηphotoproduction is due to a baryon resonance with a large $s\bar{s}$ component, which strongly couples to the ηN channel. Detailed theoretical studies including the present data will reveal the hidden resonances contributing to the bump structure.

Mizuki Sumihama for the LEPS collaboration

Faculty of Education, Gifu University

E-mail: sumihama@rcnp.osaka-u.ac.jp

References

[1] Particle Data Group, Phys. Lett. B **667** (2008) 1.
[2] S. Capstick and W. Roberts: Phys. Rev. D **49** (1994) 4570.
[3] M. Sumihama *et al.* (LEPS Collaboration): Phys. Lett. B **657** (2007) 32.
[4] *M. Sumihama, D.S. Ahn, J.K. Ahn, H. Akimune, Y. Asano, W.C. Chang, S. Daté, H. Ejiri, H. Fujimura, M. Fujiwara, S. Fukui, S. Hasegawa, K. Hicks, T. Hotta, K. Imai, T. Ishikawa, T. Iwata, Y. Kato, H. Kawai, K. Kino, H. Kohri, N. Kumagai, T. Matsuda, T. Matsumura, T. Mibe, M. Miyabe, N. Muramatsu, T. Nakano, M. Niiyama, M. Nomachi, Y. Ohashi, H. Ohkuma, T. Ooba, D.S. Oshuev, C. Rangacharyulu, A. Sakaguchi, P.M. Shagin, Y. Shiino, A. Shimizu, H. Shimizu, Y. Sugaya, Y. Toi, H. Toyokawa, A. Wakai, C.W. Wang, S. C. Wang, K. Yonehara, T. Yorita, M. Yoshimura, M. Yosoi and R.G.T. Zegers: Phys. Rev. C* ***80*** *(2009) 052201(R).*

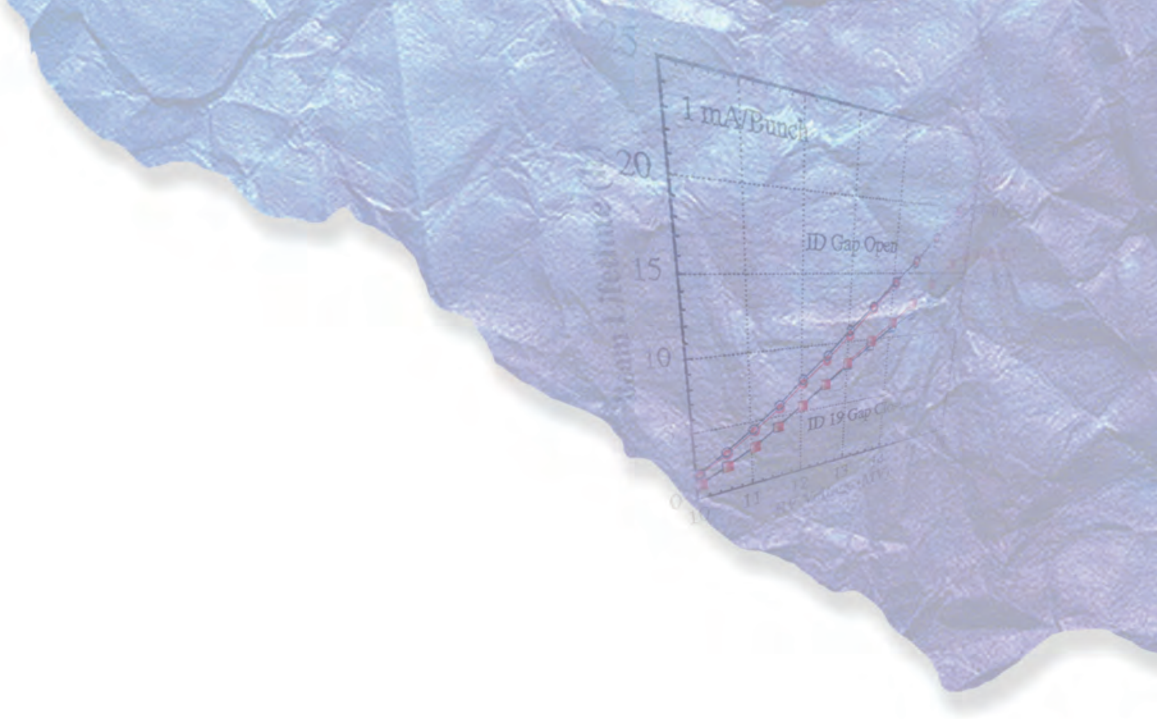

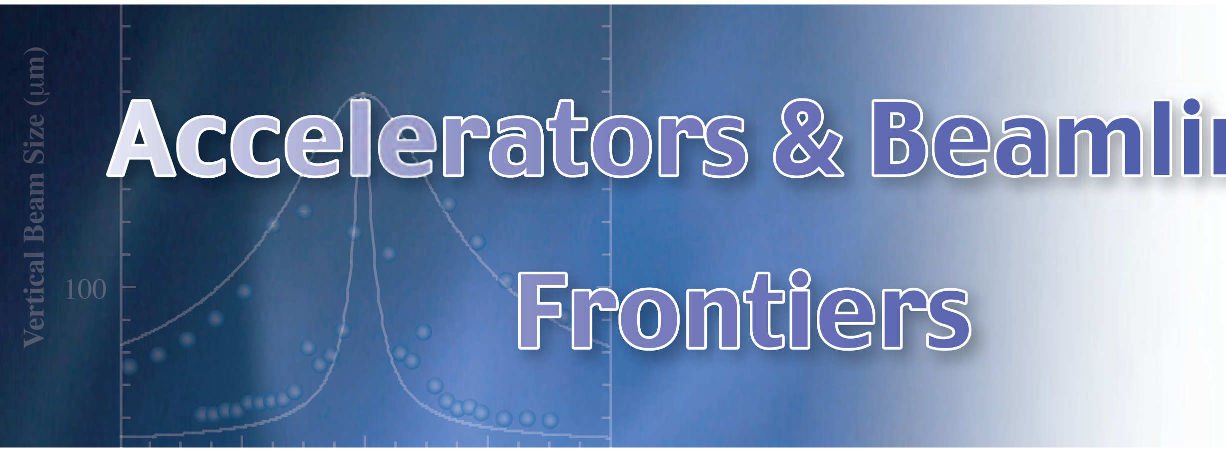

Accelerators & Beamlines Frontiers

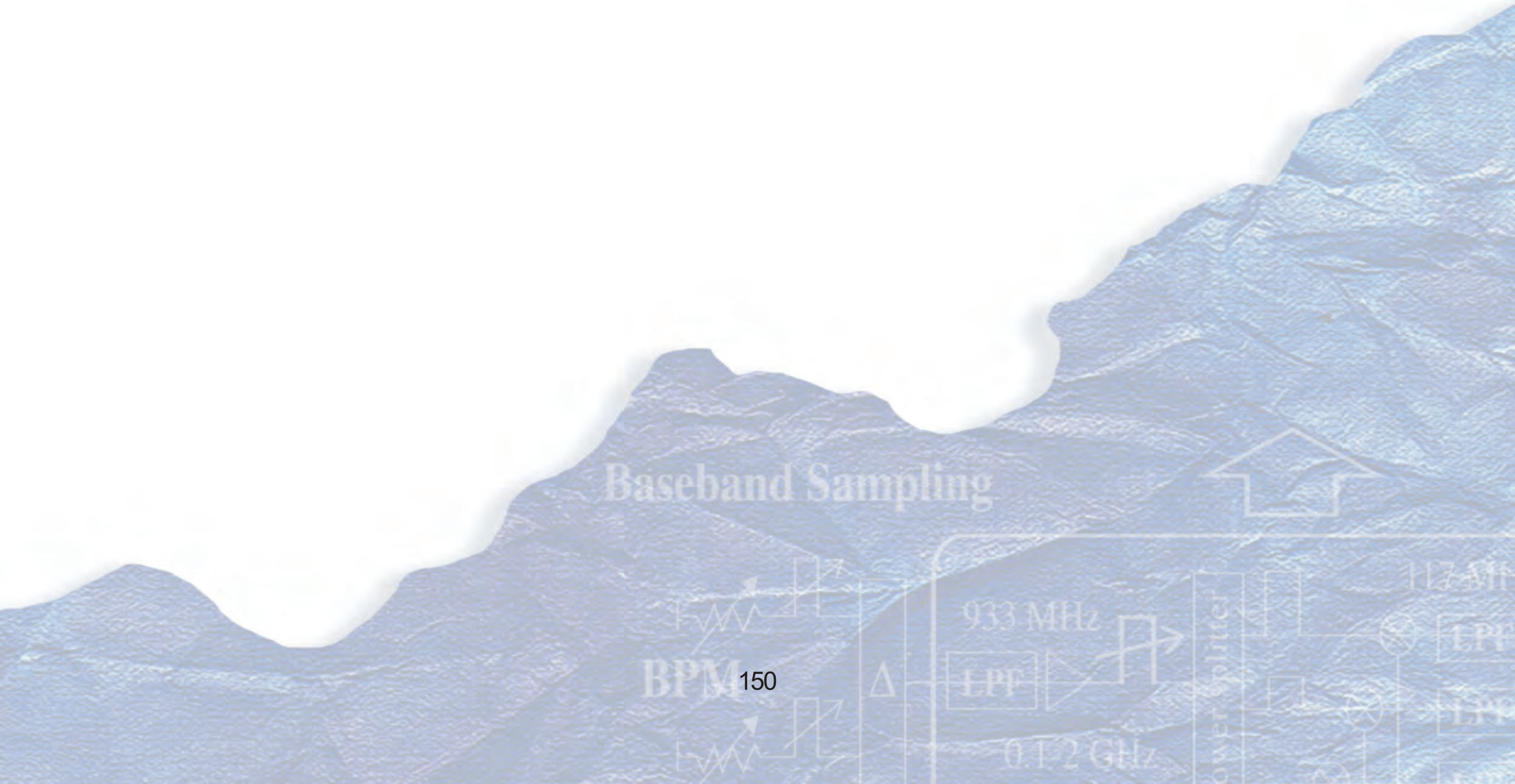

BEAM PERFORMANCE

Developments and Upgrades of Storage Ring and Booster Synchrotron

Improvement of the injection efficiency into storage ring

For recent light source facilities of the storage ring, the top-up operation is extremely important for demonstrating their thorough performance [1,2]. In the top-up operation, the beam is injected regularly to the ring during users experiment and the injection efficiency is expected to be as high as possible from the viewpoint of radiation safety and the demagnetization of insertion devices. Last year, we succeeded in improving the injection efficiency substantially and we report on it here.

Before January 2010, we operated the storage ring with the chromaticity (ξ_x, ξ_y) = (2, 6). The vertical chromaticity was set to a large value of 6 so as to suppress the beam instability in the filling mode with high current single bunches of 3 mA. Recently, we have improved the bunch-by-bunch feedback (BBF) system for suppressing instability by developing a current sensitive attenuator [3]. With this new BBF system, we could lower the vertical chromaticity ξ_y from 6 to 2. The lowering of the vertical chromaticity brought the injection efficiency improvement by about 10%. In Fig. 1, we compare the injection efficiencies in the user operations of the 2009: 5th and 6th cycles, whose averages are 85.2% and 94.1%, respectively.

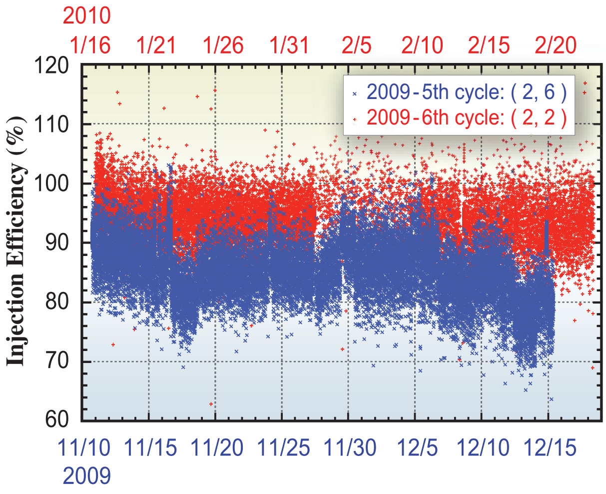

Fig. 1. Injection efficiency in user operation.

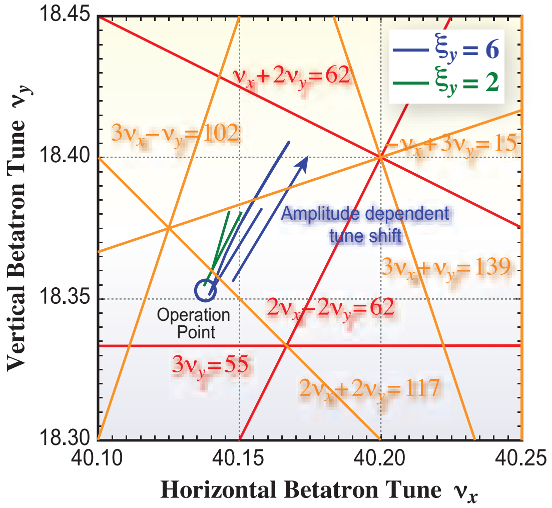

Fig. 2. Tune excursion of the beam with growing amplitude.

In the former cycle, we operated the storage ring with $\xi_y = 6$ and in the latter cycle with $\xi_y = 2$.

To elucidate the mechanism of the injection efficiency improvement, we studied the beam dynamics of electrons with large-amplitude oscillation [4]. Figure 2 shows the betatron tune excursion in the tune map for electrons with large-amplitude oscillation in the horizontal direction. The resonance lines of the third and fourth orders are also drawn, and some of these resonances, particularly the third-order ones, were found to have an impact on beam dynamics. As is well known, the betatron tune suffers an amplitude dependent tune shift due to the effect of the sextupole magnet field. This tune shift at the vertical chromaticity $\xi_y = 6$ is larger than $\xi_y = 2$. Hence, at $\xi_y = 6$, the tune of the oscillating beam with a large amplitude like that of the injected beam approaches the third-order resonance $\nu_x + 2\,\nu_y = 62$, closer than at $\xi_y = 2$. The resonance enhances the coupling of horizontal and vertical oscillations, and hence the beam becomes to oscillate in the vertical direction more strongly. As a result, the electron whose vertical oscillation amplitude has become large collides with the aperture and is lost. Thus, the injection efficiency is improved by lowering the chromaticity to prevent the betatron tune from approaching harmful resonances.

Through the study of the beam dynamics with large amplitude, we are aware of the importance of the operation point. For example, although the nominal operation point of the SPring-8 storage ring is set to (ν_x, ν_y) = (40.15, 18.35), it is observed that the injection efficiency at (40.14, 18.35) is several percent higher than that in the former. This is explained as follows. Figure 3 shows the power spectrum of the vertical oscillations of the stored beam kicked horizontally by the injection bump magnets. By exciting two of the four pulsed bump magnets, we can give some amplitude to the stored beam. The analysis of the beam oscillation gives information on the coupling resonance excitation. In the present example in Fig. 3, the mode of $2\nu_x$, which is excited by the skew sextupole magnet field, is excited larger at the operation point (40.15, 18.35). This is because the second harmonics $2\nu_x$ at the nominal operation point gets closer to the vertical tune than that at (40.14, 18.35). In other words, the operation point approaches the coupling resonance excited by the skew sextupole magnet field. Hence, the vertical oscillation for $\nu_x = 40.15$ becomes larger than that for $\nu_x = 40.14$, and the injection efficiency of the former becomes lower than the latter.

By carefully choosing the operation point to keep it away from harmful resonance lines of the third and fourth orders, we have realized a high injection efficiency, from 93% to 95%, constantly in the user operation period. When users change the gap of the insertion devices, the betatron tunes change with the quadrupole field component of their magnetic field and in some cases the operation point moves toward harmful resonance lines. To prevent the decrease in injection efficiency by this effect during user operation, we plan to add auxiliary power supplies to nearby quadrupole magnets to keep the betatron tunes constant.

(a) "ft_chrom22_y_100225.txt"

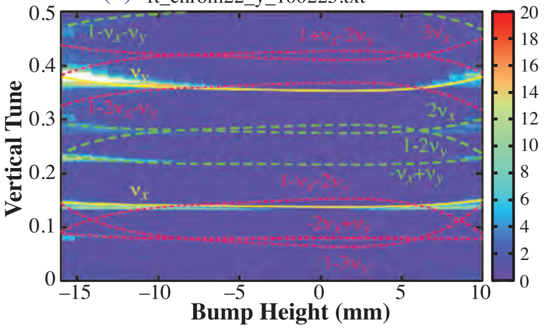

(b) "ft_id10_gfo_y_100626.txt"

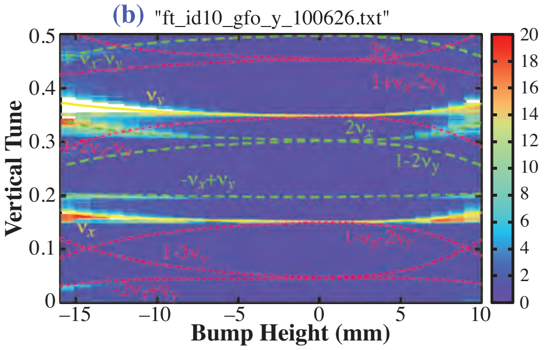

Fig. 3. Spectra of vertical beam oscillations for $\nu_x = 40.14$ (left) and 40.15 (right) when kicked by pulsed bump magnets.

Beam-based alignment for injection bump magnets of storage ring using remote tilt-control system

In the top-up operation mode, it is important to suppress the oscillation of the stored beam during beam injection. During the injection, four pulsed magnets (bump magnets, BP1 ~ BP4) are excited by four individual power supplies to generate a bump orbit. If a magnet has alignment error in rotation around the beam axis (tilt), the stored beam is oscillated in the vertical direction. In addition, even if the rotational alignment error is negligible, the beam out of the median plane is kicked in the vertical direction. Also, there is a small long-term drift of the vertical beam positions in the bump magnets, which causes the gradual increase in the extent of oscillation. Therefore, it is necessary to realign the bump magnets periodically.

We have already developed a remote tilt-control system to achieve a smooth realignment [5]. To measure vertical oscillation, the beam was stored in only one rf bucket and was shaken by the pulse of the bumps without beam injection. The beam position was measured turn-by-turn using the strip-line type beam position monitor for the bunch-by-bunch feedback system [6]. The monitor has the highest position resolution of all the position monitors in the storage ring. To obtain responses to the tilts of each magnet, the oscillations were measured under the condition that the magnets were tilted intentionally. Tilt errors were calculated by the least-squares method using the responses.

An example of the oscillation before the correction is shown in Fig. 4 (dashed line). After the correction, amplitude was suppressed to 1/25 (solid line). However, the amplitude could not be made zero or below the noise level. The residual oscillation could be attributed to the horizontal oscillation observed in the vertical axis in the position monitor coordinates. A small angle mismatch between the observation and oscillation axes introduces a false observation, because the horizontal oscillation has an amplitude

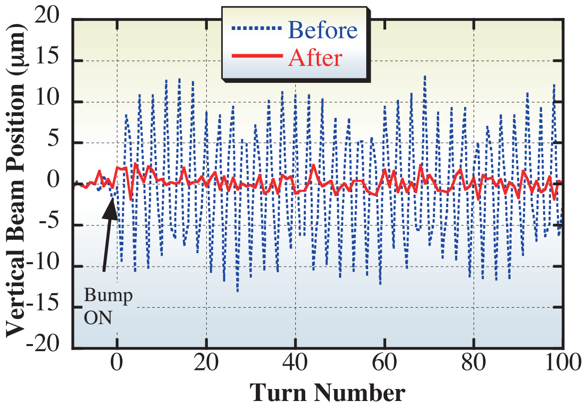

Fig. 4. Vertical beam position *versus* turn number. Dashed and solid lines indicate the positions before the correction and after the correction, respectively.

two orders of magnitude larger than the vertical one.

To confirm the source of the residual oscillation, frequency analysis was carried out by the FFT method using the position data from the 1st turn to the 128th turn. The peak amplitude *versus* frequency is shown in Fig. 5. The horizontal component could be separated from the vertical component because their frequencies agreed with the fractional tunes in the horizontal and vertical directions. Before the correction (dashed line), the vertical component was 20 times as large as the horizontal one. After the correction (solid line), the peak amplitude of the vertical component was suppressed to 0.41 µm and was smaller than that of the horizontal component. In addition, the amplitude of the horizontal oscillation remained unchanged, which meant that the observed residual oscillation came from the horizontal one.

We succeeded in suppressing the vertical oscillation due to the bump magnets to the submicron order, a value less than one tenth of the beam size.

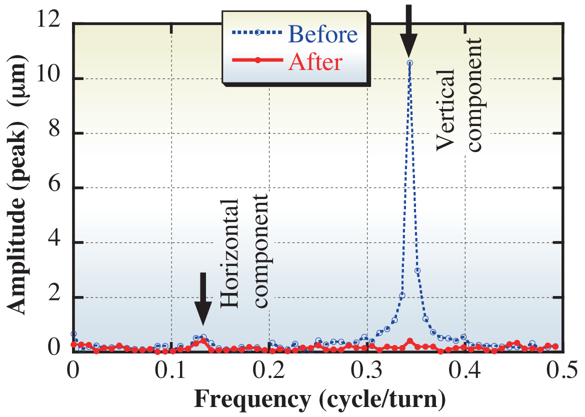

Fig. 5. Peak amplitude *versus* frequency. Dashed and solid lines indicate the amplitudes before and after the correction, respectively.

Development of bunch-by-bunch feedback system

The hybrid filling composed of high bunch current singlet bunches and low bunch current bunch trains are requested by users [3]. For this filling, the bunch-by-bunch feedback system (BBF) has to simultaneously stabilize the mode-coupling beam instabilities of the singlets and the multi-bunch instabilities of the trains, in both horizontal and vertical directions. However, the signal level from the beam position monitor (BPM) for the BBF is also proportional to bunch current; therefore, the signal level from the high bunch current singlets is two orders higher than that from the trains, and the BBF saturates for singlets. To compensate for such a bunch current dependence of the BPM signal level, the old bunch current sensitive bunch-by-bunch automatic attenuator, the attenuation range of which was 10 dB, was upgraded to a new one with a range of 40 dB [7]. The controller based on the SPring-8 BBF signal processor was developed to measure the bunch current and drive the digital and analog attenuators, as shown in Figs. 6 and 7, respectively. Also, the large feedback kick necessary to suppress the strong single-bunch instability under the large horizontal oscillation excited by the formation of the bump orbit was achieved by upgrading the kicker to a high-efficiency horizontal kicker.

With these upgrade of the BBF, we achieved the top-up operation with the filling of a singlet with 6 mA/bunch and trains with 900 bunches with 0.1 mA/bunch, under the worst-user operation condition for the instability with almost all the in-vacuum insertion devices closed to their minimum gap.

Further increase in the bunch current of the singlet to 10 mA/bunch and an increase in the freedom of the range of filling for the train are intended for use with a

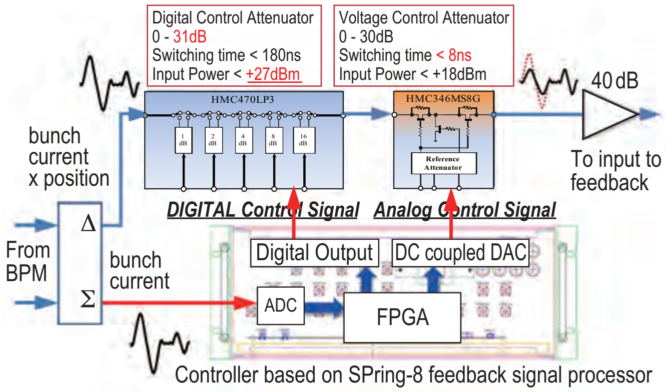

Fig. 6. Upgraded bunch current sensitive automatic attenuator.

new high-efficiency kicker under manufacture. The freedom of the range of filling will also be achieved by the operation of the fast correction kicker [8] developed by the vacuum and magnet team to reduce the oscillation amplitude excited by bump orbit formation.

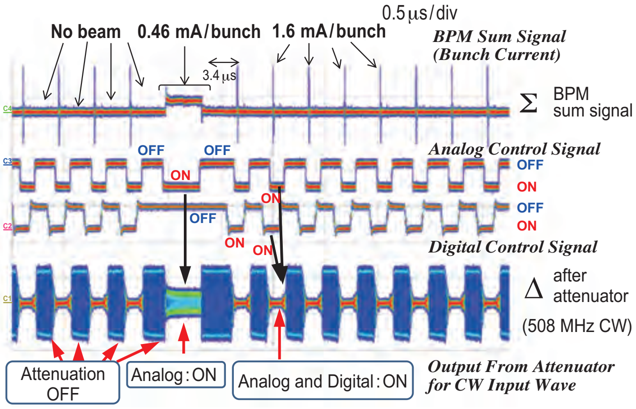

Fig. 7. Bench test result with the BPM sum signal of stored beam with 1/14 + 12 bunch filling.

Development of accelerator diagnostics beamlines

At diagnostics beamline II (BL05SS), we constructed and commissioned the transport line of the monochromatic X-ray beam from optics hutch II to the experimental hutch. The first light was successfully delivered to the experimental hutch in April 2010. We have developed a γ-ray stopper made of tungsten heavy alloy for the transport line and have installed it downstream of the double-crystal monochromator of optics hutch II. The γ-ray stopper consists of a rectangular parallelepiped block of heavy alloy with a rectangular through-hole (Fig. 8). The heavy alloy block serves as both a shield of high-energy radiation accompanying the incident white X-ray beam to the monochromator and a vacuum pipe transporting the monochromatic X-ray. It is equipped with two conversion flanges at both ends through metallic O-rings and is connected to neighboring vacuum chambers of the beamline with conflat flanges with an outer diameter of 70 mm (ICF70). The heavy alloy block as well as its sealing with metallic O-rings is leak-tight and the measured helium leak rate was less than 10^{-11} Pa·m^3/sec. The γ-ray stopper was baked at 200°C after installation in the beamline, reaching a pressure of 10^{-7} Pa in the UHV.

A fast turn-by-turn diagnostics system of the transverse emittance and the energy spread of the electron beam is being developed in the experimental hutch of diagnostics beamline II. It is based on the measurement of the angular divergence of the higher harmonics of the ID. The vertical divergence of the ID photon beam is sensitive to the energy spread of the electron beam because of the small vertical emittance of SPring-8, whereas the horizontal divergence is dominated by the horizontal emittance. The sensitivity of energy spread measurement has been studied experimentally by observing the 19th harmonics of the ID [9]. The fast diagnostics system consists of a fast fluorescent screen, an image intensifier and a fast-gated CCD camera. It is expected to be useful for tuning the injection of the high-quality beam to be delivered from the C-band linac for XFEL. Test of the fast diagnostics system is in progress by observing the injection beam from the booster synchrotron and simultaneously measuring the longitudinal bunch length with a visible streak camera (VSC) at diagnostics beamline I (BL38B2). Figure 9 shows an example of the results of the turn-by-turn bunch length measurement. The VSC operated in the dual-time base mode, which has a fast vertical scan for measuring the bunch length and a slow horizontal scan for resolving each turn after injection. Although the bunch length of the injection beam is longer than that of the stored beam in equilibrium, the energy spread of the injection beam is comparable with the stored beam. Therefore the bunch length after injection decreases in the one-quarter period of the synchrotron oscillation and then increases in the next one-quarter period. Such features of the bunch length of the injection beam have been successfully observed by the VSC.

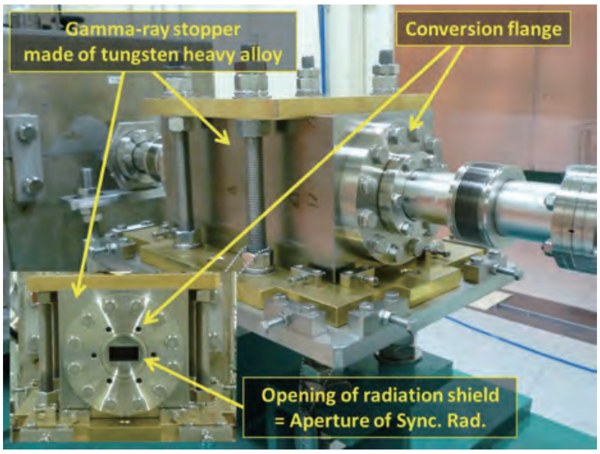

Fig. 8. γ-ray stopper made of tungsten heavy alloy developed for transport line of monochromatic X-ray beam of diagnostics beamline II.

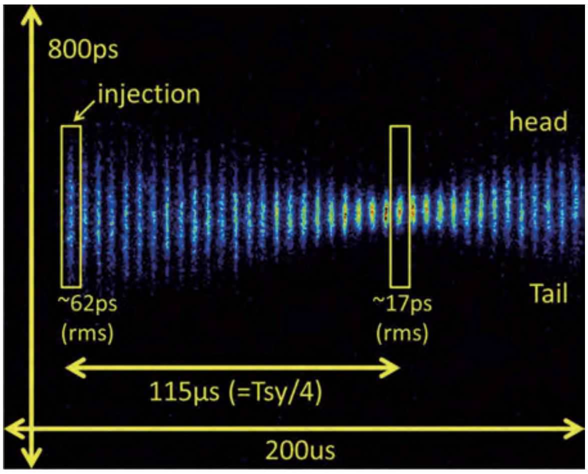

Fig. 9. Example of the results of turn-by-turn bunch length measurement of injection beam from booster synchrotron by VSC at diagnostics beamline I.

Research and development of femtosecond pulse X-ray generation

An X-ray with an energy of 10.7 keV and a pulse width of 600 fs in two standard deviations can be generated with a short-pulse generator using superconducting crab cavities in one of the long straight sections of the storage ring. A phase stability within 14 mdeg among the crab cavities is required to realize this scheme [10]. We developed a 300 kW phase shifter to stabilize the phase fluctuation and found that its performance could satisfy this requirement [11]. In this report, we describe a power supply developed as a driver of this phase shifter, which is an inductive load of 50 µH/40 mΩ.

The power supply consists of DC power supplies whose voltages are powers of 2, such as 4 V, 8 V ... and 256 V, and power MOSFET switches. Its driving frequency range is from DC to 10 kHz with a current of 50 A and a voltage of 550 V. We measured the frequency response of the power supply in an offline test using a load with the same impedance as that of the phase shifter. Preliminary results for driving currents of 10 A, 40 A and 50 A are shown in Fig. 10. Although several improvements in the stability and reliability are needed for the power supply, tests on the important parameters have already been completed.

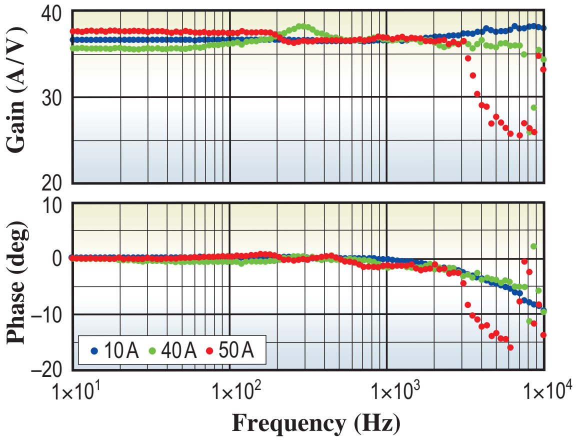

Fig. 10. Measured frequency responses of power supply.

Developments and Upgrades of Linac

Development of RF isolator for vacuum waveguide system

Although the RF waveguide systems for the regular section of the linac are evacuated by ion pumps, the waveguide system for the injector section, which is equipped with circulators, is filled with a pressurized SF_6 gas because a vacuum-type circulator has not yet been developed.

An RF phase of a microwave propagated in such a pressurized waveguide varies along with fluctuations in its insulation gas pressure, the atmospheric pressure and its body temperature. This RF phase variations result in non-negligible beam instability. Now, we are planning to update the SF_6 waveguide system to a vacuum-type one to improve its RF phase stability and renew its aged components. As SF_6 is a type of global greenhouse gas, its usage should also be reduced. We thus started an R&D of vacuum-type circulators and isolators.

Since the outgassing rate from garnet ferrites used in a circulator was expected to be very large, we measured it at an estimated operation temperature of 100°C. It was found that the outgassing rate is only about 34 times larger than that of typical stainless steel and is acceptable for evacuation by ion pumps.

Next, we examined various methods of bonding of ferrite and copper. It was found that solder bonding with a holder ring and the segmentation of ferrite could realize sufficient mechanical strength and good thermal conductivity.

As the RF power for pre-bunchers is low, we first developed an isolator in which a ferrite plate transmits the forward RF power and absorbs the backward one. The isolation of 13 dB and an insertion loss of 0.3 dB for a power lower than 100 kW were achieved with the prototype isolator shown in Fig. 11. We expect that the isolation can be improved by lengthening ferrites and magnets. Actual models of the isolator are under production.

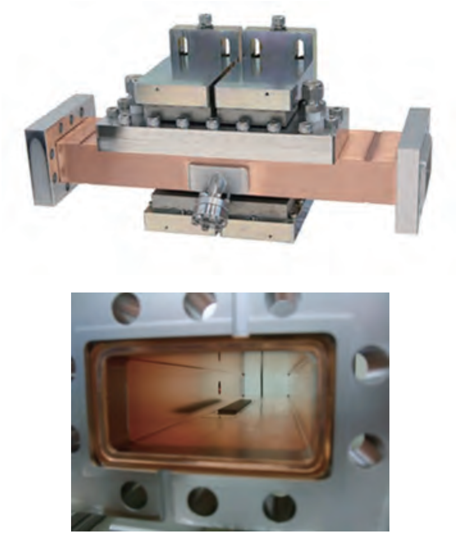

Fig. 11. **(a)** Prototype isolator composed of waveguide and permanent magnets. **(b)** Rectangular ferrite plate bonded to internal surface of waveguide.

Haruo Ohkuma*, Shigeki Sasaki and Hirofumi Hanaki

SPring-8/JASRI

*E-mail: ohkuma@spring8.or.jp

References

[1] H. Tanaka *et al*.: Proc. EPAC'04, Lucerne, Switzerland, p.1330.
[2] H. Ohkuma: Proc. EPAC'08, Genoa, Italy, p. 36.
[3] K. Kobayashi and T. Nakamura: Proc. ICALEPCS2009, Kobe, Japan, p. 659.
[4] M. Takao *et al*.: Proc. IPAC'10, Kyoto, Japan, p. 4671.
[5] K. Fukami *et al*.: Proc. EPAC'08, Genoa, Italy, p. 2172.
[6] T. Nakamura *et al*.: Proc. EPAC'04, Lucerne, Switzerland, p. 2649.
[7] T. Nakamura *et al*.: Proc. EPAC'08, Genoa, Italy, p. 3284.
[8] C. Mitsuda *et al*.: Proc. IPAC'10, Kyoto, Japan, p. 2552.
[9] M. Masaki *et al*.: Proc. SRI09, Melbourne, Australia, p. 560.
[10] T. Fujita *et al*.: Proc. IPAC'10, Kyoto, Japan, p. 39.
[11] SPring-8 Research Frontiers 2008, p. 184.

CONTROLS & COMPUTING

Wide-area remote experiment system at SPring-8

SPring-8 users have been traveling from their institutes to the SPring-8 site to conduct their experiments using beamlines during their beam time. However, this requirement/restriction has exerted various loads to users. Many users requested to perform out-of-site remote experiments in order to increase effective working time for their research and development. The use of a wide-area remote experiment system (WRES) frees users from traveling and brings a more flexible operation style of experiment such as 24-hour operation in collaboration with different groups from different countries. The WRES has been developed [1] and first experiment successfully carried out from a remote site in RIKEN Wako, located about 480 km away from SPring-8, at the end of October 2010.

To realize remote experiments, there are two important points to consider: 1) human safety and 2) security of the remote access.

1. *Safety issue*

As in other synchrotron radiation facilities, experimental equipment is installed in radiation shielding hutches. A radiation safety interlock system ensures that there is no person inside the hutch when the synchrotron radiation beam is introduced into the hutch. Under remote experiments, a radiation safety interlock also guarantees this condition.

SPring-8 staff members access the experimental equipment for the maintenance or preparation of experiments. Some of the equipment is heavy or moveable. If a remote user move equipment, it might damage lead to injury in SPring-8 staff members inside the hutch. To avoid this situation, a remote experiment interlock unit (see Fig. 1) was introduced. The unit is designed to inhibit experimental equipment operation unless the radiation safety condition is satisfied. The safety condition status is fed from the radiation safety interlock system. The radiation safety interlock guarantees that there is no person inside the hutch. This also guarantees human safety condition. The remote experiment system is designed on the basis of a message exchange system because a message filtering system can be built easily compared with systems based on virtual private network or virtual network computing used for remote access systems in other facilities. The connection server, shown in Fig. 1, filters commands from remote experiment software and relays only permitted

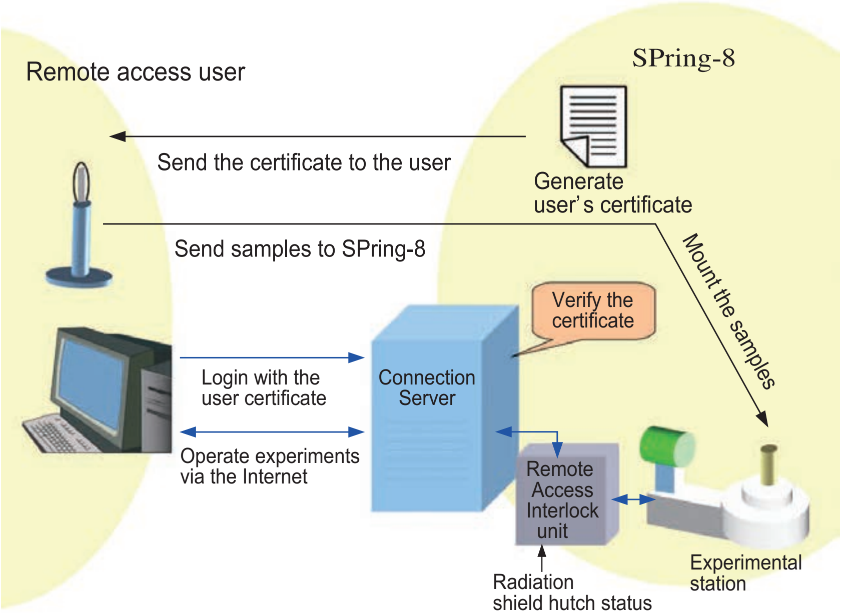

Fig. 1. Schematic view of the remote experiment.

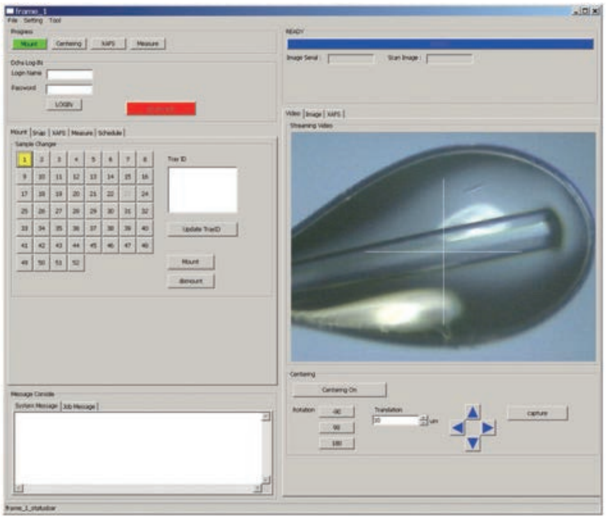

Fig. 2. Remote user's graphical user interface.

commands to the station control systems. A video streaming system is also introduced to monitor the inside of the experimental hutch. Users can also check their sample conditions using the streaming system.

2. *Security issue*

Remote experimental users can access SPring-8 via the Internet. This creates access security issue. Unauthorized individuals might access the remote experiment system intentionally or accidentally. Such an unexpected operation disturbs experiments or enables illegal access to experimental data. The secure socket layer (SSL) with bidirectional authorization is introduced to protect proper access to the system. As shown in Fig. 1, a SPring-8 staff generates a user's authentication certificate, and sends it to the user by e-mail. The certificate is locked by a password, which is sent by postal mail afterwards. The certificate contains a beam time ID. The connection server verifies the certificate and allows access by users with the authentication certificate and the password for the specified beam time. The flow of the remote experiment is shown in Fig. 1. A SPring-8 staff registers the user and the beam time information on a remote experiment information database. A user's authentication certificate, an electrical file, is generated on the basis of the registered information and sent to the remote user. The remote user sends their samples to SPring-8 and the SPring-8 staff mounts samples on the experimental equipment. The remote user accesses SPring-8 with the authentication certificate, and the connection server verifies the certificate and enables access to the experimental station control system. After establishing the connection to the experimental station, the user can perform their experiment during their beam time.

Protein crystallography experiment was chosen as the first trial remote experiment because the standardized experiment control system for protein crystallography at SPring-8 is highly automated and the experiment is suitable for adaptation to a remote experiment system. A graphical user interface (GUI) for the remote protein crystallography experiment has been developed as shown in Fig. 2. A remote user can monitor their sample on the goniometer installed inside the experimental hutch and can specify the X-ray beam irradiation position on the sample by clicking the sample image. The response time of the system is around 1 s, which is good enough to perform the experiment.

After a few years of intensive testing including the safety system, remote access server, remote user's GUI, video streaming system and experimental station control system, the first remote experiment was successfully performed from the RIKEN Wako site 480 km away from SPring-8 at the end of October, 2010.

The remote experiment system will bring flexibility for synchrotron radiation experiments and enhance international collaborations. It will be opened for protein crystallography users in October 2011; it will eventually be used in other experiments.

Yukito Furukawa

SPring-8/JASRI

E-mail: furukawa@spring8.or.jp

References

[1] *Y. Furukawa, K. Hasegawa, D. Maeda and G. Ueno: Proc. ICALEPCS 2009 (Kobe, Japan) p.615.*

NEW APPARATUS, UPGRADES & METHODOLOGY

In situ field measurement and correction for in-vacuum undulators

Shortening the magnetic period has been one of the most important targets in the development of insertion devices, in particular, undulators. It significantly enhances the brilliance in the hard X-ray region not only by increasing the number of periods but also hardening the spectral range. This is the reason why the in-vacuum undulator (IVU), in which the magnet arrays are installed inside the vacuum chamber and thus the gap can be much narrower than the conventional undulators, has been widely used in many synchrotron radiation facilities. Although the technologies for IVUs have become mature enough, there is still one concern on how to guarantee the magnetic performance, in other words, how to check the magnetic field error before installation and how to correct it if necessary. In this paper, we present the new technologies for answering these questions, which have been recently developed in SPring-8.

In situ Magnetic Measurement and Correction. Because the permanent magnets have some magnetic errors, the undulator field distribution cannot be completely sinusoidal, resulting in the degradation of the available flux. It is therefore important to measure the field distribution to check the undulator performance. If it does not satisfy the required specification, the field errors should be corrected. To measure the field distribution, the Hall-effect sensor is moved along the undulator axis using a rigid and accurate linear guide usually mounted on massive granite. This method, however, cannot be applied directly to IVUs because the magnetic arrays are installed inside the vacuum chamber. Therefore, the field measurement and the following field correction are always carried out without the vacuum chamber. After that, the magnetic arrays should be disassembled once from the mechanical frame to install the vacuum chamber, and then assembled again. If the mechanical reproducibility of the magnet arrays is poor, the field distribution may be varied during the assembling process and the undulator quality is not guaranteed. Thanks to the careful management of the assembling process, no serious problems have been reported so far in SPring-8. It should be noted, however, that the requirement of mechanical reproducibility would be more stringent for shorter-period IVUs. Thus, new technologies toward shortening the undulator period are required, which make it possible to measure the field distribution generated by the magnet array installed inside the vacuum chamber, and to correct its field error if necessary. Hereinafter, they are referred to as the *in situ* field measurement and correction techniques.

New Field Measurement System SAFALI. In order to realize the *in situ* field measurement, the most straightforward way is to install a simple and compact linear guide inside the vacuum chamber and move the Hall sensor along the undulator axis. It should be noted, however, that the straightness of the linear guide, which is so small as to be able to be inserted into the chamber, could not be sufficient good. The long linear guide can be bent owing to the weight itself or other load, which should be compensated dynamically. We have recently developed a new field measurement system that enables the *in situ* field measurement, which is schematically shown in Fig. 1.

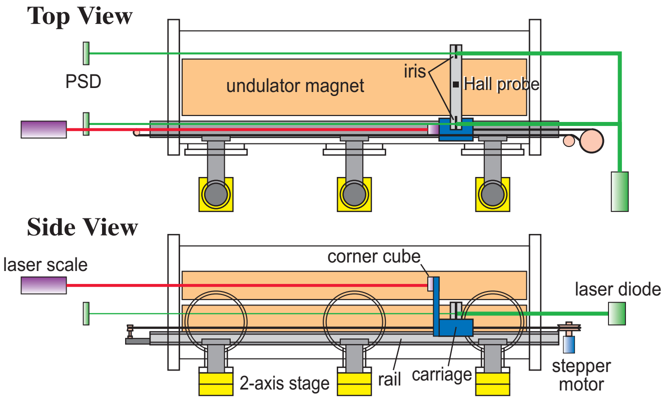

Fig. 1. SAFALI system for the *in situ* field measurement of IVUs.

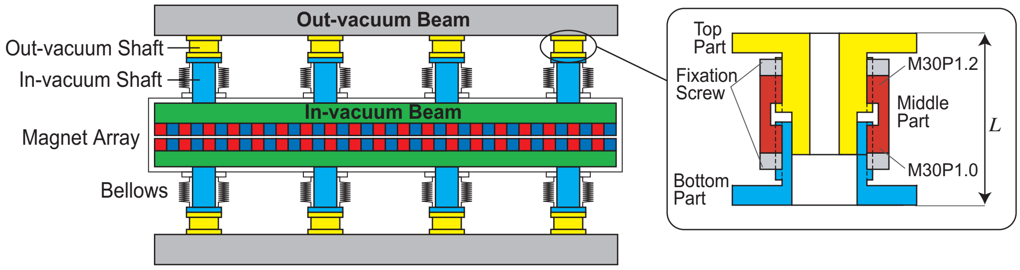

Fig. 2. Schematic illustrations of the IVU structure and differential adjuster as the out-vacuum shaft with the adjustable length.

Two laser beams are introduced to the vacuum chamber to illuminate the pinholes attached to the Hall sensor. The transverse positional variation of the Hall sensor is detected by monitoring the positions of the laser spots created by intercepting the laser beams, by means of position sensitive detectors (PSDs). The linear guide to move the Hall sensor is supported by 2-axis linear stages, with which the positional error of the Hall sensor can be corrected dynamically, once they are detected using the above scheme. This system is called "SAFALI" for Self-Aligned Field Analyzer with Laser Instrumentation.

Differential Adjuster for In situ Correction. Let us consider the possible error sources during the assembling process of IVUs using Fig. 2, which schematically shows the IVU structure. At the time of field measurement, all the components except the vacuum chamber are installed. Then, all the components excluding the out-vacuum beams and shafts are detached in order to install the vacuum chamber. If the positional reproducibility of the in-vacuum shaft is not perfect, then localized gap errors arise, resulting in the significant degradation of the undulator quality. This in turn indicates that if the length of the out-vacuum shaft is adjustable, then the gap variation can be compensated, i.e., the *in situ* field correction is possible. For this purpose, a new out-vacuum shaft has been developed as shown in Fig. 2, the length of which can be adjusted using the mechanism based on the differential screw. Thanks to the difference in the pitch of the threads in both ends, the length of the shaft can be adjusted with the resolution of 0.2 mm per revolution. We have found that the typical sensitivity of the gap error correction is better than 5 μm.

As an example, using the technologies described above, we have tested the *in situ* field measurement and correction using an IVU with the length of 1.4 m and period of 14 mm. The results are shown in Fig. 3 in terms of the phase errors as functions of the magnet pole number calculated with the field distribution data measured with the SAFALI system. Three results are indicated: before and after assembling the chamber, and after the *in situ* field correction using the differential adjusters. It is found that the phase error has increased from 2.9° to 6.1° owing to the assembling process, and reduced to 3.0° by the *in situ* correction, almost comparable to the original value.

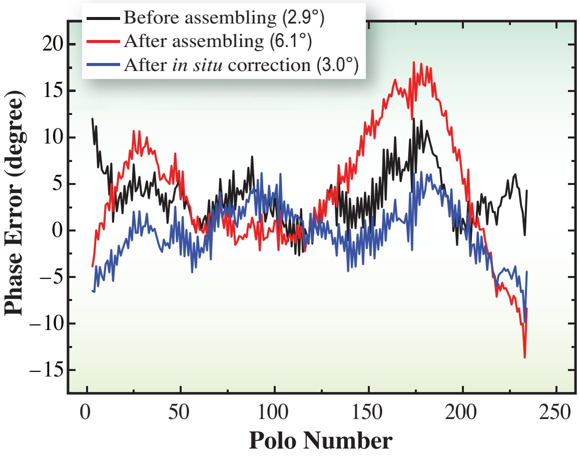

Fig. 3. Results of the *in situ* field measurement and correction for the IVU with the length of 1.4 m and period of 14 mm. The numbers in the brackets indicate the r.m.s. phase errors.

Takashi Tanaka

SPring-8/RIKEN

E-mail: ztanaka@spring8.or.jp

Formation of sub-10 nm hard X-ray beam

Third-generation synchrotron and recently operated X-ray free electron laser facilities can produce almost fully coherent light even in the hard and soft X-ray ranges. These high-performance X-rays have been stimulating research on X-ray microscopy with nanometer spatial resolution. X-ray microscopic systems must be equipped with a focusing device. In the past decade, various optical devices have been improved by the development or application of advanced manufacturing technologies. There are many types of X-ray focusing devices that utilize reflection, refraction, and diffraction. One of the features of these devices is the experimentally achieved focused beam size, which has been decreasing rapidly and has reached less than 50 nm. Such focusing devices are now commercially available.

For several years, there has been theoretical interest among many researchers in X-ray microscopy fields in the smallest beam size that can be achieved. X-rays can be focused by their interaction with matter. The focused beam size is determined by the numerical aperture of the optical design, wavelength of the employed X-rays, and several aberrations inherent to optical devices. Several theoretical simulation-based studies on each type of focusing device have been carried out. The results indicated that the realization of a focal beam size of less than 10 nm is theoretically possible.

We have been developing an optical system for sub-10 nm hard X-ray focusing using laterally graded multilayer mirrors. The Kirkpatrick-Baez optical system is used for two-dimensional hard X-ray focusing. In this optical system, hard X-rays are individually focused in the vertical and horizontal directions. Two one-dimensional elliptically curved mirrors are used. The focused beam size is determined by the optical system design. To decrease the focused beam size, the optical system should be designed so that its numerical aperture is large. The numerical aperture is strongly related to the maximum X-ray incident angle in reflective optics. Multilayer surfaces are used for reflecting X-rays with a relatively large incident angle.

Last year, we constructed a KB optical system with two multilayer mirrors and performed one-dimensional focusing tests. Figure 1 shows an optical system design. The optical system is designed assuming the use of the 1-km-long beamline **BL29XUL**, in which the experimental hutch is approximately 1 km from the monochromator and almost full coherent hard X-rays are available. The surface profile of the focusing mirror is elliptically curved in accordance with the elliptical functions determined in the optical system design.

Figure 2 shows a photograph of the experimental setup. This experimental system is now installed in the 1-km-long beamline BL29XUL. The grazing incidence deformable mirror is used to control the shape of the wavefront of the incident X-ray entering the focusing mirror. To measure the wavefront of focusing X-rays, which is originated from the imperfection of the focusing mirror, the phase retrieval method using intensity profiles around the focal point is employed. We employed the phase retrieval method, which can use many intensity profiles around the focal point.

The experiment we carried out was as follows. Initially, while maintaining a flat surface profile of the deformable mirror, the incident angle and focal

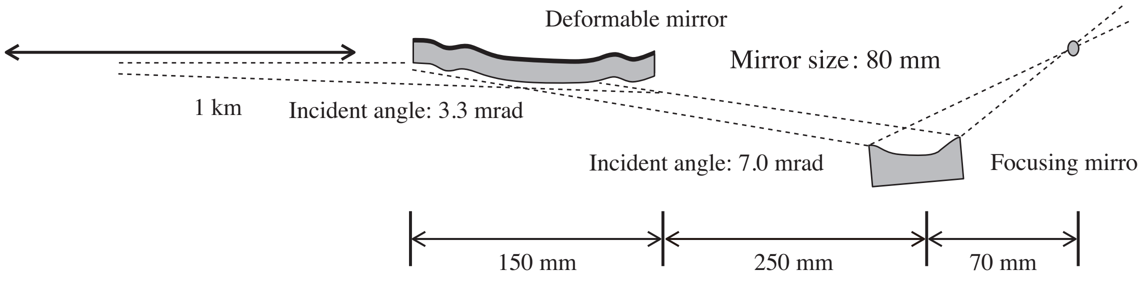

Fig. 1. Schematic of optical system for sub-10 nm hard X-ray focusing.

Fig. 2. Photograph of sub-10 nm focusing system installed in the 1-km-long beamline (BL29XUL).

length of the focusing mirror were adjusted to obtain the minimum focused beam size. Then, 16 intensity profiles around the beam waist were measured. After that, the wavefront error profile was used to estimate the phase retrieval using all the profiles. Then, the shape of the deformable mirror was adjusted in accordance with the estimated profile, to compensate for the wavefront error. Finally, the intensity profiles were remeasured after wavefront correction. The experimental conditions except for the shape of the deformable mirror were the same before and after wavefront correction.

Figure 3 shows a comparison between the ideal and measured profiles when the smallest beam size is obtained. The result indicated that nearly diffraction-limited focusing was realized. The ultimately achieved focused beam size was 7 nm.

The recent rapid advances in ultraprecise machining are the main factors responsible for breaking the 10 nm barrier. Laterally graded multilayer mirrors have the potential to be used in designs with larger NAs that permit relatively large incident angles. Based on the minimum period in multilayer films, a 3 nm beam should be achievable. A focusing system based on adaptive optics is also promising for realizing ultimate X-ray focusing.

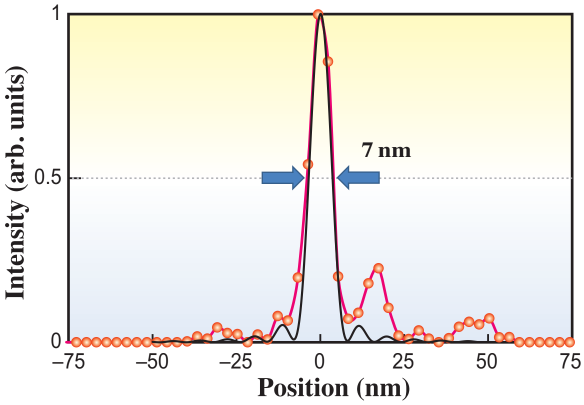

Fig. 3. Measured intensity profile of hard X-ray focused beam. X-ray energy is 20 keV.

Hidekazu Mimura†

Dept. of Precision Science and Technology,
Osaka University

E-mail: mimura@edm.t.u-tokyo.ac.jp

† Present address: Dept. of Precision Engineering,
The University of Tokyo

References

[1] *H. Mimura, S. Handa, T. Kimura, H. Yumoto, D. Yamakawa, H. Yokoyama, S. Matsuyama, K. Inagaki, K. Yamamura, Y. Sano, K. Tamasaku, Y. Nishino, M. Yabashi, T. Ishikawa and K. Yamauchi: Nature Phys.* ***6*** *(2010) 122.*

Total reflection zone plate for 15 nm line focus of 10 keV X-rays

X-ray focusing is a promising technique since it provides a secure high-spatial resolution to various X-ray analytical procedures. The focusing performances are rapidly improving, particularly in the hard X-ray region. Fresnel zone plates (FZPs), utilizing diffraction by a coaxial circular grating with decreasing spacing, and Kirkpatrick-Baez (KB) mirrors, consisting of tandem-arranged two parabolic or ellipsoidal mirrors for individual focusing in the orthogonal directions, have been widely used as typical focusing devices in the hard X-ray region. These devices that can achieve a focusing size of sub-100 nm are commercially available. Moreover, new focusing devices, such as multilayer Laue lenses and graded multilayer KB mirrors, have recently been developed and achieved the focusing size of around 10 nm, and the best focal size of 7 nm using 20 keV X-rays has been reported [1]. However, these focusing devices require ultrahigh precision for their configuration and, hence, special technology is needed for their fabrication.

Generally, when an object drawn on a flat plate is observed under a glancing condition, the observing size becomes small in the glancing direction according to the glancing angle. A schematic of this effect is shown in Fig. 1. The total reflection zone plate (TRZP) is a focusing device utilizing this effect to reduce the difficulty of fabrication. This device consists of reflective zones on a flat substrate as shown in Fig. 2, so that it can focus X-rays with a grazing incident angle satisfying the total reflection condition when the zone boundary is arranged under the same condition for conventional FZP; a path difference of diffracted X-rays cause by every adjacent zone is equal to a half the wavelength at the focal point. The effective zone size becomes much smaller than a drawn size on the substrate because the grazing incidence angle for total reflection is very small in the hard X-ray region. Since the ratio of sizes becomes greater than 100, no special process is required for the fabrication, even though the theoretical size of focus is near 10 nm. Such reflection-type zone plate has been proposed early and developed with some unsatisfactory experiments, although a theoretical consideration suggests that the TRZP has sufficient nanofocusing potential [2]. We have developed a linear-type TRZP for nanofocusing of synchrotron radiation X-rays. The focusing size of 14.4 nm, near the diffraction-limited size, has been experimentally achieved using 10 keV X-rays of undulator emission [3].

Table 1 shows parameters of the fabricated TRZP with the designed grazing incident angle of 6 mrad and X-ray energy of 10 keV. A conventional silicon wafer of 0.5 mm thickness was used as the substrate. A pattern consisting of a thousand zones made of platinum is drawn over 2.44 mm on the substrate. The pattern can be processed by conventional electron beam lithography since the zone thickness is small (20 nm) and the finest zone width is large (0.7 μm). This TRZP works as well as a binary-type FZP, since only the reflected/diffracted X-rays from the reflection zone contribute to form the focus. Half of the full zone structure was drawn to separate the focal beam from direct reflection from the substrate. The focal length (distance between the focal position and center of the full zone r_0) is 4.16 mm, and hence, the working distance (distance between the focusing point and the finest zone r_N) is 1.72 mm. The theoretical focusing size estimated using Reyleigh's criterion with the geometrically defined numerical aperture is 14.7 nm. This is much smaller than the finest drawn zone size of the TRZP.

Focusing test of the TRZP was performed using monochromatic X-rays of 10 keV at Hyogo-ID beamline **BL24XU**. Then, the coherence condition of

Table 1. Parameters of fabricated TRZP

Substrate	Silicon wafer
Zone material	Pt / Ti
Zone thickness (nm)	10 / 5
Number of zones: N	1000
Finest zone width (mm)	0.7
Pattern length (mm): r_N	2.4
Grazing incident angle (mrad)	6
Effective aperture size (μm)	14.4
Effective finest zone width (nm)	4.2
Focal length f (mm)	4.16
Diffraction-limited focal size (nm)	14.7

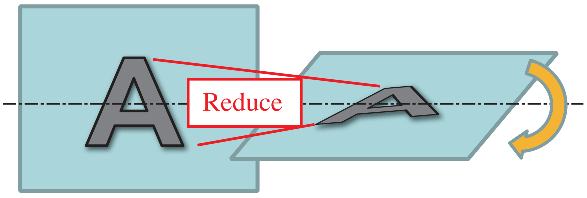

Fig. 1. Illustration of size reduction effect in glancing view.

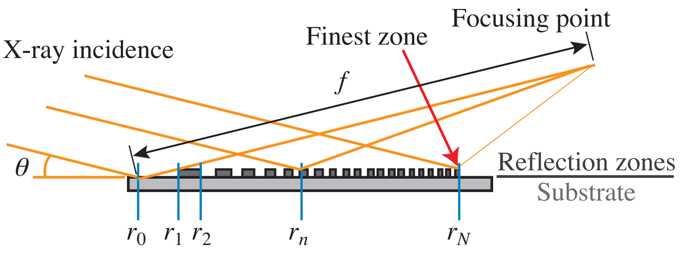

Fig. 2. Schematic of the total reflection zone plate.

the incident beam is sufficient to form a diffraction-limited focus for the TRZP with an effective aperture size of 14.6 μm and with the total zone number of 1000. The focusing beam was evaluated by a knife-edge scanning procedure in dark-field geometry. This procedure can be used to directly measure a line spread function of a focal beam with any differentiated process following the conventional knife-edge scan procedure. The spatial response is very high because of the edge-diffraction effect caused by the knife edge [4]. Figure 3 shows the measured intensity distribution of the line focus of the TRZP. A platinum wire of 300 μm diameter was used as the knife edge and scanned in the best focal plane at 2 nm steps with a piezoelectric translation stage. The focusing size of 14.4 nm in FWHM was obtained as an average of 41 repeated measurements.

Although the focusing beam includes undesirable peaks around a main peak, the main peak surely has a nearly diffraction-limited size. This shows that X-rays diffracted by not a small region of zones including near both sides of the TRZP can interfere with the phase at the focal position. According to an inspection of the drawn pattern of the TRZP, the side peaks configured by X-rays with out of phase may due to a figure error of the substrate such as warping by deposition process. Therefore, a better result may be possible only with a small upgrade for further TRZP. Moreover, the TRZP can be applied for point focus generation by introducing KB configuration, or by advanced patterning for point focusing or by introducing a conical substrate. It can be said that the TRZP is one of the most promising approaches for nanofocusing in the hard X-ray region.

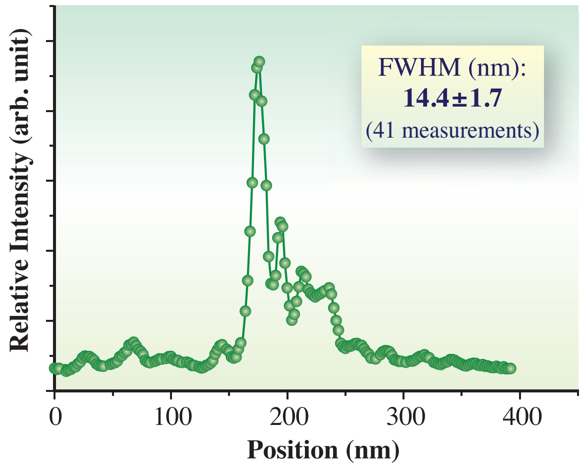

Fig. 3. Measured intensity distribution of line focus obtained with the TRZP.

Hidekazu Takano

Graduate School of Material Science,
University of Hyogo

E-mail: htakano@sci.u-hyogo.ac.jp

References

[1] H. Mimura *et al.*: Nat. Phys. **6** (2010) 122.
[2] A.G. Michette *et al.*: Opt. Comm. **245** (2005) 249.
[3] *H. Takano, T. Tsuji, T. Hashimoto, T. Koyama, Y. Tsusaka and Y. Kagoshima: Appl. Phys. Express* **3** *(2010) 176702.*
[4] S. Handa *et al.*: Nucl. Instrum. Meth. A **616** (2010) 246.

Development of Fourier transform holography imaging using soft and hard X-rays

With the recent development of coherent X-ray sources including free electron lasers or high-harmonic tabletop lasers in addition to state-of-the-art synchrotron radiation, interest in coherent imaging of nanomaterials has been growing. Among these imaging techniques, X-ray Fourier transform holography (XFTH) provides unambiguous image recovery by direct Fourier inversion. A first hologram in the X-ray region was reported in 1974 by Aoki *et al*. [1]. In 2004, Eisebitt *et al*. demonstrated the magnetic worm domain imaging of a Pt/Co perpendicular magnetized film by applying an integrated holography mask and sample design at soft X-ray [2]. In the lensless Fourier transform holography, as shown in Fig. 1(a), an observed scattering intensity can be written as $I=|A+R|^2=|A|^2+|R|^2+AR^*+A^*R$, where A is the scattering amplitude from the image and R is the reference amplitude from the point source. From the interference term $AR^*(=H)$ and $A^*R(=H^*)$, the sample image can simply be recovered by a Fourier inversion of H. We tried to extend the technique to be suitable for observing nanomaterials under various conditions by using soft and hard X-rays [3].

To perform an *in situ* observation of magnetic domain at high temperature, we developed an XFTH equipment as shown in Fig. 1(b) at the soft X-ray beamline **BL25SU**. A pinhole was placed to collimate the incident X-ray beam. A charge-coupled device (CCD) was used to record the hologram. To fabricate the integrated mask sample of Pt/Co, a 1.7-μm-thick Au layer was deposited on a SiN membrane. An illumination window of 2 μm square shape and a 0.1-μm-diameter reference hole were formed by focused ion beam (FIB). The Pt/Co layer was formed on the backside of the membrane. By applying a circularly polarized X-ray at the energy of Co L_3 edge (778 eV), we succeeded in observing the change in the magnetic domain as shown in Fig. 2(a). The results demonstrate that the method can be applied to such a high temperature. While the technique has been successfully applied, a weak point of this method is a narrow field of view of approximately 2 μm size, which was determined on the basis of the transverse coherent length and the off-axis configuration to avoid image overlapping. Another weak point is the difficulty in fabricating the integrated mask-sample specimen.

To solve the problem, we developed a scanning-type XFTH where the holography mask and imaging object was separately prepared and moved in contact with each other as shown in Fig. 1(c) and 1(d). With this configuration, we can scan the sample using a high-precision stage, and the holography mask can be used for other measurements. To confirm the method, the experiments were performed at beamline BL25SU using soft X-ray, and beamline **BL16XU** (Sunbeam) using hard X-ray. A sample can be moved by a piezo-driven X–Y translation stage. The sample stage was placed in the vacuum chamber. Figure 2(b) shows the extended magnetic domain image obtained by combining the seven images measured at each position. The spatial resolution estimated from the edge impact was 42 nm. Recently, similar results

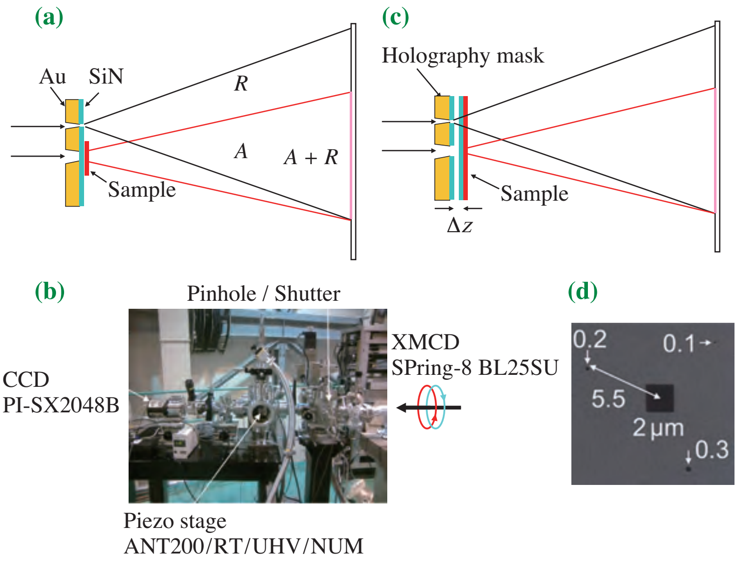

Fig. 1. **(a)** Schematic of XFTH using integrated mask-sample design. **(b)** Experimental setup of soft X-ray FTH at BL25SU. **(c)** Schematic of mask and sample separated by XFTH. **(d)** An example of holography mask.

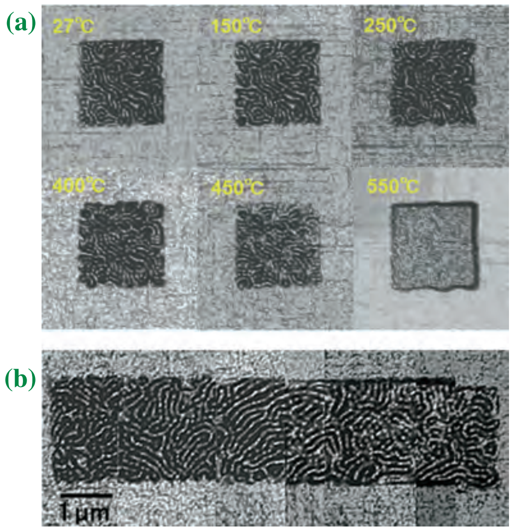

Fig. 2. **(a)** Magnetic domain pattern observed at several temperatures. The pattern changed above 400°C. **(b)** Magnetic domain in the 8 μm area, which was obtained by connecting seven recovered images measured at each position.

obtained using a circular-shaped window have been reported [4], which indicates that the method can be applicable to window of various shapes.

A hard X-ray has a high penetration power and the measurement can be performed in air ambient. XFTH experiments in the hard X-ray region have been performed at beamline BL16XU at an X-ray energy of 5500 eV. To prepare the hard X-ray holography mask, a 3.4 μm Au layer was deposited on a SiN membrane. The illumination window of 2 μm square shape and a 0.2-μm-diameter reference hole were fabricated by FIB. As a first sample, an artificial pattern of "XFEL" was milled in a Au film as shown in the upper part of Fig. 3(a). For the second sample, a cross-sectional sample of a Cu interconnect line with line and space of 0.27 μm was prepared. A detailed structure of the Cu line is shown in the upper part of Fig. 3(b). The thickness of the sample was 2 μm.

The lower part of Fig. 3(a) shows the extended image of an artificially patterned sample by combining 5 recovered images. The lower part of Fig. 3(b) shows the cross-sectional images of the Cu line. The estimated spatial resolution was 75 nm. A reason for the low resolution compared to the case of soft X-ray is the blurring due to the reference hole size of 0.2 μm, since the obtained image is a convolution of the original image and the reference hole image.

To avoid the resolution reduction in this method, we developed a deconvolution technique in which the measured hologram was divided by the estimated reference amplitude as H'=H/R*. Here, H' denotes the hologram after blurring correction. Figure 3(c) compares the original image (left) with that after the correction (right). The spatial resolution has been improved from 75 to 50 nm.

In conclusion, we applied the XFTH imaging technique for the *in situ* observation of magnetic domain pattern at high temperature. We developed a technique to extend the field of view by applying the separated mask and sample design. In addition, the problem of image blurring owing to a finite size of reference source was corrected by dividing the hologram by the estimated reference amplitude. After the treatment, the spatial resolution for hard X-ray improved from 75 to 50 nm.

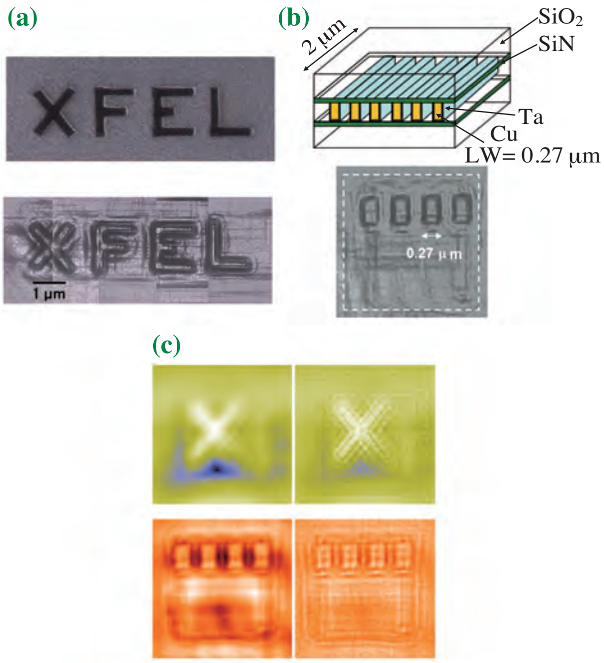

Fig. 3. **(a)** Upper is the SEM image of an artificial pattern with a width of 7 μm. Lower is a recovered image obtained by connecting five images measured at each position. **(b)** Upper is the structure of the Cu-interconnect-line sample. Lower is the recovered cross-sectional image. **(c)** Original image (left) and corrected image (right) of the artificial pattern (upper) and Cu-line sample (lower).

Naoki Awaji

Device Integration Technologies Laboratory,
Fujitsu Laboratories Ltd.

E-mail: awaji.naoki@jp.fujitsu.com

References

[1] S. Aoki and S. Kikuta: Jpn. J. Appl. Phys. **13** (1974) 1385.
[2] S. Eisebitt *et al*.: Nature **432** (2004) 885.
[3] *N. Awaji, K. Nomura, S. Doi, S. Isogami, M. Tsunoda, K. Kodama, M. Suzuki and T. Nakamura: Appl. Phys. Express* ***3*** *(2010) 085201.*
[4] D. Stickler *et al*.: Appl. Phys. Lett. **96** (2010) 042501.

Development of scanning X-ray microscope using microdiffraction

A strongly correlated electron system often exhibits various interesting physical properties such as superconductivity, dielectricity, magnetism, multiferroic, and so on. To understand these phenomena, it is important to clarify not only the configurations of charge, orbital, and spin, but also its higher order structure (such as domain structure). In order to visualize these higher order structures, a scanning X-ray microscope system using microdiffraction are installed at **BL19LXU**. Here, we report the commissioning results of the microscope system, and the observed image of the charge order domain in $LuFe_2O_4$.

In the diffraction method, the obtained signal is coming from a sample where SR X-ray is irradiated. In an ordinal SR X-ray experiment, the diffraction signal reflects bulk averaged property, because the typical beam size is several hundred μm. If a focused beam less than the size of a domain is available, we can access the property coming from the pure single domain. In addition, if the sample is scanned, we can obtain the spatial distribution of the domain in real space.

In SR X-ray diffraction method, we can probe the information of orbital and magnetic orders in addition to charge order. However, we required the high photon flux of more than 10^{10} photons/s to observe them, because the intensity ratio of a magnetic reflection to the fundamental reflection is typically 10^{-8}. We also required a spatial resolution of 100 nm to achieve a resolution smaller than that of an optical microscope. Moreover, no chromatic aberration is required to execute energy scan, which is important in resonant X-ray scattering method to enhance a weak signal and to probe an element-selective signal. From the reasons stated above, we selected Kirkpatrick-Baez (KB) mirror system as a focusing device. As for the goniometer section with sample manipulation, we built two-axes sample scanning stages perpendicular to the scattering vector on the theta stage of a two-circle goniometer. These scanning stages have a feedback control system using an internal encoder to realize 10 nm resolution.

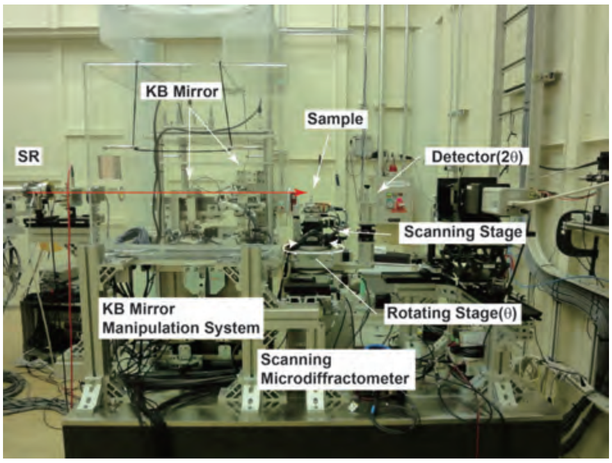

Fig. 1. KB mirror manipulation system and scanning X-ray microscope.

Figure 1 shows the photograph of the installed system. The KB mirror manipulation system is placed at the upstream side of the optical table and the goniometer follows the mirror. To increase the reduction rate of the beam size, a four-quadrant slit as the virtual light source is located 70 m upstream from the mirror, and the working distance of the mirror is designed as 100 mm. Figure 2 shows the schematic

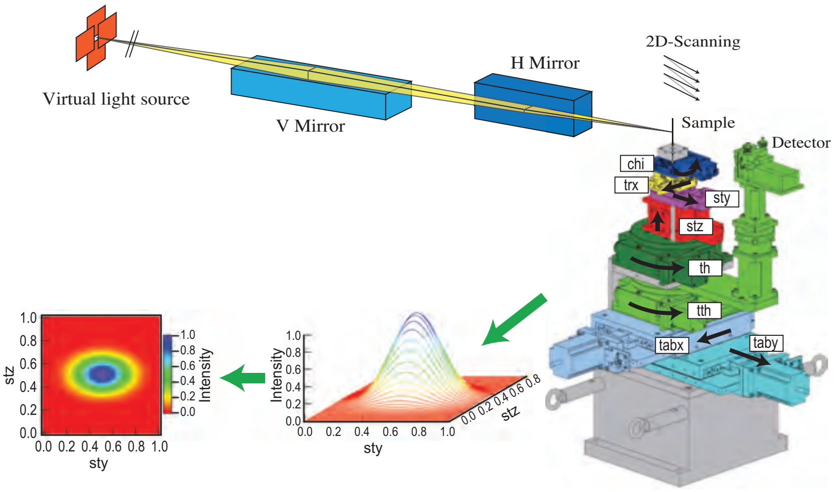

Fig. 2. Schematic of the scanning microdiffraction method.

view of this system. The goniometer consists of two translation axes for alignment of the rotation center and focal point (tabx, taby), three axes for diffraction (chi, theta, two theta), two axes for high resolution scanning (sty, stz) and one axis for sample alignment. A silicon drift detector (SDD) is adopted for energy-selective detection. To obtain a domain map, first, the three axes for diffraction are moved to the angles where a Bragg reflection can be observed. This Bragg intensity at each microregion of the sample is collected by scanning two axes (sty, stz). Then, a two-dimensional intensity map corresponding to the domain map is obtained.

As the evaluation of the KB mirror, we measured the beam profile by means of knife edge (wire) scan and photon flux of the focused beam. In this commissioning, we achieved a beam size of 100×100 nm^2 and a photon flux of 3.7×10^{10} photons/s. For the purpose of microscope evaluation, we also performed the scanning measurement of an X-ray test chart. We measured the transmitted beam intensity through the test chart in which some slit patterns are processed. As can be seen in Fig. 3, this system can be used to resolve a 100 nm structure. Furthermore, by adopting the deconvolution processing (Fig. 3), we determined that the standard deviation of the Gaussian function as a point spread function is 150 nm. It is confirmed from above results that the KB mirror system and the goniometer satisfy the performance for the observation of the higher order structures of charge, orbital and spin orders.

Finally, we show the observed charge order domain in $LuFe_2O_4$ using this system (Fig. 4). There are some superlattice reflections derived from the charge order at (1/3 1/3 *L*/2). In this observation, the goniometer axes are fixed under (1/3 1/3 37/2) reflection condition, and the sample is scanned to collect the intensity from each irradiated region. We are successful in observing some submicron domain with high resolution (the smallest size of the domain is ~300 nm).

This system will provide a new aspect to clarify interesting phenomena, such as phase coexistence or separation, and relations between domain structure and physical properties on strong correlated electron systems.

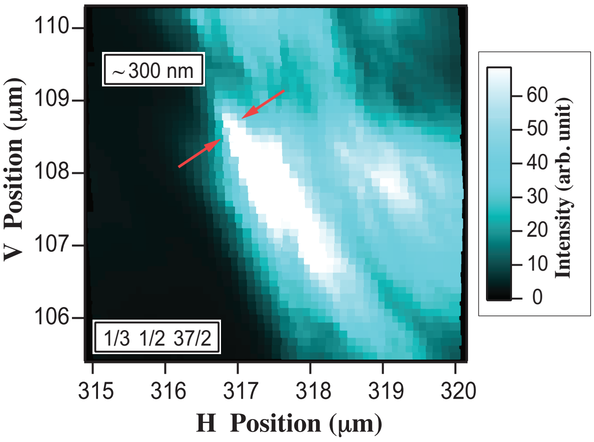

Fig. 4. Intensity map of 1/3 1/3 37/2 reflection of $LuFe_2O_4$. The distance between the arrows is approximately 300 nm.

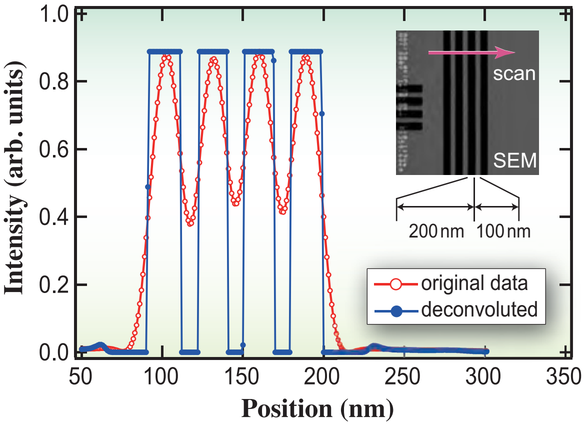

Fig. 3. Transmitted intensity profile of X-ray test chart at 200 nm line and 100 nm space. Inset shows the SEM image of the same position. The red arrow in the SEM image indicates the position of the scan.

Soshi Takeshita[a,*], Hiroyuki Ohsumi[a] and
Taka-hisa Arima[a,b]

[a] SPring-8/RIKEN
[b] Inst. of Multidisciplinary Res. for Advanced Materials,
Tohoku University

*E-mail: soshi@spring8.or.jp

Development of silicon and cadmium telluride pixel detectors

Single photon counting pixel detectors were expected to be the next-generation 2D X-ray detectors since the early stages of the third-generation synchrotron radiation facilities. SPring-8 has made X-ray photon counting measurements possible by developing the PILATUS detectors, and a cadmium telluride (CdTe) pixel detector project is ongoing for high energy X-ray applications currently. Both detectors are based on the hybrid pixel detector technology composed of a monolithic semiconductor sensor with pixelated electrodes and a custom-designed application specific integrated circuit (ASIC).

SPring-8 has closely collaborated in the PILATUS project at PSI and contributed to module fabrication and then the development of calibration methods [1-4]. Thus, two detectors of PILATUS-100K and a multi-module system of PILATUS-2M (Fig. 1) have been developed. The specifications of the standard PILATUS-100K sensor are 172 μm × 172 μm in pixel size, 195 × 487 in format, and 320 μm in silicon thickness. On the other hand, one of the PILATUS-100Ks is fabricated with a 450 μm sensor developed by SPring-8. It realizes higher sensitivity and better flatness. The other PILATUS-100K is equipped with a standard sensor, but an original cubic box is used as its housing. This design is useful for mounting the detector on complicated experimental setups.

The former applications with the PILATUS-100K at SPring-8 were an X-ray diffractometer with pulsed magnetic fields at BL19LXU and a time-resolved X-ray diffraction study of directional solidification in steels at BL46XU. These were pioneer studies applied with the PILATUS's good merits as such high frame rate capability and fast readout time in msec order. By using the high counting rate capability of up to 10^6 X-rays/sec and the 20-bit dynamic range feature, time-resolved X-ray reflectivity studies on a liquid interface were performed at BL37XU. This is 10 times faster than the conventional method with a point detector. Another unique application is the depth-resolved XAFS at BL01B1 and BL37XU, which measures grazing exit fluorescent X-rays from a sample. PILATUS-2M is used for X-ray diffractions and small angle X-ray scatterings at BL19B2 and BL46XU. In particular, an ultra-small angle X-ray scattering is measurable with about 40 m in distance from the sample to the detector at BL19B2.

The high energy X-ray beam is a powerful probe for analyzing deep inside the structure for heavy materials. The PILATUS detector is usable at such high-energy region. In fact, we have applied the PILATUS-100K detector to 70 keV X-ray diffraction experiments at BL22XU with ultra-low gain settings calibrated for high energy applications. However, its detection efficiency decreases to 30% at 20 keV and to lower than 10% above 30 keV. To improve the detection efficiency in the high-energy region, CdTe is regarded as a promising semiconductor material because of its high density and the high atomic number of its components. Therefore, we started a CdTe pixel detector project in 2008 [4-5].

The SP8-01 CdTe detector was designed as a prototype to investigate its performance for high-energy X-ray measurements. The format is 16 × 16 pixels with a pitch of 200 × 200 μm^2. The other weak point of PILATUS is the single-level comparator eliminating only lower energy X-rays than the threshold level. Therefore, a full-custom ASIC was designed as a readout circuit of SP8-01, which is equipped with a window-type discriminator. The upper discriminator realizes a low-background measurement, because X-ray beams from the monochromator contain higher-order components beside the fundamental X-rays in general.

Figure 2 shows the schematic of the SP8-01 ASIC architecture. The charge sensitive preamplifier together with a shaper converts the input charge generated in the sensor to a bandwidth-limited short pulse, with a height proportional to the energy of the incident X-ray. The content of the pseudorandom 20-bit counter is increased when the pulse falls between the lower- and higher-energy thresholds.

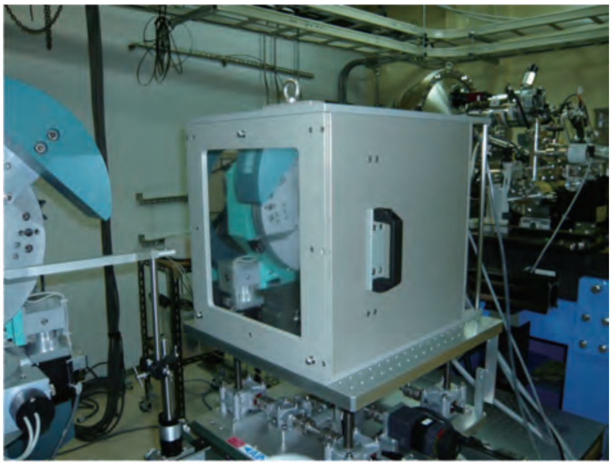

Fig. 1. X-ray diffraction experimental setup of the PILATUS-2M detector at BL46XU.

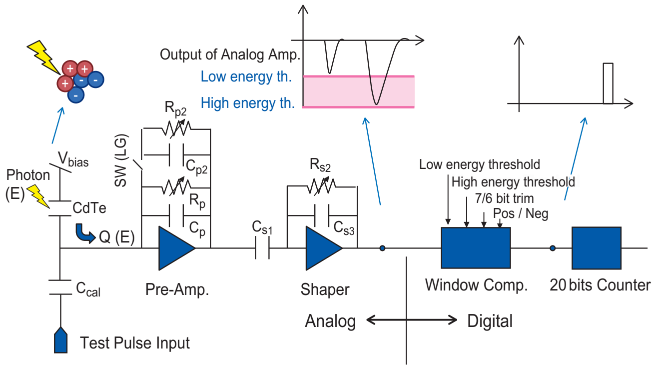

Fig. 2. Schematic of the SP8-01 ASIC architecture for CdTe pixel detector.

The preamplifier is equipped with a gain adjust switch. An additional feedback capacitor and resistor can be switched on in the low-gain mode. The designed energy ranges for the low- and high-gain modes are 15 – 40 keV and 30 – 100 keV, respectively. The parameters of the circuit were optimized to meet the requirements of dead time (less than 100 nsec) and energy linearity in the regions of interest by performing a circuit simulation with T-SPICE from Tanner Research Inc.

Figure 3 shows the SP8-01 prototype detector mounted on a ceramic package. The ASIC chips were processed with a TSMC 0.25 μm CMOS technology, and CdTe sensors were bump-bonded to the ASIC chips by a gold-stud bonding technique. The sensor thickness is 500 μm, which has an absorption efficiency of almost 100% up to 50 keV and 45% even at 100 keV.

To demonstrate the function of the window comparator, we simultaneously moved the higher- and lower-energy thresholds to maintain the difference between them. X-ray beams were attenuated with metal plates and irradiated onto the detector directly. The integral linearity for the high-gain mode was 98% in the region of 15 – 40 keV and that for the low-gain mode was 90% in the region of 30 – 100 keV.

In the next step, we proceed to the SP8-02 detector. The SP8-02 ASIC was designed as a 3-sided buttable layout with 20 × 50 pixels. The one cell architecture follows that for SP8-01. We plan to fabricate double chips and 2 × 4 chip detectors without an inter-chip gap on the sensor. The 2 × 4 chip detector will be designed as a module to build a larger-area detector.

We developed three types of CdTe sensor for SP8-01. Type 1 was designed for the electron collection operation composed of a Schottky contact with aluminum electrodes on the pixel side and a platinum electrode on the common electrode side. Type 2 is a hole collection sensor with a Schottky contact of an indium common electrode and platinum pixelated electrodes. Type 3 has ohmic contact structures on both sides with platinum electrodes. However, we could only test the type 1 sensor of SP8-01 because of bonding failures by the vendor. Therefore, we will investigate the detailed performances of these types with the SP8-02 detector.

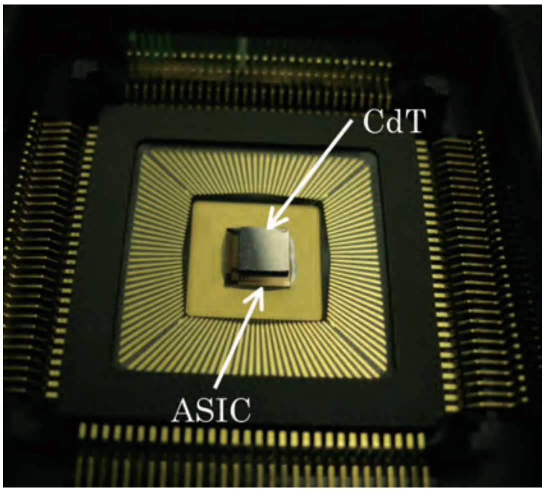

Fig. 3. SP8-01 prototype detector with CdTe sensor (200 μm × 200 μm in pixel size, 3.2 mm × 3.2 mm in detection area, and 500 μm in thickness) and ASIC (16 × 16 pixels) mounted on a ceramic package.

Hidenori Toyokawa*, Toko Hirono and Morihiro Kawase

SPring-8/JASRI

*E-mail:toyokawa@spring8.or.jp

References

[1] E.F. Eikenberry *et al.*: Nucl. Instrum. and Meth. Phys. Res. A **501** (2003) 260.
[2] Ch. Broennimann *et al.*: J. Synchrotron Rad. **13** (2006) 120.
[3] H. Toyokawa *et al.*: AIP Conf. Proc. **879** (2007) 1141.
[4] H. Toyokawa *et al.*: Nucl. Instrum. and Meth. A **623** (2010) 204.
[5] *T. Hirono, H. Toyokawa, Y. Furukawa, T. Honma, H. Ikeda, M. Kawase, T. Koganezawa, T. Ohata, M. Sato, G. Sato, M. Takagaki, T. Takahashi, S. Watanabe: Nucl. Instrum. Meth. Phys. Res. A (2011) - in press, doi:10.1016/j.nima.2010.12.207.*

Facility Status

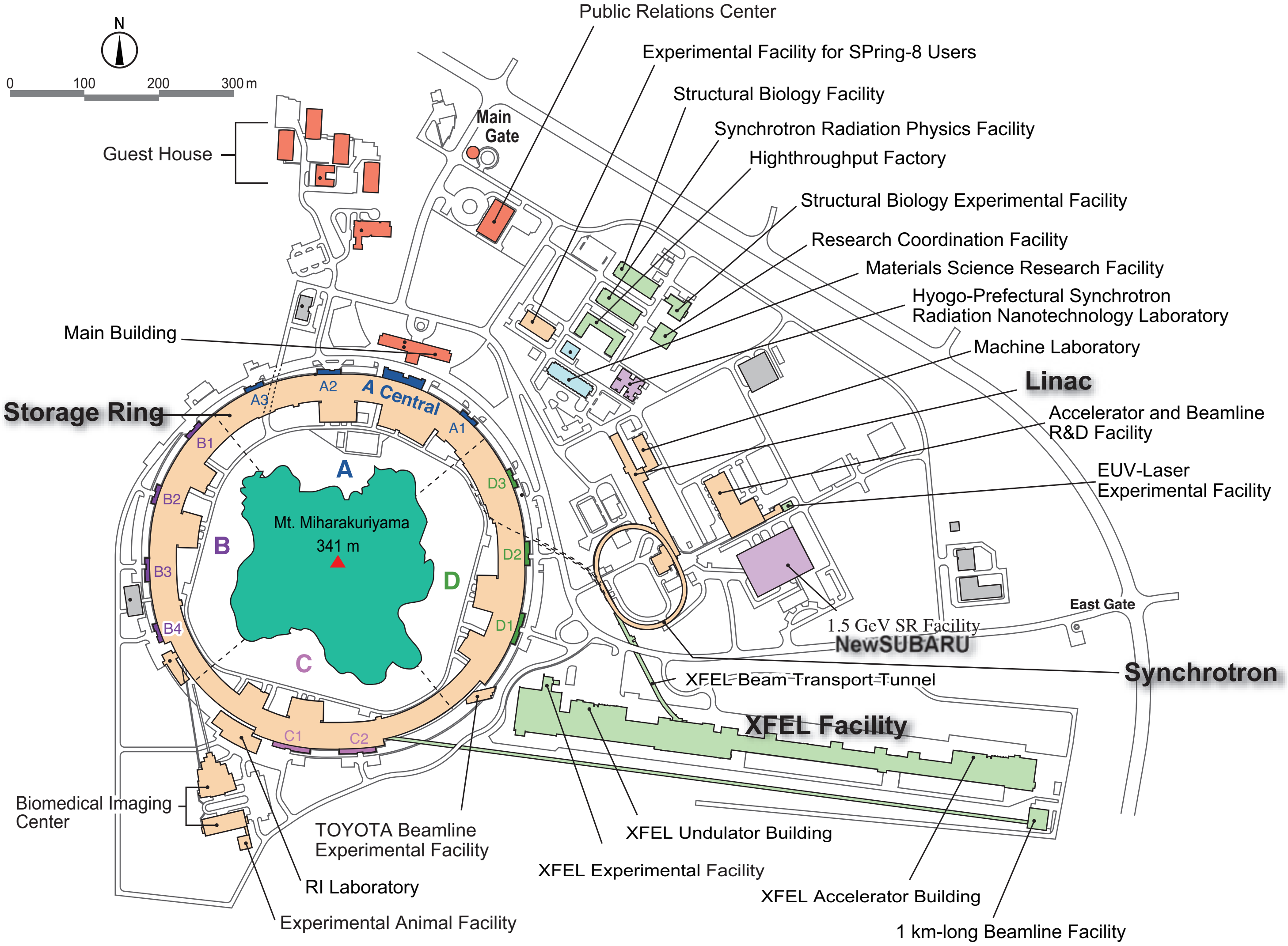

I. Introduction

As the current issue illustrates throughout, 2010 was a fruitful year for SPring-8, making steady progress as one of the most advanced third generation synchrotron radiation facilities in the world.

Among the various scientific events, most worthy of note was the successful hosting of the 12th APS-ESRF-SPring-8 Three-Way Meeting in April 2010. Since 1994, the Three-Way Meeting has been organized regularly as the collaborative activity among the three third generation synchrotron radiation facilities. This time, in addition to satellite meetings on X-ray optics and user management, the workshop program included various sessions covering facility status, upgrade plan, accelerator/light source, detector/data handling, time-resolved nanofocusing/imaging, and industrial application. It was noteworthy, in particular, that the Three-Way Meeting welcomed PETRA III as a newcomer, which just started operation in November 2009. They made presentations about their new light source and detector development. This meeting was full of future-oriented reports and discussions lively. It was concluded that the three parties would continuously expand their collaborative relationships. The next Three-Way Meeting will be held at ESRF.

Regarding the outreach work of SPring-8, one of the most challenging activities of this year was the SPring-8 special lecture entitled “Science for Cultural Heritage Illuminated with Synchrotron Light,” which was held in Nara, November 2010. Since synchrotron radiation provides a means of advanced non-destructive analysis, cultural heritage scientists have gradually begun to realize how valuable and powerful it could be for safely revealing secrets hidden in ancient artifacts and art. This special program was organized to introduce this excellent potential of synchrotron radiation to the public. It was also aimed at researchers who study archaeology and cultural properties, where synchrotron radiation analysis is highly advantageous in identifying artifacts under study. In this lecture, it was shown that the synchrotron light at SPring-8 makes it possible to identify micro-artifacts that could not be examined before and that the elemental composition of artifacts determined by advanced X-ray analysis indicates their origins and manufacturing techniques. The scientific event was successfully held with more than 300 participants. As the next step, SPring-8 will encourage potential users to utilize SPring-8 actively.

In 2010, a review committee was formed for evaluating the Medical Bio Trial Use program, which was established to invite potential users from the domain, and for evaluating the Medical Bio EX program, established to expand target research areas using the beamlines for small-angle scattering and crystal structure analysis. These programs received a high evaluation because they increased the use of synchrotron radiation by new users, especially users from overseas and from the private sector, and promoted the application of various analysis techniques to medical bio research. Although these programs were completed at the end of 2009B, it is the intention of SPring-8 to support prominent scientists continuously through research planning and data analysis, and to meet increasing expectations for research outcomes in the field of medical bio research, through which SPring-8 could substantially contribute to conquering diseases and to promoting healthier lives.

Regarding the SPring-8 beamline portfolio, there are two contract beamlines newly approved for construction in 2010. The first one is the Laser-Electron Photon II Beamline, to be constructed by the Research Center for Nuclear Physics, Osaka University. This is the second beamline dedicated to nuclear and particle physics experiments, and will realize a high-energy gamma ray beam with 10 times higher intensity than the existing one, and will be instrumented with a large-scale detector system mainly composed of a high-resolution spectrometer. The new beamline is expected to provide an ideal mean to realize a major breakthrough in quark nuclear physics including the conclusive judgment on the existence of pentaquark.

The other beamline is the Catalytic Reaction Dynamics for Fuel Cells Beamline, to be constructed by the University of Electro-Communications. During the course of realizing fuel cell automobiles, the function and lifetime of the PEFC cathode catalysts must be drastically improved. Towards this goal, the structure and electronic state of PEFC catalyst surfaces must thus be intensively investigated *in situ* during a voltage-stepping process in real time. This new beamline will be capable of providing the depth profiles measurements of XAFS as a function of time and location for samples under investigation, which is currently considered to be the only possible characterization technique. These two new beamlines will be commissioned in FY2012.

Because SPring-8 is expected to continue growing as the world's leading research facility and keeps producing cutting-edge achievements, it is essential to provide users with not only state-of-the-art instruments but also a comfortable environment to facilitate their research activities. The SPring-8 User Information website was relaunched in November 2010, to improve the convenience of online proposal and document submission by users, publication registration, and so forth. The most significant feature of the new website is "My Page," where each user can obtain information about their status regarding the procedures required and user statistics for public beamlines after logging in. It is hoped that the new website will be helpful for users to complete their paperwork much more easily.

During this year, there has been steady progress in the SPring-8 upgrade plan, called SPring-8 II. The plan is required to meet all the critical scientific and technical challenges over the next ten years so as to dramatically enhance the capabilities of SPring-8. The working group has started considering what novel values one should scientifically and technologically create through upgrading the existing SPring-8 facilities. The 2nd Symposium of the SPring-8 upgrade plan was held in Tokyo, December 2010 with the aim of figuring out the future directions of SPring-8 by updating the status of the development plan. To continue meeting the needs of the synchrotron radiation research community, the working group is intensively working on an upgrade plan that will enable users to produce outstanding research results.

II. Machine Operation

The operation statistics for the last five fiscal years are shown in Fig. 1. In FY2010, the total operation time of the accelerator complex was 5125.6 hours. The operation time of the storage ring was 5096.3 hours, of which 79.9% (4071.5 hours) was used for SR experiments. The downtime resulting from failure accounted for 0.67% (27.5 hours) of the total user time. In FY2010, no great loss of user time exceeding several hours occurred. In 2004, top-up injection was introduced. Concerning user service operation, a high availability (ratio of net user time to planned user time), i.e., 99.2%, was achieved in FY2010. A total tuning and study time of 1026.6 hours was used for machine tuning, for the study of the linac, booster synchrotron and storage ring, and also for the beamline tuning and study.

Operations in three different filling modes were provided for the following user times: 5.9% in the multi-bunch mode, 56.7% in the several bunch mode, such as the 203-bunch mode (203 equally spaced bunches), and 37.4% in the hybrid filling mode, such as the 1/14-partially filled multi-bunch mode with 12-isolated bunches. In FY2010, the several bunch mode was the dominant filling mode. In particular, the 203-bunch mode reached 30.9% of the total user time. For the hybrid filling mode, 1.0 mA, 1.4 mA, 1.6 mA, or 3.0 mA is stored in each isolated bunch. An isolated bunch impurity better than 10^{-10} is routinely maintained in the top-up operation. Table I shows a summary of the useful beam parameters of the storage ring. Table II shows a summary of the beam filling patterns.

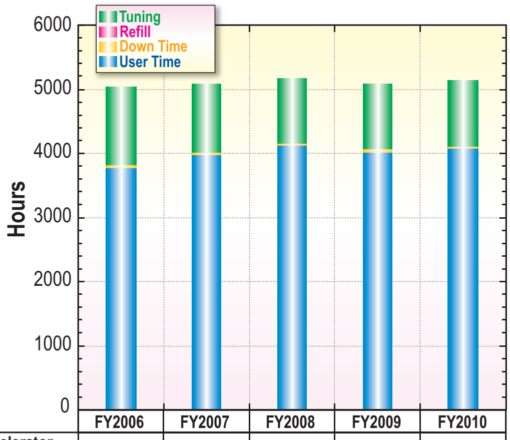

	FY2006	FY2007	FY2008	FY2009	FY2010
Accelerator Operation Time	5025.0	5063.6	5050.1	5068.8	5125.6
Storage Ring Operation Time	5012.3	5022.3	5133.3	5035.4	5096.3
Tuning & Study (Acc. & BL)	1213.8	1065.0	1008.2	1019.1	1026.6
Refill	7.6	9.5	10.1	6.3	5.0
Down Time	38.4	29.2	31.0	34.8	27.5
Mean Time Between Failures	106.0	14.4	143.2	122.9	178.4
Achieved User Time	3770.0	3969.3	4110.9	4014.9	4071.6
Planning User Time	3816.0	4008.0	4125.0	4056.0	4104.0
Availability (%)	98.8	99.0	99.0	99.0	99.2

Fig. 1. Operation statistics for last five fiscal years.

Table I. Beam parameters of SPring-8 storage ring

Energy [GeV]	8
Number of buckets	2436
Tunes (ν_x / ν_y)	40.135 / 18.345
Current [mA]:	
single bunch	12
multi bunch	100
Bunch length (σ) [psec]	13
Horizontal emittance [nm·rad]	3.4 *
Vertical emittance [pm·rad]	6.8 *
Coupling [%]	0.2
RF Voltage [MV]	16
Momentum acceptance [%]	±3 (±240 MeV)
Beam size [μm]: (σ_x / σ_y)* [μm]	
Long ID section	294 / 10
ID section	301 / 6
BM section	107 / 13
Beam divergence [μrad]: (σ_x' / σ_y')* [μrad]	
Long ID section	13 / 0.7
ID section	12 / 1.1
BM section	56 / 0.6
Operational chromaticities (ξ_x / ξ_y)	+2 / +6 **
Lifetime [h] :	
100 mA (multi-bunch)	~200
1 mA (single bunch)	~20
Horizontal dispersion [m]:	
Long ID section	0.103
ID section	0.107
BM section	0.032
Fast orbit stability (0.1 – 200 Hz) [μm]:	
horizontal (rms)	~4
vertical (rms)	~1

* Assuming 0.2% coupling for "Low Emittance Optics"
** With bunch-by-bunch feedback

Table II. Filling patterns

	bunch current (mA)	life time (h)
Multi-bunch (160 bunch-train × 12)	0.05	~ 200
203 bunches	0.5	25 ~ 30
11 bunch-train × 29	0.3	35 ~ 50
1/7 - filling + 5 single bunches	3.0 (single)	18 ~ 25
1/14 - filling + 12 single bunches	1.6 (single)	18 ~ 25
2/29 - filling + 26 single bunches	1.4 (single)	18 ~ 25

III. Beamlines

The SPring-8 storage ring can accommodate up to 62 beamlines: 34 insertion devices, 4 long undulators, and 24 bending magnets. At the time of writing, 53 beamlines were in operation, covering a wide variety of research fields of synchrotron radiation science and technology. The beamlines are classified into the following four types.

(1) Public Beamlines
(2) Contract Beamlines
(3) RIKEN Beamlines
(4) Accelerator Diagnostics Beamlines

There are now 26 public beamlines in full operation. The beamlines that have been proposed and constructed by external organizations, such as universities, research institutes, and private companies, are called contract beamlines and are exclusively used by the contractors for their own research purposes. At present, 17 contract beamlines are in operation. The contract beamlines include NSRRC BM (BL12B2) and NSRRC ID (BL12XU) beamlines, which were contracted by the National Synchrotron Radiation Research Center in Taiwan. These are the first contract beamlines installed at SPring-8 by a foreign organization. We celebrated their 10th anniversary in 2010. Currently, three contract beamlines are under construction. The beamlines constructed by RIKEN are called RIKEN beamlines and are used for RIKEN's research activities. RIKEN is now operating eight RIKEN beamlines and is constructing a new beamline called RIKEN Quantum NanoDynamics (BL43LXU). In addition, two accelerator diagnostics beamlines are in operation.

To display the beamline portfolio of SPring-8, the beamline map is shown in Fig. 2 together with the beamline classification. The research field of each beamline is presented in Table III.

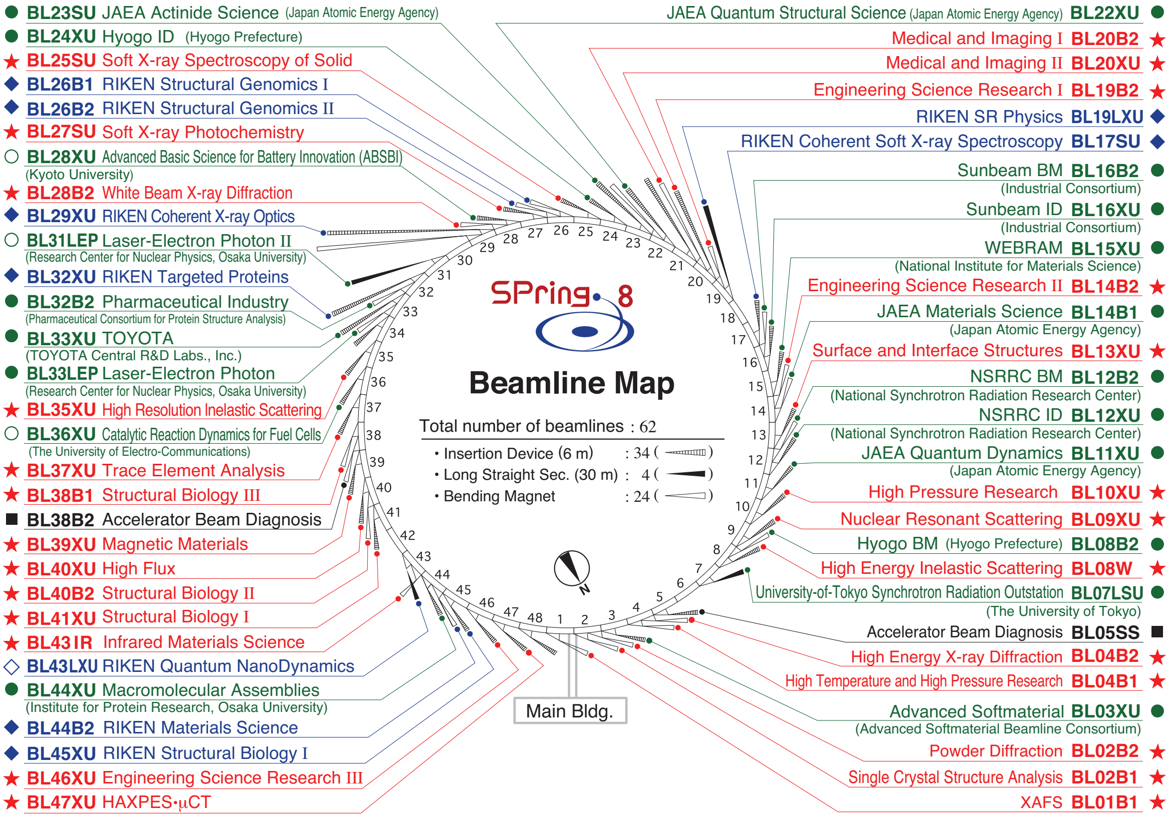

BL: Beamline
B1, B2: Bending Magnets
XU: X-ray Undulator
SU: Soft X-ray Undulator
W: Wiggler

IR: Infrared Radiation
LEP: Laser-Electron Photon
LXU: Long-length X-ray Undulator
LSU: Long-length Soft X-ray Undulator
SS: Straight Section

★ : Public Beamlines
● : Contract Beamlines
◆ : RIKEN Beamlines
■ : Accelerator Diagnostics Beamlines

○ ◇ : Planned or Under Construction

WEBRAM: Wide Energy Range Beamline for Research in Advanced Materials
NSRRC: National Synchrotron Radiation Research Center, Taiwan
HAXPES·μCT: Hard X-ray Photoelectron Spectroscopy, Micro-Tomography

Fig. 2. Beamline map.

Table III. List of beamlines

	★ Public Beamlines		
BL01B1	**XAFS**	(Oct. 1997)	XAFS in wide energy region (3.8 to 113 keV). XAFS of dilute systems and thin films. Quick XAFS with a time resolution of seconds to as tenth seconds.
BL02B1	**Single Crystal Structure Analysis**	(Oct. 1997)	Precise crystal structure analysis using high resolution data of single crystal (X-ray energy: 5 - 115 keV). Magnetic resonant X-ray scattering.
BL02B2	**Powder Diffraction**	(Sep. 1999)	Accurate structure analysis of crystalline materials using powder diffraction data by Rietveld refinements and maximum entropy method (MEM).
BL04B1	**High Temperature and High Pressure Research**	(Oct. 1997)	Mineral physics at high temperature and high pressure. Energy-dispersive X-ray diffraction and X-ray radiography using the large-volume press.
BL04B2	**High Energy X-ray Diffraction**	(Sep. 1999)	Structural analysis of glass, liquid, and amorphous materials. X-ray diffraction under ultra high-pressure.
BL08W	**High Energy Inelastic Scattering**	(Oct. 1997)	Magnetic Compton scattering. High-resolution Compton scattering. High-energy Bragg scattering. High-energy fluorescent X-ray analysis.
BL09XU	**Nuclear Resonant Scattering**	(Oct. 1997)	Lattice dynamics using nuclear inelastic scattering. Time domain Mössbauer spectroscopy, especially under the extreme conditions. Nuclear excitation by electron transition (NEET).
BL10XU	**High Pressure Research**	(Oct. 1997)	Structure analysis and phase transitions under ultra high pressure (DAC experiment). Earth and planetary science.
BL13XU	**Surface and Interface Structures**	(Sep. 2001)	Atomic-scale structural analysis of ultra-thin films, nanostructures, and surfaces of crystalline materials in air or in vacuum by combination methods of surface X-ray diffraction, microbeam diffraction, and time-resolved diffraction.
BL14B2	**Engineering Science Research II**	(Sep. 2007)	XAFS in wide energy region (3.8 to 72 keV). XAFS of dilute systems and thin films.
BL19B2	**Engineering Science Research I**	(Nov. 2001)	Residual stress measurement. Structural analysis of thin film, surface, interface. Powder diffraction. X-ray imaging, X-ray topography. Ultra-small angle X-ray scattering.
BL20XU	**Medical and Imaging II**	(Sep. 2001)	Microimaging. Hard X-ray microbeam/scanning microscopy, imaging microscopy, microtomography, phase-contrast microtomography with Bonse-Hart interferometer, X-ray holography, coherent X-ray optics, and other experiments on X-ray optics and developments of optical elements. Medical application. Microangiography, refraction-enhanced imaging, radiation therapy, phase-contrast CT using interferometer. Ultra-small angle scattering.
BL20B2	**Medical and Imaging I**	(Sep. 1999)	Microimaging: microtomography, phase-contrast microtomography with Bonse-Hart interferometer and grating interferometer for biological specimen and other kinds of specimen. Evaluation and development of various kinds of optical elements for novel imaging techniques. Large field X-ray topography.
BL25SU	**Soft X-ray Spectroscopy of Solid**	(Apr. 1998)	Observation of electronic structures by photoemission spectroscopy (PES). Observation of electronic band structures by angle resolved photoemission spectroscopy (ARPES). Magnetic state study by magnetic circular dichroism (MCD) of soft X-ray absorption. Element-specific magnetization curve measurements by MCD analysis of atomic arrangements by photoelectron diffraction (PED). Observation of magnetic domains by photoelectron emission microscope (PEEM).
BL27SU	**Soft X-ray Photochemistry**	(May 1998)	Industrial research of functional material. Atomic and molecular spectroscopy by high resolution electron spectroscopy. Surface analysis and solid state physics.
BL28B2	**White Beam X-ray Diffraction**	(Sep. 1999)	White X-ray diffraction and topography. Time-resolved energy-dispersive XAFS (DXAFS) for studies of chemical and/or physical reaction process. Biomedical imaging and radiation biology studies.
BL35XU	**High Resolution Inelastic Scattering**	(Sep. 2001)	Material dynamics on ~meV energy scales using inelastic X-ray scattering (IXS) and nuclear resonant scattering (NRS).
BL37XU	**Trace Element Analysis**	(Nov. 2002)	X-ray microbeam spectrochemical analysis. Ultra trace element analysis. High energy X-ray fluorescence analysis.
BL38B1	**Structural Biology III**	(Oct. 2000)	Structural biology. Macromolecular crystallography. Automatic data collection.
BL39XU	**Magnetic Materials**	(Oct. 1997)	X-ray magnetic circular dichroism (XMCD) spectroscopy and element-specific magnetometry under multiple-extreme conditions. Micro-XMCD. X-ray emission spectroscopy. Resonant X-ray magnetic scattering.
BL40XU	**High Flux**	(Apr. 2000)	Time-resolved diffraction and scattering experiments. Microbeam X-ray diffraction experiments. Quick XAFS.
BL40B2	**Structural Biology II**	(Sep. 1999)	Noncrystalline small and wide angle X-ray scattering.
BL41XU	**Structural Biology I**	(Oct. 1997)	Structural biology. Macromolecular crystallography. Ultra-high resolution structural analysis.
BL43IR	**Infrared Materials Science**	(Apr. 2000)	Infrared microspectroscopy. Magneto-optical spectroscopy.
BL46XU	**Engineering Science Research III**	(Nov. 2000)	Structural characterization of thin films by X-ray diffraction and X-ray reflectivity measurement. Residual stress measurement. Time resolved X-ray diffraction measurement. Hard X-ray photoemission spectroscopy.
BL47XU	**HAXPES·μCT**	(Oct. 1997)	Hard X-ray photoelectron spectroscopy. Projection type microtomography. Imaging type microtomography. Hard X-ray microbeam/scanning microscopy.

	● Contract Beamlines		
BL03XU	**Advanced Softmaterial** (Advanced Softmaterial Beamline Consortium)	(Nov. 2009)	Structural characterization of softmaterials using small- and wide-angle X-ray scattering. Grazing-incidence small- and wide-angle X-ray scattering for thin films. X-ray diffraction and reflectivity measurements for softmaterials.
BL07LSU	**University-of-Tokyo Synchrotron Radiation Outstation** (The University of Tokyo)	(Oct.2009)	Time-resolved soft X-ray spectroscopy, nano-beam photoemission spectroscopy, ultra high-resolution soft X-ray emission spectroscopy, and any methods requiring the highly brilliant soft X-ray beam.
BL08B2	**Hyogo BM** (Hyogo Prefecture)	(Jun. 2005)	XAFS in a wide energy region. Small angle X-ray scattering for structural analyses of polymer and nanocomposite materials. X-ray topography. Imaging. Powder diffraction with a high angular-resolution.
BL24XU	**Hyogo ID** (Hyogo Prefecture)	(May. 1998)	Surface/interface analysis by fluorescent X-ray analysis, strain measurements and grazing incidence X-ray diffraction. Microbeam formation studies for materials and life sciences. Micro-SAXS for local long-range structure analysis.
BL12XU	**NSRRC ID** (National Synchrotron Rad. Res. Center, Taiwan)	(Dec. 2001)	High resolution non-resonant or resonant inelastic X-ray scattering. High resolution near-edge X-ray Raman scattering. Phase transitions under high-pressure, low and high temperatures. High-resolution X-ray absorption and emission spectroscopy. X-ray physics and optics.
BL12B2	**NSRRC BM** (National Synchrotron Rad. Res. Center, Taiwan)	(Oct. 2000)	X-ray absorption spectroscopy. Powder X-ray diffraction. High resolution X-ray scattering. Protein crystallography.
BL15XU	**WEBRAM** (National Institute for Materials Science)	(Jan. 2000)	Hard X-ray photoelectron spectroscopy. Highly precise X-ray powder diffraction.
BL16XU	**Sunbeam ID** (Industrial Consortium)	(Oct. 1998)	Characterization of semiconductor materials, secondary batteries, fuel cells, catalysts, electrical display related materials, and structural materials by X-ray diffraction, X-ray microbeam based evaluation technique (including X-ray magnetic circular dichroism), and fluorescence X-ray analysis.
BL16B2	**Sunbeam BM** (Industrial Consortium)	(Oct. 1998)	Characterization of secondary battery related materials, semiconductors, fuel cells, catalysts, and several industrial materials by X-ray absorption fine structure measurements, X-ray diffraction (including X-ray reflectivity technique) and X-ray topography.
BL32B2	**Pharmaceutical Industry** (Pharmaceutical Consortium for Protein Structure Analysis)	(Apr. 2002)	Protein structure analysis for structure-based drug design: Design and optimization of new leading compounds based on pharmacodynamic action mechanism elucidated at the molecular level which obtained from a detailed interaction analysis of receptor-drug complexes.
BL33XU	**TOYOTA** (TOYOTA Central R&D Labs., Inc.)	(Apr. 2009)	Time-resolved XAFS. Characterization of industrial materials, such as catalysts, secondary batteries, fuel cells.
BL33LEP	**Laser-Electron Photon** (RCNP, Osaka University)	(Jun. 1999)	Meson photoproduction from nucleon and nucleus. Photoexcitation of hyperons, nucleon resonances, and other exotic states. Photonuclear reactions. Beam diagnoses. Test and calibration of detectors with GeV photon beam.
BL44XU	**Macromolecular Assemblies** (IPR, Osaka University)	(May 1999)	Crystal structure analysis of biological macromolecular assemblies (e.g. membrane complexes, protein complexes, protein-nucleic acid complexes, and viruses).
BL11XU	**JAEA Quantum Dynamics**	(Oct. 1998)	Nuclear scattering. Surface and interface structure analysis with MBE. Inelastic X-ray scattering. XAFS.
BL14B1	**JAEA Materials Science**	(Dec. 1997)	Materials science under high-temperature. *In situ* study on catalysis using dispersive XAFS. X-ray diffraction for structure physics.
BL22XU	**JAEA Quantum Structural Science**	(May 2002)	Materials science under high-pressure. Resonant X-ray scattering. Speckle scattering. Residual stress/strain distribution analysis.
BL23SU	**JAEA Actinide Science**	(Feb. 1998)	Surface chemistry with supersonic molecular beam. Biophysical spectroscopy. Photoelectron spectroscopy. Magnetic circular dichroism.
	◆ RIKEN Beamlines		
BL17SU	**RIKEN Coherent Soft X-ray Spectroscopy**	(Sep. 2003)	High resolution photoemission spectroscopy. Soft X-ray emission spectroscopy for liquid and biological samples. Soft X-ray diffraction spectroscopy. Surface science.
BL19LXU	**RIKEN SR Physics**	(Oct. 2000)	SR science with highly brilliant X-ray beam.
BL26B1	**RIKEN Structural Genomics I**	(Apr. 2002)	Structural genomics research based on single crystal X-ray diffraction.
BL26B2	**RIKEN Structural Genomics II**	(Apr. 2002)	Structural genomics research based on single crystal X-ray diffraction.
BL29XU	**RIKEN Coherent X-ray Optics**	(Dec. 1998)	X-ray optics, especially coherent X-ray optics.
BL32XU	**RIKEN Targeted Proteins**	(Oct. 2009)	Protein micro-crystallography.
BL44B2	**RIKEN Materials Science**	(Feb. 1998)	Structural materials science research using powder X-ray diffraction.
BL45XU	**RIKEN Structural Biology I**	(Jul. 1997)	Time-resolved and static structures of non-crystalline biological materials using small-angle scattering and diffraction techniques.
	■ Accelerator Diagnostics Beamlines		
BL05SS	**Accelerator Beam Diagnosis**	(Mar. 2004)	Accelerator beam diagnosis. R&D of accelerator components.
BL38B2	**Accelerator Beam Diagnosis**	(Sep. 1999)	Accelerator beam diagnosis. R&D of accelerator components.

IV. User Program and Statistics

IV-1. Program Overview

JASRI calls for public use proposals twice a year. The submitted proposals are reviewed by the Proposal Review Committee (PRC). As for General Proposals, 429 proposals out of 680 submitted proposals were approved in the research term 2009B, and 426 out of 593 proposals were approved in 2010A. Since the start of the Long-term Program in 2000B, 30 Long-term Proposals have been implemented, 11 and 10 proposals were carried out in 2009B and 2010A, respectively, which include 5 and 1 proposals newly approved. As for Priority Field Proposals, Nanotechnology Support Proposals, Industrial Application Proposals, Medical Bio Trial Use Proposals and Medical Bio EX Proposals were called for in 2009B, 175 proposals out of 278 submitted proposals were approved. Medical Bio Program was completed by 2009B, in the remaining two fields, 151 proposals out of 218 submitted proposals were approved in 2010A. The proposal statistics are shown in Table IV for the period from 1997B to 2010A; Power User Proposals and JASRI Proposals are excluded. During the period from 2003B to 2010A, 18 user groups were designated as Power User groups (PUs), which include 7 PUs active in 2010A. To date, a total of 3,393 shifts have been used by PUs, of which 630 shifts were spent from 2009B to 2010A.

SPring-8 provided 2,087 hours of user beamtime in 2009B and 1,977 hours in 2010A. Since the start of operation in 1997, SPring-8 has succeeded in providing users with a total beamtime of 48,989 hours. In 2009B, 997 experiments were conducted by 6,937 users at public and contract beamlines, and 978 experiments by 6,812 users in 2010A. From the start of operation in 1997 to 2010A, a total of 17,322 experiments were conducted by 117,035 users.

The beamtime available to the users, the number of experiments conducted, and the number of user visits at the public and contract beamlines are summarized in Table V and in Fig. 3.

Figure 4 shows the breakdown of the approved proposals sorted by user affiliation and of the number of experiments conducted at the public and contract beamlines from 1997B to 2010A. The percentages of experiments conducted by users from abroad were 5.0% in 2009B and 7.4% in 2010A.

Since SPring-8 is a public facility widely open not only to academic but also to industrial sectors, JASRI established the Industrial Application Division in 2005. The division's coordinators specializing in the fields of SR industrial applications are available for consultation with new users. Currently, Industrial Application Proposals account for approximately 20% of the total number of proposals conducted at the public beamlines. From 2007B, SPring-8 has introduced the Measurement Service, in which the personnel of the Industrial Application Division can carry out XAFS measurements on behalf of users at BL14B2. SPring-8 has also launched Mail-in Protein Crystallography Data Collection at BL38B1 and Powder X-ray Diffraction at BL19B2 since 2009B.

Table IV. Numbers of submitted proposals and approved proposals by research term

Research Term	Beamtime (shifts)	Deadline	Submitted proposals	Approved proposals
1997B: 1997.10 - 1998.03	168	1997.1.10	198	134
1998A: 1998.04 - 1998.10	204	1998.1.6	305	229
1999A: 1998.11 - 1999.06	250	1998.7.12	392	258
1999B: 1999.09 - 1999.12	140	1999.6.19	431	246
2000A: 2000.02 - 2000.06	204	1999.10.16	424	326
2000B: 2000.10 - 2001.01	156	2000.6.17	582	380
2001A: 2001.02 - 2001.06	238	2000.10.21	502	409
2001B: 2001.09 - 2002.02	190	2001.5.26	619	457
2002A: 2002.02 - 2002.07	226	2001.10.27	643	520
2002B: 2002.09 - 2003.02	190	2002.6.3	751	472
2003A: 2003.02 - 2003.07	228	2002.10.28	733	563
2003B: 2003.09 - 2004.02	202	2003.6.16	938	621
2004A: 2004.02 - 2004.07	211	2003.11.4	772	595
2004B: 2004.09 - 2004.12	203	2004.6.9	886	562
2005A: 2005.04 - 2005.08	188	2005.1.5	878	547
2005B: 2005.09 - 2005.12	182	2005.6.7	973	624
2006A: 2006.03 - 2006.07	220	2005.11.15	916	699
2006B: 2006.09 - 2006.12	159	2006.5.25	867	555
2007A: 2007.03 - 2007.07	246	2006.11.16	1099	761
2007B: 2007.09 - 2008.02	216	2007.6.7	1007	721
2008A: 2008.04 - 2008.07	225	2007.12.13	1009	749
2008B: 2008.10 - 2009.03	189	2008.6.26	1163	659
2009A: 2009.04 - 2009.07	195	2008.12.11	979	654
2009B: 2009.10 - 2010.02	210	2009.6.25	1076	709
2010A: 2010.04 - 2010.07	201	2009.12.17	919	665

Notes
1997B-2006B: The number of proposals are indicated as of submission deadline.
After 2007A: The total number of proposals are indicated.
The number of long-term proposals are counted by beamline, that is, if the project leader uses two beamlines, it is counted as two proposals.

Table V. Numbers of experiments and users at public and contract beamlines (by research term)

Research Term	User time (hours)	Public BL		Contract BL	
		Experiments	Users	Experiments	Users
1997B: 1997.10 - 1998.03	1,286	94	681	–	–
1998A: 1998.04 - 1998.10	1,702	234	1,252	7	–
1999A: 1998.11 - 1999.06	2,585	274	1,542	33	467
1999B: 1999.09 - 1999.12	1,371	242	1,631	65	427
2000A: 2000.02 - 2000.06	2,051	365	2,486	100	794
2000B: 2000.10 - 2001.01	1,522	383	2,370	88	620
2001A: 2001.02 - 2001.06	2,313	474	2,915	102	766
2001B: 2001.09 - 2002.02	1,867	488	3,277	114	977
2002A: 2002.02 - 2002.07	2,093	545	3,246	110	1,043
2002B: 2002.09 - 2003.02	1,867	540	3,508	142	1,046
2003A: 2003.02 - 2003.07	2,246	634	3,777	164	1,347
2003B: 2003.09 - 2004.02	1,844	549	3,428	154	1,264
2004A: 2004.02 - 2004.07	2,095	569	3,756	161	1,269
2004B: 2004.09 - 2004.12	1,971	555	3,546	146	1,154
2005A: 2005.04 - 2005.08	1,880	560	3,741	146	1,185
2005B: 2005.09 - 2005.12	1,818	620	4,032	187	1,379
2006A: 2006.03 - 2006.07	2,202	724	4,809	226	1,831
2006B: 2006.09 - 2006.12	1,587	550	3,513	199	1,487
2007A: 2007.03 - 2007.07	2,448	781	4,999	260	2,282
2007B: 2007.09 - 2008.02	2,140	739	4,814	226	1,938
2008A: 2008.04 - 2008.07	2,231	769	4,840	232	1,891
2008B: 2008.10 - 2009.03	1,879	672	4,325	217	1,630
2009A: 2009.04 - 2009.07	1,927	669	4,240	238	1,761
2009B: 2009.10 - 2010.02	2,087	722	4,793	275	2,144
2010A: 2010.04 - 2010.07	1,977	685	4,329	293	2,483
	48,989	13,437	85,850	3,885	31,185

Notes
The number of long-term proposals are counted by beamline, that is, if two beamlines were used for one experiment, those are counted as two experiments.

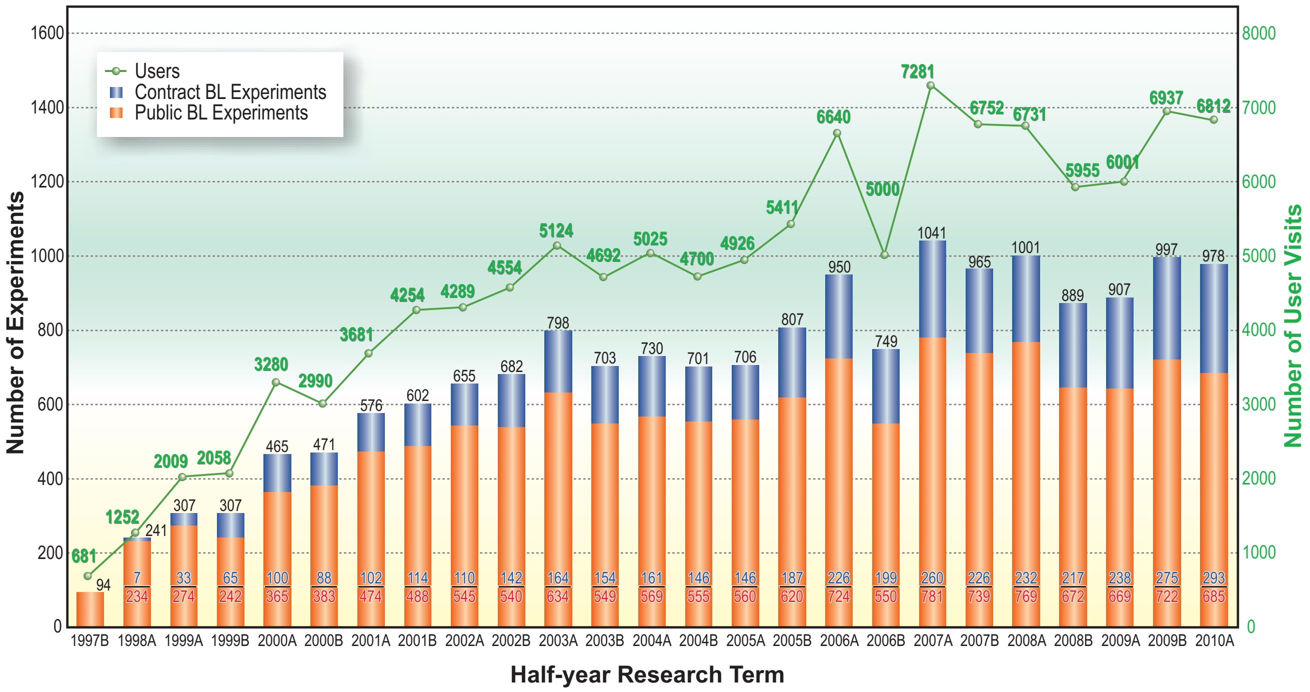

Fig. 3. Numbers of user visits and conducted experiments.

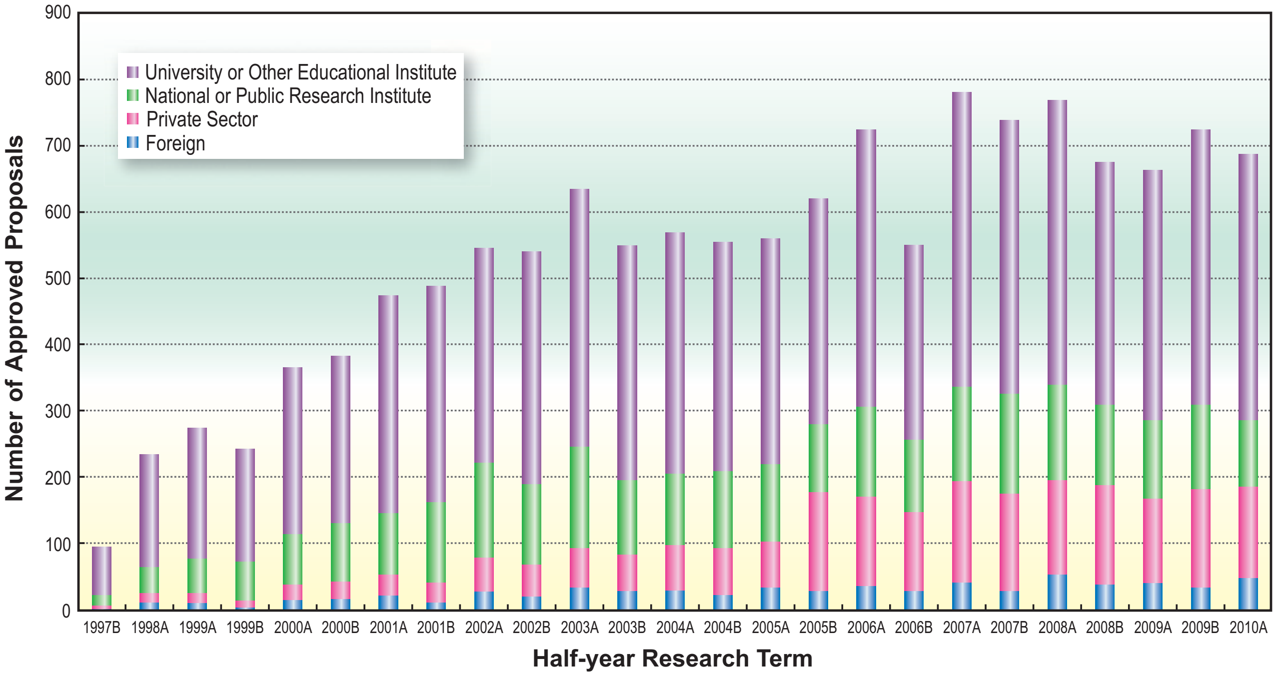

Fig. 4. Number of approved proposals by affiliation of applicants (public beamlines).

IV-2. Types of Research

(Proprietary Research and Non-Proprietary Research)

With respect to the handling of research results obtained by using SPring-8, there are two types of research at SPring-8, namely, proprietary research and non-proprietary research. For research to be considered non-proprietary, users must submit a SPring-8 Experiment Report within 60 days of the completion of each experiment to make the results available to the public. Users can use beamtime free of charge if their research is non-proprietary. As for proprietary research, research proposals are reviewed only from the viewpoint of feasibility, safety, sociality, and ethics. In this type of research, users are charged a beamtime fee of 480,000 yen/shift based on cost recovery for SPring-8 beamline operation. In return, SPring-8 Experiment Reports need not be submitted.

IV-3. Types of Proposals

A. General Research Program

(i) General Proposal

JASRI calls for General Proposals twice a year. Approved proposals are valid for six months. Up to 10% of the total beamtime is allocated to proprietary proposals.

(ii) Long-term Proposal

Three-year beam access is available for Long-term Proposals for three years in order to promote research expected (a) to produce outstanding results in the field of science and technology, (b) to establish a new research field or experimental method, and (c) to significantly improve industrial base technology by fully utilizing the characteristics of SPring-8. The call for Long-term Proposals and the review process take place twice a year prior to those for General Proposals. For this type of proposal, proprietary research is not available. The review process consists of two steps: application forms are reviewed initially and applicants who meet certain criteria will proceed to the interview.

(iii) Urgent Proposal

This system is designed for users with urgent needs to conduct experiments of great scientific significance. The PRC reviews submitted proposals on a rolling basis and promptly determines whether to approve or reject each proposals.

(iv) Budding Researchers Support Proposal

The Budding Researchers Support Program is intended to encourage doctoral students with an exploratory and original research proposal or research theme that is expected to contribute to the development of synchrotron radiation research. Under this program, successful applicants will be provided with domestic travel and lodging expenses. At the time of the experiment at SPring-8, applicants must be doctoral students who show initiative, can work independently, and are self-reliant when conducting research at SPring-8. All applicants are required to obtain permission to apply from their Ph.D. adviser, who must be included as a project team member.

(v) Non-proprietary Grant-aided Proposal

The Non-proprietary Grant-aided Program is intended for research proposals that have been reviewed and approved for a research grant available in Japan. Under this program, proposals are exempt from a scientific review process, and only the feasibility and safety of the experiment are considered. These proposals are given priority consideration for up to 20% of the user beamtime available at each beamline. Users are required to pay a program fee of 131,000 yen/shift.

(vi) Time-designated Proposal

The time-designated use is intended for users wishing to conduct proprietary research in a particular time period. The submitted proposals are promptly reviewed through a simplified process. Users are charged a beamtime fee of 720,000 yen/shift for proprietary use (incl. 50% premium).

(vii) SPring-8 Measurement Service

The staff of JASRI perform measurements on behalf of users, and users can choose whether to come to SPring-8 and be present during the measurements or to simply send their samples to SPring-8. The service is intended to provide convenience for companies and research institutes that find it difficult to retain specialized staff and, to accommodate the need for quick access. Application for the service is considered a proprietary proposal and is subject to the proprietary beamtime and user fees applicable to Time-designated Proposals (calculated in two-hour increments).

B. Priority Research Program

The Priority Research Program is categorized into the following two types: the priority field type and the priority user type. For the priority field type, JASRI designates research fields of strategic importance. For the priority user type, eligible candidates, who are highly familiar with the public beamlines and their methodological approaches, and who are expected to deepen the academic fields of SR science and technology, are designated as power users. JASRI has been providing active support for this program to produce a number of high-quality results.

B-1) Priority Field Type

Currently, the following two types of research are designated under the priority field type:

(i) Nanotechnology Support Proposal
(Period of designation: FY2007-FY2011)

On the basis of the achievements gained through the Nanotechnology Support Project (a national project from FY2002 to FY2006), the research field of nanotechnology and nanomaterials has been designated as the priority field. The purpose of this system is to support research in the field of nanotechnology and nanomaterials for innovation creation in 5-10 years time.

(ii) Industrial Application Proposal
(Period of designation: FY2007-FY2011)

This field is aimed at promoting the expansion of industrial application fields by attracting new users, developing a basic technology through the industry-academia-government collaboration, and promoting projects whose achievements are expected to contribute to companies and society. JASRI provides intensive support in the categories of “new users,” “new area,” “industrial base consortium,” and “advanced technology development.” To meet the needs of industrial users, JASRI calls for Industrial Application Proposals four times a year for the three public beamlines (BL14B2, BL19B2 and BL46XU) dedicated to industrial applications.

B-2) Priority User Type

(i) Power User Proposal

Power User Proposals are non-proprietary proposals designed for designated power user groups (PUs) to produce outstanding results in the field of pioneering use of SR using up to 20% of the beamtime allocated to beamlines accepting PUs. The power user designation period is five years. PUs are subject to an interim review of research achievements, equipment development, and user support by the Power User Review Committee at the end of the third year to determine whether to continue or discontinue the power user status. When the designation period is completed, a post implementation review is conducted by the Committee. JASRI invites applications for power user positions once a year, which takes place before the proposal calls for research term A.

IV-4. Beamtime Allocation

The beamtime allocation at public beamlines is arranged in such that more than 50% of the total beamtime is allocated to public use proposals (proposals that are submitted in response to the open calls for proposals and approved by the PRC), while up to 20% is allocated to JASRI's own research proposals. The remaining beamtime is used for seminars, trainings, setup/removal and adjustment of equipment for user experiments, and proposals with special needs and requirements (Urgent, Time-designated, and Power User Proposals). The conceptual scheme of the beamtime allocation at the public beamlines is shown in Fig. 5.

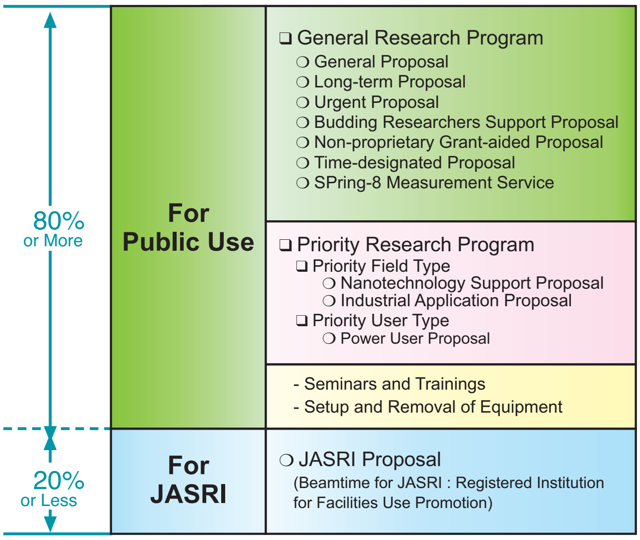

Fig. 5. Conceptual scheme of beamtime allocation at public beamlines.

IV-5. Research Outcome

When users conduct non-proprietary experiments, they are required to submit a SPring-8 Experiment Report to JASRI within 60 days of the completion of their experiments. When the research results obtained through the use of SPring-8 are published in academic journals and other publications, the project leaders are requested to report to JASRI. As of March 2011, the number of registered refereed papers is 6,151, out of which 4,906 papers resulted from the use of public beamlines, 1,061 papers from that of contract beamlines, 800 papers from that of RIKEN beamlines, and 393 papers from hardware/software R&D. The papers resulting from the use of two or more beamlines are counted at each beamline. Figure 6 shows the annual statistics of refereed papers.

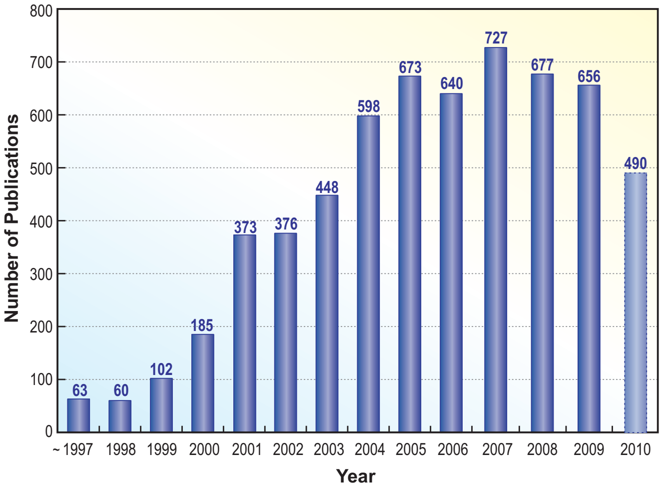

Fig. 6. Number of refereed publications as of March 2011.

V. Budget and Personnel

Since the start of operation in 1997, SPring-8 had been jointly managed by RIKEN, JAERI (JAEA, as it is known today), and JASRI. Since JAERI withdrew from the management of SPring-8 on September 30, 2005, SPring-8 has been administered by RIKEN and JASRI in a collaborative manner.

Figure 7 shows the annual budget allocated to the operation, maintenance, and promotion of the use of SPring-8 from FY1997 to date. The budget for FY2010 was 8.49 billion yen. The total number of staff members of JASRI, RIKEN and XFEL Project is 1,365 as of October 2010, as shown in Fig. 8.

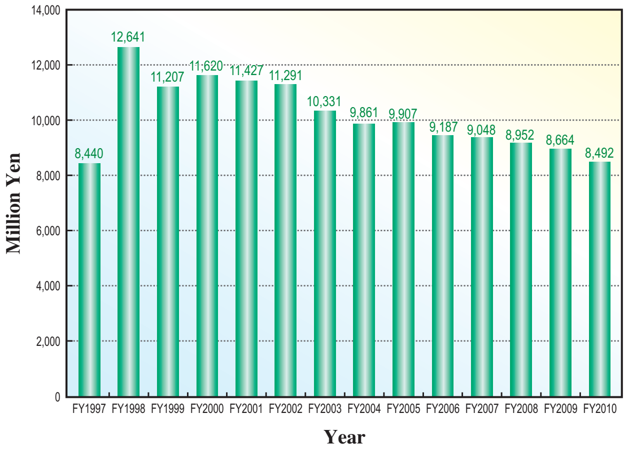

Fig. 7. SPring-8 budget.

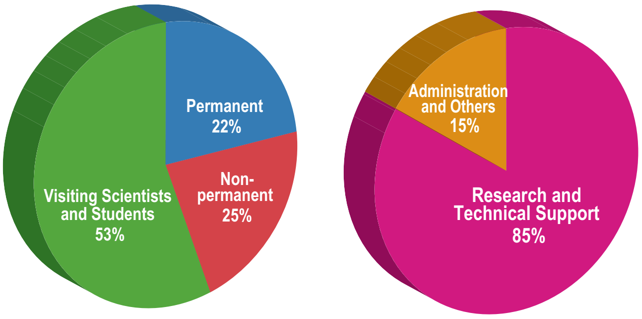

	by Type			by Field	
	Permanent	Non-permanent	Visiting Scientists and Students	Research and Technical Support	Administration and Others
JASRI	243	155	126	375	149
RIKEN	55	129	500	634	50
XFEL	1	53	103	149	8

Including double counts.

Fig. 8. Personnel at SPring-8: JASRI, RIKEN and XFEL (FY2010).

VI. Research Complex

The facilities of SPring-8, XFEL and NewSUBARU form a center of excellence at the SPring-8 campus, where JASRI, public beamline users, contractors of contract beamlines, RIKEN, and the University of Hyogo work in close cooperation to form a research complex by playing their own roles to deliver high-quality results in the field of synchrotron radiation science and technology. Figure 9 shows the SPring-8 research complex and the operation and management of each research facility. The organizational charts of RIKEN and JASRI, which form the kernel of this research complex, are shown in Fig. 10 and Fig. 11, respectively.

Fig. 9. SPring-8 research complex.

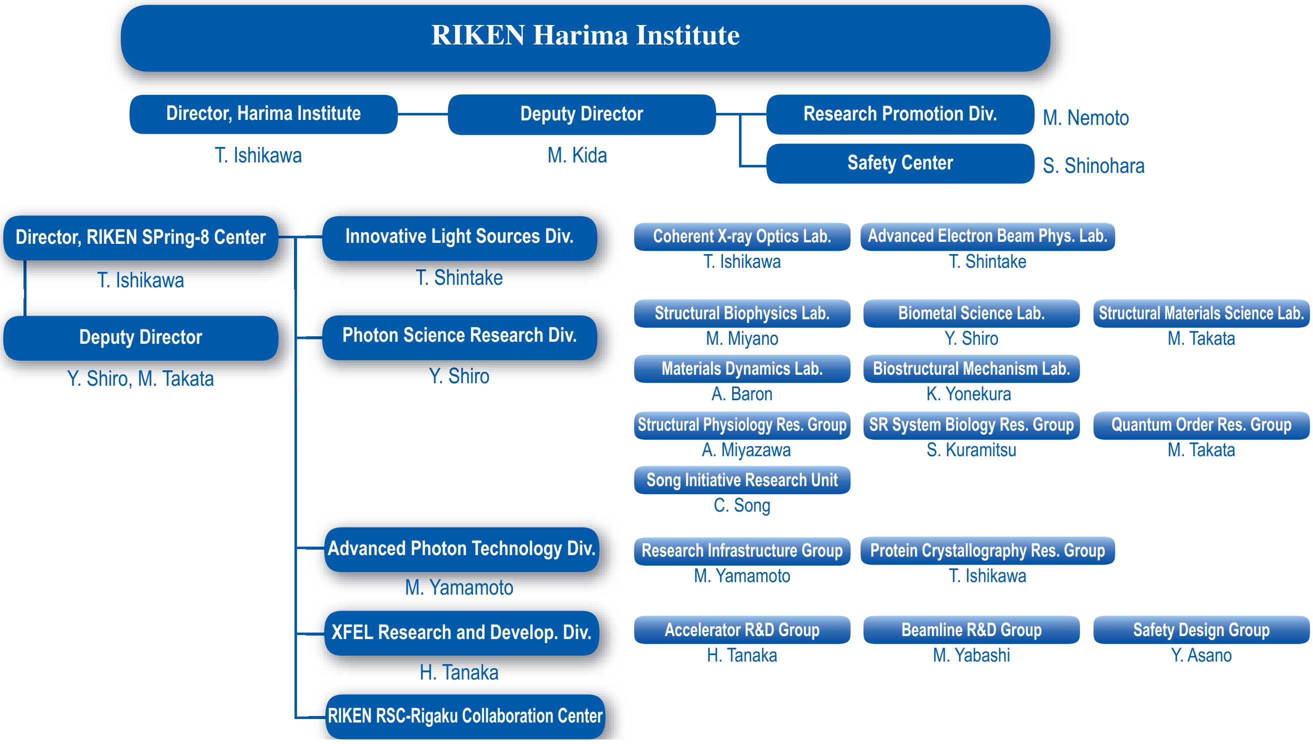

Fig. 10. RIKEN Harima chart as of April 2011.

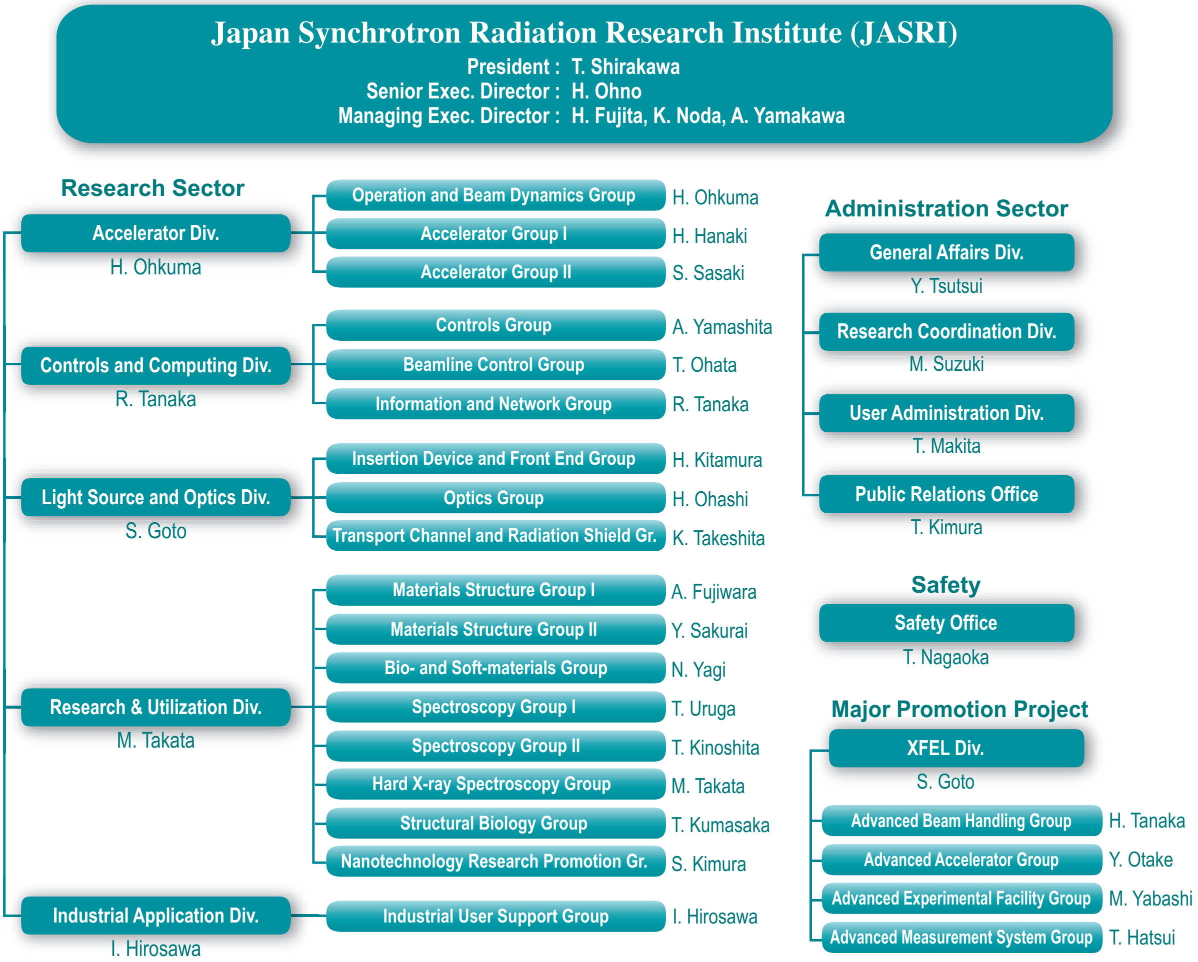

Fig. 11. JASRI chart as of April 2011.

VII. Users Societies, Conferences and Other Activities

Users Society

In May 1988, the User Group for Advanced X-ray Source was organized by potential users, aiming at discussing the research plan and user policy. On the basis of the achievements of this group, the **SPring-8 Users Society** was established in May 1993 to promote and advance the research activities of users, and it made a substantial contribution to the construction of SPring-8. The current goal is to support the upgrade of the storage ring and individual beamlines, and to promote the utilization of SPring-8. As of March 2011, 28 scientific research groups and nine committees of the Society are actively contributing to developing research activities and in information exchange between staffs members and users. The development of synchrotron radiation science for the next ten years has been discussed by these research groups, and the report entitled "Future Prospects for Scientific Activities at SPring-8" was published in March 2009. The number of members registered in the Society is 1,241 as of December 31, 2010. It changes from year to year, but it is far too small compared to that (about 4,500) of actual SPring-8 users. This situation needs to be improved to a large extent in order for the Society to play substantial role. Discussion is now being made to improve this situation.

The Industrial Users Society of SPring-8 was established by the members of various companies in September 1990 to promote the use of SPring-8 and to dedicate in the development of the SPring-8 user program. Several research groups focused on various fields of applications have been organized; nine are active. The main purpose of the society is not only to provide information on the trends of the synchrotron radiation facilities in Japan and abroad, and their latest research achievements, but also to enhance communication among the industrial sector, JASRI, and MEXT. As a result, the percentage of industrial applications has increased to 20% in terms of the number of proposals approved. The Society consists of 67 companies and one industry research organization as of December 31, 2010.

In 2009, the annual meetings of the two societies were jointly held for the first time, as the 1st SPring-8 Conference. Previously, these meetings were almost independently organized to report and discuss the outcomes from academic and industrial sectors, respectively. The success of the first joint conference was attributed to the direct exchange of information which made it possible to cross-fertilize both sectors.

Users Meeting

The 2010 meeting for users jointly organized by the SPring-8 Users Society and/or the Industrial Users Society of SPring-8, and JASRI and RIKEN.

- The 2nd SPring-8 Conference
  November 4-5, 2010 - Tokyo Station Conference, Tokyo

Conferences and Workshops

The conferences and workshops organized, sponsored, or hosted by JASRI and/or RIKEN in 2010 are listed below.

- 23rd Annual Meeting of Japanese Society for Synchrotron Radiation Research,
January 6-9, 2010 - Egret Himeji, Hyogo

- International Workshop on X-ray Imaging of Solidification of Metallic Materials
February 8, 2010 - Public Relations Center, SPring-8

- The Report Meeting of SPring-8 Medical Bio Trial Use and Medical Bio EX Proposals in FY2009-2010
March 15, 2010 - Translational Research Informatics Center, Hyogo

- The 12th APS-ESRF-SPring-8 Three-Way Meeting
April 12-14, 2010 - Public Relations Center, SPring-8

- The Annual Meeting of SPring-8 Priority Nanotechnology Support Program for FY2009
May 7, 2010 - Ritsumeikan University Biwako-Kusatsu Campus Rohm Plaza, Shiga

- The 7th Annual Meeting of Particle Accelerator Society of Japan
August 4-6, 2010 - Himeji Culture Center, Hyogo

- The 9th Annual Meeting of Structural-Biological Whole Cell Project of *Thermus thermophilus* HB8
August 20-22, 2010 - Public Relations Center, SPring-8

- Future Trend in Softmaterial Research with Advanced Light Sources
-Interdisciplinary of Bio- & Synthetic- Materials and Industrial Transferring-
September 1-3, 2010 - Public Relations Center, SPring-8

- The 6th XFEL Symposium
September 4, 2010 - Umeda Center Building Crystal Hole, Osaka

- Synchrotron Radiation Industrial Applications Seminar
-SPring-8/Ritsumeikan University SR Center Collaboration-
October 1, 2010 - Ritsumeikan University Biwako-Kusatsu Campus, Shiga

- The 3rd Workshop on the SPring-8 Budding Researchers Support Program
October 1, 2010 - Campus Innovation Centre, Tokyo

- The 6th International Workshop on Nano-scale Spectroscopy and Nanotechnology
October 25-29, 2010 - Kobe University Centennial Hall (Rokko Hall), Hyogo

- The 2nd Symposium on SPring-8 Upgrade Plan
December 4, 2010 - National Center of Sciences, Tokyo

Other Activities

- The 18th SPring-8 Open House
April 29, 2010

- The 10th SPring-8 Summer School 2010
July 24-27, 2010 - Public Relations Center, SPring-8

- The 4th AOFSRR School - Cheiron School 2010 -
October 9-18, 2010 - Public Relations Center, SPring-8

- SPring-8 special lecture entitled “Science for Cultural Heritage
Illuminated with Synchrotron Light”
November 20, 2010 - Noh Theatre of Nara Prefecture New Public Hall, Nara

Ikebana Exhibition
at the Open House

Project XFEL

2010 marked the 50th anniversary of the laser, which was invented to emit visible light at a wavelength of 694.3 nm. An interesting coincidence is that 2010 should also be remembered for the inauguration of user operations of LCLS, the first hard X-ray laser (at around 0.15 nm wavelength), at the SLAC national laboratory in the US. The X-ray lasers do not use any laser materials to amplify the X-rays, but use only free electrons with relativistic energy in a vacuum as radiating materials. Thus, these lasers are called X-ray Free Electron Lasers (XFELs). The scientific impact of the XFEL is so great that the supply of the beam time at the LCLS is far less than the demand from scientists around the world. It is now widely recognized that the few existing XFELs around the world are not enough to fulfill the demands of the frontier sciences and technologies. Scientists all over the world are waiting for the debut of our XFEL.

Another interesting coincidence is that 2010 is the final year of our XFEL construction project. We saw the completion of the Experimental Building in May, followed by the construction of radiation shields for end-stations as well as the assembly of X-ray optics including total reflection mirrors and a double-crystal monochromator. A building where both XFEL and SPring-8 beams intersect at the sample position will be completed by the end of March 2010. The intersection of the two beams enables both XFEL pump and SPring-8 probe type measurements, which enhances the synergy between XFEL and SPring-8. We started the RF aging process in October and finally started electron beam commissioning in February 2011. We are certain that we will observe lasing in the near future.

The concept of ‘Compact SASE Source’ originated by us is now widely recognized. This basically combines a high-gradient linac and a shorter period undulator. Several new XFEL projects have been proposed following our scheme, including initiatives in Switzerland, Korea and China.

The prototype EUV-FEL, known as SCSS, has been operated for users at around 60 nm wavelength. Several interesting and important experiments using the SCSS have already been carried out. In particular, we have achieved, for the first time in the world, the seeding operation with higher harmonics of the conventional laser. By seeding, temporal coherence of the FEL is greatly improved as compared with the SASE method. We are designing seeding schemes for shorter wavelength FELs.

Last but not least, we again encourage and invite completely new ideas for using the unique capabilities of our XFEL, which is located adjacent to the world’s brightest synchrotron radiation source, SPring-8.

We are pleased to announce our XFEL, named SACLA, has reached SASE lasing in June, 2011.

Tetsuya Ishikawa

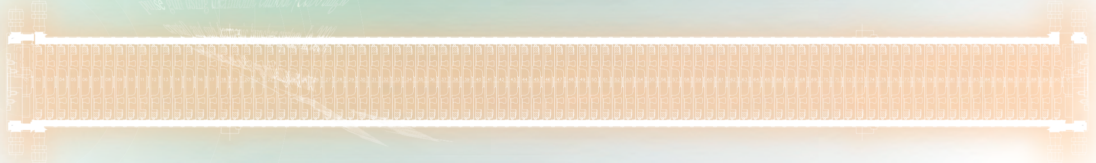

SPRING-8 COMPACT SASE SOURCE PROJECT
SCSS
SPRING-8
COMPACT
SASE
SOURCE

Progress of the XFEL Project

1. Status of XFEL Construction

A five-year construction project for an 8-GeV XFEL facility, which was started in FY2006 as one of the Key National Technologies in Japan, went well in FY2010, the final year of the construction. The manufacture of all the components was completed so full power rf aging started in October 2010.

We have completed the development of beam commissioning procedures and tools necessary for the XFEL beam commissioning. One of the most difficult developments was the modeling of the XFEL linear accelerator, which is essential for precise beam control achieving a high peak current of more than 3 kA. The model developed can consistently describe the transverse electron beam envelope and beam peak current at the lasing slice over the XFEL, i.e., from the electron gun cathode to the 8-GeV beam dump. Another difficult development was the design of a precise alignment method for a long undulator beamline over 100 m, of which the maximum allowed deviation from a reference straight line is ±4 mm. The beam-based method developed can satisfy the requirement without any iterative procedure. On the basis of the elaborate investigation, we have successfully prepared all the high-level software programs in order to perform the beam tuning required for stable high-power SASE XFEL. The beam commissioning was start on 21st February towards achieving the first lasing at least before summer 2011. Figure 1 shows the present schedule of the XFEL beam commissioning.

At the XFEL injector, a thermionic electron gun ejects 500-keV electron beam pulses from a CeB_6 cathode and the following bunching section composed of multistage rf cavities bunches and accelerates the beam to form a bunch of 30 MeV energy and 20 ps bunch width. The SCSS test accelerator has shown that this step-by-step bunching scheme promises the realization of the XFEL with its ultralow emittance beams. The installation of the XFEL injector system has almost been realized. The completed electron gun was operated to demonstrate its beam performance at the specified peak current of 1 A, as shown in Fig. 2. The multistage bunching section comprises a 238 MHz subharmonic buncher, a 476 MHz booster, L-band correction cavities, L-band accelerating structures and a C-band correction structure. Their rf powers have reached the required levels after the rf conditioning of every accelerating structure. The two L-band accelerating structures (see Fig. 3) of the alternative periodic structure (APS) type compress the 1-MeV beam bunch and accelerate it up to 35 MeV. A vacuum-type waveguide circuit is employed so as not to use insulation gases such as SF_6, that is, no circulator is available. Therefore, the circuit was carefully designed to cancel the reflected powers from the APSs so that the reflection to the klystron will not cause rf instability in the klystron output cavity [1].

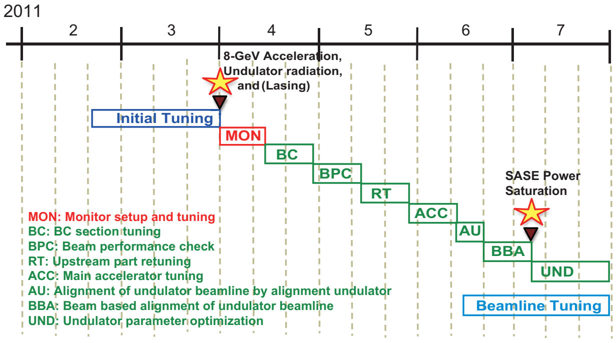

Fig. 1. Schedule of XFEL beam commissioning.

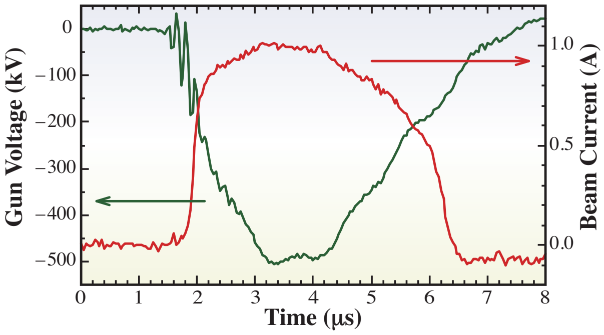

Fig. 2. Observed acceleration voltage pulse and beam current of 500-keV gun.

Fig. 3. L-band accelerating structures and their waveguide system.

The acceptable instabilities of the accelerating voltages in the gun and cavities, which permit a 10% rms variation of the peak beam current, are only about 0.01% rms in amplitude and 120 fs rms in phase according to results of the beam simulation. The long-term rf variations can be compensated by the feedback control of the rf amplitude and phase; the short-term or pulse-to-pulse variations, however, have to be reduced as much as possible by improving rf equipment such as amplifiers. Thus, we have carefully designed and manufactured rf cavities, amplifiers and control systems, giving the highest priority to the stabilization of short-term variations. Table 1 shows that the achieved short-term rf stabilities almost satisfy the requirements mentioned above.

We introduced geomagnetic correction coils to cancel the geomagnetic field by a uniform magnetic field to facilitate fine beam tuning at the long low energy section less than 1 MeV. Before the installation of the injector components, we found that the geomagnetic field was strongly distorted by the inhomogeneous magnetism of the reinforcing steel rods in the RC floor and this result suggested that the geomagnetic correction would not function well. We demagnetized the floor using a flat square coil generating an alternating and decaying field. The vertical components of the residual field with subtraction of the genuine geomagnetic field distribute in the range of 0 - 0.05 after the demagnetization, while in the range of –0.1 - 0.5 before it, as shown in Fig. 4.

Immediately after the completion of building construction and geological survey along the 400-m linear accelerator and 200-m undulator hall, the installation of the main accelerator started in Summer 2009. It took one and half years to complete the hardware components, i.e., the 128 C-band accelerator columns (1.8 m long each; Fig. 5), 64 C-band klystrons (Fig. 6), their pulse power supplies, and low power rf systems. During the fabrication and installation, we encountered several hardware problems. The most serious one was that the 50-kV PFN capacitor charger with high power switching circuitry underwent frequent breakdowns in resonant capacitors. After careful investigation, the cause was identified to be the gas discharge in the remaining micron-sized gaps among the winding aluminum foils and insulators. By optimizing the capacitor size, interior material and oil immerse process, this problem was successfully solved. Other problems were mostly trivial and were solved properly, and the hardware was successfully installed into the accelerator. From October 2010, we started the high power processing of the S-band (2856MHz) and C-band (5712 MHz) accelerators. After 300 hours of high power operation at 60 pps, the C-band reached 38 MV/m or more, while the S-band required 1000 hours to reach 17 MV/m. We confirmed the superior performance of the C-band system in terms of its high gradient acceleration capability. Some of the C-band klystrons showed multipacting discharge phenomena at lower power operation. Fortunately, it did not cause serious limitation in machine performance. The beam operation is scheduled to start in March 2011, and the first lasing at 1 Å is expected before Summer 2011.

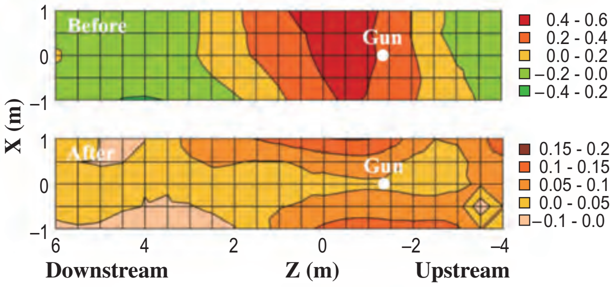

Fig. 4. Vertical magnetic field distribution on horizontal plane at height of beam (80 cm) in injector area before/after demagnetization. The geomagnetic components are subtracted.

Table. 1. Tolerances and achievements of short-term accelerating voltage variations

	Tolerance (σ)		Achievement (std.)	
	ΔV/V	Δϕ	ΔV/V	Δϕ
Gun	0.003%	—	0.001%	—
SHB	0.01%	0.01°	—	0.02°
Booster	0.01%	0.02°	0.013%	0.014°
L-Correction	0.03%	0.06°	0.026%	0.062°
L-APS	0.01%	0.06°	0.002%	0.004°
C-Correction	0.1%	0.1°	0.002%	0.004°

The XFEL/SPring-8 undulator is composed of 18 segments of in-vacuum undulators (IVUs), each of

Fig. 5. C-band acceleration unit installed in accelerator building.

Fig. 6. Modulator and timing systems in klystron gallery.

which has a magnetic period of 18 mm and a magnetic length of 5 m. The maximum K of 2.2 is available at a minimum gap of 3.5 mm. The design of each IVU is based on that of the SPring-8 storage ring with a minor revision to resist the larger mechanical load due to the stronger magnetic field. The construction of the IVUs was started in October 2008 and the construction of the first undulator was completed in October 2009. After the installation in the undulator hall, "*in situ*" field measurement, i.e., the measurement of the field distribution in the vacuum chamber, was carried out to check the magnetic quality variation during the assembly process in the field measurement facility and the transport to the XFEL facility. The field errors found in the measurement were corrected by finely adjusting the gaps at several positions along the undulator axis. Regardless of minor problem concerning vacuum components, the construction, installation, and *in situ* field measurement of all the undulator segments were completed by the end of August 2010 on schedule except for the installation of a few components. Figure 7 shows a photograph of the 18 segments installed in the undulator hall taken from the downstream side.

The installation of basic beam instruments, such as beam position monitors (BPM), current transformer (CT), and screen monitors (SCM), in the XFEL building proceeded after mass production of the instruments [2]. By the end of 2010, the installation was almost finished. Figure 8 shows the current state of the installation of the BPM and CT. Even though the installation is almost complete this year, we still have a problem that needs to be solved with a new idea, namely, the difficulty in measuring the position of a very horizontally flat beam shape in the energy-dispersive part, such as a bunch compressor chicane, and in observing a bunch length in the femtosecond region. Therefore, a multi-stripline beam position monitor (M-BPM) [3] with five 50 Ω striplines placed along a horizontal cross section for observing a beam position at the energy dispersive part was developed. This monitor can observe not only the mass center of a beam intensity distribution along a transverse direction, but also its rough distribution. Position sensitivity, as shown in Fig. 9, was measured at the SCSS test accelerator using a prototype M-BPM with three striplines. This sensitivity is sufficient for the beam tuning of the XFEL. For the bunch length measurement, monitor systems using optical transition radiation (OTR) observed with a streak camera, coherent synchrotron radiation (CSR) observed with

Fig. 7. Installed 18 IVU segments.

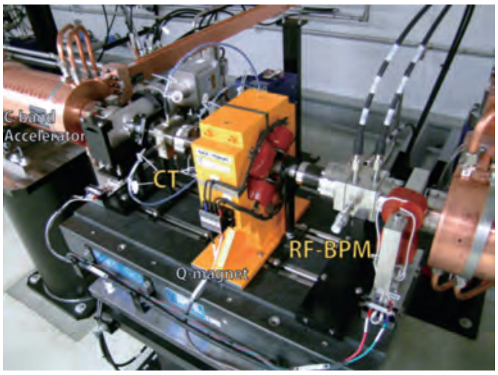

Fig. 8. BPM and CT installed in accelerator tunnel.

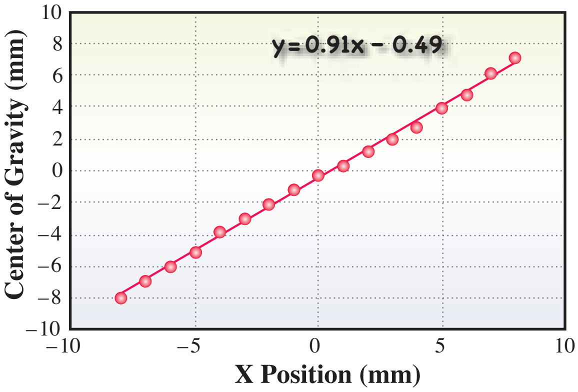

Fig. 9. Horizontal beam position dependence of gravity center of M-BPM signal. A linear function fitted to the data is also plotted.

a pyrodetector, and coherent transition radiation observed with a waveguide spectrometer have been developed [4].

The mass production of timing and low-level rf components, such as in-phase, quadrature phase and amplitude (IQ) detectors and modulators, as well as 600 W solid-state amplifiers for driving 50 MW high-power klystrons operated at the L- (1428 MHz), S- (2856MHz), and C- (5712 MHz) bands, was almost completed in the beginning of 2009 [5]. Furthermore, an optical time-reference signal transmission system, comprising a master oscillator, optical fiber cables, and electrical/optical and optical electrical converters using 1550 nm laser diodes and pin-photo diodes, for driving klystrons was fabricated [5,6]. After this mass production, all the instruments were installed into water cooling 19 inch racks; these racks were set in the XFEL building in 2009. At the end of 2009, the installation of the racks was almost finished, and rf conditioning for accelerating structures was started in December using these racks and an optical time-reference transmission system. During the rf conditioning operation, the racks and signal transmission system worked well without any major problems. Figure 10 shows the side-band noise level of a 5712 MHz carrier signal measured at the output of the system. This low-noise level of -150 dBc at a 1 MHz offset frequency is clear evidence of the soundness of our installed system.

The electromagnets of the XFEL/SPring-8 consist of 10 magnetic lenses (2 types), 114 quadrupole magnets (5 types), 121 steering magnets (5 types) and 28 bending magnets (7 types). Different from those of a storage ring, their magnetic fields and sizes should be increased with the beam energy along the linac. Therefore, a wide variety of magnet types are required. Since most of the magnets are operated by DC, pure iron blocks are used as a yoke material to reduce production cost except steering magnets. The installation of the magnets was completed by Summer 2010. Figure 11 shows a 6.7-m-long bending magnet installed before the 8 GeV beam dump. The magnetic fields of important magnets were remeasured after its installation in the accelerator tunnel. To avoid the hysteresis of iron yokes, the magnets are excited using a fixed current pattern. A magnetic field reproducibility on the order of 10^{-4} is attained with the pattern excitation. Since the steering magnets will be used for an orbit feedback system, their yokes are made of permalloy to reduce hysteresis. A field reproducibility of about 10^{-4} has been achieved for the steering magnets without any initialization or pattern excitation processes. The magnet power supplies are controlled by a VME-based optical linked I/O system. A remote VME card (i-DIO) is installed in a power supply chassis and one i-DIO card controls two output channels. An FPGA is also mounted in the i-DIO card, which evaluates and provides the status of the power supply for interlock systems.

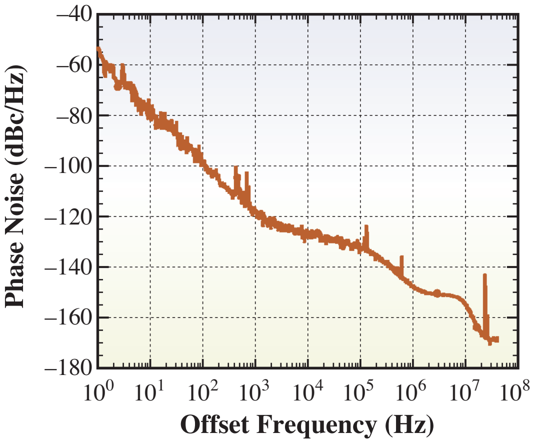

Fig. 10. Phase noise spectrum of 5712 MHz output signal from optical electrical converter installed at CB05-4 unit.

Fig. 11. Bending magnet installed before final beam dump.

The vacuum component assembly and installation, cabling installation, leak test and vacuum system operation test were completed in FY2010. The pressures were on the order of 10^{-7} Pa or less. The cold cathode gauge (CCG) arranged near the beamline was inserted into the steel pipe to decrease the leakage magnetic field of its permanent magnet. For the beam-based-alignment technique, the allowable magnetic field upstream of the insertion devices is below 0.4 mG. To decrease the magnetic field, the material of the chamber support was changed from SS400 to SUS316L, and the magnetic field sources such as the sputter ion pump and CCG were placed far from the beam. The vacuum pipes were wrapped with a magnetic shielding sheet. The undulator and the adjacent motion stage on which the electromagnet and the BPM are mounted can move independently. The allowable tolerance of the bellows connected to their vacuum chambers was 2 mm. The limit switches were set to prevent the bellows from damage caused by large deformation. The limits of the motion along the vertical and horizontal directions were set at ±1.41mm, and the measured repeatability error within a short period was 3 μm.

In the installation and alignment of the XFEL facilities, although the accelerator building is a base of pile foundation supported by a bedrock layer, a 0.1 mm/month subsidence was observed in December 2010 at the midpoint of the building, where the embankment is thickest (50 m). Accelerating structures, BPM, and Q-magnets (Q-Mags) in the building were aligned within ±0.3 mm along a smooth line. The light source building was more stable. For this building, a direct foundation on a bedrock or an artificial layer replaced by excavation with crusher stone was adopted. Insertion devices, BPM and Q-Mags in this building were aligned within ±0.2 mm along a straight line.

An Electron Beam Transport Line was designed to transport a high-quality electron beam from XFEL-Linac to the SPring-8 storage ring (XSBT). The fabrication of all components of the XSBT was completed in March 2010. The installation and final alignment works in the XFEL undulator building were completed in summer 2010. Field measurements for all the bending magnets were completed prior to their installation.

Several key experimental facilities were completed in 2010. After the inauguration of the XFEL Experimental Building in May, four experimental hutches were constructed in the experimental hall (Fig. 12). The beamline components and X-ray optical devices, such as mirrors and double-crystal monochromator (DCM), were installed in the optics hutch. A laser booth for containing the synchronization laser and a timing distribution system were prepared. A beamline for the XFEL-SPring-8 Experimental Facility, which is built for the simultaneous utilization of XFEL and SPring-8 undulator radiation, has also been designed.

Fig. 12. Experimental hutches.

In parallel with the construction works, R&D for XFEL utilization has been performed. In particular, the Plasma Chemical Vaporization Machining (Plasma CVM), which was developed by Osaka University, was used in fabricating thin crystal devices as key components of an X-ray beam splitter. We found that a strain-free, thin window of sub-100 micron thickness is achievable using this technique.

The development of seeding technologies is crucial for upgrading FEL radiation properties and achieving the Fourier-limited pulses. A test experiment was performed at the SCSS test accelerator in close collaboration with RIKEN ASI, JAEA, and the University of Tokyo. A 13th harmonic of a Ti:sapphire (Ti:S) laser in a plateau region was injected as a seeding source into the SCSS. Random and uncontrollable spikes in the Self-Amplified Spontaneous Emission (SASE)-based FEL radiation were found to be strongly suppressed to form a narrow-band, single peak profile at 61.2 nm when the seeding conditions were fulfilled. This technology will be extended to shorter-wavelength regions such as the water-window region between 2 to 4 nm (Fig.13).

In the XFEL experiments, two-dimensional (2D) X-ray detectors optimized for XFEL applications are required to explore the full potential of the XFEL source. As the standard 2D X-ray detector of the facility, the multi-port CCD (MPCCD) detector was developed in March 2009. In 2010, MPCCD sensors and their readout electronics were manufactured and characterized. Detector noise, which is one of the most important performance features, has been demonstrated. The detector assembly for single, dual, and octal sensor detector systems is in progress. Advanced 2D sensor development based on silicon-on-insulator CMOS technology has been carried out. The use of floating-zone wafer has enabled 500-mm-deep depletion. This deep depletion together with back-illumination geometry will improve radiation

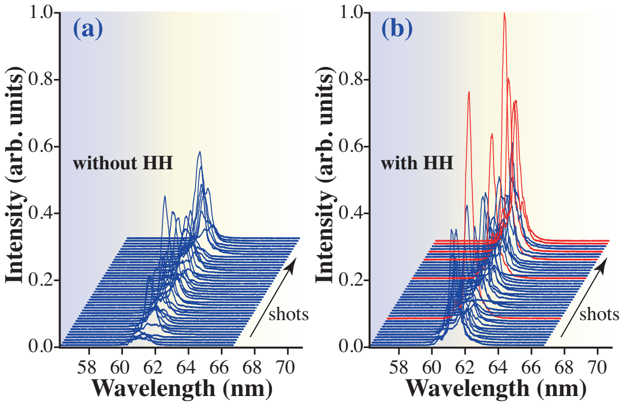

Fig. 13. Comparison of radiation spectra of FEL under unseeded (a) and seeded (red curves in b) conditions.

hardness and quantum efficiency enough to meet the XFEL requirements. After obtaining these results, the development of production detector was started. A data acquisition system for MPCCD, commercial cameras, and waveform digitizers is now being developed. All the data are labeled by trigger numbers and stored by high-speed storage. The development of a DAQ system for the optical hutch and other experimental hutches is now in progress.

2. Operation Status of the SCSS Test Accelerator

After the proof-of-principle experiment showing that an FEL system based on the SCSS concept can generate a high-performance SASE FEL, the test accelerator has been improved aiming at an ideal FEL operation. Despite the day-by-day operation, the continuous power saturation of a SASE FEL has been routinely obtained at wavelengths from 50 to 60 nm. In FY2010 (9 months from April to December), the total beam time is 155 days, and 54% of this or 83 days was provided to user experiments. The regular beam time in a day is currently 9 h from 10:00 a.m. to 7:00 p.m.

2-1. Summary of user experimental programs

In 2010, the EUV-FEL experimental facility accommodated about 100 scientists representing 18 scientific groups not only from Japan but also worldwide, such as Germany, Italy, Netherlands, and Czech Republic. Research using EUV-FEL is carried out in a large variety of disciplines, including technical research preparatory for XFEL experiments, atomic and molecular physics, coherent diffraction imaging methods, damage of optics, materials science, and the science of various devices such as advanced scintillators and nonlinear X-ray devices. The number of publications from the users of EUV-FEL in FY 2010 was ten [i - x].

Here, we show one of the specially chosen research highlights. The group of Hikosaka has observed a multiphoton double ionization in an intense EUV field using shot-by-shot photoelectron spectroscopy [v]. Figure 14 shows photoelectron spectra in the range of the Ar^{2+} $3p^{-2}$ peaks, derived from single-shot basis analysis. The experiment illustrated that the dominant ionization pathway of argon atoms has two steps: first, a single laser photon is absorbed to create singly ionized argon, and then two more photons are absorbed to create doubly ionized argon. In addition, Hikosaka's group found that the intermediate argon ion states have energy levels, or energy resonances, that induce this pathway.

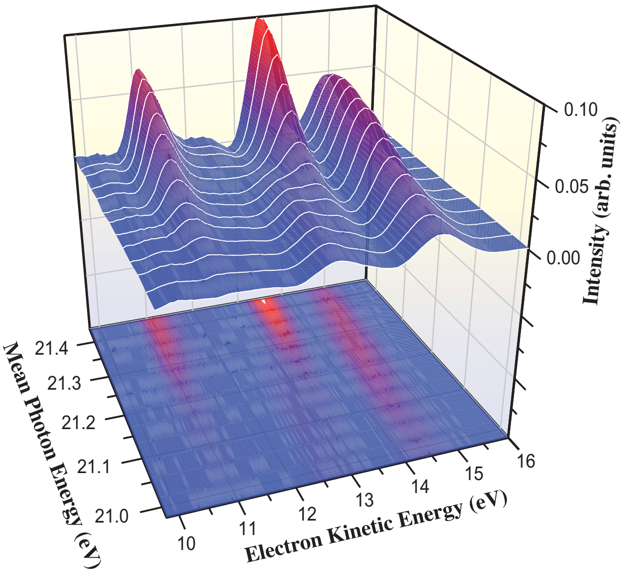

Fig. 14. Photoelectron spectra in range of $Ar^{2+}3p^{-2}$ peaks, derived from single-shot basis analysis.

SPring-8 Joint-Project for XFEL

E-mail: Project-XFEL@riken.jp

References

[1] H. Hanaki *et al.*: Proc. of IPAC'10 (2010) 1722.
[2] S. Matubara *et al.*: Proc. of IPAC'10 (2010) 957.
[3] H. Maesaka *et al.*: Proc. of IPAC'10 (2010) 945.
[4] Y. Otake *et al.*: Proc. of BIW10 (2010) - *in press*.
[5] N. Hosoda *et al.*: Proc. of IPAC'10 (2010) 2191.
[6] T. Ohshima *et al.*: Proc. of IPAC'10 (2010) 1390.

Publication list from the users:

[i] H. Ohashi *et al.*: Nucl. Instrum. Meth. A (2011) - *in press*.
[ii] Y. Nishino *et al.*: Appl. Phys. Exp. **3** (2010) 102701.
[iii] K. Nagaya *et al.*: J. Electron Spectros. Relat. Phenom. **181** (2010) 125.
[iv] M. Kato *et al.*: Metrologia **47** (2010) 518.
[v] Y. Hikosaka *et al.*: Phys. Rev. Lett. **105** (2010) 133001.
[vi] K. Yamanoi *et al.*: Opt. Mater. **32** (2010) 1305.
[vii] H. Iwayama *et al.*: J. Phys. B: At. Mol. Opt. Phys. **43** (2010) 161001.
[viii] A. Yamada *et al.*: J. Chem. Phys. **132** (2010) 204305.
[ix] H. Fukuzawa *et al.*: J. Phys. B: At. Mol. Opt. Phys. **43** (2010) 111001.
[x] S.Y. Liu *et al.*: Phys. Rev. A **81** (2010) 031403(R).

NewSUBARU

The 1.5 GeV synchrotron radiation ring named NewSUBARU is the main facility of the Laboratory of Advanced Science and Technology for Industry (LASTI) at the University of Hyogo. NewSUBARU is at the site of SPring-8 and can provide light beams from IR to soft X-rays. We have achieved storing 500 mA at 1 GeV and 200 mA at 1.5 GeV. At present, NewSUBARU has six bending section beamlines (i.e., BL-2, BL-3, BL-5, BL6, BL-10, and BL-11), a short undulator beamline (BL-7), a long undulator beamline (BL-9) and an optical-klystron beamline (BL-1), as shown in Fig. 1.

The topics of the NewSUBARU research activities of this year are as follows. First is the basic characteristic research of NewSUBARU electron storage ring and imaging with laser Compton scattering gamma rays. Second is EUV (extreme ultraviolet) activities that include the mask observation using a coherent EUV scattering microscope, nanostructure pattern replication using a newly developed EUV interference lithography system, and the development of new EUV resists with a low LER (line edge roughness). BL-9C branched from BL-9B for use in EUV interference lithography for the evaluation of the exposure characteristics of EUV resists. Third is micro- and nano-devices such as a high-aspect ratio microcoils, three-dimensional lab-on-CDs and X-ray gratings for X-ray Talbot interferometer. Fourth is the materials science of various materials such as hydrogenated DLC, a-C:H and BN.

Furthermore, the performance of the material analysis beamline BL-5 for industrial enterprises was evaluated by NEXAFS spectra measurements using standard samples of graphite, BN, LiCl and MgO.

Most of our research activities are being conducted in collaboration with industries, government research institutes and some universities.

We will continue to respond to the community's demand by offering new science and technologies.

Shinji Matsui
Director of LASTI, University of Hyogo

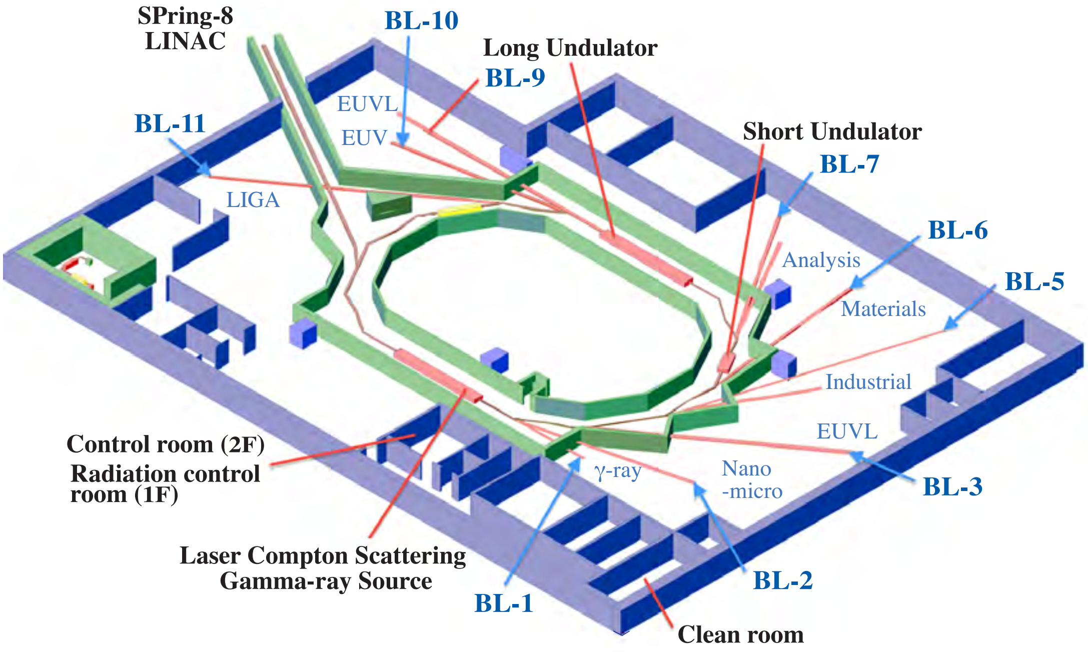

Fig. 1. Beamline arrangement in NewSUBARU.

Major Activity of NewSUBARU

1. Imaging for Stress Corrosion Cracking in Stainless Steel with Laser Compton Scattering γ-ray

Stress corrosion cracking (SCC), a defect occurring in structures of nuclear power plants or chemical plants, has very intricate ramification and produces narrow cracks. Thus far, it has been difficult to observe the actual 3D SCC shape of small specimens. Therefore, we performed an imaging experiment using γ-ray for large specimens (a few dozens of mm thick). SUS316L stainless steel samples were used as specimens in this imaging experiment. In each specimen, SCC was artificially developed in high-pressure pure hot water at 300°C. The imaging experiment was performed using γ-ray in NewSUBARU BL-1A. Figure 1 shows the experimental equipment used. In this experiment, γ-ray was generated by the collision between a CO$_2$ laser and electrons. Imaging measurement using 1.76 MeV γ-ray was performed for stainless steel specimens with SCC or artificial slit. A clear slit image was confirmed for a stainless steel specimen up to 30 mm thick. On the other hand, an SCC image was confirmed for a 10-mm-thick specimen, although the image was not as clear as that shown in Fig. 2. The result indicates that laser Compton scattering γ-ray imaging may be a good non-destructive defect detection technique compared with ultrasonic testing.

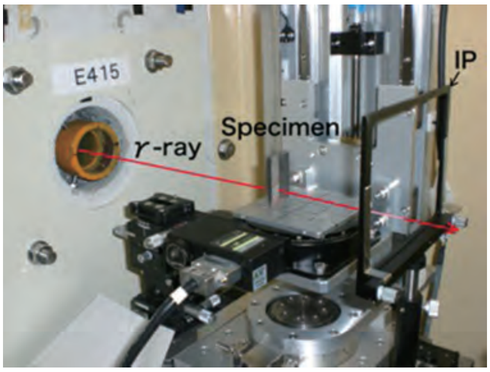

Fig. 1. Experimental equipment.

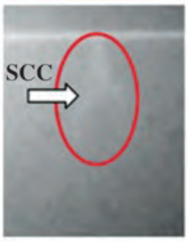

Fig. 2. Image of SCC in SUS316L specimen.

2. Imaging Performance Improvement of an Extreme Ultraviolet Microscope

The extreme ultraviolet microscope (EUVM) has been developed for the actinic mask inspection of an EUV finished mask and an EUV blank mask. Using this microscope, amplitude defects on a finished mask and phase defects on a glass substrate are observed. However, it has a problem of low contrast, which originates from (i) the thermal noise of a charge-coupled device (CCD) camera, (ii) wave aberrations of an optical component, and (iii) a non-uniform illumination intensity. To resolve these issues, EUVM was improved. (i) To reduce thermal noise, a cooled CCD camera was installed. (ii) To remove wave aberrations of a back-end turning mirror, a Mo/Si multiplayer-coated thick glass substrate with a high surface accuracy was employed instead of a Si wafer substrate. Furthermore, *in situ* alignment was carried out to remove wavefront aberrations for a Schwarzschild imaging optics. In addition, (iii) by installing a scanning system on the front-end turning mirror, a highly uniform illumination intensity was achieved. As a result, images of less than 100 nm without astigmatism were obtained and are shown in Fig. 3.

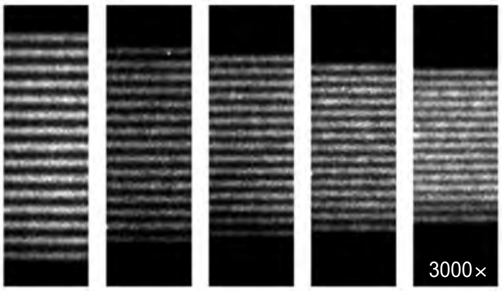

Half pitch	150	130	120	110	100 nm
Contrast	0.34	0.26	0.25	0.22	0.18

Fig. 3. EUVM images of 150-, 130-, 110- and 100-nm-hp patterns and their contrast values.

3. Fabrication of X-ray Grating Using X-ray Lithography for X-ray Talbot Interferometry

X-ray radiographic imaging is very important in various fields such as medical, biological, inspection, and materials science. However, it is not sufficient to obtain clear X-ray images of samples with low absorbance materials, such as biological soft tissues. Thus, we used X-ray phase imaging method of an X-ray Talbot interferometer (XTI). In this method, X-ray gratings are required to have a narrow pitch and a high aspect ratio structure. Therefore, we fabricated X-ray gratings with a pitch of 5.3 μm and a large effective area of 60 × 60 mm^2 for X-ray Talbot interferometry. A carbon wafer as a membrane material of an X-ray mask was used to solve problem of the heat transformation of the membrane that happened at the time of X-ray exposure, as shown in Fig. 4. To make a higher aspect ratio X-ray grating, we developed a fabrication process composed of X-ray lithography and micro-electroforming method. In X-ray lithography, sticking was observed because of surface tension. Therefore, to avoid the sticking, the top surface of X-ray grating was modified by overexposure. The result showed that a resist structure with a high aspect ratio and a narrow pitch was obtained without surface tension in a large area. After Au electroforming, a large area and narrow pitch X-ray grating was fabricated, as shown in Fig. 5.

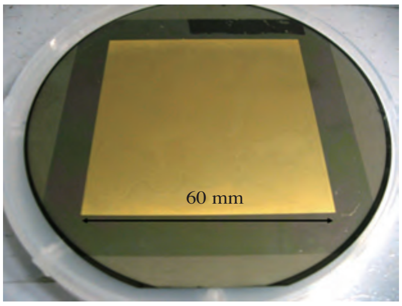

Fig. 4. Photograph of carbon X-ray mask.

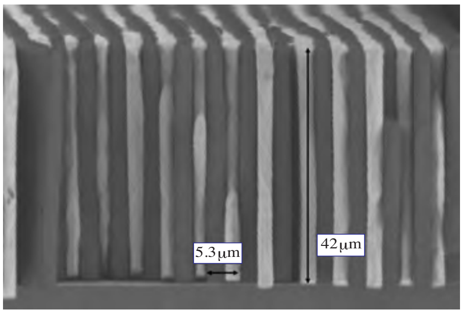

Fig. 5. SEM image of X-ray grating in cross section.

4. High-Precision Analysis for Material Analysis Beamline at BL-5 for Industrial Enterprises

A material analysis beamline for industrial enterprises was completed at BL-5 in March 2008. BL-5 consists of two branch lines, a double-crystal monochromator beamline (BL-5A) for use in the higher-energy region (1300-4000 eV) and a varied line spacing plane grating (VLSPG) monochromator beamline (BL-5B) for use in the lower-energy region (50-1300 eV), that cover the whole energy range of the soft X-ray region from 50 eV to 4000 eV. Both branch lines can be operated simultaneously. X-ray absorption fine structure (XAFS) measurements of total electron yield (TEY) and fluorescence yield (FLY) can be performed at BL-5A and BL-5B. In addition, X-ray photoelectron spectra (XPS) can be measured at BL-5B. We measured standard samples by the TEY method at BL-5B and obtained absorption spectra in each grating, i.e., 100 or 300 or 800 lines/mm. Figure 6 shows the boron *K*-edge near-edge X-ray absorption fine structure (NEXAFS) spectra of *h*-BN. The spectrum has been normalized to I_0 and had the linear pre-edge background removed. For *h*-BN, an intense peak at 191 eV appeared clearly in Fig. 6, which is assigned to transition from B1s to the unoccupied B2*p* π*, the spectrum of which was of the same shape as that reported by Jiménez *et al*. [1].

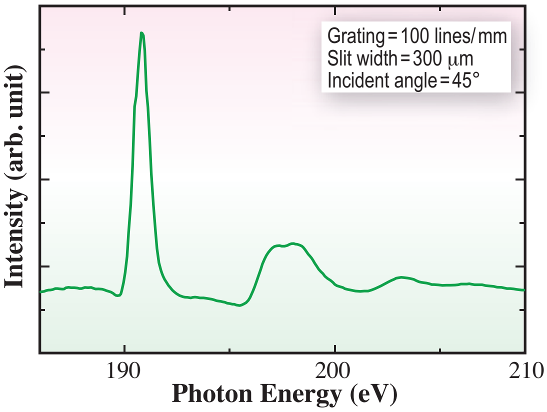

Fig. 6. *h*-BN B *K*-edge NEXAFS spectrum.

References

[1] I. Jiménez *et al*.: Phys. Rev. **B55** (1997) 12027.

Editor
Seishi Kikuta
SPring-8 / JASRI

Editing, Design & Layout
Marcia M. Obuti-Daté
SPring-8 / JASRI

Printing
ROKKO Publishing & Sale Co.

JASRI
Library and Information
Users Administration Division

1-1-1 Kouto, Sayo-cho, Sayo-gun
Hyogo 679-5198 • JAPAN
Tel. +81-(0)791 58-2797 Fax. +81-(0)791 58-1869

frontiers@spring8.or.jp
http://www.spring8.or.jp/

August 2011

Japan Synchrotron Radiation Research Institute
1-1-1 Kouto, Sayo-cho, Sayo-gun, Hyogo 679-5198 JAPAN

http://www.spring8.or.jp